

# **XMM AND ROSAT OBSERVATIONS OF CLUSTERS OF GALAXIES**

A thesis submitted for the degree of  
Doctor of Philosophy  
at the University of Leicester.

by

**Louise Spurgeon**

X-ray and Observational Astronomy Group  
Department of Physics and Astronomy  
University of Leicester

September 2002

UMI Number: U486354

All rights reserved

INFORMATION TO ALL USERS

The quality of this reproduction is dependent upon the quality of the copy submitted.

In the unlikely event that the author did not send a complete manuscript and there are missing pages, these will be noted. Also, if material had to be removed, a note will indicate the deletion.



UMI U486354

Published by ProQuest LLC 2013. Copyright in the Dissertation held by the Author.  
Microform Edition © ProQuest LLC.

All rights reserved. This work is protected against  
unauthorized copying under Title 17, United States Code.



ProQuest LLC  
789 East Eisenhower Parkway  
P.O. Box 1346  
Ann Arbor, MI 48106-1346

## Abstract

I present an investigation into the X-ray properties of galaxy clusters, consisting of a principal component analysis of ROSAT data and studies of three clusters observed with the XMM-Newton satellite.

The principal component analysis provides an investigation into similarities between cluster surface brightness profiles. Initial results for 42 clusters are presented and compared to existing models. The cluster profiles are reproduced to good accuracy using three principal components. Correlation of the principal components to physical properties is investigated but the results are inconclusive.

Observations of Abell 1413, Abell 665 and Abell 2163 made with XMM-Newton were investigated spectrally and spatially to determine cluster properties. Global temperatures were found to be  $7.08 \pm 0.13$  keV for Abell 1413;  $5.46 \pm_{0.13}^{0.14}$  keV for Abell 665 and  $11.98 \pm 1.2$  keV for Abell 2163. The temperature and abundance profiles of the clusters are very different, with some differences attributed to the recent merging of sub-clusters in Abell 665 and Abell 2163. Spatial analysis of the cluster surface brightness profiles is undertaken with  $\beta$  and NFW models.

The profiles produced for the three clusters are used to estimate the variation of gas, gravitational and iron mass with radius. These are used to draw general conclusions, such as supernovae numbers ( $N_{SNI} \sim 10^{9-11}$ ). The cosmological density and matter density parameters are found;  $\Omega_0 = 0.22 - 0.33 \pm 0.1$  and  $\Omega_m \geq 0.12 \pm_{0.04}^{0.06}$ . This suggests a low density universe, but is subject to uncertainty due to extrapolation to larger radii.

*For my grandparents*

# Acknowledgements

I would like to start by thanking my parents for their constant love and support over the years, without which none of this would have been possible.

Thank you to Gordon for his supervision over the past three years and Sergio for his help in understanding clusters and introducing me to the joys of Fortran 77.

I would like to thank my office mates over the three years I have been in Leicester, for their friendship, amusing comments and ability to find fun things to do that don't involve too much work!! Thanks to Becky, Unal, Chris, Anastasia, Fraser, Mike, Tim, Owen, Sam and Dave. I would also like to thank Dan, Roland, Charlotte, Norma and all the other Theory and XRA postgrads and postdocs for making my time here in Leicester a memorable one. Thanks to my house mates Eva and the two Caroline's for being there to commiserate with after a hard days work.

Thank you to my friends from elsewhere in the country, for always taking an interest and for providing useful diversions whilst I was away from Leicester. Thanks to Laura, Paula, Jennie, Stephen, Claire, all the MUSC caver's and everyone else who has remembered me despite my being so far away.

Finally my special thanks goes to Tim, who never gave up on me even when I was a real pain and saying 'I'll never finish, ever!!'. Thank you for all the support and the help with programming and even basic maths when my brain had ceased to be able to manage it. Thanks for being such good company in these last few months and always being there to cheer me up. All in all thanks for being such a very good friend!

Lastly thanks to anyone else whom I have missed in the above ....I've not forgotten you honestly!!

# Contents

<b>1</b>	<b>Introduction</b>	<b>1</b>
1.1	Overview . . . . .	1
1.2	Galaxy Clusters . . . . .	1
1.3	Optical Properties of Clusters . . . . .	4
1.3.1	Cluster Classifications . . . . .	4
1.3.2	Cluster Morphologies . . . . .	4
1.3.3	Galaxy content . . . . .	5
1.3.4	cD Galaxies . . . . .	6
1.3.5	The Virial theorem . . . . .	7
1.4	X-ray emission from clusters of galaxies . . . . .	8
1.4.1	The King potential . . . . .	8
1.4.2	The NFW distribution . . . . .	11
1.4.3	Principal Component analysis . . . . .	15
1.4.4	The Intra-cluster Medium . . . . .	15
1.4.5	The X-Ray Spectrum . . . . .	16
1.4.6	Determination of Cluster Mass . . . . .	17
1.4.7	Origin of the Intra Cluster Medium . . . . .	18

<b>CONTENTS</b>	<b>II</b>
1.4.8 Cooling Gas . . . . .	19
1.4.9 Steady State Conduction model . . . . .	20
1.5 Dark Matter Component in clusters of galaxies . . . . .	21
1.5.1 Gravitational Lenses . . . . .	21
1.5.2 The Sunyaev-Zel'Dovich effect . . . . .	22
1.5.3 Cosmology . . . . .	23
1.6 This thesis . . . . .	25
<b>2 Instrumentation</b>	<b>27</b>
2.1 Overview . . . . .	27
2.2 Introduction . . . . .	27
2.3 XMM-Newton Configuration . . . . .	29
2.4 X-ray mirror assembly . . . . .	29
2.5 The EPIC detectors . . . . .	33
2.5.1 Performance characteristics . . . . .	37
2.6 ROSAT . . . . .	41
2.6.1 The Position Sensitive Proportional Camera (PSPC) . . . . .	41
<b>3 Data Reduction and Analysis Techniques</b>	<b>44</b>
3.1 Introduction . . . . .	44
3.2 XMM EPIC data processing techniques . . . . .	44
3.2.1 Data products . . . . .	44
3.2.2 EPIC data processing pipeline . . . . .	45
3.2.3 XMM-Newton X-ray Background . . . . .	45

<b>CONTENTS</b>	<b>III</b>
3.2.4 Soft Proton Events . . . . .	47
3.2.5 Background Subtraction . . . . .	48
3.2.6 Other Corrections . . . . .	51
3.3 Spectral Analysis . . . . .	52
3.3.1 Epic fitting procedures . . . . .	52
3.3.2 Spectral Models . . . . .	53
3.4 EPIC Image Analysis . . . . .	55
3.4.1 Radial Profiles . . . . .	55
3.5 ROSAT PSPC reduction . . . . .	56
<b>4 A PCA of Cluster Surface Brightness Profiles</b>	<b>59</b>
4.1 Overview . . . . .	59
4.2 Introduction . . . . .	59
4.3 The Cluster sample . . . . .	61
4.4 Initial Data Reduction . . . . .	63
4.4.1 Creation of Median profiles . . . . .	63
4.4.2 Cubic Spline Interpolation . . . . .	65
4.5 Principal Component Analysis . . . . .	67
4.6 Discussion . . . . .	71
4.6.1 The Principal Components . . . . .	71
4.6.2 Physical Correlations and Trends . . . . .	71
4.6.3 Non detection of expected correlations . . . . .	78
4.7 Conclusions and Future work . . . . .	86

<b>CONTENTS</b>	<b>IV</b>
<b>5 A study of the galaxy cluster A1413</b>	<b>88</b>
5.1 Overview . . . . .	88
5.2 Introduction . . . . .	88
5.3 Observation and Data Reduction . . . . .	90
5.4 Spatial Analysis and Cluster Morphology . . . . .	92
5.4.1 King profile fits . . . . .	92
5.4.2 Comparison between the King profile and the NFW profile . . . . .	94
5.5 Spectral Analysis . . . . .	94
5.5.1 Background subtraction . . . . .	96
5.5.2 Single Temperature vs Cooling Flow Fits . . . . .	96
5.6 Discussion . . . . .	103
5.6.1 Global Cluster Temperature . . . . .	103
5.6.2 Temperature profiles . . . . .	105
5.6.3 Steady state conduction model . . . . .	108
5.6.4 Abundance profiles . . . . .	110
5.6.5 Determination of Gas Mass and Gravitational Mass . . . . .	112
5.6.6 Determination of Cluster Iron Mass . . . . .	115
5.7 Summary . . . . .	117
<b>6 A study of the galaxy cluster A665</b>	<b>120</b>
6.1 Overview . . . . .	120
6.2 Introduction . . . . .	120
6.3 Observation and Data Reduction . . . . .	121
6.4 Spatial Analysis . . . . .	123

6.4.1	Comparison between the $\beta$ profile and the NFW profile . . . . .	124
6.5	Spectral Analysis . . . . .	127
6.5.1	Background subtraction . . . . .	127
6.5.2	Spectral Fitting . . . . .	127
6.5.3	Power Law Fits . . . . .	133
6.6	Temperature Maps . . . . .	134
6.7	Discussion . . . . .	136
6.7.1	Global Cluster Temperature . . . . .	136
6.7.2	Temperature profiles . . . . .	137
6.7.3	Abundance profiles . . . . .	139
6.7.4	Gas and Gravitational Mass Estimates . . . . .	141
6.7.5	Iron Mass Estimate . . . . .	145
6.8	Summary . . . . .	146
<b>7</b>	<b>A study of the galaxy cluster A2163</b>	<b>148</b>
7.1	Overview . . . . .	148
7.2	Introduction . . . . .	148
7.3	Observation and data reduction . . . . .	149
7.4	Spatial Analysis . . . . .	152
7.4.1	Comparison between the $\beta$ profile and the NFW profile . . . . .	152
7.5	Spectral Analysis . . . . .	154
7.5.1	Background subtraction . . . . .	155
7.5.2	Spectral Fitting . . . . .	155
7.6	Discussion . . . . .	161

7.6.1	Global Temperature of the Cluster . . . . .	161
7.6.2	Temperature profiles . . . . .	161
7.6.3	Abundance Profiles . . . . .	164
7.6.4	Gas and Gravitational Mass Estimates . . . . .	166
7.6.5	Iron Mass Estimate . . . . .	169
7.7	Summary . . . . .	172
<b>8</b>	<b>How Self Similar are Clusters of Galaxies?</b>	<b>174</b>
8.1	Overview . . . . .	174
8.2	Comparisons of Physical Properties between the three clusters . . . . .	175
8.2.1	Temperature Profiles . . . . .	175
8.2.2	Abundance Profiles . . . . .	178
8.2.3	Gas and Gravitational Masses . . . . .	181
8.3	Global Implications . . . . .	183
8.3.1	Supernovae and chemical enrichment . . . . .	183
8.3.2	Mass-Luminosity Relation . . . . .	186
8.3.3	Luminosity-Temperature relation . . . . .	188
8.3.4	Mass Temperature relation . . . . .	190
8.3.5	Gas Mass fractions . . . . .	190
8.4	Self Similarity . . . . .	193
8.5	Future Work . . . . .	194

# Chapter 1

## Introduction

### 1.1 Overview

Galaxy clusters are the largest gravitationally bound structures in the universe. They are large,  $\sim 2\text{-}5$  Mpc, massive  $\sim 10^{15} M_{\odot}$  and contain of order 100-1000 galaxies. They also contain large amounts of a hot optically thin plasma, at  $T \sim 10^{7-8}$  K which emits in X-rays mainly via the thermal bremsstrahlung process.

This thesis looks at emission from 3 rich clusters observed with XMM-Newton as well as 42 clusters observed with the ROSAT PSPC. In this chapter the background to this study is discussed, including results from earlier studies and other wave bands. This is then used in subsequent chapters to compare with the results obtained from this investigation.

### 1.2 Galaxy Clusters

Galaxy clusters are the largest clearly defined objects in the universe. They consist of three main components; galaxies, gas and dark matter. There are typically 100-1000 galaxies in a cluster, which are bound by a common gravitational potential. An example

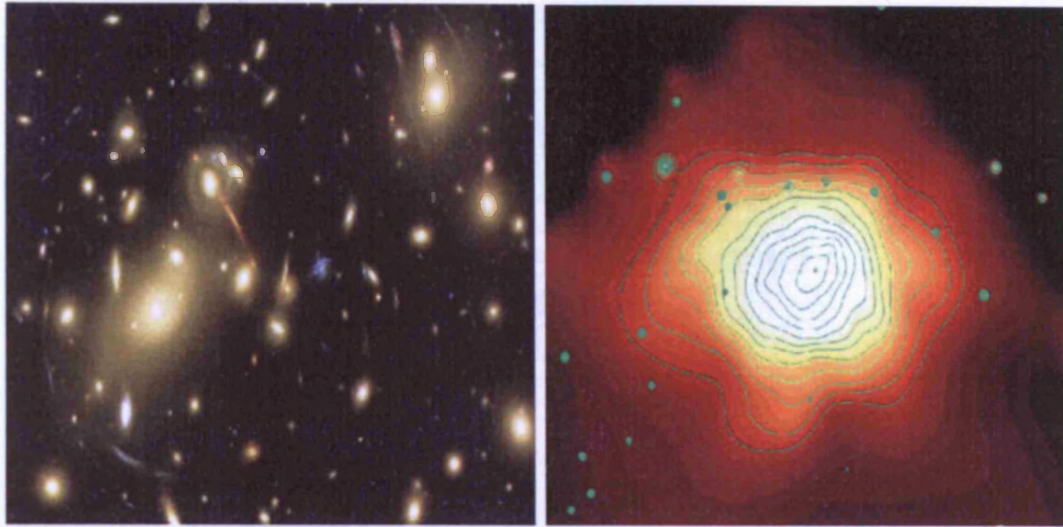


FIGURE 1.1. Images of lensing cluster Abell 2218. The optical image is from the HST WFC. The X-ray image is a smoothed Chandra image of the cluster from (Machacek et al. 2002). The contours are X-ray emission intensity contours superimposed on the X-ray image.

of an optical image of a cluster is shown in figure 1.1. This image is of a lensing cluster, Abell 2218 and was taken using the Hubble Space Telescope (HST). It shows a large number of cluster galaxies, as well as some background sources, including the lensed galaxies. The radial extent of a cluster to which galaxies are seen, is generally about 2-5 Mpc. Approximately 50% of clusters have a dominant central galaxy (cD) (Sarazin 1988) which is commonly a giant elliptical, sitting in the centre of the cluster potential. The total gravitational mass of a typical relaxed cluster is of the order  $10^{14-15}M_{\odot}$ .

Clusters contain large amounts of hot ionised gas which is at a temperature of  $10^{7-8}$  K. This gas emits radiation at X-ray wavelengths via thermal bremsstrahlung emission. The mass of gas in the cluster tends to be about 10-20% of the total mass of the cluster (White, Jones & Forman 1993). An example of an X-ray image is shown in figure 1.1 for the cluster Abell 2218.

It has been known for some time that the total mass of galaxy clusters estimated both from the virial theorem and using hydrostatic equilibrium (explained later) is greater than the sum of the gas and galaxy masses. (The mass to light ratio for clusters is  $\sim 300$

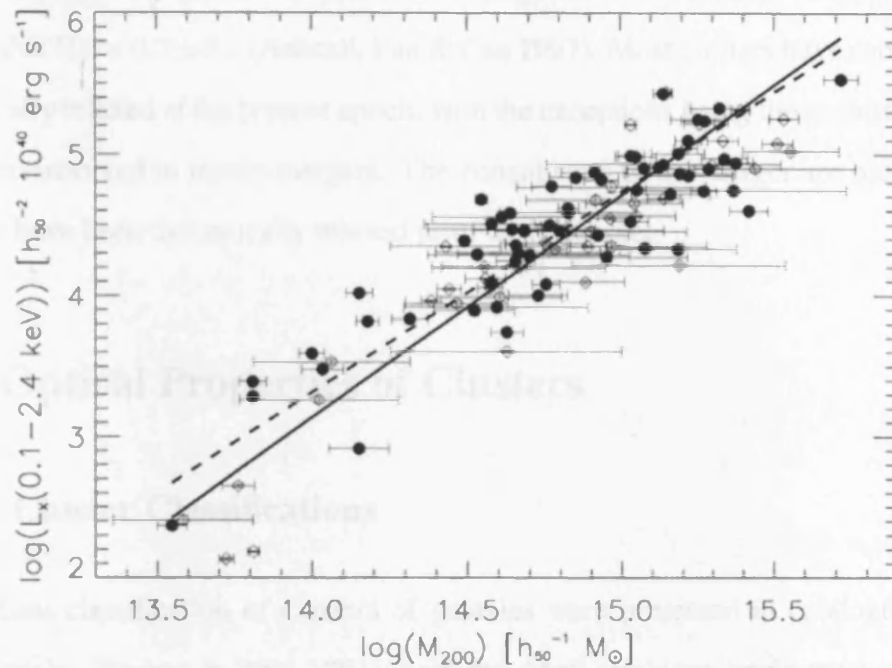


FIGURE 1.2. Mass to light ratio of a sample of clusters of galaxies produced by (Reiprich & Bohringer 2002). This shows a linear relationship between mass and luminosity. The luminosity is X-ray luminosity in the ROSAT band, but the relationship is the same using a bolometric luminosity

(Sarazin 1988)). Therefore the missing matter must be in the form of dark matter that is not directly detectable. One way of determining the mass of the dark matter component is to look at gravitational lenses. As can be seen by the optical image in figure 1.1 the cluster lenses a background galaxy and produces images in a partial ring. The mass of the material lensing the galaxy (i.e. the cluster mass) can be determined from this. The dark matter is included in this mass estimate since it is the total cluster mass that distorts the light from the background galaxy. The mass to luminosity ratio of a galaxy cluster is also an estimate of how much of the matter in the cluster is in the form of dark matter. Mass to luminosity ratios have been determined for many clusters and an example of the relationship between mass and luminosity is given in figure 1.2. The Mass to luminosity relationship shown uses ROSAT data (Reiprich & Bohringer 2002).

Clusters of galaxies were among the first structures formed in the universe, which is why they are important for cosmological studies. The way that high mass clusters

develop depends strongly on the type of cosmology used. Present simulations of clusters suggest that  $\Omega_0 \approx 0.3 \pm 0.1$  (Bahcall, Fan & Cen 1997). Most clusters have evolved to be dynamically relaxed at the present epoch, with the exceptions being those clusters which have been involved in recent mergers. The constituents of the merger are old however, and may have been dynamically relaxed prior to the merger.

## 1.3 Optical Properties of Clusters

### 1.3.1 Cluster Classifications

The earliest classification of clusters of galaxies were presented in catalogues (Abell 1958, Zwicky, Herzog & Wild 1961), with the Abell catalogue being most commonly used. The Abell catalogue is based on identifying the richness of clusters by their spatial over-density. The criteria for the richest Abell clusters of galaxies is that the cluster contains at least 50 galaxies in the magnitude range  $m$  to  $(m + 2)$  where  $m$  is the magnitude of the third brightest cluster galaxy. It is also a requirement that these galaxies be contained in a circle of radius  $R_A = 1.7/z$  arcminutes or  $3h_0^{-1}\text{Mpc}$ , where  $z$  is the estimated cluster redshift, usually in the range  $0.02 \leq z \leq 0.2$ .  $R_A$  is the Abell radius of the cluster. The Abell catalogue contains 1682 clusters which meet this requirement and contains 2712 clusters in total. The clusters of galaxies discussed later in this thesis are rich clusters (richness class 2-5 in the Abell scheme).

### 1.3.2 Cluster Morphologies

Clusters of galaxies can be classified based on their optical morphology. They can be represented as a one dimensional sequence which goes from irregular to regular clusters. There is evidence that regular clusters are more dynamically evolved, and therefore more relaxed than irregular ones. Of the clusters considered in this thesis, most are evolved, relaxed clusters, though some show evidence of recent mergers which can disrupt the

cluster. The most recent classification of clusters was by Struble and Rood (1982), which is an updated version of the Rood and Sastry, 1971, scheme. Both of these schemes divide clusters into six main classes, which are determined by the nature and distribution of the ten brightest cluster members. The six classifications are:

- cD, where the cluster is dominated by a cD galaxy
- B where the cluster is dominated by a pair of luminous galaxies
- L where at least three of the brightest galaxies form a straight line
- C where four or more of the cluster galaxies form a core to the distribution
- F where the brightest galaxies form a flattened distribution on the sky rather than a more spherical one.
- I where the distribution of the brightest cluster galaxies is irregular with no identifiable pattern to it.

The clusters in this thesis are mostly classed as cD clusters and the significance of this is explained further in later sections.

### **1.3.3 Galaxy content**

The galaxy content of clusters correlates indirectly to the cluster morphology as well as to the cluster size and redshift (Fasano, Poggianti, Couch, Bettoni, Kjaergaard & Moles 2000). In regular clusters the majority of galaxies are elliptical whereas irregular clusters tend to be spiral rich. This could be due to a difference in the fraction of spirals and elliptical created at formation (Dressler 1980). Dressler also suggests that the different types of galaxies could be a result of S0 type galaxies locating preferentially in dense regions, which have short dynamical timescales and so have already relaxed. Observations have shown that regular clusters are symmetrical in shape with a large number of

the cluster galaxies concentrated toward the cluster core, they also tend to be rich and compact. Contrastingly irregular clusters show little symmetry or central concentration but show significant sub clustering. Regular clusters such as Abell 1413 discussed later in this thesis.

### **1.3.4 cD Galaxies**

Centrally dominant (cD) galaxies are the central galaxies in many clusters. They are giant ellipticals which sit in the middle of the cluster potential well as is determined by their optical position and velocity. They were defined by Matthews, Morgan & Schmidt (1964) as galaxies with a nucleus like that of a very luminous elliptical galaxy embedded in a low surface brightness halo.

One of several theories on the origin of cD galaxies is that they result from galactic cannibalism. This relies on dynamical friction, where the motion of a mass (e.g. a large galaxy) through the cluster results in a gravitational attraction between the mass and the other objects in the cluster. This produces a region of high density along the mass's path which results in a tidal wake trailing the mass. This results in a net gravitational force on the mass, slowing it down and transferring kinetic energy to the surrounding media. This causes a decay in the orbits of the more massive galaxies and results in them falling toward the cluster centre where they merge into a super-massive galaxy. As other galaxies pass through the cluster centre they are also accreted, all of which heats and inflates the resultant galaxy. Evidence for this theory is seen by the fact that some cD's contain multiple nuclei. (Tremaine 1987) However, it has been shown that ram pressure stripping, where the wind caused by the relative motion of the galaxies strips gas from the cluster galaxies (Shu 1982), may reduce the accreted mass and frequency of mergers making this theory incompatible with observations.

Other theories are that cD's are formed early in the lifetime of clusters. Hierarchical cosmological models have shown that cD's form early through mergers of several mas-

sive galaxies flowing inwards along filaments (Oegerle & Hill 2001). The simulations agree well with values from observations except that they don't produce the high central surface brightness required for rich clusters. To create rich clusters it is necessary to include sub cluster mergers, whereby the cluster formed from several separate clumps. It is also possible that cD's can be the result of gas accretion by cooling flows onto a central cluster galaxy, although this would require a large mass inflow rate as typical mass deposition rates of  $\sim 100M_{\odot}$  per year could only have produced galaxies with masses up to  $10^{11}M_{\odot}$  within the age of the universe whereas cD galaxies typically have masses closer to  $10^{12-13}M_{\odot}$

### 1.3.5 The Virial theorem

The virial theorem provides a simple connection between the velocity dispersion and the total mass of a system. If a cluster is assumed to be a bound stationary system then :

$$E = T + W < 0 \quad (1.1)$$

where E is the total energy, T is the kinetic energy and W is the gravitational potential energy.

$$T = \frac{1}{2} \sum_i m_i v_i^2 \quad W = -\frac{1}{2} \sum_{i \neq j} \frac{Gm_i m_j}{r_{ij}} \quad (1.2)$$

where G is the gravitational constant. The sums are over all the galaxies,  $m_i$  and  $v_i$  are the  $i$ th galaxy mass and velocity and  $r_{ij}$  is the separation of the galaxies  $i$  and  $j$ .

Integrating the equations of motion of the galaxies gives;

$$\frac{1}{2} \frac{d^2 I}{dt^2} = 2T + W \quad (1.3)$$

where  $I$  is the moment of inertia of the system,  $I = \sum m_i r_i^2$ , where  $r_i$  is the position of the  $i^{\text{th}}$  galaxy. For a stationary non-evolving cluster configuration  $d^2I/dt^2 = 0$ . Therefore

$$W = -2T, E = -T \quad (1.4)$$

This is the virial theorem. An estimate of the cluster mass can be made using the velocity dispersion  $\sigma$  ( $3\sigma_r^2 = \sigma^2$  for isotropic orbits, where  $\sigma_r$  is the radial velocity dispersion) and the gravitational radius  $R_G$ ;

$$M_{\text{tot}} = \frac{3R_G\sigma_r^2}{G} \quad (1.5)$$

where

$$R_G \equiv 2M_{\text{tot}}^2 \sum_{i \neq j} \left[ \frac{m_i m_j}{r_{ij}} \right]^{-1} \quad (1.6)$$

Both the velocity dispersion and the gravitational radius can be determined from observations with typical values of  $\sigma_r = 10^3 \text{ km s}^{-1}$  and  $R_G \sim 1 \text{ Mpc}$  which gives  $M_{\text{tot}} \sim 10^{15} M_{\odot}$ .

## 1.4 X-ray emission from clusters of galaxies

### 1.4.1 The King potential

The velocity distribution of the galaxies in clusters is conventionally modelled as a Gaussian distribution characterised by the radial velocity dispersion about the mean  $\sigma_r$ , which is defined as

$$\sigma_r \equiv \langle (v_r - \langle v_r \rangle)^2 \rangle^{1/2} \quad (1.7)$$

where  $v_r$  is the radial velocity, which is the line of sight component of the galaxy velocity.

In relaxed clusters, galaxies tend to have a smooth spatial distribution, along with a dense core. The model normally used to approximate the cluster distribution was developed by Ivan King in 1966. This model, which assumes a Gaussian velocity distribution for the inner regions of the cluster models a galaxy number density of

$$n_{gal}(r) = n_o \left( 1 + \left( \frac{r}{r_c} \right)^2 \right)^{-3/2} \quad (1.8)$$

where  $r_c$  is the cluster core radius. This is a good approximation at small radii. However in reality the galaxy density falls to zero at some finite radius, whereas the above relation will continue to fall as  $r^{-3}$  for large values of  $r$ .

Combining the equation of hydrostatic support with an assumed gravitational potential makes it possible to parameterise the spatial distribution of the cluster gas. The gravitational potential is usually assumed to be that of the self gravitating isothermal sphere, known as the King potential as shown in equation 1.10. The density distribution for the King model is given by:

$$\rho(r) = \rho_o (1 + x^2)^{-3/2} \quad (1.9)$$

where  $x = r/r_c$  and  $\rho(r) \propto n(r)$ . The relations between the line of sight velocity dispersion, the central density and the core radius are used to express the gravitational potential of the cluster as

$$\phi(r) = -4\sigma_r^2 \frac{\ln[x + (1 + x^2)^{1/2}]}{x} \quad (1.10)$$

If the equation for hydrostatic support is rewritten for  $\rho_{gas}$  then;

$$\rho_{gas}(r) = \rho_{gas,0}(1 + x^2)^{-3\beta/2} \quad (1.11)$$

where  $\beta$ , as defined in equation 1.15, is dimensionless . Furthermore, the surface brightness of a cluster, at a projected radius  $b$ , is proportional to the emission integral, EM;

$$EM \equiv \int n_e^2 dl \quad (1.12)$$

where  $dl$  is the distance along the line of sight through the cluster.

Combining the last two equations gives the X-ray surface brightness as a function of projected radius  $b$ , (Cavaliere & Fusco-Femiano 1976);

$$S_x(b) = S_o \left( 1 + \left( \frac{b}{r_c} \right)^2 \right)^{-3\beta+1/2} \quad (1.13)$$

This form is often used to model the surface brightness distribution of clusters. An important thing to note is the fact that

$$\rho_{gas} \propto \rho_{gal}^\beta \quad (1.14)$$

The parameter  $\beta$  measures the difference in scale heights of the galaxy and gas distributions. The surface brightness equation in the form above is known as the  $\beta$  model.

Work by Jones and Forman (1984), on Einstein data found an average value of  $\beta$  from fits to the surface brightness data, which came out as  $\langle \beta_{image} \rangle = 0.65$ . However, an alternative measure can be found using the galaxy to gas velocity dispersion which is;

$$\beta = \frac{\mu m_p \sigma^2}{kT} \quad (1.15)$$

This equation for  $\beta$  assumes the galaxies have an isotropic velocity dispersion. Parameters in this equation such as temperature can be obtained from spectral measurements ( $\beta = \beta_{spec}$ ). Values from Edge and Stewart (1991), for EXOSAT data give the value of beta to be  $\beta_{spec} \approx 1.2$ . Thus, there is a discrepancy between the two differently determined values of  $\beta$  although there is a greater error on the spectrally determined values. More recent work has reduced this discrepancy (Xue & Wu 2000) giving values for  $\beta_{spec} = 0.78 \pm 0.37$  and  $\beta_{image} = 0.83 \pm 0.33$ . Other recent papers such as Vikhlinin et al (1999), find values of  $\beta$  determined for ROSAT PSPC data by surface brightness fits as between 0.65 and 0.85 depending on the cluster, reaching 0.9 for Abell 2163. Use of a double  $\beta$  model may assist in reducing the difference between the spectral and spatially determined values of  $\beta$ . Other alternatives to this model are to use a different density profile such of that of Navarro, Frenk and White (1995), Burkett (1995) and Shapiro et al (1999).

### 1.4.2 The NFW distribution

The Navarro Frenk and White (NFW) distribution is used as an alternative to the King model in order to get around the  $\beta$  discrepancies discussed above. It uses results of N-body/Hydrodynamical (SPH) simulations. These simulations suggest that the cluster potential is better described using a dark matter profile steeper than an isothermal one. They use  $\beta_T$  defined as

$$\beta_T = \frac{\mu m_p \sigma_{DM}^2}{kT} \quad (1.16)$$

The studies by Navarro et al (1995), suggest that cluster dark matter halos are not well modelled by isothermal spheres but instead have changing logarithmic slopes. An alternate density profile has been developed by Navarro et. al. (1996,1997) and is defined as;

$$\frac{\rho(r)}{\rho_{crit}} = \frac{\delta_c}{(r/r_s)(1+r/r_s)^2} \quad (1.17)$$

where  $r_s = r_{200}/c$  is the characteristic scale radius and  $\rho_{crit} = 3H^2/8\pi G$  is the critical density ( $H$  is the current value of the Hubble constant).  $\delta_c$  and  $c$  are dimensionless constants which are linked to the fact that the mean over-density within  $r_{200}$  must be  $200 \times \rho_{crit}$ .  $\delta_c$  is the characteristic over-density and is defined as (Navarro, Frenk & White 1996);

$$\delta_c = \frac{200}{3} \frac{c^3}{[\ln(1+c) - (c/(1+c))]} \quad (1.18)$$

where  $c$  is defined as the concentration of the characteristic over-density and is equivalent to  $r_{200}/r_s$ . This can be estimated given values of  $\eta$ ,  $r_s$  and  $T_0$

The density profile can be simplified to;

$$\rho_{NFW} = \frac{\rho_s}{(x)(1+x)^2} \quad (1.19)$$

where  $x = r/r_s$  and  $\rho_s = \rho_{crit} \delta_c (1+z)^3 \Omega_0 / \Omega_z$  and  $\Omega_0$  and  $\Omega_z$  are the cosmological parameters at the present epoch and at redshift  $z$  (Ettori 1998, Navarro, Frenk & White 1997).

The dark matter distribution has a gravitational potential defined as;

$$\frac{d\phi}{dr} = -4\pi G r_s \rho_s \frac{\ln(1+x) - (x/(1+x))}{x^2} \quad (1.20)$$

This is then applied to an isothermal sphere ( $T = T_{iso}$ ) in the same way as the  $\beta$  model potential. This potential produces a cluster gas density distribution of the form;

$$\rho_{gas} = \rho_{gas,0}(1+x)^{\eta/x} \quad (1.21)$$

where

$$\eta = 4\pi G r_s^2 \rho_s \mu m_p / k T_{iso} = 1.5 \delta_c (1+z)^3 (\Omega_0 / \Omega_z) H_0^2 r_s^2 \mu m_p / k T_{iso} \quad (1.22)$$

The Navarro Frenk and White density profile models the dark matter profile of a cluster by modelling the cluster halo. The NFW profile has been used to fit density profiles of clusters of galaxies in order to overcome the problems of the  $\beta$  model. An example of a fit using a NFW profile is shown in figure 1.3. The plot shows that the fit to ASCA data is improved by using the NFW profile rather than an isothermal beta model as it correctly models the slope of the data. The figure is from Markevitch et al (1999), who found  $r_s = 0.18$  and  $0.36$  Mpc respectively for Abell 2199 and Abell 496 and values of  $c$  of about 10 and 6 for the two clusters. The data in this plot must however be considered with caution as it comes from the ASCA satellite where there have been problems with the point spread function (PSF) which has led to inconsistencies in results obtained by different authors on the same data who have used different methods to account for the PSF.

### 1.4.3. Physical Component analysis

The problem with using the  $\beta$  and NFW models are that they are reliant on the knowledge of certain physical parameters, most notably temperature. Therefore the model fits are the correlated physical parameters and are not fully independent. A principal component analysis is used to de-correlate and normalise the data to determine physical parameters of a cluster without any correlation between the fit.

The objective of a principal component analysis is to reduce the number of uncorrelated variables into one or two principal axes which represent as much of the original data as possible (Figure 1.3). The original data consists of a set of data which each have

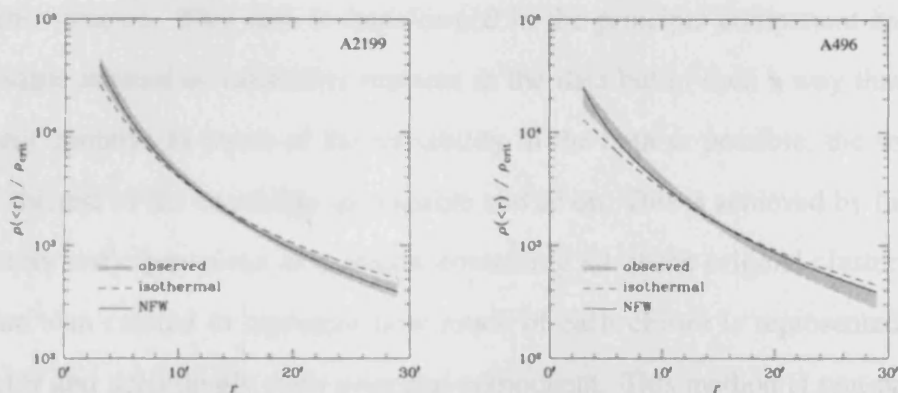


FIGURE 1.3. This figure shows density profiles of Abell 496 and Abell 2199 from (Markevitch et al. 1999). It gives a comparison between the NFW profile and an isothermal fit to the ASCA data.

### 1.4.4. The Intercluster Medium

The intercluster medium is the low density of hot gas which resides between the galaxies. The gas has a typical density of  $n \sim 10^{-5}$  cm<sup>-3</sup> and so is so tenuous that on smaller scales the gas is transparent. At a typical  $10^8$  K, the temperature at which it is highly ionised, the mean free path is about 0.1-0.5 kpc and the thermal ionisation heating dominates. The gas is ionised and ionised by the high energy photons from the hot stars and galaxies. The ionisation of the gas is not uniform and has been estimated

### 1.4.3 Principal Component analysis

The problem with models like the  $\beta$  and NFW models are that they are reliant on the knowledge of certain cluster parameters, most usually temperature. Therefore the model fits can be correlated to certain parameters and are not fully independent. A principal component analysis however, is non-parametric and so may be able to determine physical parameters of a cluster without any correlations affecting the fit.

The purpose of a principal component analysis is to reduce a number of uncorrelated datasets to a set of uncorrelated axes which represent as much of the original data as possible (Daultrey 1976). The original data consists of  $n$  sets of data which each have a different variance. This data is transformed in the principal component analysis so that the same amount of variability remains in the data but in such a way that the first component contains as much of the variability in the data as possible, the second, as much of the rest of the variability as possible and so on. This is achieved by finding the eigenvectors and eigenvalues of a matrix containing all of the original cluster profiles. Scores are also created to represent how much of each cluster is represented by each eigenvector and accordingly each principal component. This method is non parametric as it requires no prior knowledge about the datasets being used in order to produce the eigenvectors and scores. It is a purely mathematical exercise. The problems with this come in providing a physical interpretation of the results produced.

### 1.4.4 The Intra-cluster Medium

The intra-cluster medium consists mainly of hot gas which resides between the galaxies. The gas has a central density of  $n = 10^{-3} \text{ cm}^{-3}$  and so is optically thin on cluster scales. The gas is heated to approximately  $10^8 \text{ K}$  a temperature at which it is highly ionised. It emits most of its radiation in the 0.1-30 keV X-ray band via thermal bremsstrahlung emission. The gas is concentrated toward the centre of the cluster potential and the density drops of radially. The drop off of the gas density with radius has been investigated

using the profiling methods discussed above. The emission can be distorted by other factors such as a cluster merger, which may produce shocks or hotspots in the gas for example in Abell 665 (Markevitch & Vikhlinin 2001) and Abell 1795 (Fabian, Sanders, Ettori, Taylor, Allen, Crawford, Iwasawa & Johnson 2001) and also by radio synchrotron emission which can blow holes in the emission such as in the Perseus cluster (Fabian, Celotti, Blundell, Kassim & Perley 2002). This happens when there are magnetic fields in the cluster which are needed to produce the synchrotron emission.

### 1.4.5 The X-Ray Spectrum

The X-ray spectrum of the intra-cluster gas consists mostly of continuum emission with very few spectral lines. Models of the emission are based on assuming a thermally ionised plasma. Much of the X-ray emission observed is thermal bremsstrahlung (braking radiation) emission. This is free-free emission whereby an electron passing close to an ion loses energy by emitting a photon and slows down as a result. This emission mechanism occurs at a continuous range of wavelengths and is the major source of the continuum emission in the cluster. This emission mechanism produces a characteristic spectrum for gas in the temperature range  $2 \times 10^7 - 10^8$  K. For a fully ionised hydrogen plasma the energy emitted per unit time between frequencies  $\nu$  and  $\nu + d\nu$  is

$$l_\nu d\nu = 5.44 \times 10^{39} (4\pi n_e^2) T^{1/2} e^{h\nu/kT} d\nu \text{ ergs}^{-1} \text{ cm}^{-3} \quad (1.23)$$

where  $T$  is the gas temperature,  $k$  is the Boltzmann constant,  $n_e$  is the number density of free electrons and  $h$  is the Planck constant (Carroll & Ostlie 1996). Support for this emission model is also provided by the presence of the strong 6.7 keV iron emission line seen in cluster spectra, as it is difficult to reconcile the existence of this line with non-thermal emission mechanisms (Bahcall & Sarazin 1977).

It has been observed that at low temperatures (below  $10^7$  K) the spectrum of an optically thin plasma is dominated by emission lines with the most important feature being

the iron  $K_\alpha$  complex which is mostly  $\text{Fe}^{+24}$  and  $\text{Fe}^{+25}$ . Other important low energy features come from other metals such as C, N, O and S. The iron L complex is an important feature in the  $\sim 1$  keV range.

### 1.4.6 Determination of Cluster Mass

A cluster will be in hydrostatic equilibrium if its sound crossing time is much less than the age of the cluster e.g. Sarazin (1986) and attributed authors therein. The sound crossing time for a cluster, diameter  $D$  is given by;

$$t_s = 6.6 \times 10^8 \left( \frac{T}{10^8 K} \right)^{-1/2} \left( \frac{D}{\text{Mpc}} \right) \text{yr} \quad (1.24)$$

If the gas is in hydrostatic equilibrium then the following relation applies;

$$\frac{1}{\rho_{gas}} \frac{dP}{dr} = -\frac{d\phi}{dr} = -\frac{GM(r)}{r^2} \quad (1.25)$$

where  $M(r)$  is the total mass enclosed within a radius  $r$ . This is known as the equation for hydrostatic support. Combining the equation for hydrostatic support with the ideal gas equation,  $P=nkT$  gives the mass relation to be;

$$M(< r) = -\frac{kT r}{\mu m_p G} \left( \frac{d \log \rho_{gas}}{d \log r} + \frac{d \log T}{d \log r} \right) \quad (1.26)$$

where  $m_p$  is the proton mass and  $\mu m_p$  is the mean atomic mass.  $\mu$  is assumed to be 0.6 throughout. This gives another method for mass determination other than the virial mass since the temperature and density profiles can be determined from X-ray measurements. The advantage it has over the virial method is that it is model independent whereas the virial theorem requires assumptions about the galactic orbits to be made.

### 1.4.7 Origin of the Intra Cluster Medium

There are two groups of models for the origin and formation of the Intra Cluster Medium (ICM). The first suggestion has the ICM being primordial gas which had fallen into the cluster. If the gas fell into the cluster during its collapse at formation then it would have the same energy per unit mass as the cluster galaxies (Sarazin 1988) thus;

$$\frac{kT_{gas}}{\mu m_p} \approx \sigma_r^2 \quad (1.27)$$

The temperatures obtained from this relation are consistent with the values from observations which tend to be in the range 3-10 keV ( $4 \times 10^7$  to  $16 \times 10^7$  K) for  $\sigma_r \sim 10^3$  km s<sup>-1</sup>. This temperature is sustainable providing the gas cooling time is large enough ( $\sim 10^{10}$  yr) for any part of the cluster.

This model alone cannot, however, explain the observed abundance of heavy metals, (0.3 solar on average), since this indicates that at least some of the cluster gas must have been processed through stars. This is because the only way of producing the heavy elements is through thermonuclear processes in stars. These elements are then ejected into the surrounding medium via supernovae. Star formation alone cannot be the only source of the gas as there is more intra-cluster gas than stellar mass. Also enrichment alone would result in a higher metal abundance than is observed, since each star produces material with approximately solar metallicity. Numerical models predict that galaxies can enrich the ICM in this way, but a limit of 50% of the original stellar mass can be lost to the ICM (David, Forman & Jones 1991). It is difficult to distinguish between gas entering the ICM via enrichment and primordial gas because the kinetic energy of the gas ejected from galaxies is dependent on the velocity with which the gas is ejected from the supernova and the velocity of the galaxy is it ejected from. Therefore the relation between temperature and velocity dispersion is the same as in equation 1.27 for the primordial gas. The most likely scenario is that highly enriched gas ejected from galaxies is diluted by the primordial gas to give the abundances observed in the ICM.

It is also possible that gas is heated through the friction between galaxies, but this will produce significant mass segregation as the galaxies will lose a reasonable portion of their kinetic energy via this process. This sort of mass segregation is not seen in the observed data (Sarazin (1988) and associated authors therein).

### 1.4.8 Cooling Gas

The core of a cluster is the region which contains the densest concentration of gas and therefore, also has the shortest cooling time;

$$t_{cool} \approx \frac{5}{2} \frac{kT}{n_e \Lambda(T)} \quad (1.28)$$

where  $\Lambda$  is the cooling function which describes the cooling power at a temperature,  $T$ . It has variable contributions from thermal bremsstrahlung, forbidden line cooling and semi-forbidden line cooling (Raymond & Smith 1977).

When the cooling time is significantly less than the age of the cluster, the energy of the gas within a cooling radius  $r_{cool}$  (radius where the cooling time equals the age of the cluster) drops. In order to maintain the overlying gas pressure the density must rise and therefore the gas must flow inwards. If the pressure and density rise enough then the gas may not actually be seen to cool (as the rise in potential energy exceeds the drop in thermal energy of the gas).

The mass flow rate within the above region,  $\dot{M}$ , can be found by assuming the luminosity in the region ( $L_{cool}$ ) is due to the thermal energy. This is done by assuming the work done on the gas as it moves inwards ( $PdV$ ) is negligible. This gives

$$\dot{M} \sim \frac{2}{5} \frac{\mu m_p}{kT} L_{cool} \quad (1.29)$$

where  $\mu$  is the mass per unit particle in gas units of the proton mass ( $\mu=0.6$  as before) This models represents an idealised homogeneous cooling flow where each radius has a unique density and temperature associated with it. The major uncertainty with cooling flow models is that they allow gas to cool down to low temperatures and there is little evidence of the gas cooling below 1 keV from the X-ray spectra. This was made particularly apparent with the XMM-Newton RGS spectrum of Abell 1795 (Tamura, Peterson, Paerels, Mittaz, Trudolyubov, Stewart, Fabian, Mushotzky, Lumb & Ikebe 2001). The X-ray spectra shown in this paper provide evidence that the gas cools to 1 or 2 keV only and then is stopped by some mechanism. There is evidence however of cooler gas in other wave bands however such as in radio where cool ( $T \ll 100\text{K}$ ) molecular gas is seen in clusters (Edge 2001). The amount of this type of gas observed is consistent with the amount expected if the mass deposition rates and timescales are of order those found by recent studies (e.g Fabian et. al. (2001)).

There are several possible suggested solutions for this problem. These include the idea that the cooler gas is in small clouds surrounded by larger regions of warmer gas and so can gain and lose energy via conduction or convection. Other suggestion (Fabian, Mushotzky, Nulsen & Peterson 2001, Voigt, Schmidt, Fabian, Allen & Johnstone 2002) have been: heating, where the gas is cooled to 3 keV and then is heated back up from this temperature by some method; mixing where the gas is cooled to say  $10^4$  K and then is mixed with hotter gas thus rendering it undetectable in the X-ray; differential absorption, whereby the photons from the cooler gas are more absorbed than those from the hot gas, thus becoming undetectable; and metallicity variations where most of the gas is metal poor (ie  $Z \sim 0$ ) and only a small amount is metal rich (Morris & Fabian 2001, Ettori & Fabian 2001).

### 1.4.9 Steady State Conduction model

A steady state conduction model (DosSantos 2001) can be fitted to temperature profiles in clusters as an alternative to the above models. This model assumes a perfect gas in

hydrostatic equilibrium for the intra-cluster medium with no sources or sinks of heat due to conduction. If spherical symmetry is also assumed then the model gives the cluster temperature as

$$\frac{T(x)}{T_{200}} = \left( 1 + (\eta^{7/2} - 1) \frac{x_0}{x_0 - 1} \frac{x - 1}{x} \right)^{2/7} \quad (1.30)$$

where  $x = r/R_{200}$ . If hydrostatic equilibrium is assumed to hold then  $R_{200}$  is the radius where the interior density is 200 times the mean (critical) density of the universe, which also corresponds to the virial radius in this case (Evrard, Metzler & Navarro 1996a).  $\eta = T_0/T_{200}$ , where  $T_0$  is the inner temperature and  $T_{200}$  is the temperature at the virial radius. This formula can be rearranged in order to get  $T(x)$  which can be fitted to a temperature profile. This model works on the region outside the cooling flow region of the cluster (the point where the model can start is signified by the parameter  $x_0$ ). The model is fitted to the data for different values of  $x_i$  (where  $x_i = T_0/T(x = 1)$ ). This model is designed to work out to the virial radius of the cluster and degeneracies in the fits can occur when the data is not fit out to this radius.

## 1.5 Dark Matter Component in clusters of galaxies

### 1.5.1 Gravitational Lenses

It has been known for some time that Clusters of Galaxies act as Gravitational Lenses to background galaxies. When a cluster lenses a background object the object is seen to form arcs which are a part of an Einstein ring (Carroll & Ostlie 1996). The equation for the angular radius of an Einstein ring is as follows;

$$\theta_e = \left( \frac{4GM}{c^2} \frac{D_{ls}}{D_s D_l} \right)^{1/2} \quad (1.31)$$

where  $D_l$  is the distance to the lens and  $D_s$  is the distance to the source. The mass,  $M$  is the mass of the cluster including the dark matter component. The value of  $\theta_E$  can always be calculated even when the Einstein ring is not complete. The total mass of the lensing cluster Abell 2218 shown in figure 1.1 is  $2.75 \times 10^{14} M_\odot$  as obtained by AbdelSalem, Saha & Williams (1998).

### 1.5.2 The Sunyaev-Zel'Dovich effect

The Sunyaev-Zel'Dovich (SZ) effect is secondary cooling of the cluster gas via Inverse Compton scattering off of the Cosmic Microwave Background (CMB). This scattering is inelastic and thus results in a net energy gain by the CMB photons. This in turn distorts the CMB. The energy density of the CMB is enhanced towards clusters by small linear amount which is then detectable. One advantage of using SZ with clusters is that it gives a gas mass to total mass fraction which is in agreement with cosmology (i.e.  $M_g/M_T \neq \Omega_b/\Omega_0$ ) (Desert 2002 (in press)). It also provides velocity estimates for galaxy clusters and can therefore provide information on whether clusters are moving more quickly or slowly with respect to the CMB with increasing redshift which provides constraints on whether the expansion of the universe is slowing down or speeding up.

The combination of SZ measurements of  $\int T_e n_e dl$  and the X-ray measurements of emission measure  $\int n_e^2 dl$  and the electron temperature  $T_e$  give an estimate of the true physical depth of the cluster. If the cluster is assumed to be spherical in shape this depth can be compared with the angular size of the cluster and its redshift to give an estimate of the Hubble constant  $H_0$ . The SZ effect can also be used as a cosmological probe to give values of  $\Omega$ . These measurements imply a value for  $H_0$  of  $60 \pm 10 \text{ km s}^{-1}$  (Birkinshaw 1999) and a value of approximately  $0.3 \pm 0.5$  for  $\Omega$  (Molnar, Birkinshaw & Mushotzky 2002).

### 1.5.3 Cosmology

The current structure of clusters is very sensitive to the density fluctuations that occurred shortly after the big bang. Therefore, clusters are important probes of large scale structure in the cosmological models.

The current most popular cosmological model is the CDM (cold dark matter) model. This model assumes that all the missing mass in the universe is in the form of low energy particles such as axions and photinos. The prediction of this model is that the dark matter will be distributed on similar scales as the luminous matter. It is also known as the model for a critical density universe ( $\Omega = 1$ ). It predicts the formation of the small scale structure first which means that large scale structure formed via hierarchical mergers of smaller clumps of material. This is compatible with X-ray measurements of the cluster luminosity function (Diaferio, Kauffmann, Balogh, White, Schade & Ellingson 2001). The standard CDM model cannot explain the large scale temperature anisotropies in the cosmic microwave background.

The most credible alternative model is the  $\Lambda$ CDM model. This model is similar to the CDM model but the mass density is lower ( $\Omega_m = 0.3$ ), with the shortfall made up by the cosmological constant ( $\Omega_\Lambda = 0.7$ ). The cosmological constant,  $\Lambda$ , is introduced to explain the deviation of the observed Universe from  $\Omega = 1$  models (i.e.  $\Omega = \Omega_m + \Omega_\Lambda$ ). This is the model that is most consistent with observed cluster data. Other models include hot dark matter (HDM) universe model where the constituent elements are high energy particles like massive neutrinos. This model predicts dark matter scales to be much larger than that of clusters with the smaller structures forming after the larger ones. This model underestimates the amount of small scale structure observed especially at high redshift. The correct solution may well lie with a hybrid of the models but this is still a matter of debate at the present time.

The value of Hubble's constant is also still a matter of debate with current values from the Hubble Key project giving values for  $H_0$  as  $72 \pm 8 \text{ km s}^{-1}$  (Freedman, Madore,

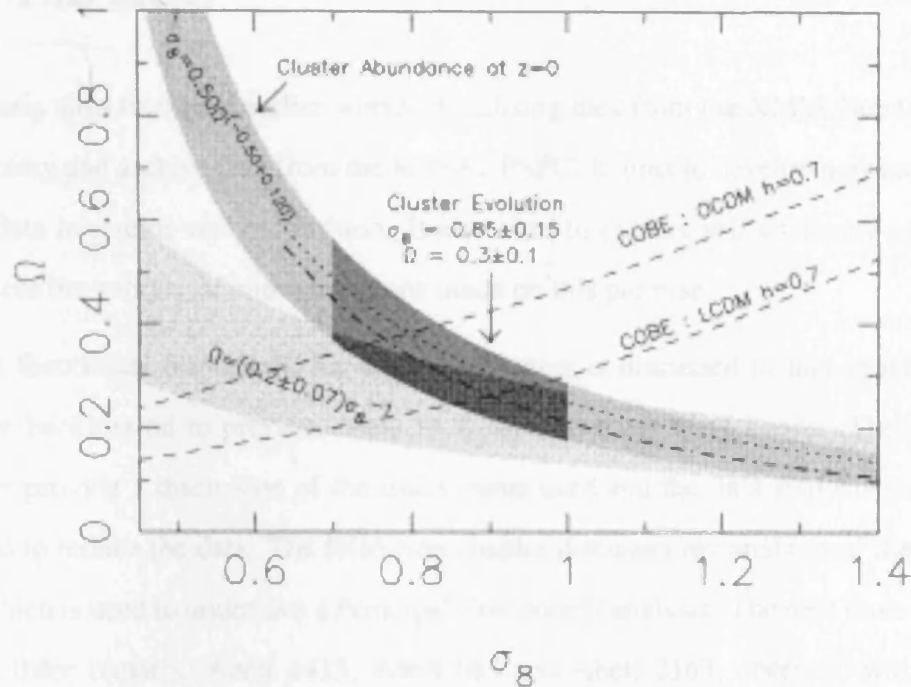


FIGURE 1.4. This plot from (Bahcall et al. 1997) shows the range of values which are possible for these parameters using present cluster observations.

Gibson, Ferrarese, Kelson, Sakai, Mould, Kennicutt, Ford, Graham, Huchra, Hughes, Illingworth, Macri & Stetson 2000). Estimates have also been made using the Sunyaev-Zel'Dovich effect, as described in the previous section, giving a value of  $H_0$  of  $60 \pm 10 \text{ km s}^{-1}$  (Birkinshaw 1999).

It is possible to determine the values of some cosmological parameters using clusters of galaxies. Clusters have long been used in order to determine values of  $\Omega$ . Recent values of  $\Omega$  from observations of clusters (Bahcall et al. 1997) give  $\Omega = 0.3 \pm 0.1$  for a  $\Lambda = 0$  model and  $\Omega = 0.34 \pm 0.13$  for a  $\Lambda = 1$  model. This implies that the Universe is low density. Figure 1.4 from Bahcall shows the observational constraints for  $\Omega$  and  $\sigma_8$  from cluster observations and also from COBE data. It shows that  $\Omega$  is constrained to be between 0.2 and 0.4 from Cluster evolution with higher values expected if only clusters at  $z=0$  are studied.

## 1.6 This thesis

This thesis aims to extend earlier works by utilising data from the XMM-Newton X-ray observatory and archive data from the ROSAT PSPC. It aims to develop new methods of fitting data in a semi-analytic fashion. It also aims to explore self similarity in clusters and assess the validity of approximations made on this premise.

The theoretical framework for studying clusters is discussed in this chapter along with the background to previous work in X-ray and other wave bands. The next two chapters provide a discussion of the instruments used and the data analysis techniques required to reduce the data. The following chapter discusses my analysis of the ROSAT data, which is used to undertake a Principal Component analysis. The next three chapters discuss three clusters, Abell 1413, Abell 665 and Abell 2163, observed with XMM-Newton and investigated via detailed spectral and spatial analysis. This is followed by a comparison of the three clusters in order to investigate the deviations of the clusters from self similarity.

The ROSAT study uses a new method of modeling cluster radial profiles. The motivation behind this work is that cluster profiles produced using models such as the  $\beta$  model are correlated to some of the physical parameters of the cluster. The result being that any physical parameter derived from the fit will have uncertainties associated with the parameters that are correlated to the model. The aim of this work is to use a principal component analysis as a non parametric method of evaluating the data.

The study with the XMM-Newton data is undertaken to gain a deeper understanding of clusters Abell 1413, Abell 665 and Abell 2163, and investigates their physical properties. Detailed temperature and abundance profiles have been created from cluster spectral data in order to look for radial variations. Prior to XMM-Newton, satellites did not have the spatial and spectral resolution necessary to produce these profiles to a high degree of accuracy. Spatial analysis of the clusters is also carried out and detailed radial surface brightness profiles can be obtained, which are fitted with  $\beta$  and NFW models.

The profiles  $M_{gas}$ ,  $M_{grav}$ ,  $M_{fe}$  and  $f_{gas}$  are calculated and their implications for cluster morphology are discussed. The clusters are compared and the deviations from self similarity are discussed. Physical interpretations are applied to try to resolve the differences seen between the clusters.

Global implications of this work are discussed in the context of cluster scaling relations and henceforth cosmological parameters, with comparisons to previous work being made. Finally the potential for future work on the topic are discussed in the context of issues that remain unresolved and the new satellites that will aid our understanding of clusters, their evolution and their differing morphologies.

# Chapter 2

## Instrumentation

### 2.1 Overview

The XMM-Newton satellite combines good spectral resolution in the 0.3-10 keV X-ray band making it highly effective at detecting X-ray emitting hot gas from clusters. The three EPIC detectors which consist of the two Metal Oxide Semiconductor (MOS) ccd detectors and silicon implanted with p and n type material (PN) ccd detector were principally used in this work. The operation of these detectors is discussed in detail within this chapter. Data from the ROSAT position sensitive proportional counter (PSPC) detector were used in this work, the data being used for the principal component analysis. The ROSAT PSPC is discussed briefly towards the end of this chapter.

### 2.2 Introduction

XMM-Newton is an ESA built satellite which was launched on 10 December 1999 from French Guiana by an Ariane 5 rocket. It is mainly used in pointing mode to observe individual objects, but is also observes serendipitous sources. The satellite consists of 3 X-ray telescopes with 5 X-ray detectors and an optical monitor. The X-ray detectors

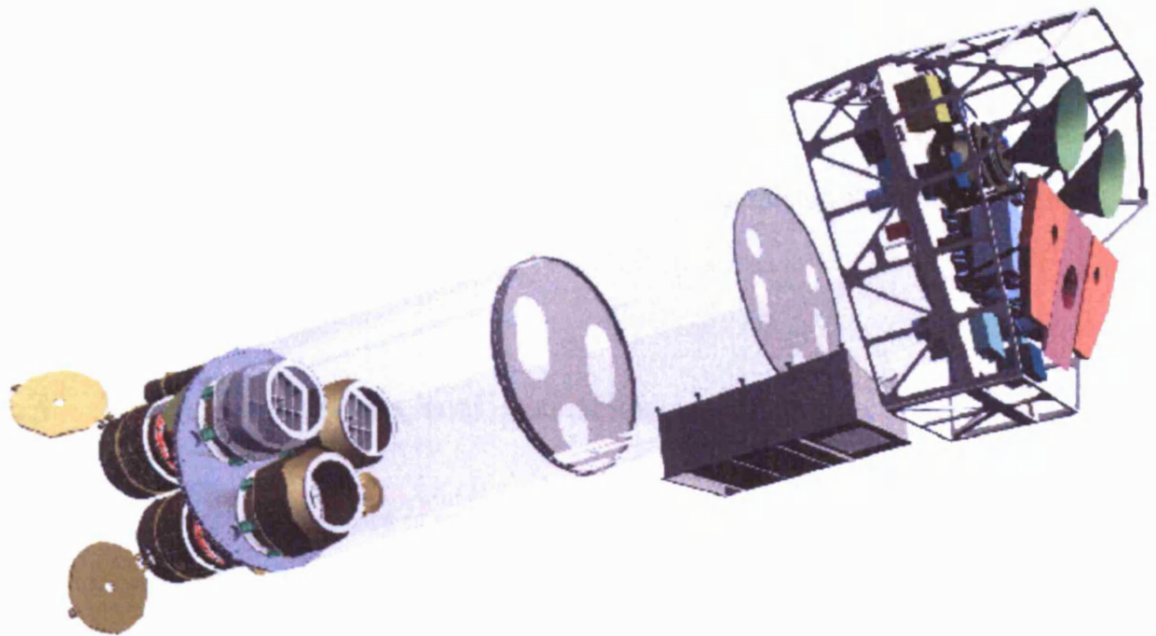


FIGURE 2.1. A diagram of the XMM mirror and detector system showing the 3 X-ray mirrors and the positions of the 5 array detector arrays.

consist of the 3 EPIC detectors which combine spectral and spatial resolution and the 2 RGS detectors which are used solely for spectroscopy. A diagram of XMM-Newton is shown in figure 2.1.

The EPIC cameras that were principally used for this work have spectral and spatial resolution in the 0.3-10.0 keV part of the X-ray spectrum. This is useful since the gas in clusters emits principally at these energies and it also covers the 6.4 keV iron line the wavelength of which gives an indication of the cluster redshift. It also gives information about various line strengths which provides information about the metal abundances in the cluster. The spatial resolution meant that it was possible to take radial profiles of various physical parameters in order to see how they varied over the cluster. This was

not possible with previous satellites such as ASCA which had good spectral resolution but reduced spatial resolution.

The ROSAT PSPC detector worked over the smaller 0.1-2.4 keV band. The advantage of using ROSAT data is that it produced a large catalogue of observations which enables comparisons of large numbers of clusters to be undertaken. This is useful in the PCA analysis which required a significant number of cluster observations to work effectively.

### 2.3 XMM-Newton Configuration

The XMM-Newton observatory is an array of three mirrors with five X-ray detectors. The optical monitor sits at the top of the assembly whilst the five X-ray detectors are arranged below the X-ray mirrors. The detectors are arranged as pairs of RGS's and MOS's with the PN on it own. In most cases for my work the PN instrument has been used as prime instrument.

### 2.4 X-ray mirror assembly

The XMM-Newton mirrors are co-aligned to an accuracy better than about 1'. Each mirror consists of shells of parabolic and a hyperbolic sections, constituting a Wolter design. This design shortens the focal length of the mirrors from about 30m to 7.5m. The use of the two mirror design also reduces astigmatism. The Wolter design is the X-ray equivalent of the Cassegrain design of optical telescope. The mirror shells are made of a nickel coating with gold inside. This gold layer must be as smooth as possible in order to correctly focus the X-rays. One mirror module consists of 58 mirror shells of varying radii (*XMM X-ray mirrors* 1999).

One of the mirror modules focus's directly on the EPIC PN instrument whereas the other two have their light split between the MOS and the RGS instruments. The light is

split by a reflection grating with 50% of the light going to the MOS detector and 40% onto the RGS.

The effective area of the three mirrors combined is shown in figure 2.2. From the graph the useful energy range is 0.1-10 keV with a maximum about 1 keV and an edge at 2 keV. Most of the emission from clusters falls in the 0.3-2 keV range which includes the maximum in efficiency. The mirror effective area at 1 keV is  $4650\text{cm}^2$ . The effective area for the MOS instruments is lower than for the PN because only part of the incoming radiation falls onto these detectors as they are partially obscured by the grating arrays. The off-axis effective area falls off as shown in figure 2.3. The drop seen in this graph over the 15 arcmin range is vignetting and is more pronounced for higher X-ray energies. The graph shows that XMM-Newton also has a moderate field of view comparable to previous missions such as ROSAT and ASCA. This is well matched to typical cluster sizes, and potentially enables things such as temperature and metal abundance to be measured out to larger radii than was previously possible, depending on the background.

The angular resolution of the EPIC detectors is determined by the point spread functions of the individual mirror modules. The pixel sizes for the MOS and PN are 40 and  $150\ \mu\text{m}$  respectively. For the XMM-Newton focal length of 7.5m this gives an angular resolution, which is dependent on the mirror approximately 1.1 arcseconds (4.1 arcseconds for the PN). The on-axis point spread function (PSF) for XMM-Newton's mirrors is 6 arcseconds, which is much less than the ASCA PSF (73 arcseconds) but is larger than the PSF of Chandra or ROSAT (0.2 and 3.5 arcseconds respectively). Structure in the PSF can be seen in bright XMM-Newton images, it is caused by the spider structure that is used to support the mirror modules. This results from input fluxes which are higher than the readout rate of the detector which can result in two low energy photons being read out as high energy photons. For very high fluxes (e.g.  $400 \times 10^{-12}\text{ergs}^{-1}\text{cm}^{-2}$ ) this results in about 20% of the flux being lost to the spider structure. The count rate limitations for the MOS detectors are defined as 2 photons per MOS CCD frame and 0.5 per PN CCD frame. This is a major problem for point sources but isn't such a major

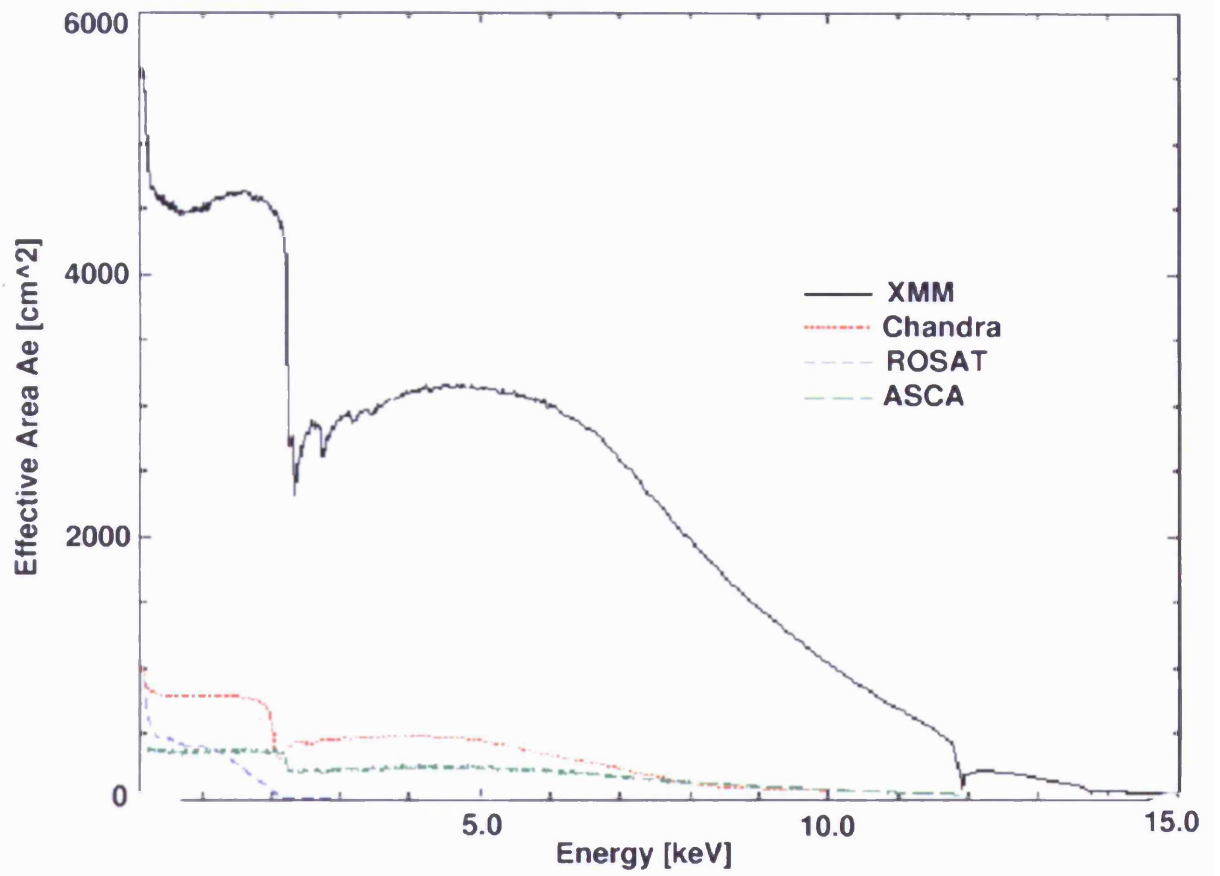


FIGURE 2.2. Graph of effective area of several recent X-ray telescope as compared to the XMM-Newton effective area. The peak at 1 keV and edge at 2 keV are clearly visible.

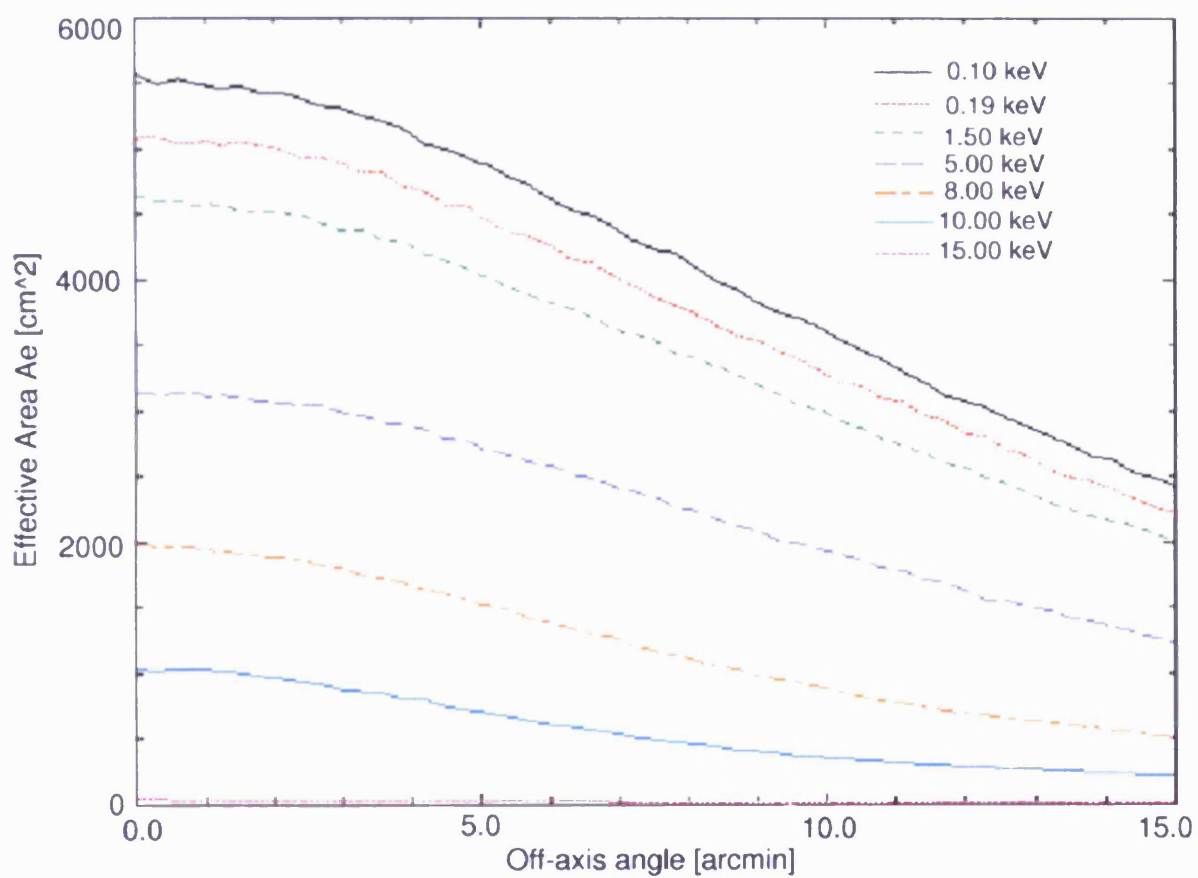


FIGURE 2.3. Graph showing the change in effective area over a 15 arcmin range for different energies.

problem for clusters, although it will still have some affect which must be taken into account.

Figure 2.4 shows the dependence of the radius at which 90% of the total energy is encircled with off axis angle. Part of the source flux is lost to chip boundaries past 10', this has greatest effect at large energies where variations in the PSF are most prominent. This is important when studying extended objects where the point spread function will change over the source since it is spread out over a large area of the detector. Therefore XMM-Newton will be much more sensitive to material in regions of the cluster detected on the centre of the detector than to those further out. Therefore it is important to know the shape of the PSF at various positions in the field of view so that the source flux is correctly calculated.

The shape of the PSF is not a constant over the field of view of the telescope. At large angles it is asymmetric and is more bean shaped than circular. The off-axis PSF for the MOS instruments is also affected by scattering from the RGS. It is important to account for the off-axis PSF so that source flux is not lost over chip edges etc. The off-axis PSF is particularly important to clusters as these are extended and often cover much of the field of view. Therefore if the shape of the PSF is changing over the field of view different parts of the cluster will have a different shaped point spread function. Thus when fitting the data from a cluster it is important to consider emission from the areas which are more off-axis in separate annuli to the inner ones and change the response used accordingly.

## 2.5 The EPIC detectors

There are 3 EPIC detectors on-board XMM-Newton, 2 MOS detectors and a PN detector. The 2 MOS arrays consist of 7 CCD's set in a hexagonal shape around a central chip. The PN array consists of 12 CCD's set in 2 adjacent rows of 6. The chips in the MOS detector are Metal Oxide Semiconductor front illuminated chips. They were manufactured by EEV of Chelmsford, UK and are 600 by 600 pixels in size. The cameras

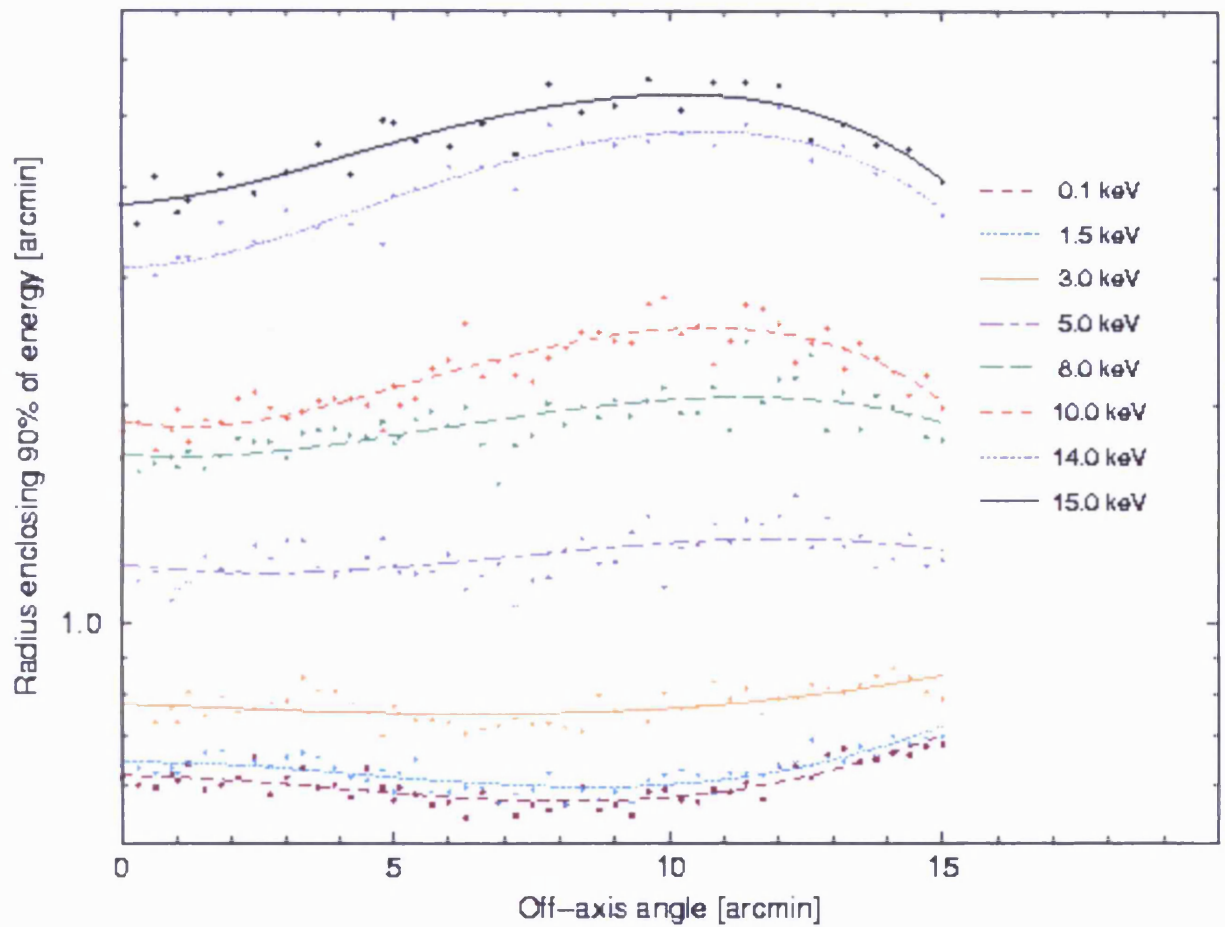


FIGURE 2.4. Curves of radii encircling 90% of the total energy of a point source at various off axis angles. Past about 10' some flux is lost to the chip edges (especially at high energies where the PSF is most prominent)

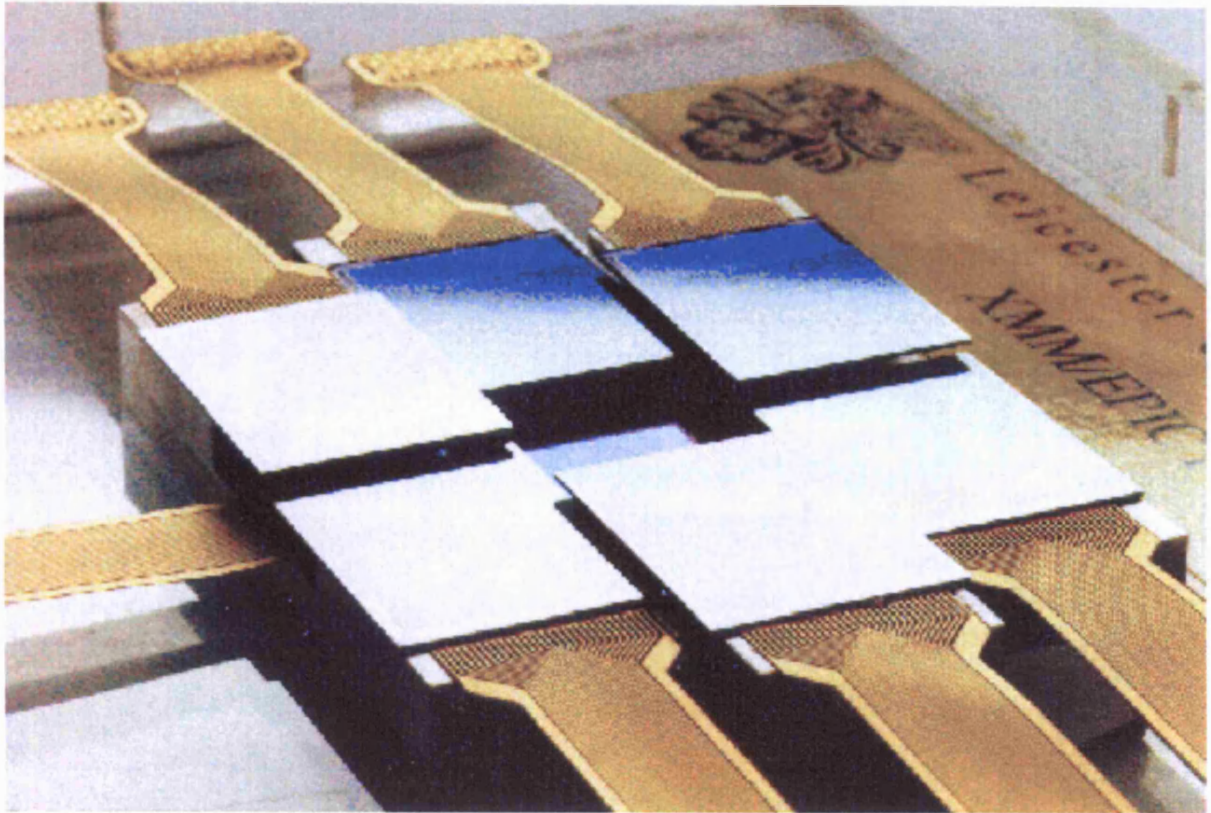


FIGURE 2.5. The layout of the MOS chips in XMM-Newton. The design features a hexagonal arrangement of chips surrounding one central chip. This design provides a large field of view.

use a revolutionary open electrode structure which increase the quantum efficiency of the detectors by about 30% at low X-ray energies (around 270 eV) (*XMM European Photon Imaging Camera (EPIC)* 1999). The chips are wired up individually then arranged in the hexagonal pattern around a deeper set central chip. This provides the large 30' field of view of XMM-Newton. Figure 2.5 shows the MOS chips on their mounting pre-flight.

The PN camera CCD's X-ray back illuminated chips with the 2 rows of 6 chips being produced on a single wafer rather than separately as with the MOS chips. The silicon wafer is implanted with p and n type material which gives it the name. There are  $400 \times 400$  pixels, designed to match the XMM-Newton spatial resolution. This layout gives a field of view the same as the MOS cameras. The chip array is embedded in a board which also carries the camera electronics. Figure 2.6 shows the layout of the PN

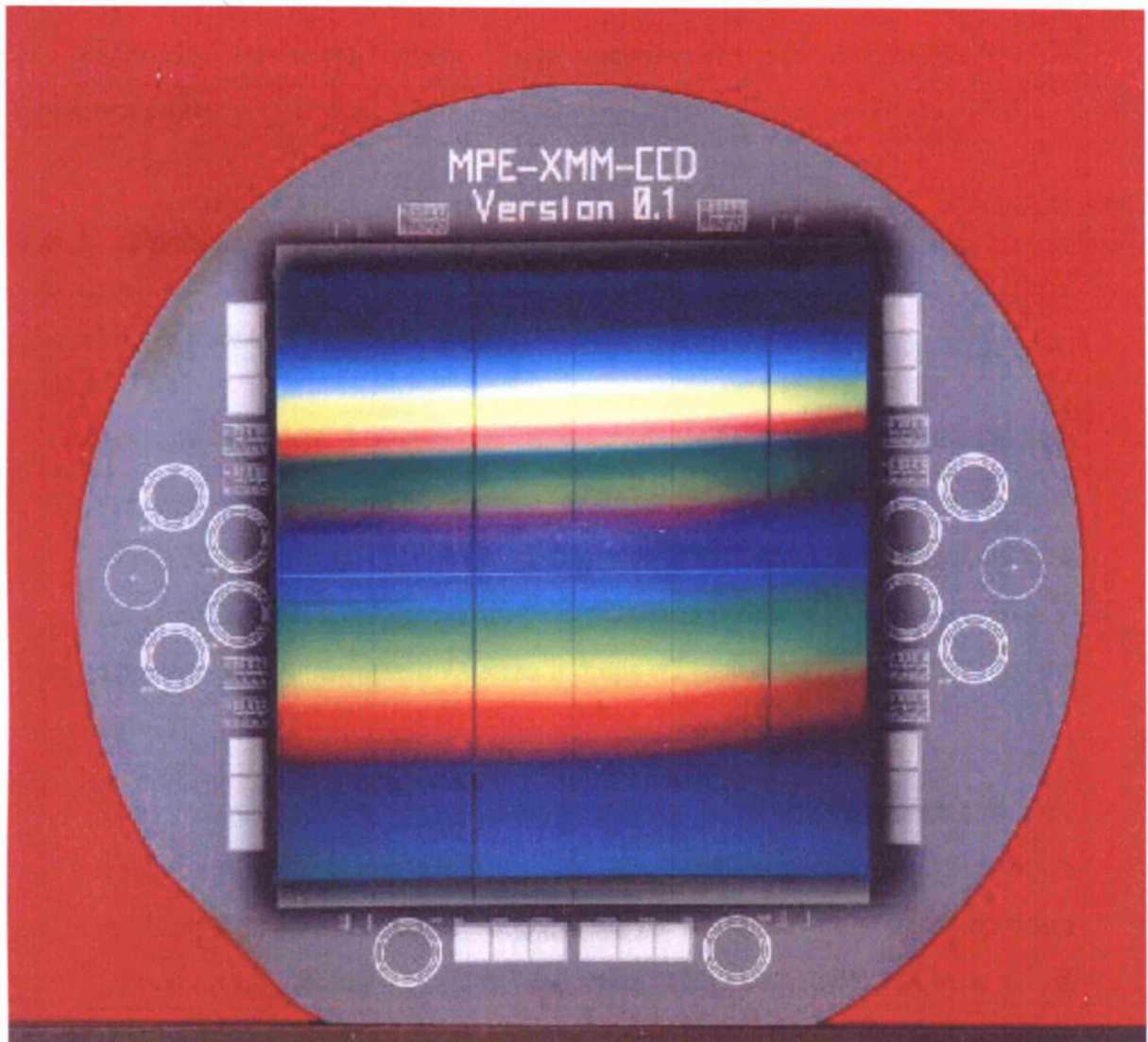


FIGURE 2.6. The layout of the EPIC PN array. Here the chips are made from a single wafer and are laid out in 2 rows of 6 chips

array. The advantage of the single wafer on the PN chip is that it reduces the amount of data lost on chip boundaries which is a problem with the MOS. This is particularly useful on extended sources which tend to extend over more than one chip in the MOS. It also achieves a faster readout rate than the MOS

The EPIC chips can be operated in three ways either full window mode, partial window mode or timing mode. For cluster datasets full window mode is mostly used as this provides a large field of view to work with (28 arcminutes for the MOS). The CCD's op-

erate in photon counting mode to produce event lists which allows simultaneous imaging and spectroscopy due to the intrinsic energy resolution of the pixels (*The XMM users handbook* 1999).

### 2.5.1 Performance characteristics

The principal performance characteristics of XMM-Newton are as follows:

- **Quantum efficiency:** The quantum efficiency of the MOS detectors limits the high end of the energy passband, whereas the PN instrument can detect photons up to 15 keV. The quantum efficiency of both types of EPIC detectors is shown in figure 2.7. From this it is seen that the quantum efficiency is over 90% for the 0.5-10 keV range for the PN instrument whereas it drops off to about 40% by 10 keV for the MOS.
- **Energy resolution:** The energy resolution of the EPIC detectors determines the resolving power of the instrument. The energy resolution of the MOS is shown in Figure 2.8. Also plotted on the graph are the in-flight FWHM of the on-board calibration lines during three different orbits. This shows there has been a 13% degradation in efficiency in the 500 days since launch. The plot of the energy resolution of the PN instrument is shown in Figure 2.9
- **Spatial resolution:** The spatial resolution of XMM-Newton is essentially the angular resolution. As seen earlier the angular resolution for the MOS and PN instruments are 1.1 and 4.1 arcseconds respectively. The spatial resolution over detector varies with the point spread function as discussed earlier. This is important when looking at extended sources since the change in point spread function is not insignificant over the extent of the source as discussed earlier in this section. Thus the change in spatial resolution over the source as you move further off axis must also be taken into account when performing scientific analysis.

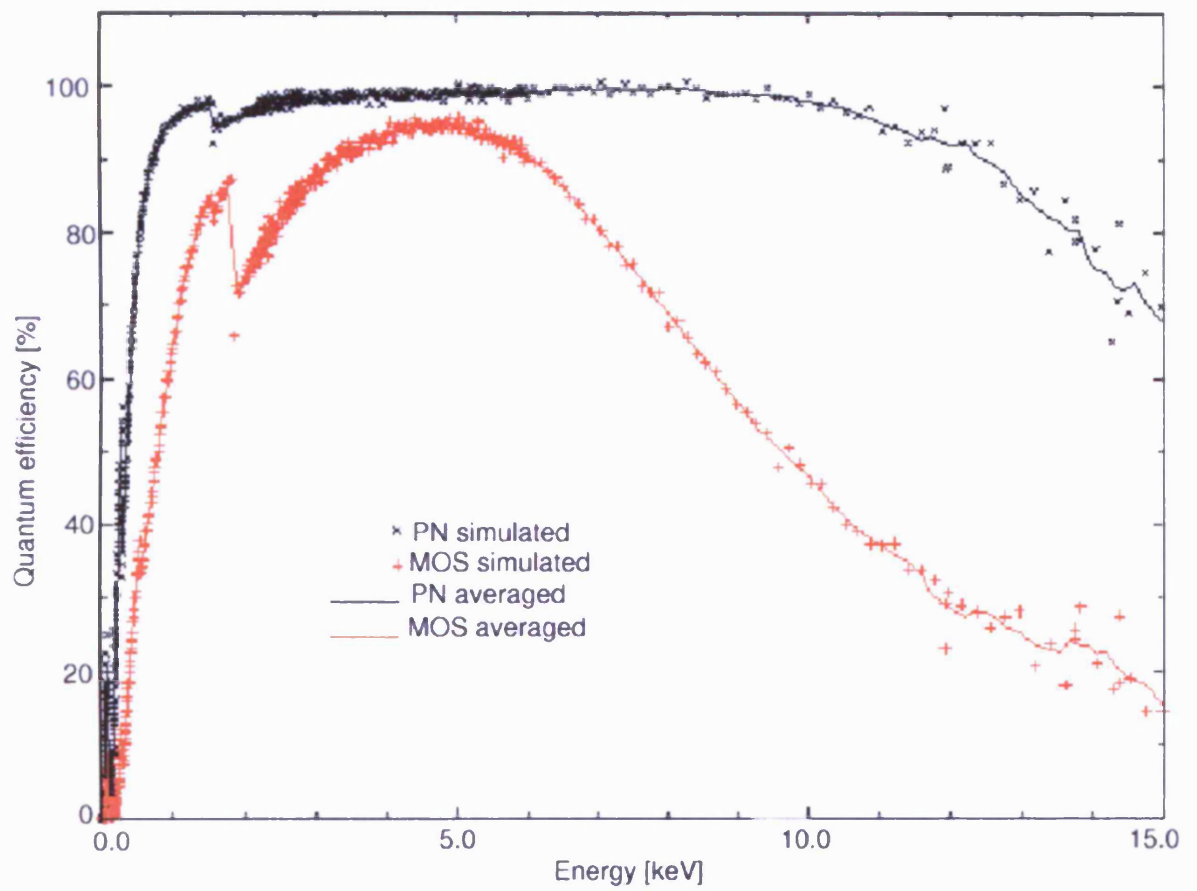


FIGURE 2.7. Graph of Quantum efficiency for the EPIC MOS and PN cameras as a function of photon energy

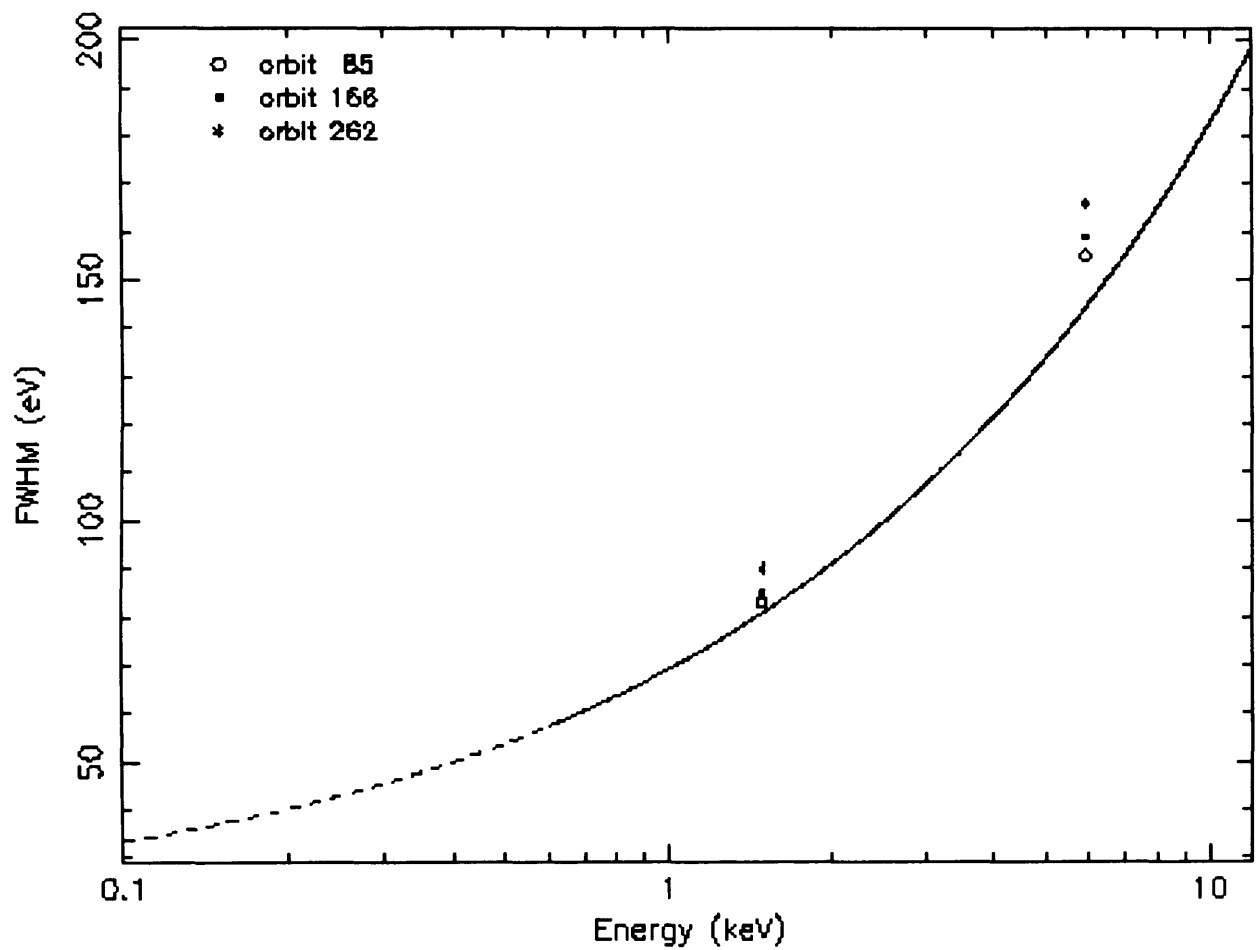


FIGURE 2.8. Graph of Energy resolution of the MOS chips. The different orbit positions show the degradation in resolution since the telescope was launched

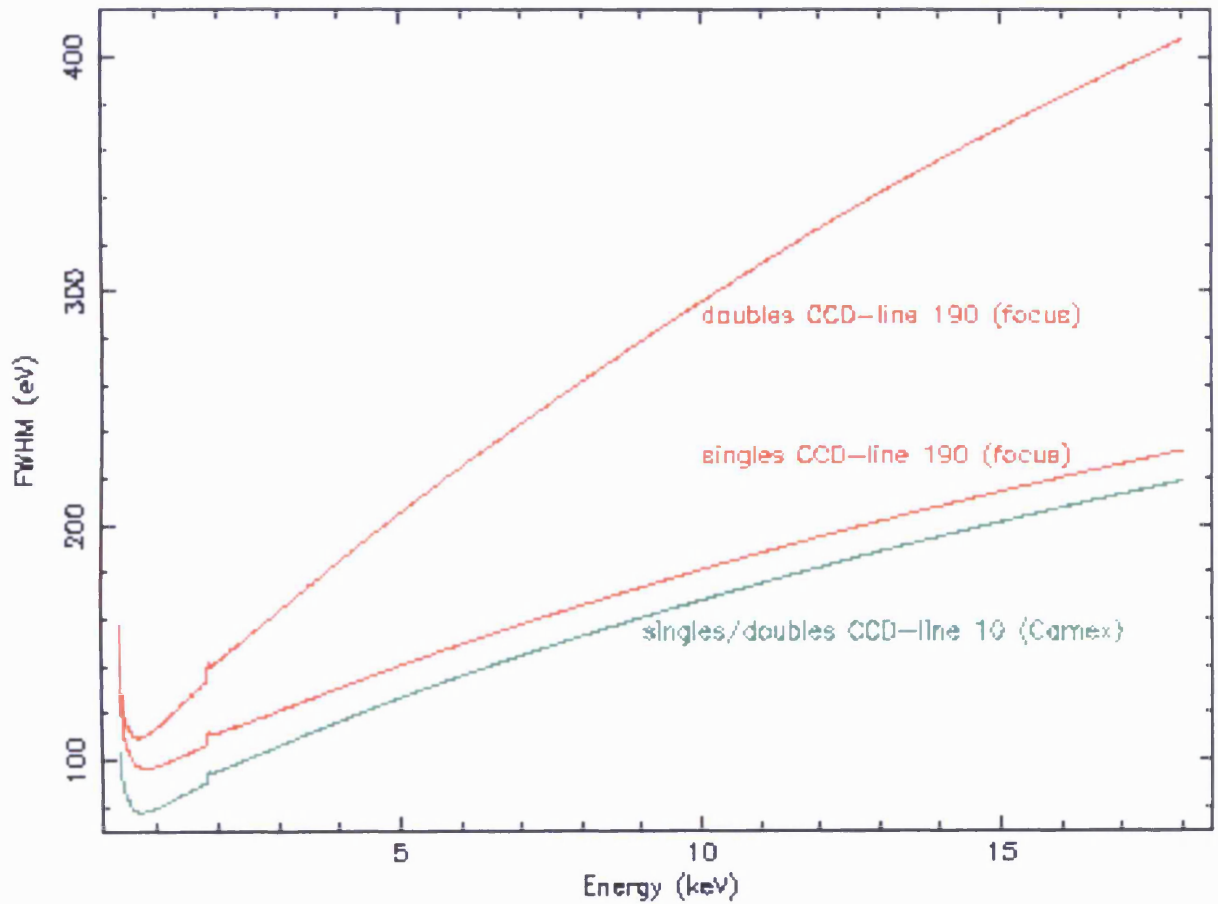


FIGURE 2.9. Graph of Energy resolution of the PN chips for the most recent response matrices. The curves are for single and double events at the focus position as well as 10 pixels away from the readout node.

- Timing resolution: The timing resolution of the MOS is 1ms and for the PN is 0.03ms.

## 2.6 ROSAT

ROSAT (Rontgensatellit) was a German satellite launched on June 1 1990 from Cape Canaveral. It ran a pointed program which over the lifetime of the satellite built up a large amount of X-ray data which now makes up an extensive catalogue that is available through LEDAS at Leicester. Like XMM-Newton it had a Wolter mirror design but with an effective area of  $400 \text{ cm}^2$  at 1 keV. The angular resolution of ROSAT is better than 30 arcseconds within a radius of 20 arcmin. A diagram of the ROSAT telescope is shown in figure 2.10.

### 2.6.1 The Position Sensitive Proportional Camera (PSPC)

There were two PSPC cameras originally installed on ROSAT. PSPC C was used for all pointings before January 1991 and subsequently PSPC B was used after the PSPC C was irreparably damaged after the satellite was inadvertently pointed at the Sun. The PSPC is a basic multiwave proportional camera with an  $8\text{cm}$  ( $2^\circ \times 2^\circ$ ) field of view. The PSPC was supported by an aluminium plate made up of a central ring of 20 arcmin and 8 radial struts (*ROSAT Users Handbook* 1996). This field of view was large enough such that most cluster emission could be contained in the central ring and a large annulus from the outer ring could be used as a background region.

The quantum efficiency of the PSPC was related to the absorbing power of the gas in the counter. Below 2 keV the absorbing power is almost 100% and the quantum efficiency is only reduced by the mirror supports. Above 2 keV this drops off quickly meaning that the PSPC was only usable in the 0.3-2 keV energy range. This meant that for cluster work it mainly measured the soft X-ray emission and not emission up to the

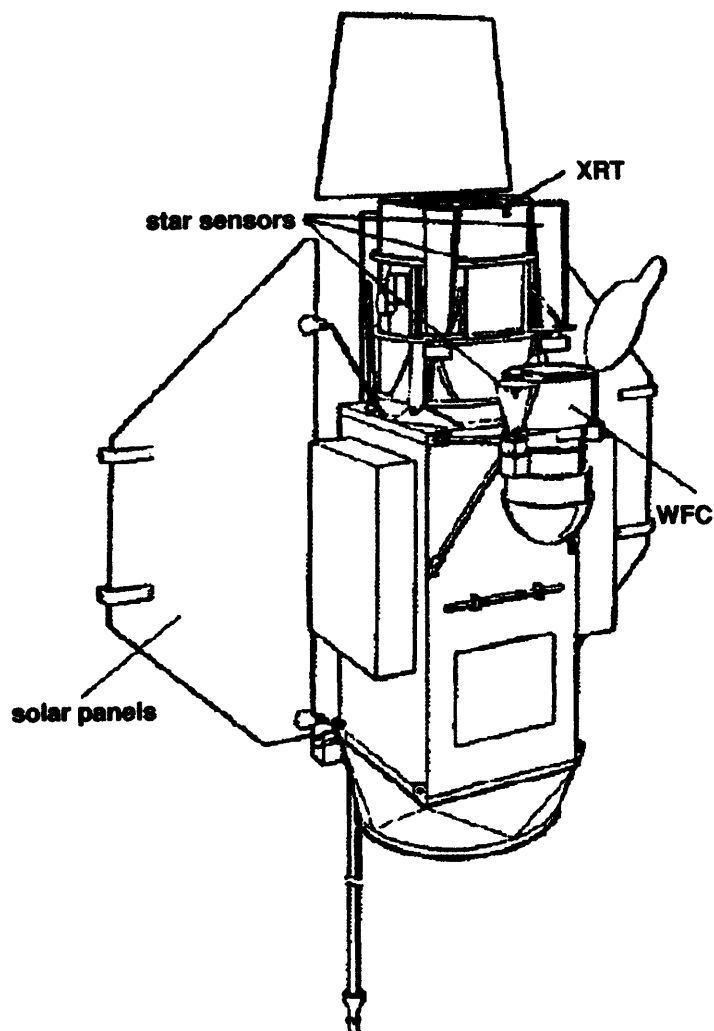


FIGURE 2.10. Diagram of the ROSAT mirror assembly showing the position of the detectors.

global gas temperature, as for most clusters this lies above 3 keV. The energy resolution of the PSPC is given by  $\Delta E/E = 0.4E^{1/2}$  where E is in keV. The spatial resolution of ROSAT gives an angular resolution of  $\sim 25$  arcseconds. This deviates by  $\approx 5\%$  over the area of the detector. This change in angular resolution is fairly small but will have some effect on cluster scales.

# **Chapter 3**

## **Data Reduction and Analysis**

### **Techniques**

#### **3.1 Introduction**

There are several techniques employed to analyse the X-ray data studied in this thesis. They are similar for all clusters, though they differ slightly between instruments. This chapter gives a detailed description of the XMM processing and reduction for the EPIC detectors. Firstly the pipeline processing is discussed and then the background subtraction before a discussion of the more specialised techniques needed for spectral and spatial analysis. ROSAT PSPC analysis is also discussed briefly in this chapter.

#### **3.2 XMM EPIC data processing techniques**

##### **3.2.1 Data products**

The EPIC instruments provide event lists of spectral, spatial and timing information for each photon detected. Using the spatial information, images are made of the observation.

These are usually binned to  $600 \times 600$  pixels for the MOS detectors. Lightcurves can also be generated from the timing information which are useful for identifying flare events. Spectra are generated from the PHA (pulse height analysis) or PI (pulse integration) columns which identify the photons with their incident energy.

### **3.2.2 EPIC data processing pipeline**

The raw event data from the satellite detectors is analysed using the Science Analysis Software (SAS) by the XMM-SSC (Survey Science Centre) before being passed to the Science Operations Centre (XMM-SOC) for distribution. Figure 3.1 shows schematically how the XMM-Newton pipeline works. The EPIC MOS files are passed through a pipeline called EMCHAIN which runs a series of routines to correct the raw event files for good time intervals, bad pixels and attitude. It also puts in the columns for PI and PHA. The final output of this chain is a FITS (flexible image transport) file for each of the three EPIC detectors.

The data can be processed further by the user who can also run some of the pipeline processes again in order to refine the data, using the original raw data files. The FITS files that are created from the processing pipeline can be put into the SAS program XMM-SELECT which acts as a graphical interface to the EVSELECT routine. This program allows the user to filter the event list, create spectra, images, lightcurves and histograms. The outputs of these routine are also FITS files so can be transported into other analysis programs for further work.

### **3.2.3 XMM-Newton X-ray Background**

There are several components that make up the X-ray background in the XMM data. These are :

- Cosmic rays



- Galactic soft X-ray diffuse background
- Extragalactic X-ray background
- Soft protons

The dominant component of the XMM background up to 6 keV is the diffuse X-ray background. This can be modeled by two thermal plasmas within the galaxy (at 0.05 keV and 0.12 keV, the former is unabsorbed, the latter has a column density of  $1.66 \times 10^{20} \text{ cm}^{-2}$ ). The extragalactic component is modeled by a power law with photon index 1.46 and the same column as above (*The XMM users handbook* 1999). The galactic diffuse background is also variable across the sky by up to a factor of two as determined by the ROSAT all sky maps. The extra galactic component is thought to be from distant X-ray sources such as QSO's.

Above 1.5 keV the cosmic ray background starts to affect the data. This generates  $\gamma$ -rays within the spacecraft. The normal particle flux for the MOS is estimated at  $1.5 \times 10^{-4} \text{ counts cm}^{-2} \text{ s}^{-2} \text{ keV}^{-1}$ . This component produces a virtually flat spectrum. For the EPIC PN this is likely to be approximately a factor of two higher. The cosmic ray flux also varies by up to a factor of two over the orbit of XMM. The particle background component is related to the event rates for the detector. A study of the XMM-Newton background has been undertaken by Katayama et al (2002), in order to understand its effect on low surface brightness objects such as the outer regions of cluster.

### 3.2.4 Soft Proton Events

The soft proton background is caused by low energy protons from the sun hitting the detectors once they are outside the Earth's radiation belts. The energy of these soft protons is smaller than a few 100 keV. These protons are funneled towards the detectors by the X-ray mirrors. Most of the time these events do not contribute considerably to the X-ray background but from time to time there are flares of protons which can increase

the count-rate on the detector from the order of ten counts per second to thousands. This large increase in proton flux reduces the signal to noise of the data and so it is a usual precaution to create a lightcurve for the data before any analysis. These events show up clearly in this lightcurve and it is then possible to cut the time intervals where these events occur from the datasets.

### 3.2.5 Background Subtraction

For the MOS instruments there are standard background files which were created by D. Lumb (Lumb 2002a). These are generated by combining several high latitude background pointings from XMM as shown in figure 3.2. For the PN, an offset pointing of Abell 2163 was used, which contained no obvious sources of emission. The dataset was checked for emission by overlaying contours onto the image. An increase in the density of the contours would indicate a source of emission. For spectral fitting the background regions were taken to be the same size as the source regions. The regions were extracted in detector co-ordinates as these are constant between datasets. The background count rates for each detector were, for MOS1  $3.685 \pm 0.4002 \times 10^{-3} \text{ cts}^{-1} \text{ arcmin}^{-2}$ , MOS2  $4.130 \pm 0.4804 \times 10^{-3} \text{ cts}^{-1} \text{ arcmin}^{-2}$ , and PN  $15.36 \pm 0.798 \times 10^{-3} \text{ cts}^{-1} \text{ arcmin}^{-2}$ .

The background files were also normalised for different clusters by scaling the background so that the  $\chi^2$  was minimised on fits to the data with a single temperature model. This scaling varies with detector as well as between clusters. The spectra were also inspected to see if there was evidence of the 1.4 keV Aluminium line in either absorption or emission as shown in figure 3.3. This line indicates whether the background is over or under subtracted since the line comes from the materials used to build XMM and is always visible in unsubtracted spectra.

Correct subtraction of the soft X-ray background of XMM has been found to be important (Pratt & Arnaud 2001). It has been found that if the soft X-ray background is not correctly subtracted the fit to the  $n_H$  (galactic column density) component can be

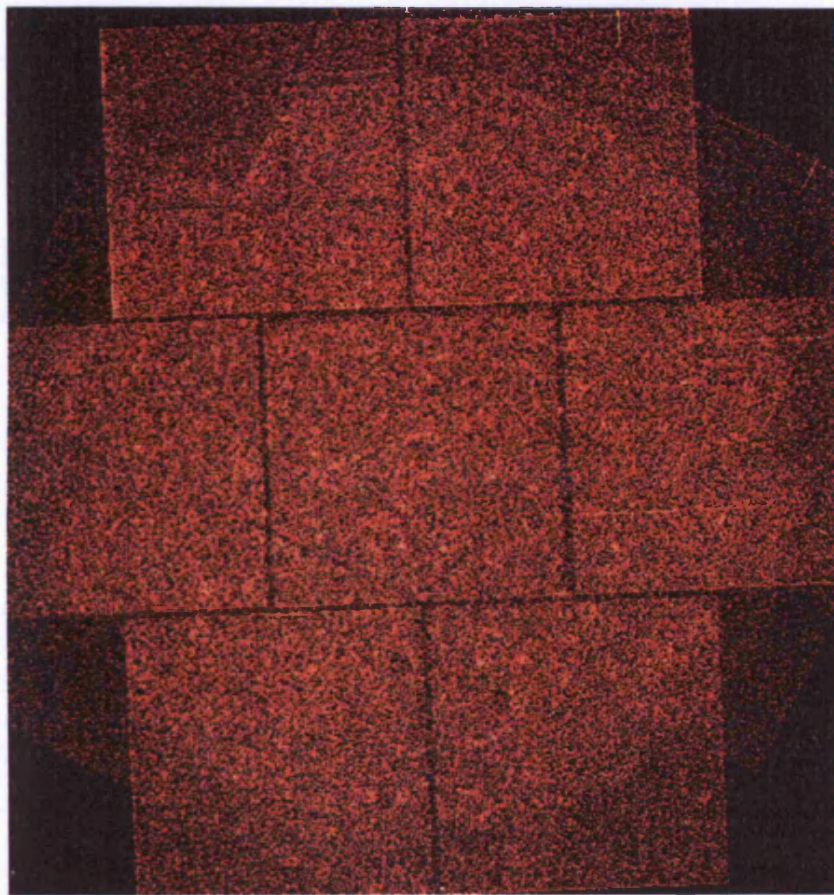


FIGURE 3.2. This is the mos1 background image taken as a mosaic of blank fields in order to produce a standard XMM background for the chip

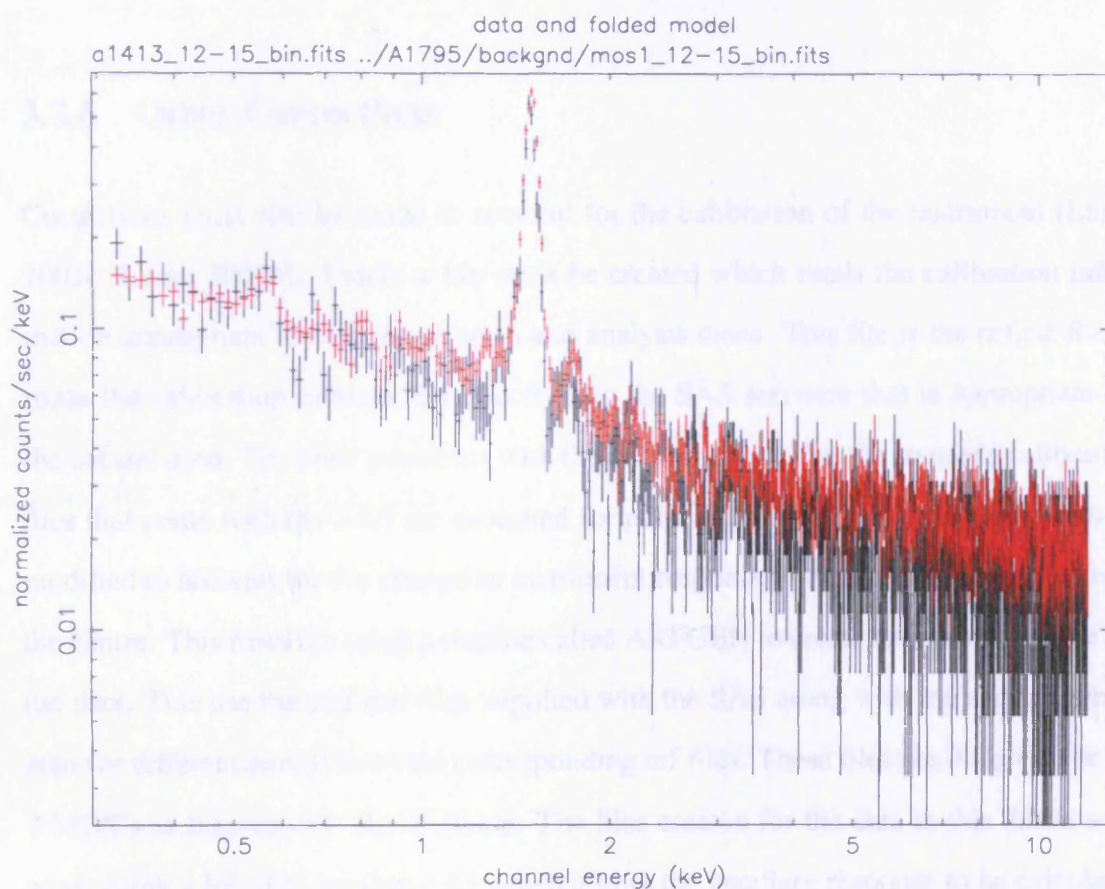


FIGURE 3.3. This shows the spectrum from the data in a region external to the cluster emission (12-15 arcmin) as black compared to the same region generated for the background file (red). This is for the MOS1 camera.

affected. Incorrect subtraction causes a raised fit temperature if the  $n_H$  component is fixed, whereas if the  $n_H$  is left free the temperature is unaffected but the resultant  $n_H$  value is lowered. Therefore, the fits were always checked with both fixed and free  $n_H$  to see if the background had been correctly removed.

For spatial analysis, the background is approximated as a constant which represents the amount of flux remaining after the profile levels off.

### 3.2.6 Other Corrections

Corrections must also be made to account for the calibration of the instrument (Lumb 2002c, Lumb 2002b). Firstly a file must be created which reads the calibration information appropriate for the observation and analysis dates. This file is the `ccf.cif` file, it reads the calibration information directly into the SAS software that is appropriate for the dataset used. The other problems with the calibration are that the standard calibration files that come with the SAS are designed for point sources. Therefore they need to be modified to account for the change in instrument response with azimuthal distance from the centre. This involves using a routine called `ARFGEN` to create azimuthal arf files for the data. This use the `ccd rmf` files supplied with the SAS along with the spectra generated for different annuli to create corresponding arf files. These files are different for the 2 MOS's as they are 90° out of phase. The files created for the data in this thesis were made using `ARFGEN` version 1.43 which allows the ancillary response to be calculated over an annulus. Arf files were created over 2 arcmin sized regions, over this scale the off axis response is not thought to vary significantly. The current version of `ARFGEN` does not correct for the variation in the point spread function but does account for things such as telescope effective area and quantum efficiency.

### 3.3 Spectral Analysis

In this section the methods for analysing the XMM-Epic data are discussed.

#### 3.3.1 Epic fitting procedures

To create a spectrum of the EPIC data the data is firstly run through XMMSELECT to create an image of the data. Regions can then be selected from the image and spectra appropriate for those regions extracted from the data. To save time all the images were created in detector co-ordinates so that the process could be automated. The automation involved using a shell script to perform the data selection which was then carried out by the EVSELECT routine which is more usually run from the XMMSELECT gui. The regions were selected in close proximity to each other in the central regions due to the increased number of counts and also to measure any cooling effects. In contrast the outer annuli were more widely spaced due to lower numbers of counts in this area.

The data was then put into the XSPEC fitting routine along with the equivalent scaled background regions and the two appropriate calibration files. Models were then applied to the data depending on the previous determination of the cluster as having a cooling flow component or not. The goodness of fit of the models was determined by minimising the  $\chi^2$  per degrees of freedom. The different models tried are detailed in the next section.

The errors on the data were calculated at the 90% confidence level unless otherwise stated. These errors were taken by running the error command on the data in XSPEC once a model had been fitted to the data. This command works by calculating the values possible to a given confidence level. No additional systematic errors were included in the fit to the XMM-Newton data other than those already accounted for in the calibration.

Table 3.1. Parameters of the single temperature thermal bremsstrahlung (MEKAL) plus photometric absorption (PHABS) model used on the cluster fits

Parameter	Setting
Plasma Temperature	Free Parameter
Hydrogen density	$1 \times 10^{-3} \text{cm}^{-3}$
Metal Abundance	Free Parameter
Redshift	Cluster dependent
Switch parameter	Calculate (0)
Normalisation	Free Parameter
Column Density	Cluster dependent ( $10^{20} \text{cm}^{-2}$ )

### 3.3.2 Spectral Models

There are several models that can be fitted to the spectra of clusters. These vary in complexity and physical feasibility. The aim of all of the models is to gain an insight into the physics associated with the cluster gas producing the X-ray emission studied.

#### Single temperature plasma model

The spectrum of the cluster gas can be modeled by an single temperature plasma based on the model of Raymond and Smith (1977). This model mostly consists of thermal bremsstrahlung emission from an optically thin plasma but also incorporates recombination, and line emission. A refinement of this model by (Mewe & Gronenschild. 1985, Mewe, Lemen, & van den Oord 1986, Mewe 1994) known as the MEKAL model in XSPEC was used in this analysis. The parameters of this model are shown in table 3.1 This model has an option in it which allows the user to either calculate the model spectrum for each temperature or interpolate the model spectrum from a pre-calculated table. The version which calculated the model was used in all cases since it is more accurate.

The main feature of the XMM cluster spectra is the 6.7 keV Iron line, so when models are fitted this provides accurate constraints on the redshift parameter. A poor fit to the iron line suggests a poor fit to the model for a dataset where the redshift is already well known. The model ties the abundances of all the elements used to fit the lines, and is,

usually, initially set to a value of 0.3. The ratios of the elements are set by the XSPEC solar command which, as a default, sets the ratios as solar abundance ratios. There is also a version of the model called VMEKAL which allows for the different element abundances to vary, but this does not tend to improve the fit significantly.

### Photo-electric Absorption

The photometric absorption model is used to find the amount of X-ray absorption by interstellar hydrogen clouds along the line of sight between the observer and the source. The XSPEC model PHABS is used to model this absorption and uses the following to find the absorption along a given line of sight;

$$A(E) = \exp(-n_H \sigma(E)) \quad (3.1)$$

where  $A(E)$  is the photo-electric absorption at energy  $E$ ,  $n_H$  is the equivalent hydrogen column density and  $\sigma(E)$  is the photo-electric cross section (not including Thomson scattering)

### Cooling flow models

The cooling flow model primarily used in this work is called MKCFLOW and is in the XSPEC package. This differs from the standard CFLOW model in XSPEC in that it sets the emissivity function to be the inverse of the cooling time. This model is based on (Mushotzky & Szymkowiak 1988) and uses the MEKAL model discussed previously to compute the individual temperature components of the fit. It assumes steady state cooling flow. The high and low temperatures from the MKCFLOW model are weighted by their cooling times as follows;

$$F(E) \propto \dot{M} \int_{T_{low}}^{T_{high}} \frac{\epsilon(E, T)}{\Lambda(T)} dT \quad (3.2)$$

where  $F(E)$  is the cooling flow flux as a function of energy  $E$ ,  $\epsilon$  represents the spectrum of the thermal plasma at temperature  $T$  (from the MEKAL model) and  $\Lambda(T)$  is the cooling function. The low temperature is fixed at a temperature corresponding to 0.1 keV (approx  $10^6$  K) and the upper temperature is the one from which the gas is cooling (i.e. the model uses the MEKAL temperature equivalent to that from the single temperature model). The mass deposition rate ( $\dot{M}$ ) is gained from the normalisation.

The spectral resolution of XMM is such that the high temperature component can be found by looking at the spectrum above about 3 keV and fixing it to the best fit value for these energies. This is because most of the expected cooling flow line blends occur in energies between about 1 and 2 keV. Once the upper temperature has been determined this can be fixed and then the cooling part of the model can be allowed to fit to the lower energy parts of the spectrum.

## 3.4 EPIC Image Analysis

The EPIC detectors of XMM-Newton also have good spatial resolution. Therefore the images can be analysed to provide information about the structure of the clusters. The methods used to extract the spatial information from the data are discussed in this section.

### 3.4.1 Radial Profiles

One of the most common ways of analysing cluster data spatially is to make surface brightness profiles from images of the cluster. This is achieved by producing images of the data in particular energy bands. For example it is possible to take a profile just in the ROSAT 0.3-2 keV band or just in the hard energy band (2-8 keV) In general for this work data was taken over a full band (usually 0.3-8 keV) as well as in the soft and hard bands. The hardest energy was usually taken to be 8 keV as for most clusters there is very little emission seen at these energies and it is hard to distinguish emission from

background. However in very hot clusters (ie those with temperatures above 8 keV) then the full XMM energy range up to 10 keV must be considered.

Once the images are generated they are then analysed using the ASTERIX package which produces radial surface brightness profiles from the image. This is achieved by selecting a centre point of the image using the `icent` command and then producing a radial profile from this centre to a given radius using the `iradial` command. The radial scale of the ASTERIX plots is in pixels but this can be converted into other units upon exiting the program. The output produced by the ASTERIX package consists of an `sdf` file and/or a text file. It is the text file which is input into QDP (see below) in order to fit a model to the radial profile.

The QDP package is used to fit a King model to the surface brightness profile produced by ASTERIX. The King profile fit consists of 3 parameters which are the core radius,  $r_c$ , the negative index of the surface brightness equation,  $-IN = -3\beta + 1/2$  and the central surface brightness,  $S_0$ . We also fit a constant parameter which is used to model the background. A typical profile produced by this technique is shown in 3.4. From the fit to the model the parameter beta can be determined and from this an estimate of the cluster gas mass can be obtained.

### 3.5 ROSAT PSPC reduction

The ROSAT PSPC data was taken from the LEDAS web-site in the form of calibrated event lists and images. The data needed further reduction appropriate for extended sources and this was done using the ESAS software (Snowden & Kuntz 1994, Revised 1998). This software corrects extended X-ray sources for the different types of ROSAT background as well as correcting the exposure and vignetting. At the end of this reduction background subtracted images are produced which can then be analysed.

Following the initial reduction the data was passed into a Fortran program which initially produced a raw radial profile of the each cluster, followed by a median profile

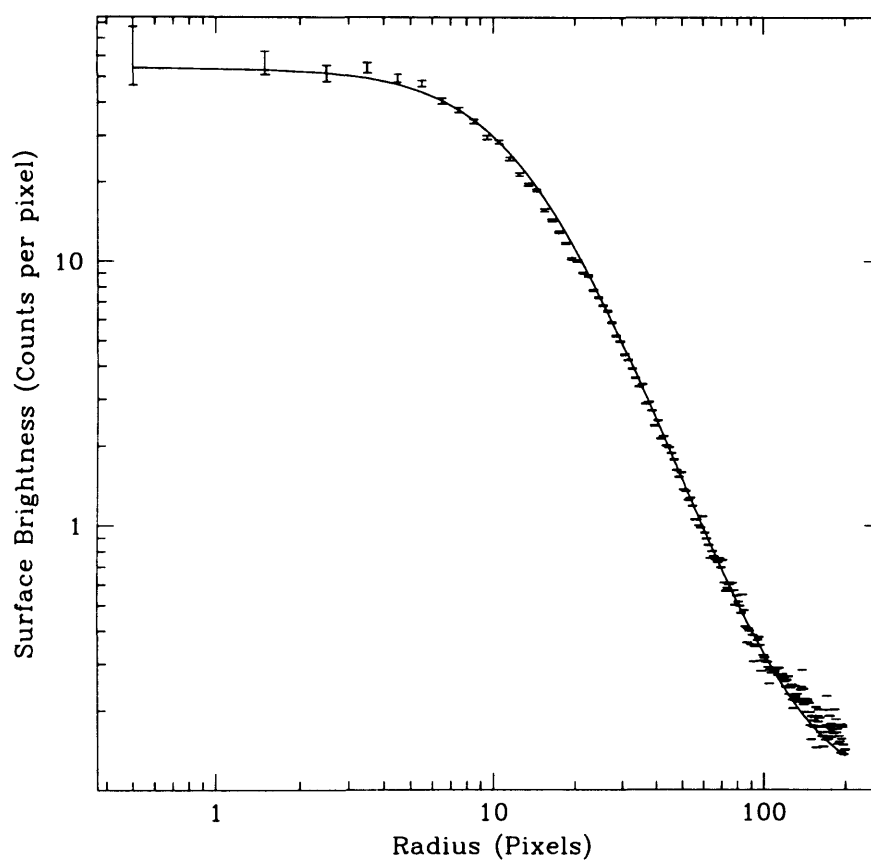


FIGURE 3.4. This shows a fit to a typical surface brightness profile using the King model. The data was processed using ASTERIX and then fitted in QDP. The background was fitted as a constant in QDP and as a result there is a small residual amount of background remaining

which represented most of the initial data from the raw profile but significantly reduced the scatter. The data was also binned up and rescaled at the same time. This procedure was repeated for many clusters and the data for all the clusters was passed into a routine which did a principal component analysis (PCA) on the all the cluster datasets.

# Chapter 4

## A PCA of Cluster Surface Brightness

### Profiles

#### 4.1 Overview

Self-similarity of cluster surface brightness profiles is of interest, as any non-gravitational energy release into the ICM would be expected to cause departures from it. Studies so far have used analytical fits to profile data, which can introduce spurious parameter correlations. In this chapter, initial results of an investigation into properties of 42 clusters are presented. After standard data reduction, a principal component analysis (PCA) is used to extract information from the surface brightness profiles. The degree of self-similarity amongst the clusters, the minimum number of parameters needed to describe a profile and possible comparisons with analytic models (eg  $\beta$ -model) are discussed.

#### 4.2 Introduction

Recent work on the surface brightness of rich clusters has shown they are self-similar on large scales (Mohr, Mathieson & Evrard 1999, Vikhlinin, Forman & Jones 1999).

A correlation between the asymptotic slope,  $\beta$  and core radius ( $r_c$ ) has also been outlined (Pownall 1997, Neumann & Arnaud 1999). These studies used 1 or 2  $\beta$ -model components to represent radial profiles. The problem with using  $\beta$  profiles to analyse the clusters is the dependence that some of the fit parameters have on each other. If the parameters are correlated, as has been found then an uncertainty in one parameter propagates through the fit. A non-parametric method, for example a principal component analysis, does not have this problem and so is a more rigorous way of investigating cluster surface brightness profiles.

Work has also been carried out which suggests that the luminosity temperature relationship between clusters and groups differs (Helsdon & Ponman 2000b). This suggests that there is not just a simple scaling relation between clusters and groups and that they may have different physical properties. It is hoped that the principal component analysis will be able to provide some evidence as to whether or not this is the case by investigating the differences between the profiles of clusters and groups. This has important implications to the formation of clusters and groups.

In this chapter the results of a Principal Component Analysis of 39 low redshift (0-0.25) ROSAT PSPC rich ( $kT > 2$  keV) clusters is presented. Also included were 3 nearby groups which are at slightly lower temperatures (ie  $kT \geq 1.0$  keV). Only nearby groups are taken so that they are bright enough to produce a clear profile. The clusters were mostly taken from the sample used in Pownall (1997). A preliminary analysis has been carried out on 17 clusters using a hybrid of Fortran and IDL programs, presented in Spurgeon et. al. 2002.

The Principal Component analysis was undertaken using a specially produced Fortran 90 code. The results of the analysis are interpreted to produce some of the physical properties of the cluster. The aim of this work is to investigate the number of components needed to describe a cluster profile and to provide a physical interpretation of the components. It is also hoped that any differences in the profiles of clusters and groups will become apparent.

### 4.3 The Cluster sample

The cluster sample of Pownall (1997), was used as a basis, as it provides a list of bright low redshift clusters observed by the ROSAT PSPC. This data is easily obtainable from the ROSAT database on LEDAS (University of Leicester). The cluster datasets were retrieved from LEDAS and then checked to see if the sources were clear and were contained within the central ring of the detector. In the cases where there were more than one observation of a cluster the longest exposure was used in order to gain more source counts and produce a clearer profile. A few bright nearby clusters which hadn't been included in the Pownall sample were also added. A few groups were also added to see if there are any distinct differences between these and clusters

Information about temperature and redshift was also required in order to normalise the clusters and groups so that they are comparable. These parameters were mostly obtained from Pownall but those which were not available, were taken from other sources (Helsdon & Ponman 2000*a*, Helsdon & Ponman 2000*b*, Ebeling, Voges, Bohringer, Edge, Huchra & Briel 1996, Lloyd-Davies, Ponman & Cannon 2000, White 2000). The clusters along with their redshifts and temperatures are given in table 4.1. The clusters are presented here in the same order they were analysed. As can be seen from the table, the sample contains clusters at a large range of temperatures and redshifts. The sample contains three nearby groups all at lower temperatures than the clusters, these are HCG62, HCG42 and NGC5044. Gas temperatures used by Pownall were obtained from (David, Slyz, Jones, Forman, Vrtilrk & Arnaud 1993) and the cluster redshifts were from (Struble & Rood 1983)

Table 4.1. Table of clusters used in the Principal Component Analysis, including values for the temperature and Redshift. Most of the values were taken from Pownall (1997) with the rest taken from various other sources as discussed in the text

Cluster	Temperature (keV)	Redshift (z)
HCG62	1.00	0.013
A1795	7.00	0.061
NGC5044	1.00	0.008
A1060	3.20	0.012
A1068	4.10	0.139
A119	5.60	0.044
A1367	3.90	0.021
A1413	7.30	0.141
A1656	8.67	0.231
A1763	7.30	0.187
A133	3.80	0.060
A1664	6.50	0.128
A1837	2.40	0.038
A1914	10.5	0.171
A1991	5.40	0.059
A2063	4.10	0.034
A2107	4.20	0.042
A2163	13.3	0.170
A2199	4.50	0.031
A2204	9.00	0.152
A2218	6.72	0.176
A2634	3.40	0.032
A2657	3.40	0.041
A2717	3.10	0.050
A3301	3.00	0.055
A3526	3.90	0.011
A3558	3.80	0.048
A3562	3.80	0.050
A400	2.50	0.023
A401	7.80	0.075
A4038	3.30	0.028
A426	5.50	0.018
A496	3.91	0.032
A500	3.50	0.067
A539	3.00	0.027
A545	5.50	0.154
A665	8.26	0.182
A754	9.10	0.053
AWM7	3.60	0.018
HCG42	0.82	0.013
HydraA	3.80	0.052
MKW4	1.70	0.051

## 4.4 Initial Data Reduction

### 4.4.1 Creation of Median profiles

The cluster data was reduced using Snowden's software for extended sources. This reduction produced background subtracted images of the clusters which could then be transformed into the 1-D profiles. The *cfitsio* routines (HEASARC 2001) were utilised in order to read the images into the program as they were produced in fits format from the Snowden package. First and second-order moments of the counts distribution were used to find the emission centre, ellipticity  $\epsilon$  and position angle  $\theta$  of the cluster major axis. For each pixel, a radial distance from the centre was computed correcting for  $\epsilon$  and  $\theta$ . This correction allows for the ellipticity of the cluster. Raw profiles are produced by plotting the number of counts against this corrected radius. Figure 4.1 is an example of a raw surface brightness profile produced using this method. The vertical lines seen in the raw profile are from unsubtracted point sources.

A median sliding filter was then applied to the data to obtain a median surface brightness profile, which was divided by the exposure time then rescaled accounting for cosmological dimming and cluster temperature (using ASCA cooling-flow corrected temperatures(White 2000)). The median filtering involved radial re-binning of the data into  $n$  bins with the radial widths depending on the distance from the centre. The first eight bins were binned up by a factor of  $2^{(m-1)}$ , where  $m$  is the number of the bin. The rest of the bins were set to have 128 pixels each. The binning was undertaken using the NAG routine G01AAF which performed the sorting and binning of the profile. Documentation on this routine can be found at the Numerical Algorithms Group (NAG) web-site. This was so that the central regions of the cluster, which have higher signal to noise and which change shape more rapidly are sampled more frequently than the outer bins where there are less counts. The radius was then rescaled by the characteristic radius  $r_{500}$ , estimated from numerical simulations, and cluster temperatures (Evrard, Metzler & Navarro 1996b). The radius  $r_{500}$  corresponds to the the radius where the over-density

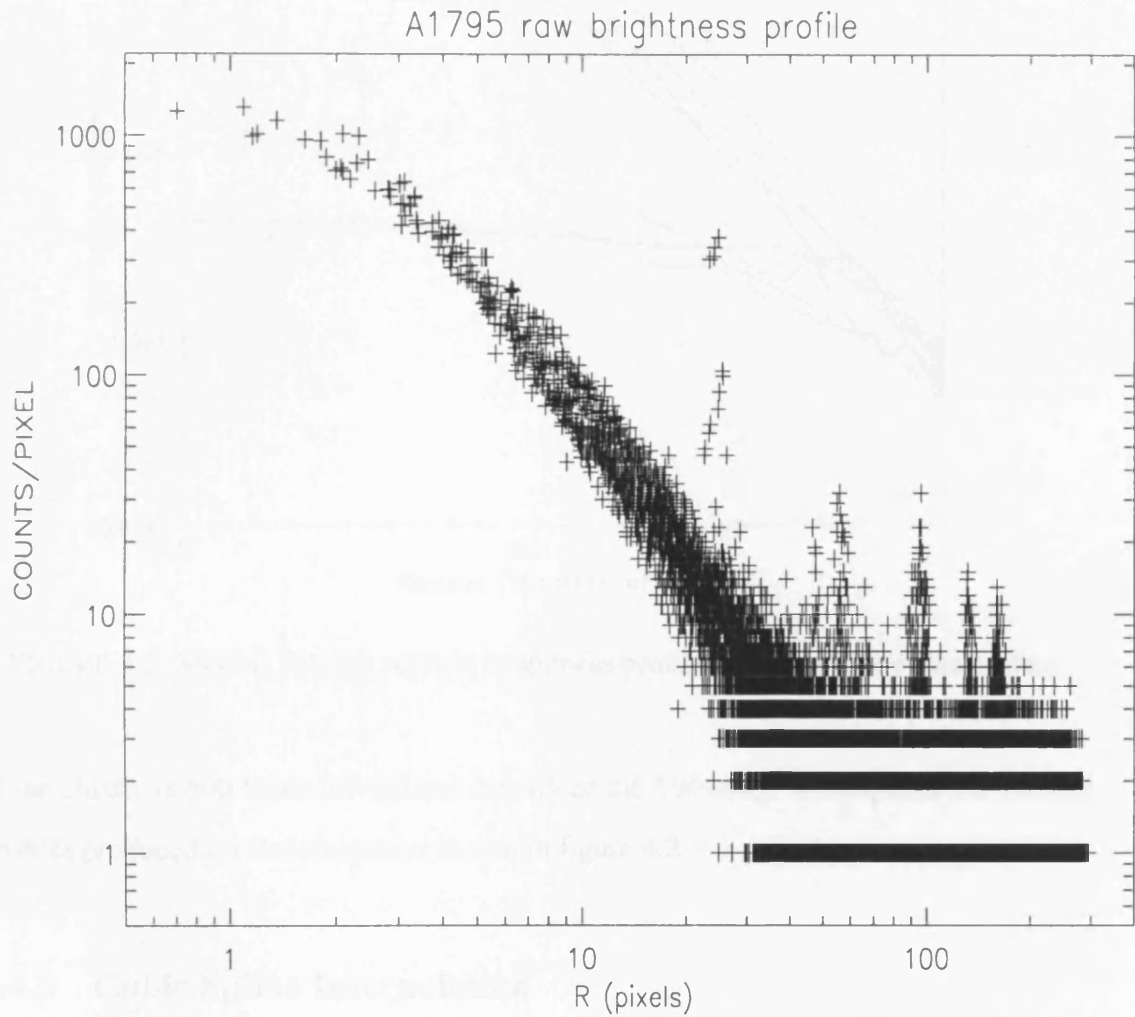


FIGURE 4.1. Raw surface brightness profile of the cluster Abell 1795. The vertical lines in the profile correspond to point sources in the data

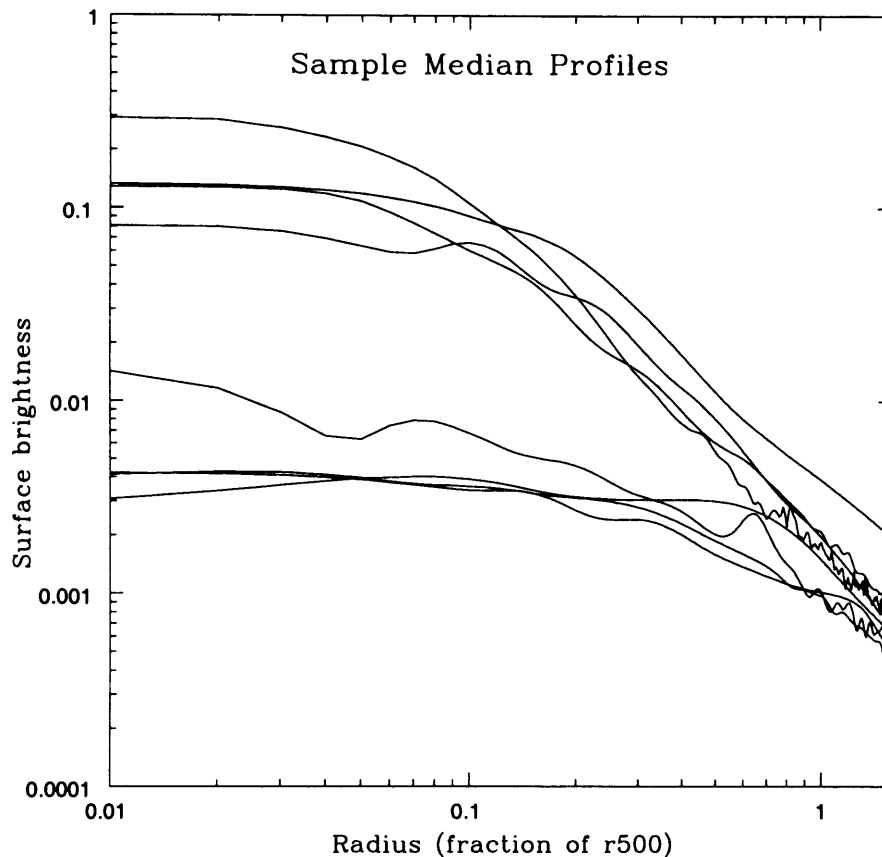


FIGURE 4.2. Median filtered surface brightness profiles of some of the cluster data.

of the cluster is 500 times the critical density of the Universe. A sample of the median profiles produced for the clusters is shown in figure 4.2.

#### 4.4.2 Cubic Spline Interpolation

Each median surface brightness profile was then fitted with cubic splines to produce the surface brightness value at equally spaced radii ( $\delta r = 0.01$ ). This was done utilising routines found in Numerical recipes called SPLINE and SPLINT. The SPLINE routine applied the splines to the data and then the SPLINT routine applied the interpolation. The idea of a cubic spline is to get an interpolation formula that is smooth in the first derivative and continuous in the second derivative. Therefore we set up as if we have a

tabulated function (of the form  $y = Ay_j + By_{j+1}$ ) and also a tabulation of its second derivatives. Thus between each interval it is possible to add terms for a linearly varying second derivative which gives a cubic polynomial. It is also important to set the endpoints of the polynomial  $x_j$  and  $x_{j+1}$  at zero as not to spoil agreement with the tabulated function values at the endpoints. The resulting polynomial is

$$y = Ay_j + By_{j+1} + Cy_j'' + Dy_{j+1}'' \quad (4.1)$$

where

$$A \equiv \frac{x_{j+1} - x}{x_{j+1} - x_j} \quad B \equiv 1 - A = \frac{x - x_j}{x_{j+1} - x_j} \quad (4.2)$$

and

$$C \equiv \frac{1}{6}(A^3 - A)(x_{j+1} - x_j)^2 \quad D \equiv \frac{1}{6}(B^3 - B)(x_{j+1} - x_j)^2 \quad (4.3)$$

In reality however we do not already have the second derivatives of the formula but we can gain the second derivatives by requiring that the first derivatives are continuous across the boundary between two intervals. The key concept of a cubic spline is that this requirement be satisfied. The required equations are obtained from the first derivative of 4.1 (Press, Teukolsky, Vetterling & Flannery 1999) and are a series of  $N-2$  linear equations in the  $N$  unknowns  $y_j'', j = 1, \dots, N$ . The equations are:

$$\frac{x_j - x_{j-1}}{6} y_{j-1}'' + \frac{x_{j+1} - x_{j-1}}{3} y_j'' + \frac{x_{j+1} - x_j}{6} y_{j+1}'' = \frac{y_{j+1} - y_j}{x_{j+1} - x_j} - \frac{y_j - y_{j-1}}{x_j - x_{j-1}} \quad (4.4)$$

For unique solutions we also specify boundary conditions on  $x_1$  and  $x_N$  which typically involves setting one or both of  $y_1''$  and  $y_N''$  to zero, giving a natural cubic spline

otherwise one or both of these are set to a predetermined value. In our case the first derivatives are set to zero and so therefore making the function use a natural cubic spline. The output from the cubic spline was then re-binned once more into a square array so that it could be inputted into the principal component analysis routines.

## 4.5 Principal Component Analysis

The principal component analysis is performed by inputting cluster data into a matrix and finding the eigenvalues and eigenvectors of that matrix. The resulting eigenvector matrix is multiplied by the original matrix in order to produce a variance-covariance matrix, known as the matrix of principal component scores. These represent how much of the information from each dataset is represented by each component. The relationship between the matrices is;

$$\{C\} = \{A\} \cdot \{E\} \quad (4.5)$$

where A is the matrix of the original dataset, E is the matrix of the eigenvectors and C is the variance-covariance matrix of the original dataset. The eigenvector matrix can be transposed and multiplied by the original data in order to completely reproduce the original dataset.

The eigenvalues of the original matrix describe how important each of the principal components are. Each eigenvalue, is therefore maximised, in order that each eigenvector describes as much of the remaining variation as possible. The eigenvector matrix is the matrix representing the principal components, with one eigenvector representing each principal component. The length of the eigenvectors is defined by the number of variables in the analysis. Each eigenvector and thus each component, is calculated to describe the variation of the data for all variables. Therefore the dimensions of the eigenvector matrix are number of variables against component number. The scores matrix however,

shows the relationship between each principal component and the original datasets and has dimensions corresponding to the number of clusters against component number.

The principal component analysis was undertaken utilising the NAG routine G03AAF which produces the eigenvectors, eigenvalues and principal component scores described above. This array uses the square array inputted from the cubic spline routine and then computes the principal components. The routine compares each set of data with  $N-1$  others, where  $N$  is the number of clusters, in this case 42. The program is limited to only being able to compute for  $NVAR$  components where  $1 \leq NVAR \leq \min(N-1, M)$ . In this case  $M$  corresponds to the number of variables, which is the number of radial bins. This is why the output of the cubic spline has to be re-binned into a square array before inputting into the PCA routine. In this case the re-binning was by a factor of four and was undertaken by averaging the values in sets of four and using the average value for the binned value. The reason for doing the analysis is to minimise the number of components needed to completely describe the data. This made it important to maximise the size of the first few eigenvalues and thus eigenvectors. The eigenvalues produced from the array were studied to see which of the principal components were describing most of the variation in the data. The eigenvalues obtained are shown in table 4.2. From the table it is clear that the greatest contribution is from the first eigenvector which describes 76% of the variation and then the second describes 16% with the third eigenvector describing 4.2%. Therefore the first three eigenvectors (and thus principal components) describe a cumulative 96% of the variation between them. It is also evident from the fit that most of the latter components have a very small effect on the fits with most of the eigenvalues tending to zero and having little contribution to the percentage variation described. It is apparent from table 4.2 that in fact only the first 16 components have any measurable significance on the variation and hence the fit, with the first 5 eigenvalues describing over 99% of the variation.

Since most of the variation between the clusters can be described by the first 3 components, they were studied in greater detail. The values of the first 3 sets of scores are



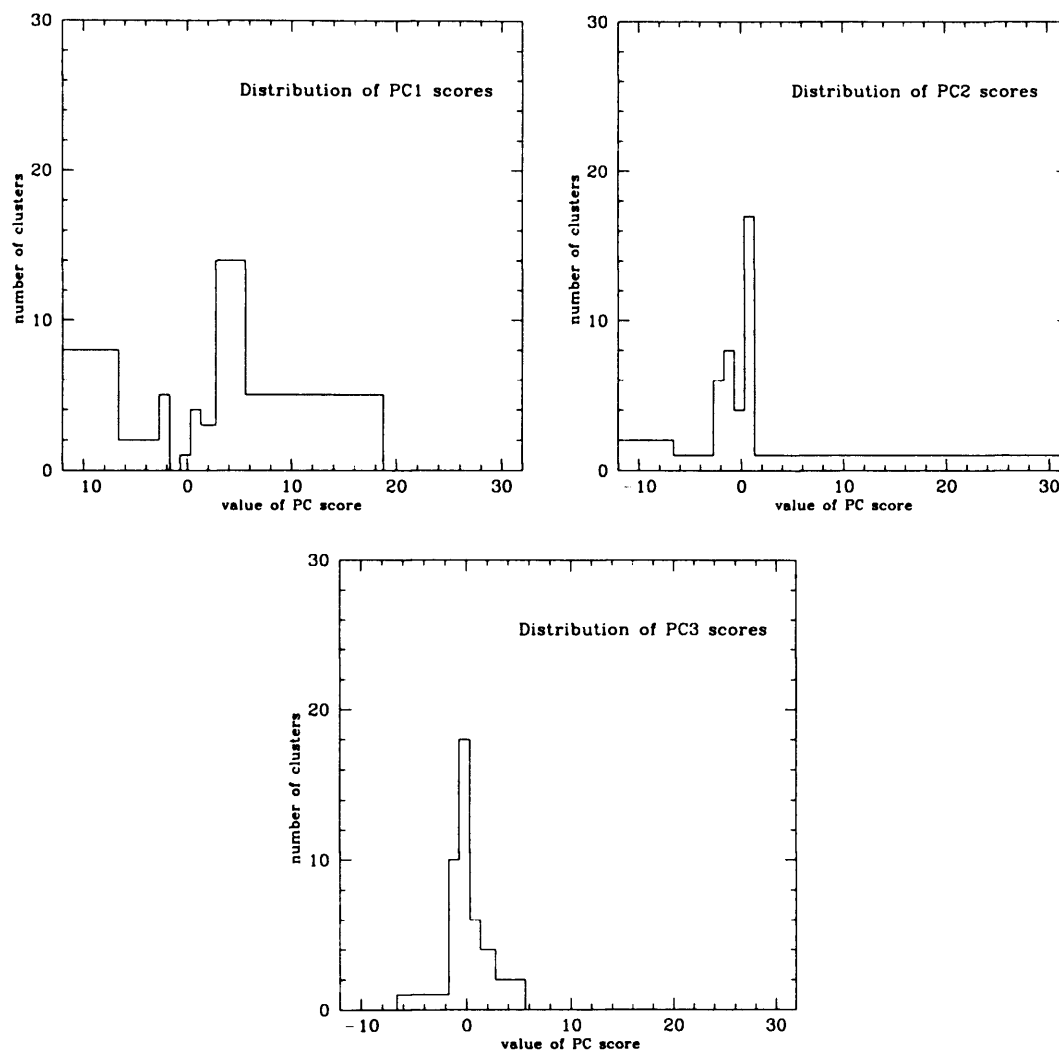


FIGURE 4.3. Histograms of the scores for the first three principal components. These show the different distributions of values for each component

shown as histograms in figure 4.3. The histograms show that the score distribution is quite different for the three principal components.

## 4.6 Discussion

### 4.6.1 The Principal Components

The mean surface brightness profiles for the first three components are shown in figure 4.4. It is clear to see from this plot that the first principal component is straight with a slight falloff with radius and would seem to model most of the basic shape of the cluster. The second component has most significance in the centre and a little towards the outer regions of the cluster. The third component is also significant in the cluster centre, possibly the cooling flow region and also toward the outer region of the cluster, though to a different extent than the second component. The shape of these components could be important for future reference as it may give an indication as to the physical origin of each component.

To see how well individual cluster profiles can be described by the first three components, the scores for an example cluster, were multiplied by the eigenvector corresponding to each of the first three components and the three results summed. The results of this on two example clusters is shown in figure 4.5

The graphs in figure 4.5 show that the profile can be reproduced accurately utilising just the first three principal components as was predicted from the percentage variation for each component shown in table 4.2. It is clear that if physical parameters can be attributed to individual components then it will be possible to reconstruct physical information relating to any cluster without having the problems of correlating parameters as was discussed as the problem with earlier analysis, such as the beta fits.

### 4.6.2 Physical Correlations and Trends

The scores were studied to see whether any physical cluster parameters such as temperature and redshift correlated with any of the scores, or any ratio of the scores. The scores, and ratios of scores were ranked by size so that any correlations between the size of the

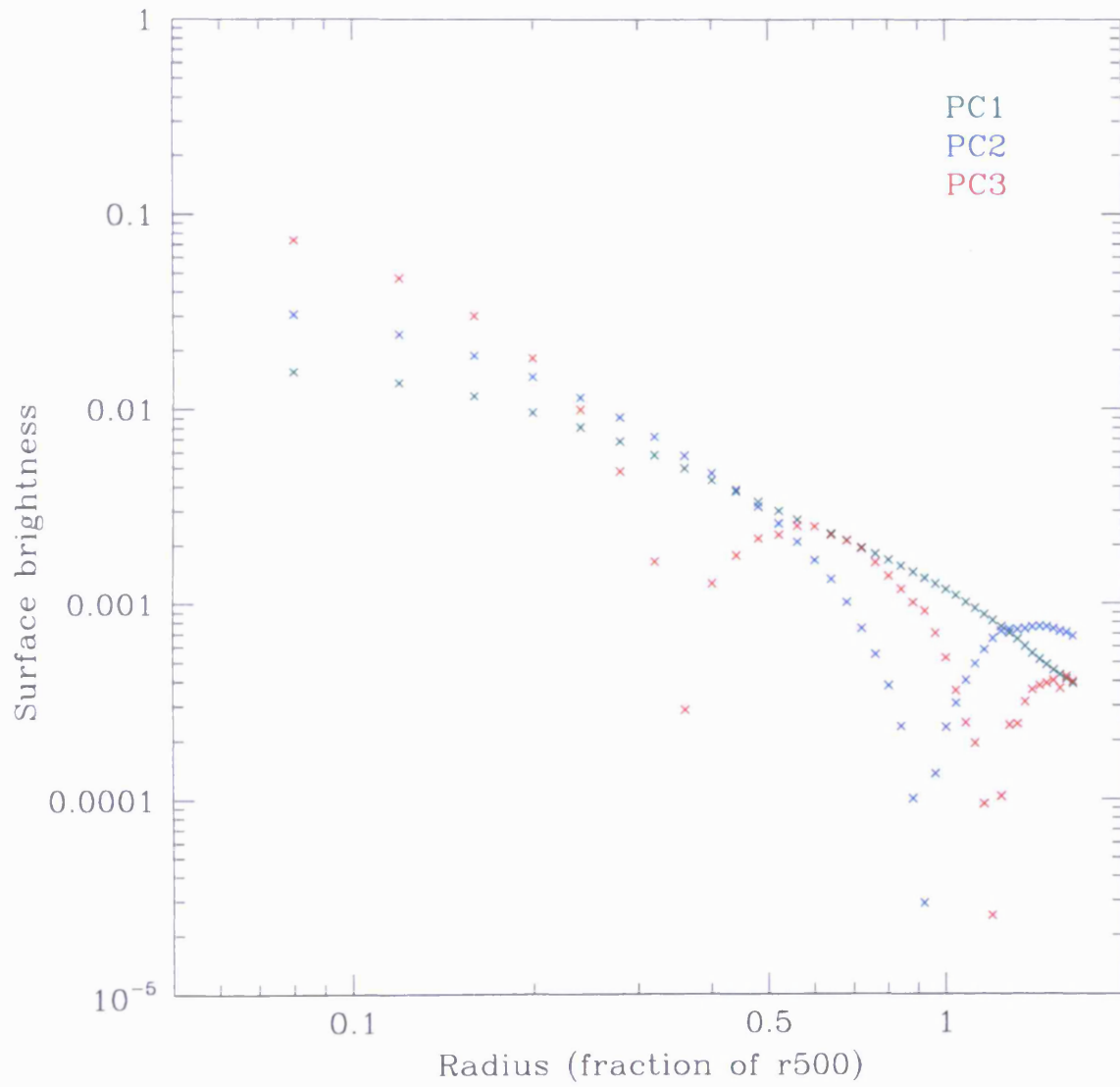


FIGURE 4.4. Profiles for the first three principal components. PC1 is green, PC2 is blue and PC3 is red.

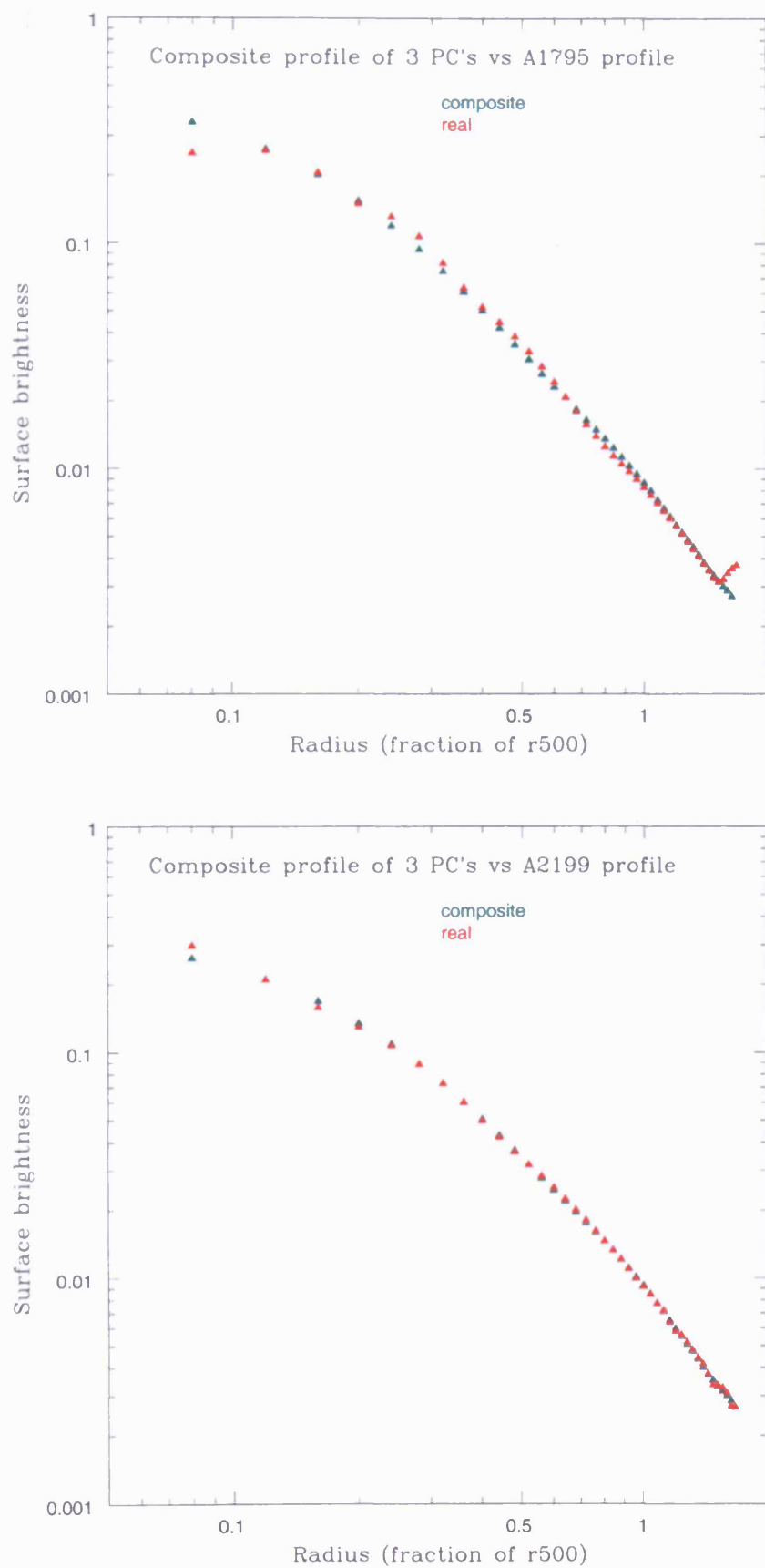


FIGURE 4.5. Profiles produced of clusters Abell 1795 and 2199 using the first 3 PC's only

score and the size of the parameter could be seen. For all of the physical parameters no more than one or two values of the scores and ratios of scores ranked the same as the parameter. This amount of correlation is very small and is of order what would be expected by chance. The lack of evidence for correlations seen from ranking prompted the decision to look for more general trends in the data as described below.

Initially all of the physical parameters were plotted against each of the three sets of PC scores and ratios of scores in order to look for signs of correlation. The most promising candidates were plotted in excel and trend lines were added. Plots of the six best correlations are shown in figures 4.6, 4.7 and 4.8. The  $R^2$  value shown on the graphs, otherwise known as the coefficient of determination, gives an indication of how closely the estimated values for the trend line correspond to the real data. None of the fits undertaken give  $R^2$  very close to one which suggests that the trend lines do not correspond well to the data.

The best fit to the trend lines is found for PC2 vs the core radius,  $r_c$ , where the value of  $R^2$  obtained is 0.2. This means that only 20% of the values are fitted by the trend-line, which suggests that the correlation is poor. We expect that if  $r_c$  is correlated to a principal component then  $\beta$  will also show some correlation to that same component, since the two parameters are interdependent. This is only true in this case to a very small degree as only 4% of the data fits the trend for PC2 vs  $\beta$  (both plots are shown in figure 4.7). For the other components with possible correlations to  $r_c$ , which are the ratio PC1/2 and PC3, the correlation is weaker (with only 5% and 7% of the values being fitted by the trend-line respectively) and there is no correlation to  $\beta$ . Therefore the most promising correlation to  $r_c$  on both counts, is that for PC2, however the  $R^2$  value is not large enough to be certain of a correlation. Data from more clusters would be required in order to provide conclusively whether there is any correlation, as currently the fit is not good enough to prove that the correlation exists. A correlation to PC2 would seem sensible as this is the principal component which falls off at a certain radius, which could possibly be related to the core radius.

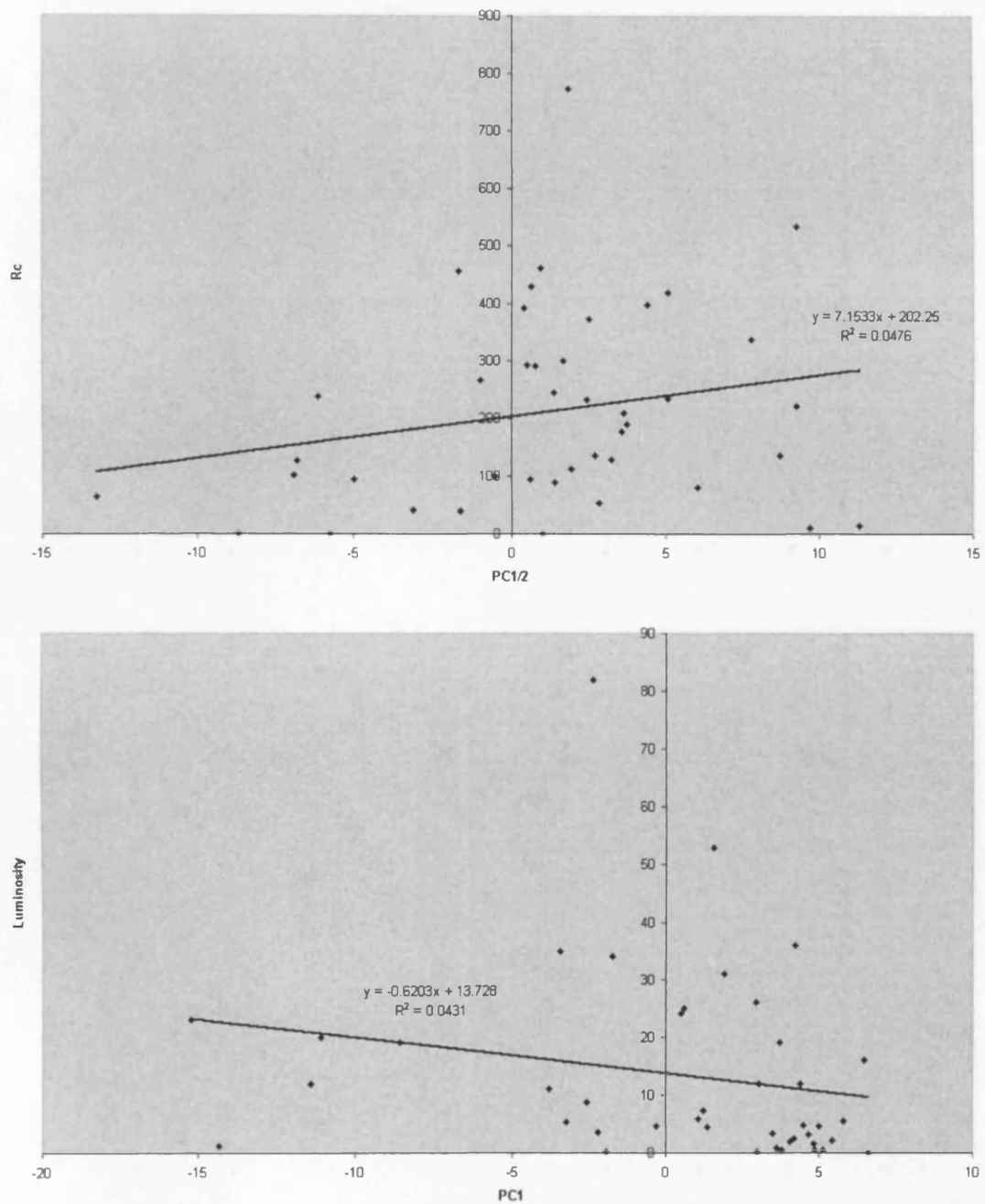


FIGURE 4.6. Plot to show correlations of ratio PC1/2 to  $r_c$  and PC1 to luminosity. The trend lines are the best fit lines to the data.

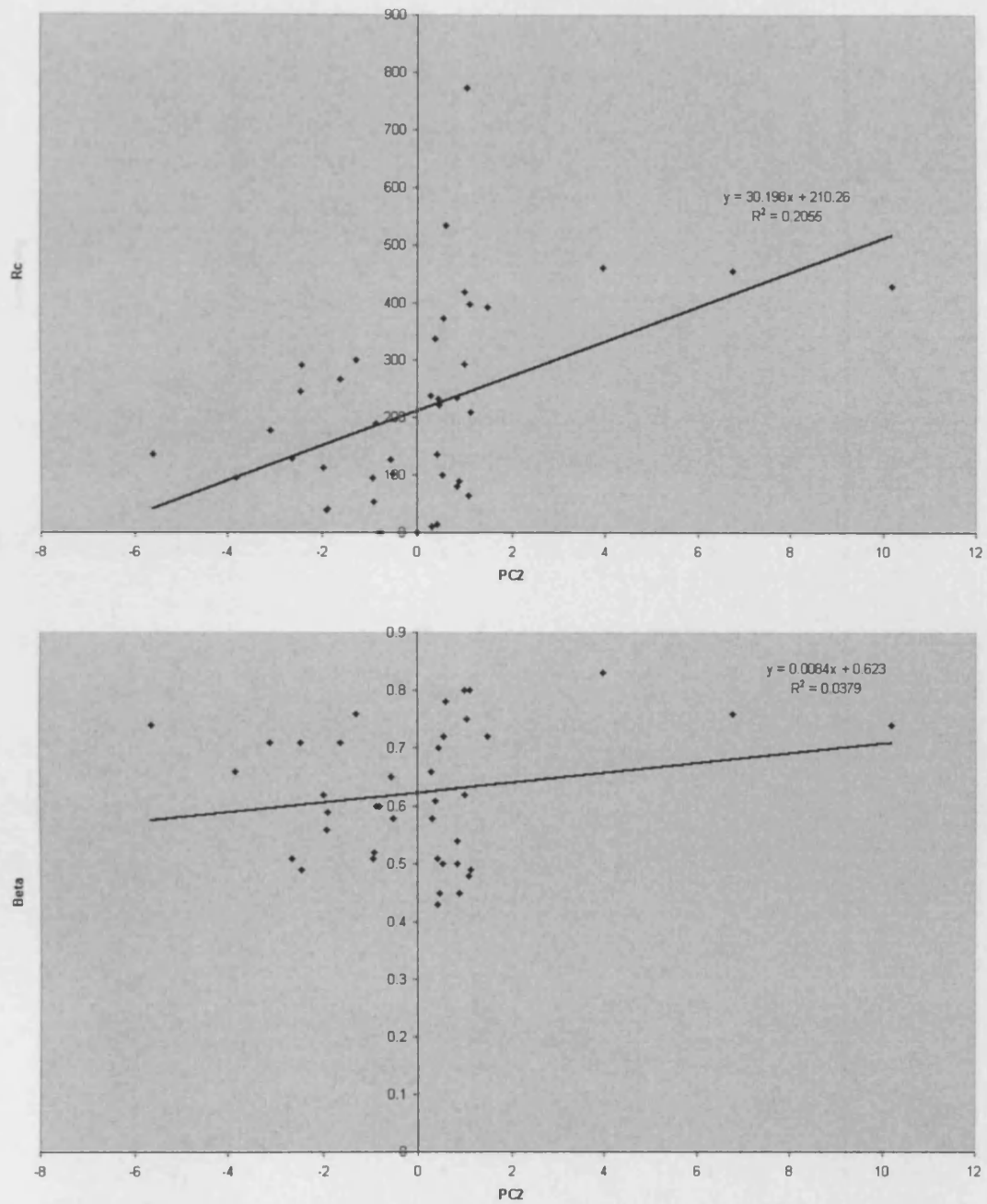


FIGURE 4.7. Plot showing the correlations of PC2 to  $r_c$  and PC2 to  $\beta$  with trend lines shown.

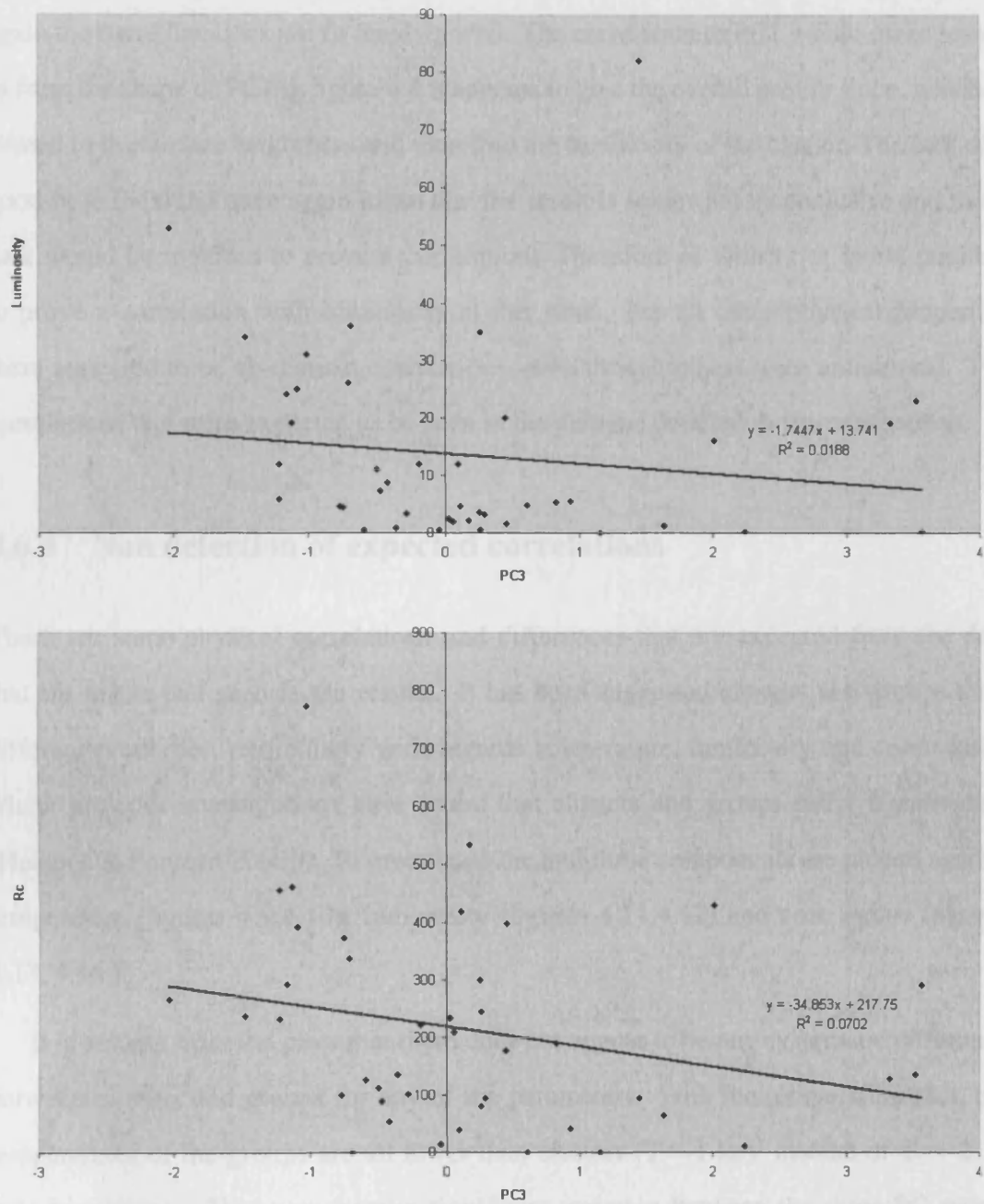


FIGURE 4.8. Plot of the correlations of PC3 to luminosity and PC3 to  $r_c$  with best fit trend lines.

The other physical property for which we have fitted trend lines is luminosity which shows some correlation to PC1 and PC3 (4% and 2% of the values fit the trend-lines respectively). The correlation for PC1 seems more promising than for PC3, but once again the trend line does not fit the data well. The correlation to PC1 would make sense, as from the shape of PC1 in figure 4.4 it appears to give the overall profile slope, which is related to the surface brightness and therefore the luminosity of the cluster. The lack of a good fit to the trend once again mean that the result is somewhat inconclusive and more data would be required to prove a correlation. Therefore as with  $r_c$ , it is not possible to prove a correlation with luminosity at this time. For all other physical properties there appeared to be no distinct correlations, even though others were anticipated. The correlations that were expected to be seen in the data are detailed in the next section.

### 4.6.3 Non detection of expected correlations

There are some physical correlations and differences that are expected from the data that are not in fact seen in the results. It has been suggested clusters and groups have different properties, particularly with regards temperature, luminosity and core radius, where previous investigations have found that clusters and groups differ significantly (Helsdon & Ponman 2000*b*). To investigate the first three components are plotted against temperature (figures 4.9,4.10), luminosity (figures 4.11,4.12) and core radius (figures 4.13, 4.14 ).

It is evident from the plots that there does not appear to be any systematic difference between clusters and groups for any of the parameters. With the temperature plot, the temperatures of the groups are all lower than clusters ( $T \sim 1$  keV instead of  $T \sim 2-10$  keV for clusters. However there is significant variation between the three PC scores obtained for the groups (range for PC1: -1.9-6.6, PC2: -2.4-0.3, PC3: 1.1-3.5) and so despite the groups having very similar temperatures they do not seem to have been grouped together by the PCA. This also appears to be the case for the luminosity plot where the low luminosities ( $\sim 10^{42} - 10^{43}$  ergs  $s^{-1}$  of the groups do not seem to result

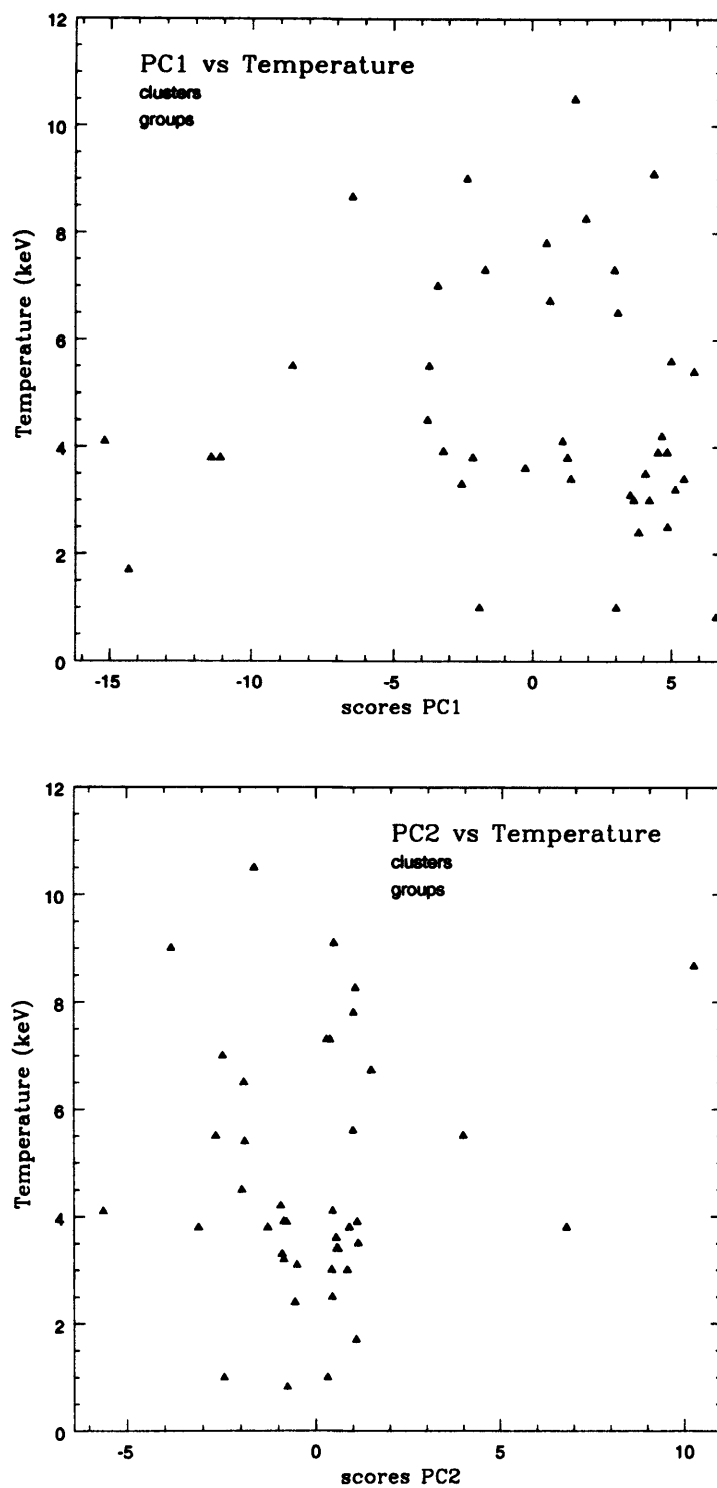


FIGURE 4.9. Temperature plots for the first two components with clusters and groups plotted in different colors to look for differences between the two types of objects

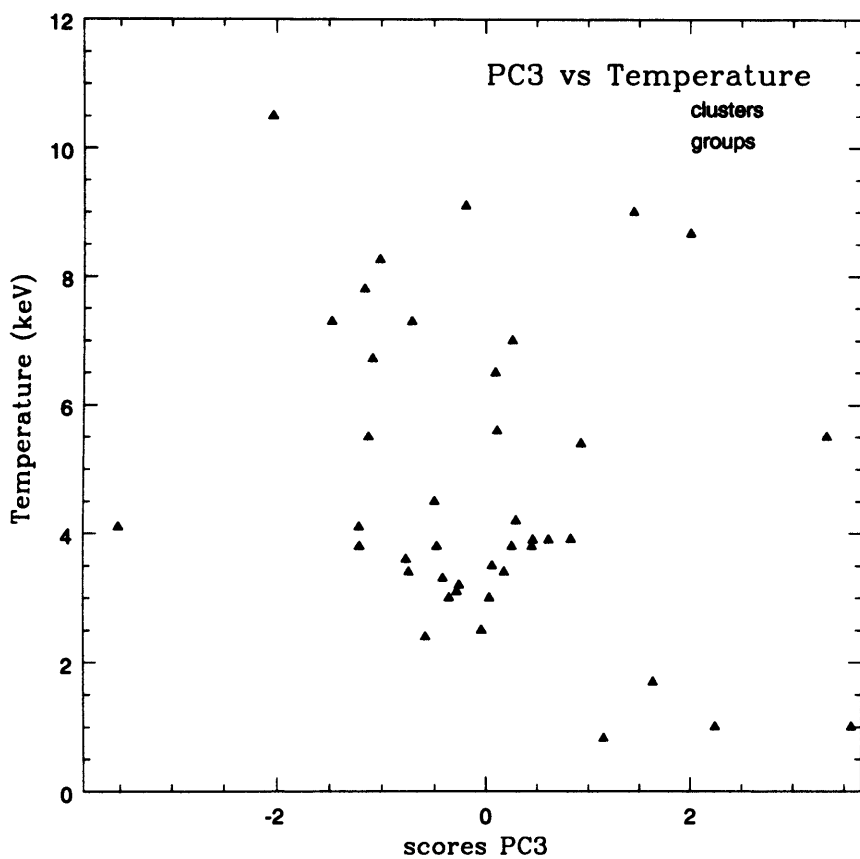


FIGURE 4.10. Temperature plot for the third components with clusters and groups plotted in different colors to look for differences between the two types of objects

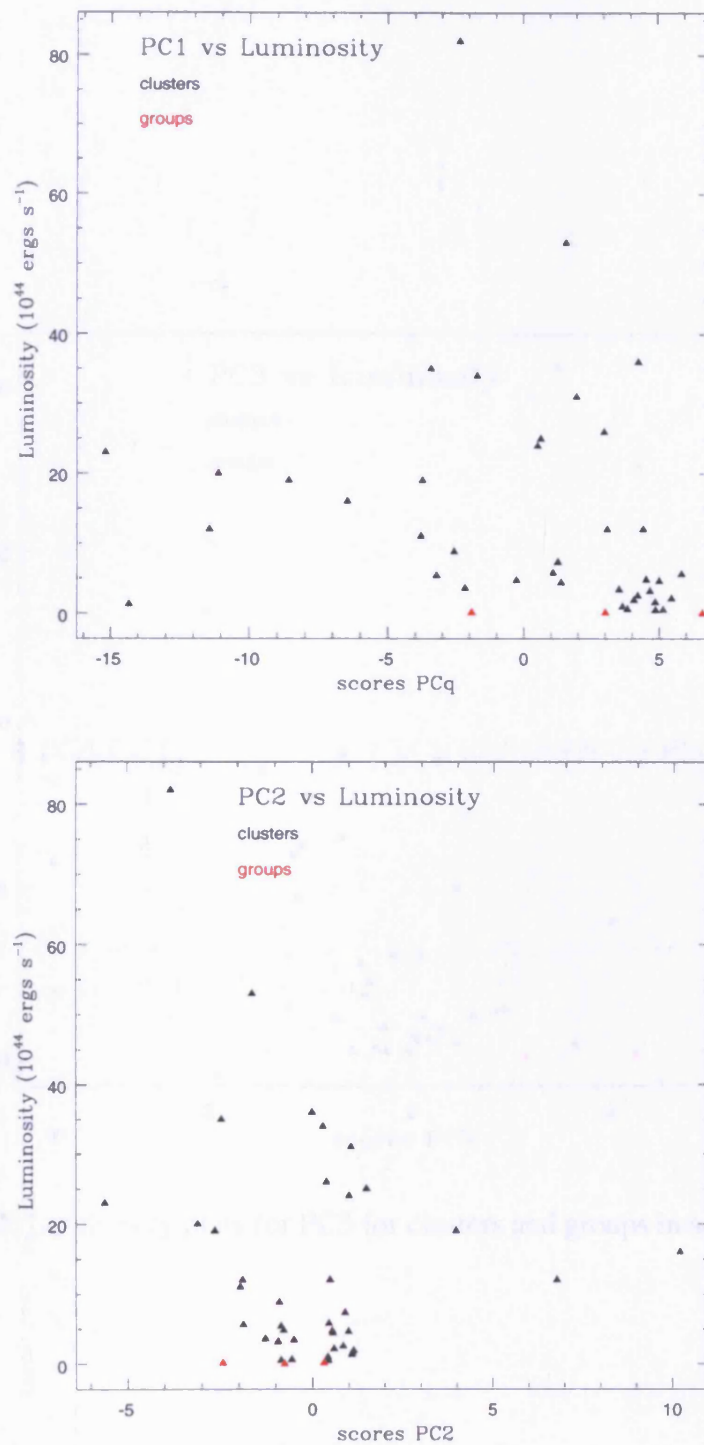


FIGURE 4.11. Luminosity plots for PC1 and 2 for clusters and groups in separate colours.

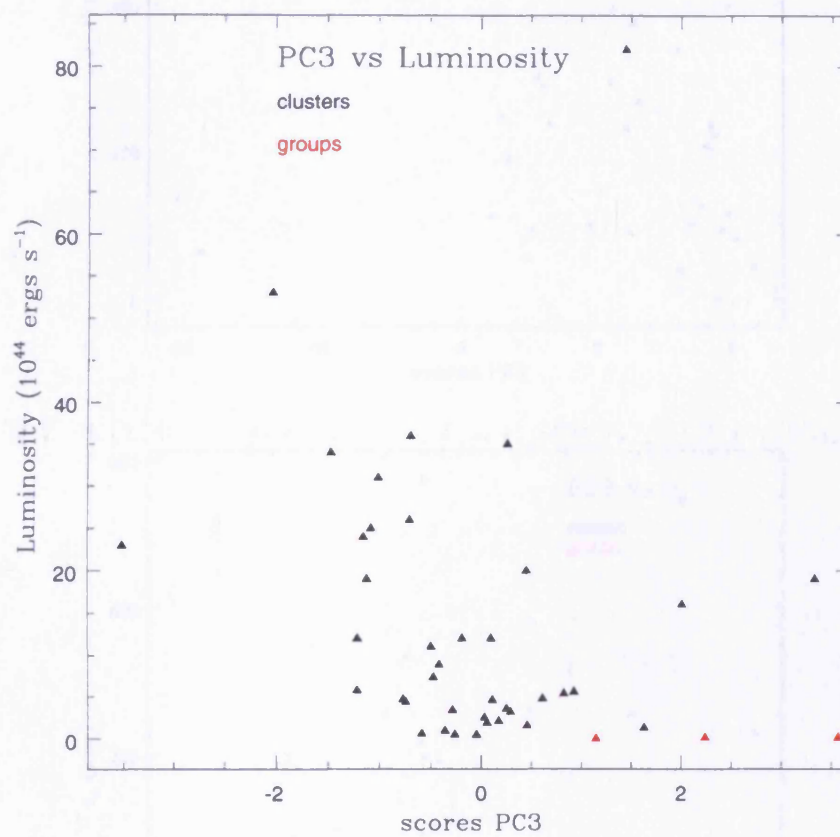
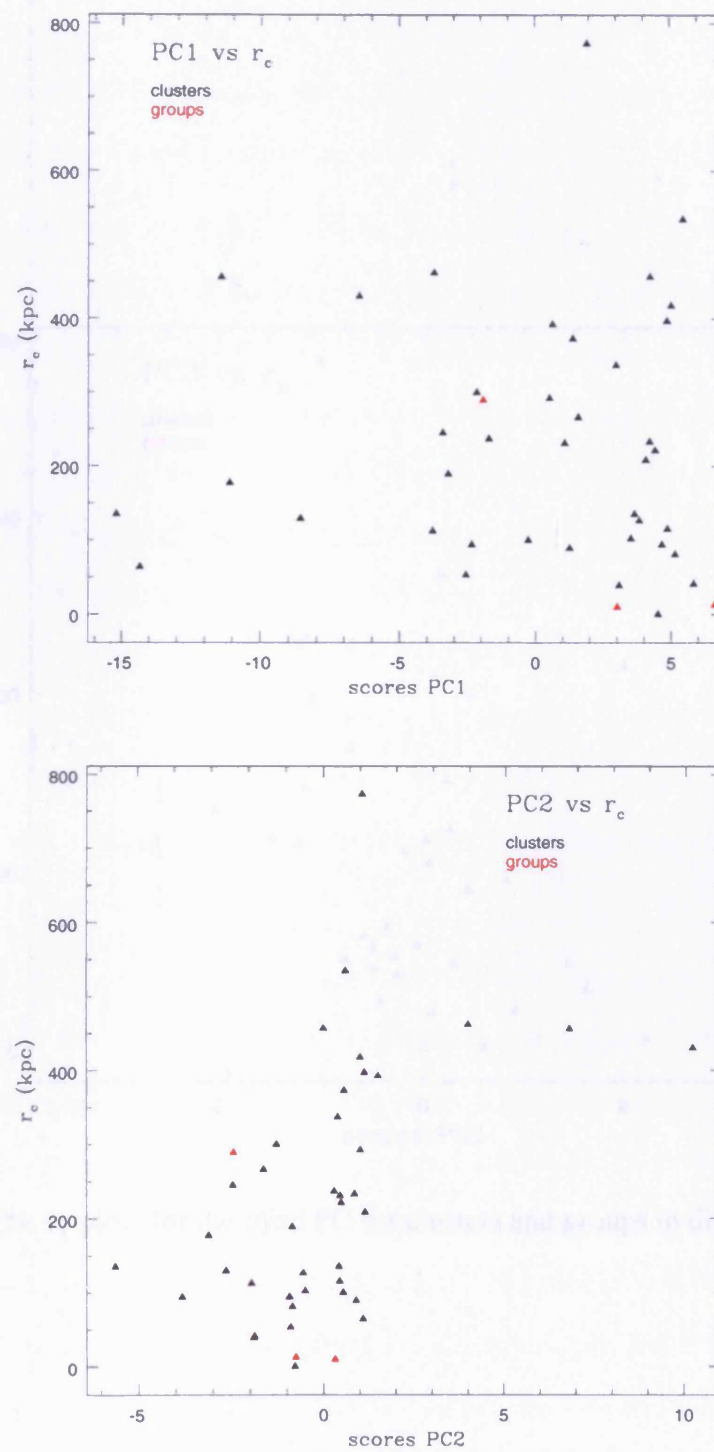


FIGURE 4.12. Luminosity plots for PC3 for clusters and groups in separate colours.

FIGURE 4.13.  $r_c$  plots for the two PC's for clusters and groups in different colours

in increasing  $\lambda$  increased PC scores correspond to the clusters. For the case radius it is a little different: most of the groups with  $M < 50M_{\odot}$  has a much larger  $r_e$  (about 200 kpc) than the other two (about 100 kpc) but has a larger  $r_e$  than the other two groups for PC3 and smaller scores for PC1 and PC2. As with the other two parameters the PC3 for the radius and groups are not explainable.

The mean values of  $r_e$  (in kpc) for clusters are close to zero (PC1 = 41.3, PC2 = 42.7 and PC3 = 0.178), while for groups the values are more dispersed (PC1 = 1.76, PC2 = 0.53, PC3 = 1.17). The dispersion that the mean scores values for the groups are more dispersed than the clusters is not surprising, as the number of the clusters is small.

It is now clear that the radius of groups is also the reason for no clear difference between clusters and groups are seen as there may be enough to tell if they are different to clusters for a range of galaxies. It is clear from the scatter plot that the radius of groups is not a significant contributor to the overall PCA analysis. However, even though the total number it would be expected that some difference in the scores for groups and the clusters would be seen, which in fact we did.

It was also expected that there would be differences in the scores for cooling flow and non-cooling flow clusters as that the work for the cooling flow clusters (or those with groups) would be greater than for non-cooling flow clusters. An example of raw scores of the  $M$  parameters is given in figure 4.13. This plot was for PC3 which the largest amount

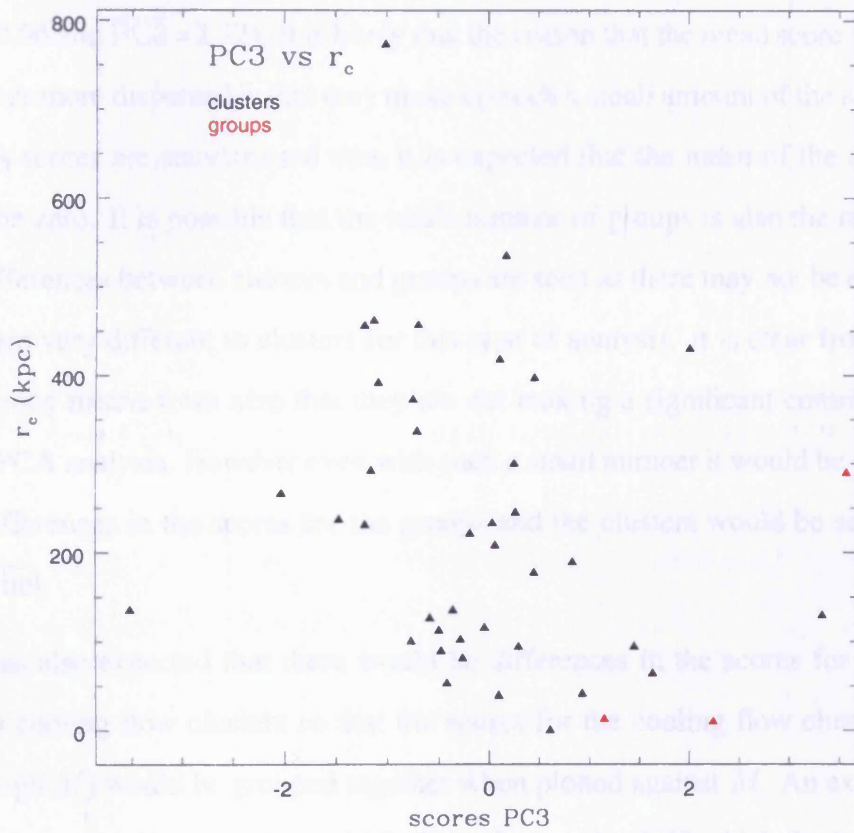


FIGURE 4.14.  $r_e$  plots for the third PC for clusters and groups in different colours

is, is to distinguish between cooling flow region, no correlation or sign of grouping have been found in any of the first three PCs or radius, in fact more scores to be uncorrelated between the radius of  $M$  and the signs of any of the PC. If the cooling flow clusters were being treated differently it would have been expected that the PC3 would be more to the size of  $M$  separating the clusters into cooling flow groups which is clearly not seen. For the 2D view of the 3D projection found, the value of  $R^2$  is very low

in correspondingly grouped PC scores compared to the clusters. For the core radius it is a little different as one of the groups, NGC5044 has a much larger core radius ( $r_c=290$  Kpc) than the other two (where  $r_c \sim 10$  Kpc) but has a larger score than the other two groups for PC3 and smaller scores for PC1 and PC2. As with the other two parameters the PC's for the clusters and groups are not distinguishable.

The mean values of the three scores for clusters are close to zero ( $\overline{PC1} = -0.2$ ,  $\overline{PC2} = 0.07$  and  $\overline{PC3} = -0.178$ ) whereas for groups the values are more dispersed ( $\overline{PC1} = 2.56$ ,  $\overline{PC2} = -0.96$  and  $\overline{PC3} = 2.32$ ). It is likely that the reason that the mean score values for the groups are more dispersed is that they make up such a small amount of the sample. Since the PCA scores are standardised then it is expected that the mean of the entire sample should be zero. It is possible that the small number of groups is also the reason that no clear differences between clusters and groups are seen as there may not be enough to tell if they are very different to clusters for this type of analysis. It is clear from the scatter of the group means from zero that they are not making a significant contribution to the overall PCA analysis. However even with such a small number it would be expected that some differences in the scores for the groups and the clusters would be seen, which in fact are not.

It was also expected that there would be differences in the scores for cooling flow and non cooling flow clusters so that the scores for the cooling flow clusters (ie those with a high  $\dot{M}$ ) would be grouped together when plotted against  $\dot{M}$ . An example of one of the  $\dot{M}$  plots is shown in figure 4.15. This plot was for PC3 which the largest amount of correlation to the parameter. This is as expected from figure 4.4 which shows PC3 has the most significance in the cooling flow region.. No correlations or signs of grouping have been found in any of the first three PC's or ratios. In fact there seems to be no correlation between the size of  $\dot{M}$  and the value of any of the PC. If the cooling flow clusters were bring treated differently it would have been expected that the PC would correlate to the size of  $\dot{M}$  separating the clusters into two distinct groups which is clearly not seen. For the plot show of the best correlation found, the value of  $R^2$  is very low

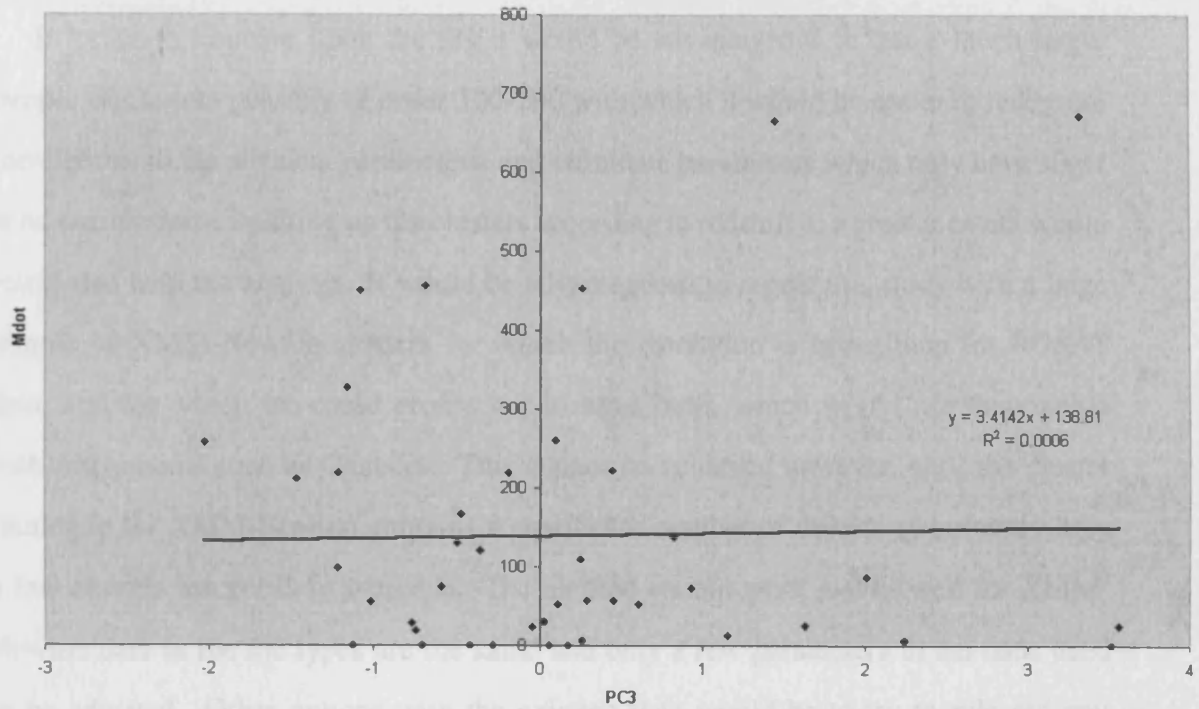


FIGURE 4.15. Example of the correlation of  $\dot{M}$  to one of the principal components. There is no significant correlation between  $\dot{M}$  and the size of the PC.

essentially ruling out any sort of correlation for this parameter possibly because of the relatively low number of clusters in the sample.

## 4.7 Conclusions and Future work

From the study made with 42 clusters it is clear that the PCA analysis technique has a fair way to go before it can be used as a viable alternative to the  $\beta$  or NFW models in fitting cluster profiles. It has become clear that is relatively easy to reproduce the cluster profiles with a small number of Principal components but the difficulties arise when trying to apply a physical interpretation to the resulting components. The analysis has suggested possible correlations of  $r_c$  to PC2 and luminosity to PC1, but these correlations are fairly tenuous and much more work is needed in order to tie down the true physical

interpretation of the components.

In order to improve upon the fits it would be advantageous to use a much larger sample of clusters possibly of order 100-200 with which it would be easier to recognise correlations to the physical parameters, and eliminate parameters which only have slight or no correlations. Splitting up the clusters according to redshift to a greater extent would also help the analysis. It would be advantageous to repeat this study with a large sample of XMM-Newton clusters for which the resolution is better than for ROSAT data, and for which we could profile out to large radii, which would not be possible with instruments such as Chandra. This cannot be achieved however, until the cluster catalogue for XMM-Newton contains a significant number of objects as currently only a few clusters are publicly available. The method should work just as well for XMM-Newton data as the file types are the same and only a few parameters in the code need to be adjusted. Other options with the existing data would be to try to rule out any systematic effects which could be affecting the data, for example problems caused by profiling out to the full extent of the detector when the cluster emission may end well before this. Also trying to fit composite or polytropic physical parameters to the principal components may result in better fits

# Chapter 5

## A study of the galaxy cluster A1413

### 5.1 Overview

Abell 1413 is an Abell richness class 3 cluster containing over 150 galaxies (Austin & Peach 1974). It is dominated by a cD galaxy which is one of the brightest known ( $M_v = -24.89$ ). It is located in an uncrowded region of the sky which avoids problems of contamination by foreground objects (optical cluster centre RA 11:52:07.00, dec +23:40:06.0 (J1950)). Noonan (1972) gives the redshift of Abell 1413 to be 0.1427. Emission has been measured out to a scale of 3.8 Mpc ( $H_o = 50 \text{ kms}^{-1}\text{Mpc}^{-1}$ ) with ASCA (White 2000). The X-ray luminosity was measured in the ROSAT 0.5-2.5 keV band and found to be  $1.9 \times 10^{44} \text{ ergs s}^{-1}$  (Grainge & Jones 1996). The velocity dispersion of the galaxies in the cluster has been estimated at  $1460 \text{ kms}^{-1}$  (Maurogordato, Proust, Cappi, Slezak & J.Martin 1997).

### 5.2 Introduction

Abell 1413 is a hot cluster with an X-ray temperature of  $7.32 \pm_{0.24}^{0.26} \text{ keV}$  as measured by ASCA (White 2000). Previous analysis determined Abell 1413 as a cooling flow cluster

with the peak of its X-ray emission corresponding with the optical position of the central cluster cD galaxy. With a cooling component included in the model fit to the ASCA spectrum the gas temperature increased to  $8.0 \pm_{0.86}^{1.28}$  keV. ASCA results (White 2000) suggest a cooling flow of  $210 M_{\odot} \text{yr}^{-1}$  which compared favourably to the ROSAT result of  $200 M_{\odot} \text{yr}^{-1}$  (Allen & Fabian 1995) found using spatial deprojection methods. The ROSAT deprojection results also suggested that the cluster mass deposition was not very centrally concentrated and that there were no emission lines from the cluster.

This study of Abell 1413 was undertaken to investigate the gas structure in more detail and thus improve on earlier results. XMM-Newton was chosen because of the improvements in spectral and spatial resolution it provides over ASCA and ROSAT as described in chapter 2. This increased resolution enables analysis of the physical properties of the gas based on emission at different radii from the cluster centre. The greater resolution may also confirm whether or not the mass was centrally concentrated. It is also possible to produce annular spectra over fairly narrow regions with XMM-Newton due to the high count rates achieved over the long exposure. This is useful in obtaining profiles of the temperature and metal abundance which could not be well defined with the earlier studies.

This chapter presents an X-ray spatial and spectral analysis of the EPIC MOS and EPIC PN data for Abell 1413 from XMM-Newton. The aim of the spatial analysis was to determine physical information about the cluster such as the mass and density distributions of the gas, using a  $\beta$  model. The analysis is also used to determine the extent of the cluster emission so that when the spectra were fitted, the point where the emission had fallen off to background levels can be compared. The aim of the spectral analysis is to fit the cluster gas in concentric annuli so that its structure and radial temperature variation can be investigated. The temperature and abundance profiles are traced out as far as possible ( $\sim 2$  Mpc). This type of detailed analysis enables makes it possible to look for cooling towards the centre and if so, where the cooling starts. The variation of metal concentrations in the cluster are also studied. The intention of this work is to

investigate whether spectral analysis reveals that the cluster data is well constrained by a single temperature thermal model and whether the temperature profile shows evidence of a temperature gradient.

### 5.3 Observation and Data Reduction

Abell 1413 was observed by XMM-Newton on 12th June 2000 as part of the guaranteed time program. The observation was centred on the EPIC PN instrument. The data was preprocessed using the SAS software prior to analysis. In addition, before scientific analysis of the data was undertaken a lightcurve was created in order to check for proton flares, which increase the X-ray background as described in chapter 3. There were no flaring events in the Abell 1413 lightcurve and so no time intervals had to be cut from the data. Resultant exposure times for the data from each detector after cleaning by the EPIC team were as follows; MOS1 was 25697 seconds, MOS2 was 25607 seconds and for the PN was 20675 seconds.

The data reduction was undertaken as described in chapter 3 utilising the SAS routines XMMSELECT and EVSELECT. As well as producing images and spectra this technique enables the event list to be filtered to remove proton events as described above. A problem that particularly affected the MOS2 data for this cluster was the presence of bad pixels in the data that had not been included in the bad pixel lists. These cause abnormal peaks in the spectra and had to be removed. The calibrated event lists had undergone too much preprocessing to allow these events to be removed from them directly and so the data had to be re-run through the EMCHAIN routines with a more constrained bad pixel threshold in place in order to remove these events.

The EPIC instruments on XMM-Newton are used for imaging and spectral analysis in the 0.3-10 keV band. A 0.3-10 keV band image of A1413 is shown in figure 5.1. The emission is extended and elliptical in shape, orientated approximately north to south. The centre of the emission is at RA 11:55:19.262, dec +23:22:25.60 (J2000) and is consistent

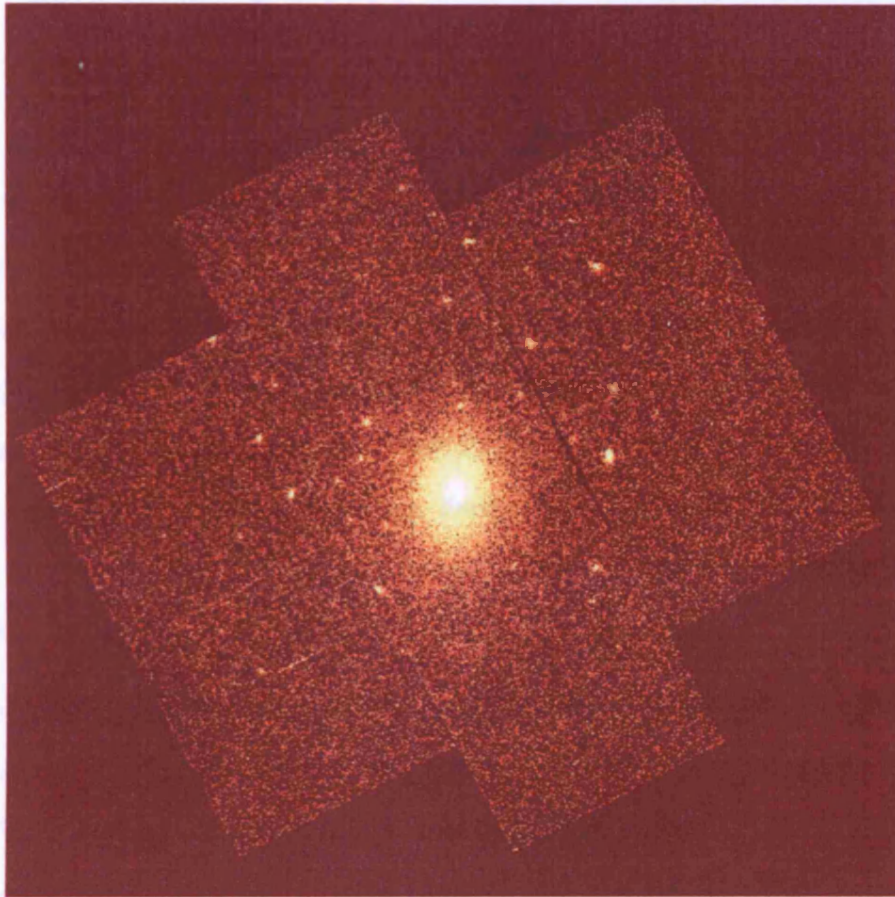


FIGURE 5.1. Image of Abell 1413

An image of Abell 1413 in the 0.3-10 keV band. The image was binned to 75 pixels per bin resulting in a scale of 16 binned pixels per arcminute (1200 unbinned pixels per arcminute). The image is on the MOS1 detector and is shown in image co-ordinates and with a logarithmic scaling. The cluster is centred on the central chip and is clearly visible as an extended source. There are several point sources evident in the image, some of which may be galaxies within the cluster and some external to it. The resolution of XMM-Newton allows such a large number of point sources to be observed.

with the optical centre and the ROSAT X-ray centre (RA 11:55:18.5, dec +23:24:28.4 (J2000) (Grainge & Jones 1996)).

## 5.4 Spatial Analysis and Cluster Morphology

### 5.4.1 King profile fits

Spatial analysis of cluster data is undertaken using cluster surface brightness profiles. These were created using the ASTERIX package as described in chapter 3. The profiles were then fitted to a King ( $\beta$ ) model in the qdp package, using an additional constant to model the background counts. The results of this fit gave values for the central surface brightness,  $S_0$ , in units of counts per pixel and the core radius,  $r_c$ , in pixels. The fit also gives a value for the index of the slope, from which a value of  $\beta$  can be gained. The surface brightness of the cluster is directly proportional to the count rate and hence, the X-ray flux.

The profile gained from the MOS1 data of Abell 1413 is shown in figure 5.2. The profile shows that the emission is fairly steady and then drops off sharply after the core radius ( $r_c = 0.65 \pm 0.05$  arcmin which corresponds to  $0.16 \pm 0.012$  Mpc). This is smaller than the core radius determined from Einstein data of 0.5 Mpc (White et al. 1993) but is of order that found by Allen (2000) for ASCA data of 0.13 Mpc. The radial fit is stopped at 10 arcmin (2.5 Mpc). Fitting beyond this point makes very little difference to the resulting fit. Most of the emission is detected within the first 1.25 Mpc which corresponds to about the 5-6 arcmin spectral ring.

From this fit the profile slope was determined to be -1.364. This slope corresponds to  $(1/2 - 3\beta)$  in the model. This gives a value of  $\beta$  to be  $0.62 \pm 0.02$ . This is close to the value determined by Pownall (1997) of  $0.66 \pm 0.05$  for ROSAT data on the cluster. The spectrally determined value of  $\beta$  was also calculated using the velocity dispersion and the global cluster temperature (discussed later) and was found to be  $1.1 \pm 0.1$ , which is significantly higher than the spatially determined value therefore showing that some  $\beta$  discrepancy is being seen in the data.

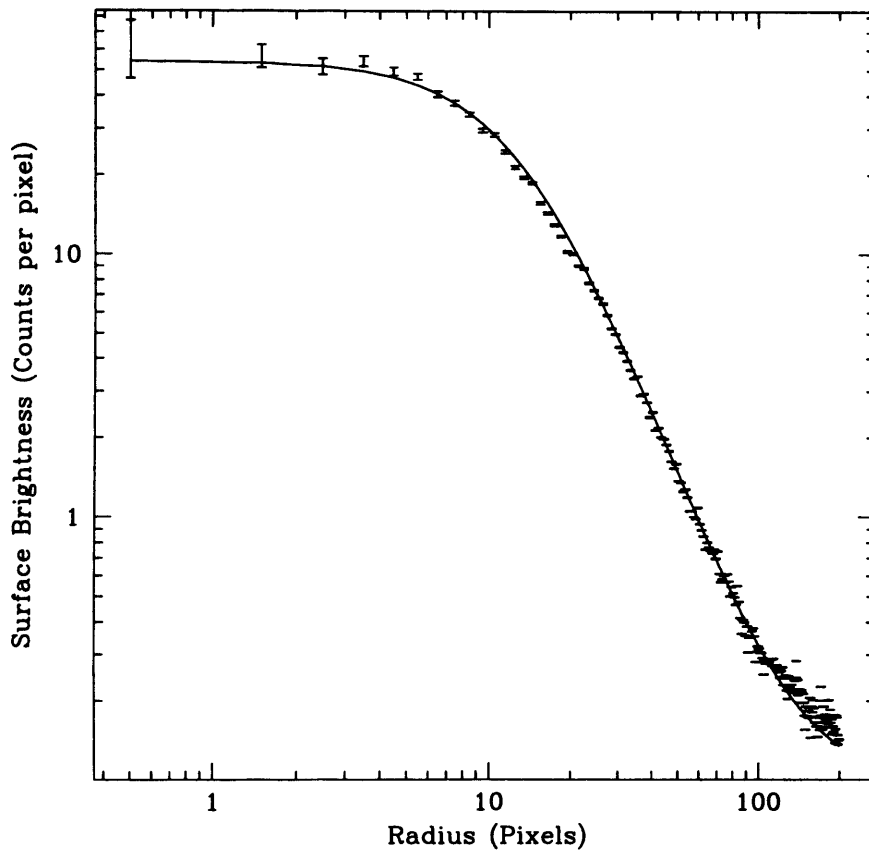


FIGURE 5.2. Surface brightness profile of Abell 1413 for MOS1 data. The profile goes out to 2.5 Mpc. The fit may be affected by the ellipticity of the cluster which means that the surface brightness along the long axis may be different from that along the short axis. This will affect the overall shape and extent of the profiles obtained. The plot shown here is taken between the two extremes and so does not fully represent the ellipticity.

## 5.4.2 Comparison between the King profile and the NFW profile

The King profile is limited in its ability to describe the cluster surface brightness profile and as seen above there differences in the spectral and spatial values. The  $\beta$  model does not correctly model all of the dark matter component of the cluster when calculating the density. Therefore a suggested improvement to this is to use the Navarro Frenk and White (NFW) density profile (equation 1.21) instead.

To fit the NFW to the data, the density profile is integrated along the line of sight to calculate the predicted surface brightness. This is done numerically using a trapezium rule integration. This integration method can be used as the density profile is not very steep as any sharp variation in the profile shape would result in the integral being over estimated. The values of  $\eta$  and  $r_s$  are iterated until the closest match to the real profile is found.

Fitting the NFW model to the surface brightness profile results in values of  $\eta = 8.05 \pm 0.05$  and  $r_s = 0.57 \pm 0.01$  Mpc. The uncertainty in the values is mostly due to the accuracy of the iterative fit to the data. The  $\beta$  and NFW fits to the cluster data are shown in figure 5.3. The figure shows that both profiles provide a good fit to the data. The data levels off at large radii due to background radiation which the models do not take into account and so we see a divergence between the models and the real data. The NFW model fits the real data better at small radii with the beta model fitting better at large radii. The slope of the NFW also seems to fit slightly better to the raw profile. Within the errors given however it is not clear that either model gives a distinct improvement on the fit to the data.

## 5.5 Spectral Analysis

The spectral characteristics of the cluster were studied by taking spectra from nine annuli in concentric rings about the cluster's X-ray centre. The annuli taken and the background

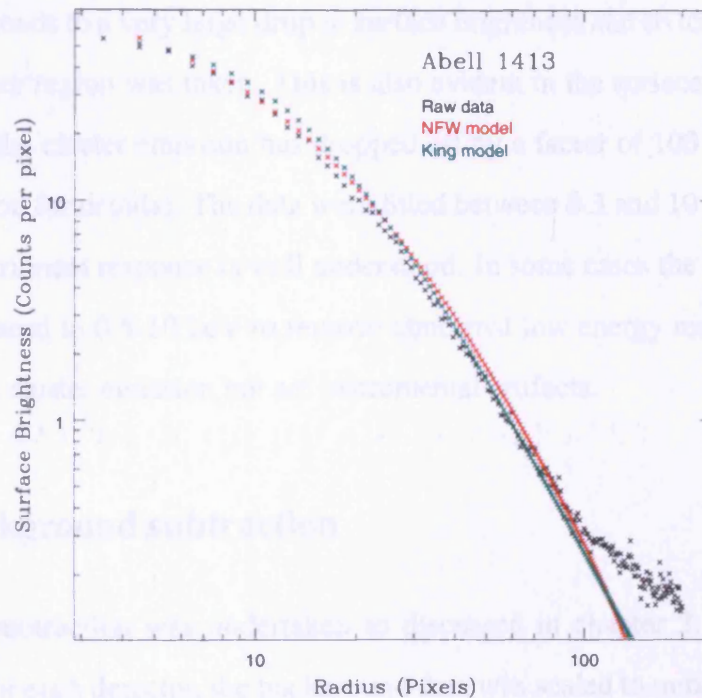


FIGURE 5.3. Comparison of the  $\beta$  and NFW models to the raw surface brightness profile. The plots are normalised to the raw data. The plots use the following values  $\beta = 0.62$ ,  $r_c = 0.16$  Mpc,  $\eta = 8.05$ ,  $r_s = 0.57$  Mpc. The background has not been removed from the data and is approximated separately as a constant within QDP (not shown in this plot).

subtracted count rates for the 3 EPIC detectors are summarised in table 5.1. The table shows that the PN has a count-rate approximately twice that of the MOS instruments, with 0.7 counts per second in the inner ring for PN as opposed to 0.35 for the MOS. This is because the incident flux of the MOS cameras being shared with the RGS. The central annuli (i-iv) are narrower in order to investigate the clusters cooling region. The outer regions investigate the cluster global temperature. The outer ring (xi) was largest due to a low cluster count rate here (about a factor of 3 less than in the central regions), which corresponds to a very large drop in surface brightness and so to increase the signal to noise a larger region was taken. This is also evident in the surface brightness profile, which shows the cluster emission has dropped off by a factor of 100 by this annuli (see previous section for details). The data were fitted between 0.3 and 10 keV only, as this is where the instrument response is well understood. In some cases the energy range fitted had to be reduced to 0.5-10 keV to remove abnormal low energy residuals which were not part of the cluster emission but are instrumental artifacts.

### **5.5.1 Background subtraction**

Background subtraction was undertaken as discussed in chapter 3. To normalise the background for each detector, the background data was scaled to minimise the chisquare of the fit and minimise the presence of the 1.4 keV aluminium line as described in chapter 3. The scalings that were found to work the best were 80% background for MOS1 and 100% for MOS2 and the PN.

### **5.5.2 Single Temperature vs Cooling Flow Fits**

The data was fitted using a single temperature plasma emission model known as the MEKAL model (Mewe & Gronenschild. 1985) along with a photometric absorption model called PHABS as described in chapter 3. The XSPEC package was used to fit the models to the data. A list of model parameters is shown in table 3.1. The param-

Table 5.1. The nine annuli over which spectra were taken. The count rates are for the energy range 0.3-10 keV. The detectors MOS1, MOS2 and PN have different count rates with the PN receiving twice the photons of the individual MOS's.

Region	Inner Radius arcmin	Outer Radius arcmin	Mean Radius Mpc	MOS1 Count Rate $cts^{-1}$	MOS2 Count Rate $cts^{-1}$	PN Count Rate $cts^{-1}$
i	0	0.5	0.0623	$0.35 \pm 0.0037$	$0.39 \pm 0.0039$	$0.70 \pm 0.0059$
ii	0.5	1	0.1868	$0.51 \pm 0.0045$	$0.50 \pm 0.0048$	$0.98 \pm 0.0095$
iii	1	1.5	0.3115	$0.39 \pm 0.0039$	$0.39 \pm 0.0040$	$0.81 \pm 0.0065$
iv	1.5	2	0.4136	$0.37 \pm 0.0039$	$0.29 \pm 0.0035$	$0.62 \pm 0.0058$
v	2	3	0.6229	$0.35 \pm 0.0040$	$0.36 \pm 0.0040$	$0.74 \pm 0.0066$
vi	3	4	0.8720	$0.19 \pm 0.0031$	$0.18 \pm 0.0032$	$0.40 \pm 0.0053$
vii	4	5	1.1212	$0.12 \pm 0.0027$	$0.11 \pm 0.0028$	$0.25 \pm 0.0049$
viii	5	6	1.3703	$0.09 \pm 0.0026$	$0.09 \pm 0.0027$	$0.18 \pm 0.0050$
ix	6	10	1.9932	$0.15 \pm 0.0049$	$0.10 \pm 0.0052$	$0.18 \pm 0.0088$

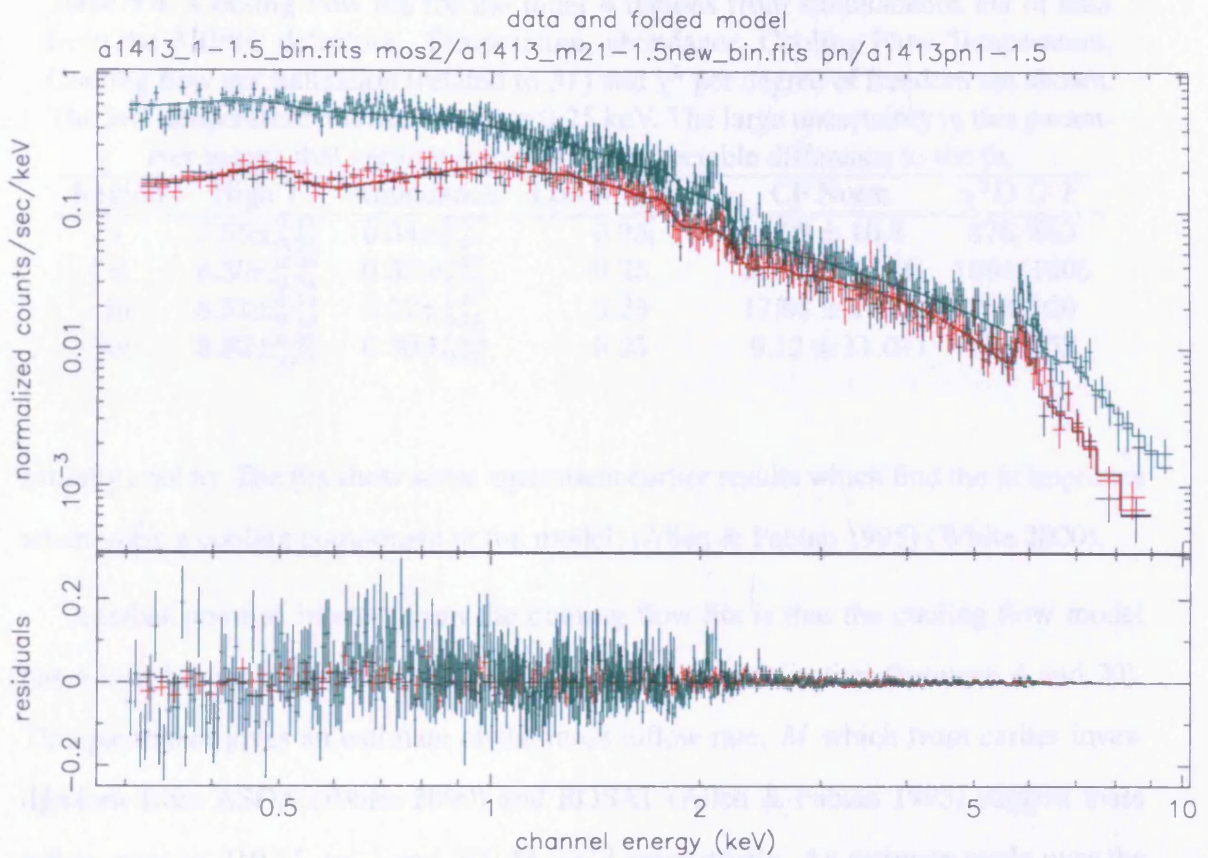
eters of temperature and abundance were left untied and allowed to fit naturally. The initial temperature was taken from the White (2000) analysis of the ASCA data with  $T = 7.32$  keV. The initial abundance was set at 0.3 solar. The datasets from each camera were initially fitted separately and the results of these fits are shown in table 5.2. The errors shown on the data are 90% confidence errors. It can be seen that there is a general trend of temperature decreasing with increasing radius in all three cases, as well as an abundance decrease. The fits are in general consistent between the three cameras.

To improve the statistics of the fits, the 3 datasets were then fitted simultaneously which improved the  $\chi^2$  values especially in the central regions. An example of the spectra being fitted in the way is shown in figure 5.4. This data is for one of the inner annuli (1.5-2 arcminutes), which is a region where the statistics of the fit are best. The results of the simultaneous fit are given in table 5.3. For this fit the outer annuli has been split into two to create a 6-8 and an 8-10 arcminute annulus, since by combining the three detectors there are enough counts to do this. This fit shows the temperature decreasing as before, but with tighter constraints, with the uncertainty on the temperature in the inner ring reducing from 0.5 to 0.3. In the outermost rings the quality of the background subtraction has a greater effect, so any remaining problems become evident, resulting in a significant increase in the uncertainty in these regions (hence the reduced  $\chi^2$  value for this region is closer to 1.4 as opposed to 1 for the inner rings).

The single temperature thermal model provides a good fit to the data because the residuals of the fit are small (reduced  $\chi^2$  approximately unity) particularly for the inner rings. Using a cooling flow model improves the fit slightly as the  $\chi^2$  is slightly better than with the single temperature model, despite increasing the number of degrees of freedom. Table 5.4 shows the parameters obtained for a mekal model plus mekal cooling flow model fit to the cluster data for various parameters. The cooling flow model assumes that the gas is multi-phase with different temperature components down to a low temperature limit (Low T in the table). As can be seen in the table the errors on the low temperature parameter are large and so is difficult to be certain how low temperature the gas does

Table 5.2. Single temperature fits over different regions for the 3 different EPIC detectors fitted separately. Temperature, Abundance and  $\chi^2$  per degree of freedom parameters are shown. The low temperature in the outermost region suggests that the bulk of the emission is coming from the background rather than from the cluster by this radius.

Region	MOS1			MOS2			PN		
	Temperature keV	Abundance Solar	$\chi^2 D.O.F$	Temperature keV	Abundance Solar	$\chi^2 D.O.F$	Temperature keV	Abundance Solar	$\chi^2 D.O.F$
i	$7.84 \pm_{-0.57}^{+0.64}$	$0.38 \pm_{-0.13}^{+0.13}$	210/207	$7.31 \pm_{-0.51}^{+0.57}$	$0.36 \pm_{-0.12}^{+0.12}$	255/217	$7.38 \pm_{-0.40}^{+0.53}$	$0.31 \pm_{-0.10}^{+0.10}$	410/438
ii	$8.13 \pm_{-0.51}^{+0.57}$	$0.39 \pm_{-0.12}^{+0.12}$	260/248	$7.58 \pm_{-0.49}^{+0.54}$	$0.29 \pm_{-0.10}^{+0.12}$	300/244	$7.81 \pm_{-0.41}^{+0.49}$	$0.28 \pm_{-0.09}^{+0.09}$	525/512
iii	$7.46 \pm_{-0.51}^{+0.57}$	$0.44 \pm_{-0.13}^{+0.14}$	299/222	$7.40 \pm_{-0.53}^{+0.60}$	$0.28 \pm_{-0.10}^{+0.12}$	230/221	$7.88 \pm_{-0.50}^{+0.55}$	$0.33 \pm_{-0.10}^{+0.10}$	483/476
iv	$8.27 \pm_{-0.68}^{+0.78}$	$0.31 \pm_{-0.13}^{+0.13}$	235/230	$7.28 \pm_{-0.61}^{+0.69}$	$0.37 \pm_{-0.14}^{+0.15}$	197/196	$7.78 \pm_{-0.52}^{+0.67}$	$0.32 \pm_{-0.16}^{+0.28}$	419/422
v	$7.11 \pm_{-0.57}^{+0.66}$	$0.25 \pm_{-0.12}^{+0.13}$	229/230	$6.13 \pm_{-0.43}^{+0.49}$	$0.26 \pm_{-0.12}^{+0.12}$	207/223	$7.21 \pm_{-0.47}^{+0.48}$	$0.16 \pm_{-0.10}^{+0.10}$	493/470
vi	$6.37 \pm_{-0.66}^{+0.82}$	$0.26 \pm_{-0.18}^{+0.19}$	217/188	$6.22 \pm_{-0.61}^{+0.86}$	$0.28 \pm_{-0.18}^{+0.20}$	184/191	$6.23 \pm_{-0.66}^{+0.70}$	$0.19 \pm_{-0.14}^{+0.15}$	333/351
vii	$5.38 \pm_{-0.85}^{+1.07}$	$0 \pm_0^{+0.18}$	188/168	$4.39 \pm_{-0.70}^{+0.90}$	$0 \pm_0^{+0.24}$	191/169	$5.27 \pm_{-0.90}^{+1.15}$	$0.05 \pm_{-0.05}^{+0.22}$	322/263
viii	$5.31 \pm_{-0.99}^{+1.23}$	$0.26 \pm_{-0.26}^{+0.36}$	160/151	$7.21 \pm_{-1.69}^{+2.71}$	$0.02 \pm_{-0.02}^{+0.41}$	177/162	$5.03 \pm_{-0.87}^{+1.15}$	$0.10 \pm_{-0.10}^{+0.25}$	303/298
ix	$1.94 \pm_{-0.31}^{+0.32}$	$0 \pm_0^{+0.18}$	353/318	$0.98 \pm_{-0.14}^{+0.13}$	$0 \pm_0^{+0.23}$	353/318	$0.65 \pm_{-0.07}^{+0.14}$	$0 \pm_0^{+0.32}$	1393/683



les 15-Jun-20

FIGURE 5.4. Spectra of A1413 for the 3 EPIC detectors fitted simultaneously using a mekal plus phabs model. The black plot is MOS1 red is MOS2 and green is PN. The data is from the 1.5-2 arcminute annulus in all cases

Table 5.3. Simultaneous single temperature fits for 3 EPIC detectors. Temperature, abundance and  $\chi^2$  per degree of freedom are shown.

Region	Temperature	Abundance	$\chi^2 D.O.F$
i	$7.49 \pm_{0.29}^{0.31}$	$0.34 \pm_{0.07}^{0.07}$	878/866
ii	$7.83 \pm_{0.27}^{0.28}$	$0.30 \pm_{0.05}^{0.06}$	1089/1008
iii	$7.58 \pm_{0.30}^{0.31}$	$0.34 \pm_{0.07}^{0.07}$	945/923
iv	$7.77 \pm_{0.35}^{0.39}$	$0.33 \pm_{0.08}^{0.08}$	855/852
v	$6.79 \pm_{0.29}^{0.32}$	$0.21 \pm_{0.06}^{0.06}$	938/927
vi	$6.40 \pm_{0.41}^{0.46}$	$0.26 \pm_{0.10}^{0.10}$	710/719
vii	$5.04 \pm_{0.47}^{0.54}$	$0 \pm_{0}^{0.20}$	720/623
viii	$5.74 \pm_{0.68}^{0.86}$	$0.16 \pm_{0}^{0.18}$	632/603
ix	$1.97 \pm_{0.22}^{0.26}$	$0 \pm_{0}^{0.2}$	1050/780
x	$1.19 \pm_{0.39}^{0.73}$	$0 \pm_{0}^{0.25}$	1051/793

Table 5.4. Cooling flow fits for the inner 4 regions from simultaneous fits of data from the 3 EPIC detectors. Temperature, abundance, Cooling Flow Temperature, Cooling flow normalisation (related to  $\dot{M}$ ) and  $\chi^2$  per degree of freedom are shown. The low temperature has been fixed at 0.25 keV. The large uncertainty in this parameter means that varying it makes no appreciable difference to the fit.

Region	High T	Abundance	Low T (fixed)	CF Norm	$\chi^2 D.O.F$
i	$7.55 \pm_{0.31}^{0.31}$	$0.34 \pm_{0.07}^{0.07}$	0.25	$4.28 \pm 10.8$	876/863
ii	$8.30 \pm_{0.33}^{0.29}$	$0.32 \pm_{0.05}^{0.07}$	0.25	$20.01 \pm 11.56$	1084/1005
iii	$8.51 \pm_{0.42}^{0.42}$	$0.37 \pm_{0.07}^{0.07}$	0.25	$17.98 \pm 10.16$	933/920
iv	$8.52 \pm_{0.51}^{0.51}$	$0.30 \pm_{0.05}^{0.05}$	0.25	$9.12 \pm 11.07$	855/852

actually cool to. The fits show some agreement earlier results which find the fit improves when using a cooling component to the model, (Allen & Fabian 1995) (White 2000).

Another point of interest from the cooling flow fits is that the cooling flow model has a low, but nevertheless significant value for its normalisation (between 4 and 20). This parameter gives an estimate of the mass inflow rate,  $\dot{M}$  which from earlier investigations from ASCA (White 2000) and ROSAT (Allen & Fabian 1995) suggest mass inflow rates of  $210 M_{\odot} \text{yr}^{-1}$  and  $200 M_{\odot} \text{yr}^{-1}$  respectively. An estimate made over the entire cooling flow region predicts a mass inflow rate of  $56.50 \pm 17.49 M_{\odot} \text{yr}^{-1}$ . This is significantly smaller than previous estimates. All in all this investigation suggests that there is marginal evidence for a cooling flow in this cluster, with small but significant,  $\dot{M}$  and the gas cooling to a temperature of  $\sim 0.2$  keV .

For the fits shown in tables 5.2 and 5.3 the column density was fixed at the galactic value of  $1.98 \times 10^{20}$  atoms  $\text{cm}^{-2}$  but the fits were also checked with the parameter free, for consistency. The measured  $n_H$  values for the different annuli as compared to the fixed galactic value are shown in figure 5.5. The values seem to vary around the galactic value but are zero for some of the outer annuli. The largest annuli has a value close to the galactic value, but there is a large error on this data point, though the error is mostly in the direction towards zero. Pratt & Arnaud (2001) predict that if the background subtraction is incorrect that the column density will decrease with increasing radius getting worse towards the edge of the cluster. This indeed could be true for the outer regions of the

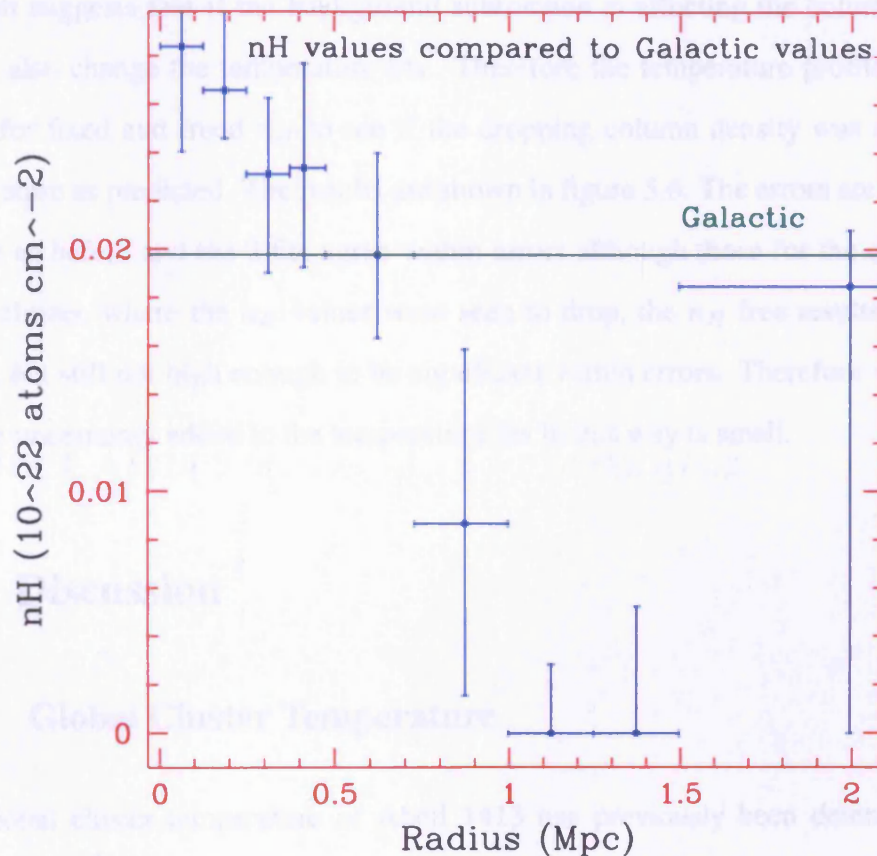


FIGURE 5.5. Plot of column densities obtained for the 3 EPIC datasets fitted simultaneously with  $n_H$  as a free parameter. The line shown in green represents the Galactic Column density expected for the cluster.

cluster where within errors the measured column density does fall to zero. Since our background subtraction was determined to minimise the background on the spectral fits it is possible than in the outer regions the background subtraction is still not optimised for removal of this kind of the emission. It is also possible that there might be off axis soft X-ray sources that haven't been removed by the background subtraction that may be affecting the fit to the column density.

Pratt suggests that if the background subtraction is affecting the column density it should also change the temperature fits. Therefore the temperature profiles were produced for fixed and freed  $n_H$  to see if the dropping column density was affecting the temperature as predicted. The results are shown in figure 5.6. The errors are at 90% confidence as before and the 2 fits agree within errors although those for the outer regions of the cluster, where the  $n_H$  values were seen to drop, the  $n_H$  free results are slightly higher, but still not high enough to be significant within errors. Therefore we conclude that the uncertainty added to the temperature fits in this way is small.

## 5.6 Discussion

### 5.6.1 Global Cluster Temperature

The global cluster temperature of Abell 1413 has previously been determined to be  $7.32 \pm_{0.24}^{0.26}$  keV using ASCA (White 2000). The XMM analysis undertaken by (Pratt & Arnaud 2002) found that the temperature was lower than this at  $6.56 \pm_{0.44}^{0.65}$  keV for data within the first 5 arcminutes of the cluster. We also made an estimate on the global cluster temperature based on simultaneous fits out to 6 arcmin and found a global cluster temperature of  $7.08 \pm 0.13$  keV, which is between the two results. This was based on a single temperature fit using the MEKAL and PHABS model and didn't include a cooling component. The value we find for the global cluster temperature is lower than our central cluster temperature, but this is to be expected given the large temperature gradient seen

the temperature profiles obtained here. Our value is consistent to the ASCA value and to the XMM fit value.

### 5.6.2 Temperature profiles

The main goal of the spectral analysis was to produce temperature profiles for Abell 1413. These were made using the results obtained by the simultaneous fit discussed earlier. The profile is shown in figure 5.6 along with the results found by Pratt & Arnaud (2001). They find a similar distribution with a cooling radius. Our results are consistent with those of Pratt & Arnaud (2002) over most of the range with the most difference being seen at the largest radii.

There is a slight increase in temperature of the innermost structure, possibly due to the presence of the cooling core. From the temperature it is possible to determine the cooling time using equation 1.28. The cooling time at various radii was found to vary from 3.5 with the central cooling time found to be  $5.40 \pm 0.13 \times 10^7$  yr. The main goal in this paper was the same as that the temperature calculations are the same as those of Pratt & Arnaud (2002). The figure shows that the cooling time of the cluster increases with radius with only the innermost cooling time being significantly smaller than the size of the Universe (Age of the Universe is  $13.7 \times 10^7$  yr (Ferreira, Mota, & 2007)). The cooling time is calculated for the cluster by Fabian (1993) is higher than we

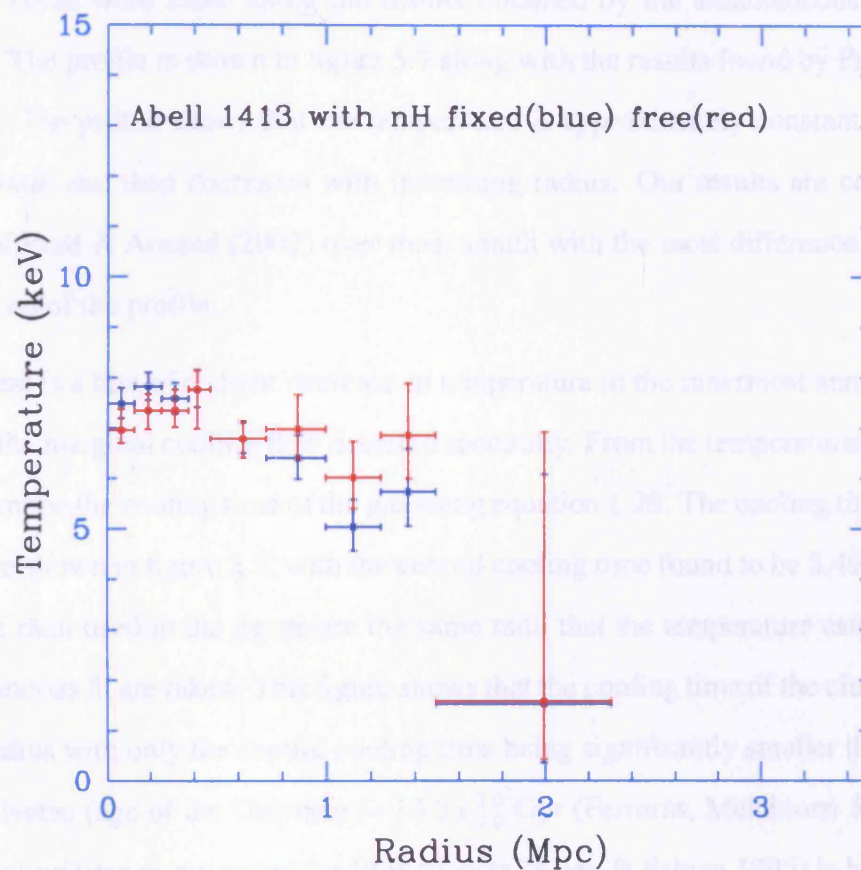


FIGURE 5.6. Comparison of temperature profiles of Abell 1413 with  $n_H$  fixed (blue) and  $n_H$  free (red). They show that the difference between fixing and freeing the  $n_H$  values is the same within errors.

in the temperature profiles discussed below. Our value is consistent to the ASCA value and to the other XMM fit value.

## 5.6.2 Temperature profiles

The main focus of the spectral analysis was to produce temperature profiles for Abell 1413. These were made using the results obtained by the simultaneous fit discussed earlier. The profile is shown in figure 5.7 along with the results found by Pratt & Arnaud (2001). The profile shows that the temperature is approximately constant over the first four annuli and then decreases with increasing radius. Our results are consistent with those of Pratt & Arnaud (2002) over most annuli with the most difference being seen at either end of the profile.

There is a hint of a slight decrease in temperature in the innermost annulus, possible due to the marginal cooling flow detected spectrally. From the temperatures it is possible to determine the cooling time of the gas using equation 1.28. The cooling times at various radii are shown in figure 5.8, with the central cooling time found to be  $5.49 \pm 0.11 \times 10^9$  yr. The radii used in the figure are the same radii that the temperature estimates for the simultaneous fit are taken. This figure shows that the cooling time of the cluster increases with radius with only the central cooling time being significantly smaller than the age of the Universe (age of the Universe  $\sim 13.2 \pm_{2.0}^{3.0}$  Gyr (Ferrerias, Melchiorri & Silk 2001)). The cooling time as estimated for ROSAT data (Allen & Fabian 1995) is higher than we see at  $\sim 8 \times 10^9$  yr. This value is low enough to provide further evidence for the cooling flow seen in the spectral data. Pratt & Arnaud (2002) find a cooling time of  $2.4 \times 10^9$  yr for their analysis of the cluster data. Therefore the value from this analysis sits between both of the other values.

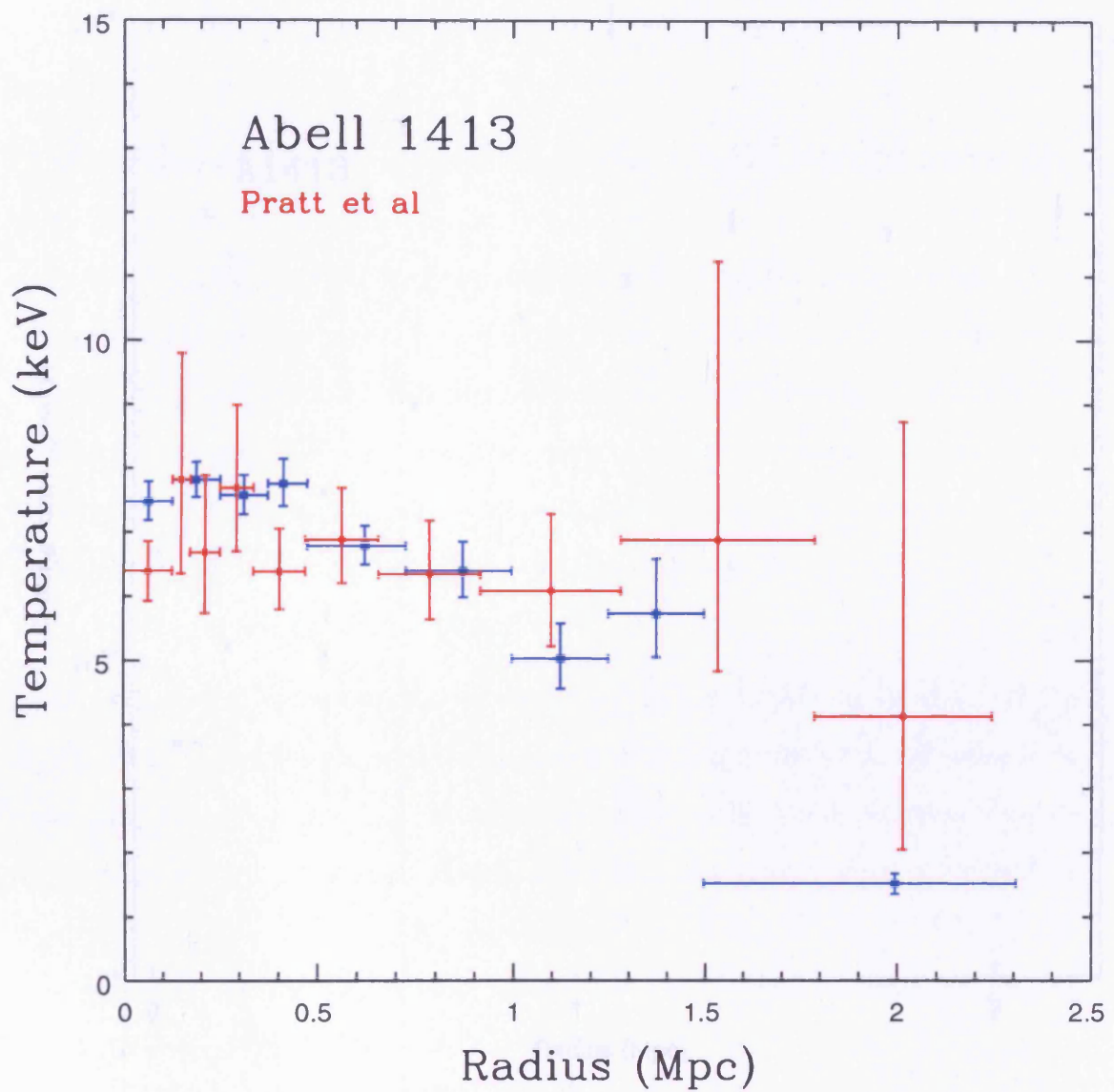


FIGURE 5.7. Temperature profile of Abell 1413 produced from a simultaneous fit of the 3 EPIC instruments and compared with the analysis by Pratt et. al. (red)

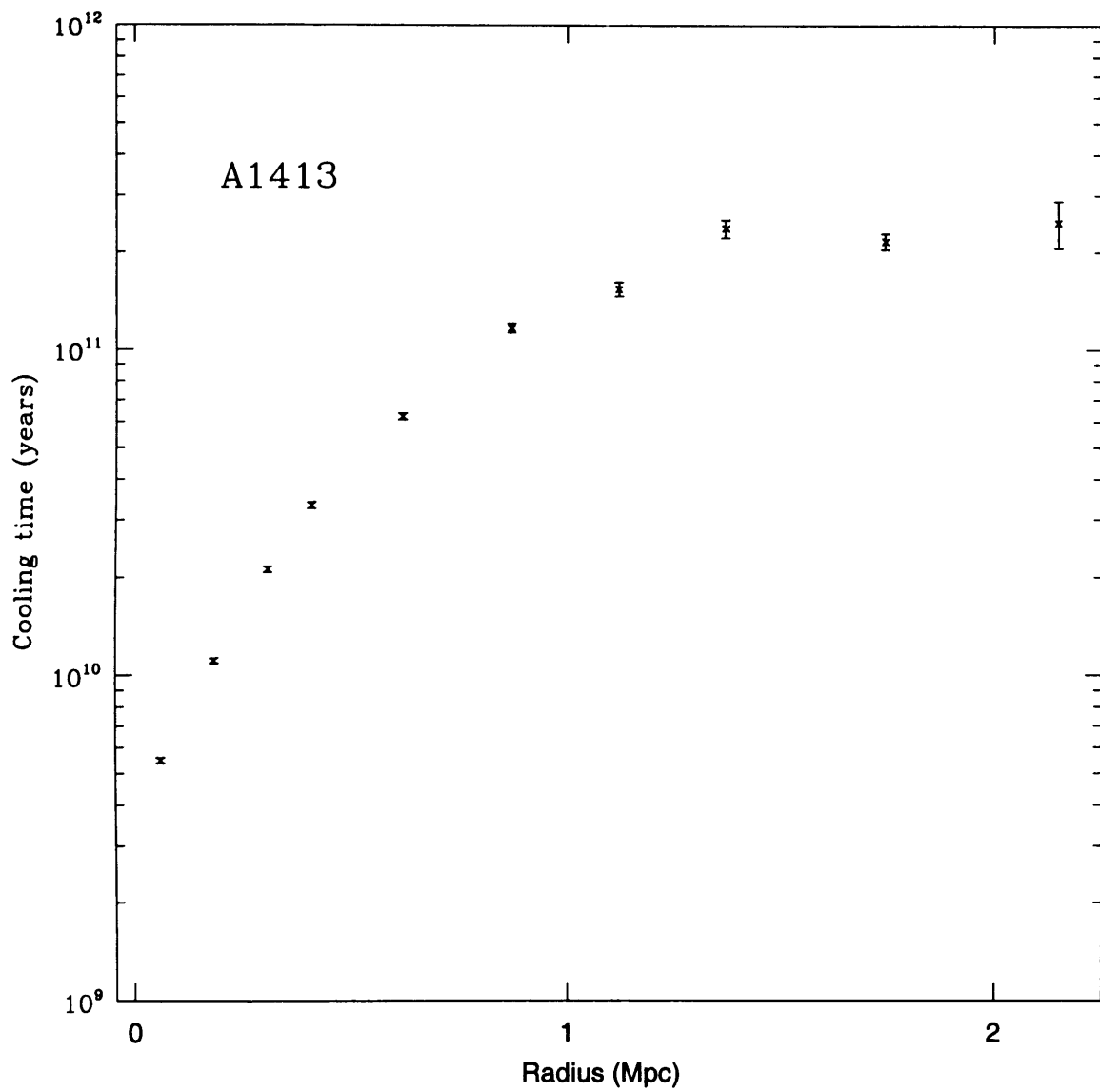


FIGURE 5.8. Cooling times for gas at various radii in the cluster. The figure shows that the cooling time is greater than the age of the universe at all radii.

### 5.6.3 Steady state conduction model

To try to understand the temperature profile a steady state conduction model (DosSantos 2001) was fitted to the data. This model assumes a perfect gas in hydrostatic equilibrium for a spherically symmetric intra-cluster medium, with no sources and sinks of heat due to conduction. Details of how this model is set up can be found in section 1.7.6 of this thesis.

The temperature of the cluster over  $T_{200}$  is given by equation 1.25 and can be rearranged to just give the temperature  $T(x)$  which can be fit to the profile. Before the fit was carried out, the  $x$ -axis of the profile was rescaled by the virial radius so that it was in units of  $x$  (which corresponds to  $r/r_v$ ) rather than  $r$ . Also the fit only works properly at radii greater than where the cooling flow would be (ie the fit begins where the profile starts to decline and doesn't fit where the profile is level in the centre, see figure 5.9 for clarification). The radius  $x_0$  is defined to be the radius where this decline begins. The fit to the profile is shown in figure 5.9 for 2 different values of  $x_i$  ( $x_i = T_0/T(x = 1)$ ). The value of  $x_0$  is taken as 0.18 in these fits.

From figure 5.9 it is evident that the model fits the data within uncertainties, with the line for  $x_i=0.2$  providing a better fit to the lower data points including the outermost data point. The dashed line with  $x_i=0.5$  provides a better fit to the slightly higher data points and does not include the outer data point. The fits correspond to a temperature decrease by a factor of 5 and 2 respectively over the range  $x=0.18$  ( $x_0$ ) to  $x=1$ . Both fit the data reasonably until the last two data points where the fit is not so well constrained. Overall the model seems to be a poor fit to the data. The reason for this deviation is believed to be that we only have data out to  $x=0.7$  and not out to the virial radius ( $x=1$ ). The steady state conduction model is designed to fit data out to the virial radius and the degeneracy between the fits occurs when the data doesn't extend to this radius. The main difference between the two fits lies at the last two data points but before this point there is no real deviation between the two fits. To distinguish accurately between the fits, the data points would have to be extended out to the virial radius in order not to extrapolate to this point

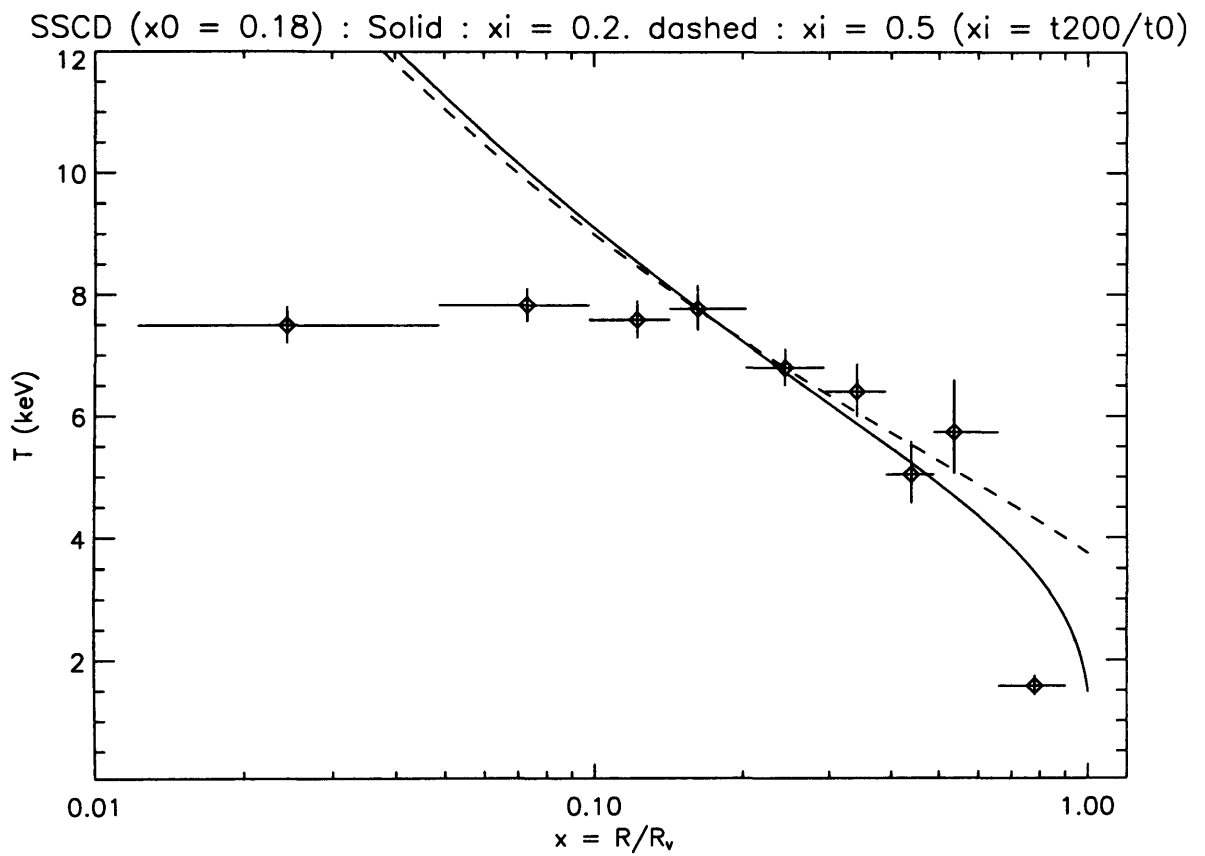


FIGURE 5.9. Temperature profile of Abell 1413 fitted with Steady-state conduction-driven model. Values of  $\xi$  are 0.2 for the solid line, 0.5 for the dashed line ( $\xi = T_0/T(x = 1)$  see earlier for details).

as the model requires. Previous fits to cluster temperature profiles tried to fit the profiles using a polytropic relation (Markevitch, Forman, Sarazin & Vikhlinin 1998) where they find an average polytropic index of  $\gamma \sim 1.24 \pm_{0.12}^{0.20}$ . A recent fit to this same dataset by Pratt & Arnaud (2002) finds a polytropic index to this data of  $\gamma \sim 1.07 \pm 0.01$ .

#### 5.6.4 Abundance profiles

Measurements were made of the abundance at different radii in the same way as temperature in order to see if this varied radially as well. A change in the metallicity over the cluster could suggest that material from star forming regions has been deposited preferentially in certain places such as in a cooling flow region. This would then support the model that the metals in the cluster were stripped from galaxies and then mixed with primordial gas in the ICM as described in chapter 1. This may result in varying metallicity if the gas was not properly mixed. The abundance profile for A1413 was created from the simultaneous fit data, like the temperature profile, and the resulting profile is shown in figure 5.10.

The profile shows a decreasing metallicity with radius, going from 0.34 solar to 0 with the abundance staying approximately constant within the inner four annuli (the first 0.4 Mpc). The abundance profile we obtain has values similar to those of Pratt & Arnaud (2002) with their central abundance being  $0.34 \pm 0.1$ . Their profile does not drop off as sharply with increasing radius, although they do not profile out as far. The uncertainty on the abundance profile is much greater than on the temperature profile which makes it harder to quantify the extent of any gradient. For the last 3 bins the abundance falls towards zero within the accepted errors, becoming zero for the last two bins.

The concentration of the metals (ie the higher abundances seen) towards the centre of the cluster can be explained by the fact that the metals enriching the ICM originates in galaxies. Both galaxies and gas sit preferentially towards the centre of the cluster potential. Since it is assumed that the ICM was enriched early in the cluster lifetime, then the

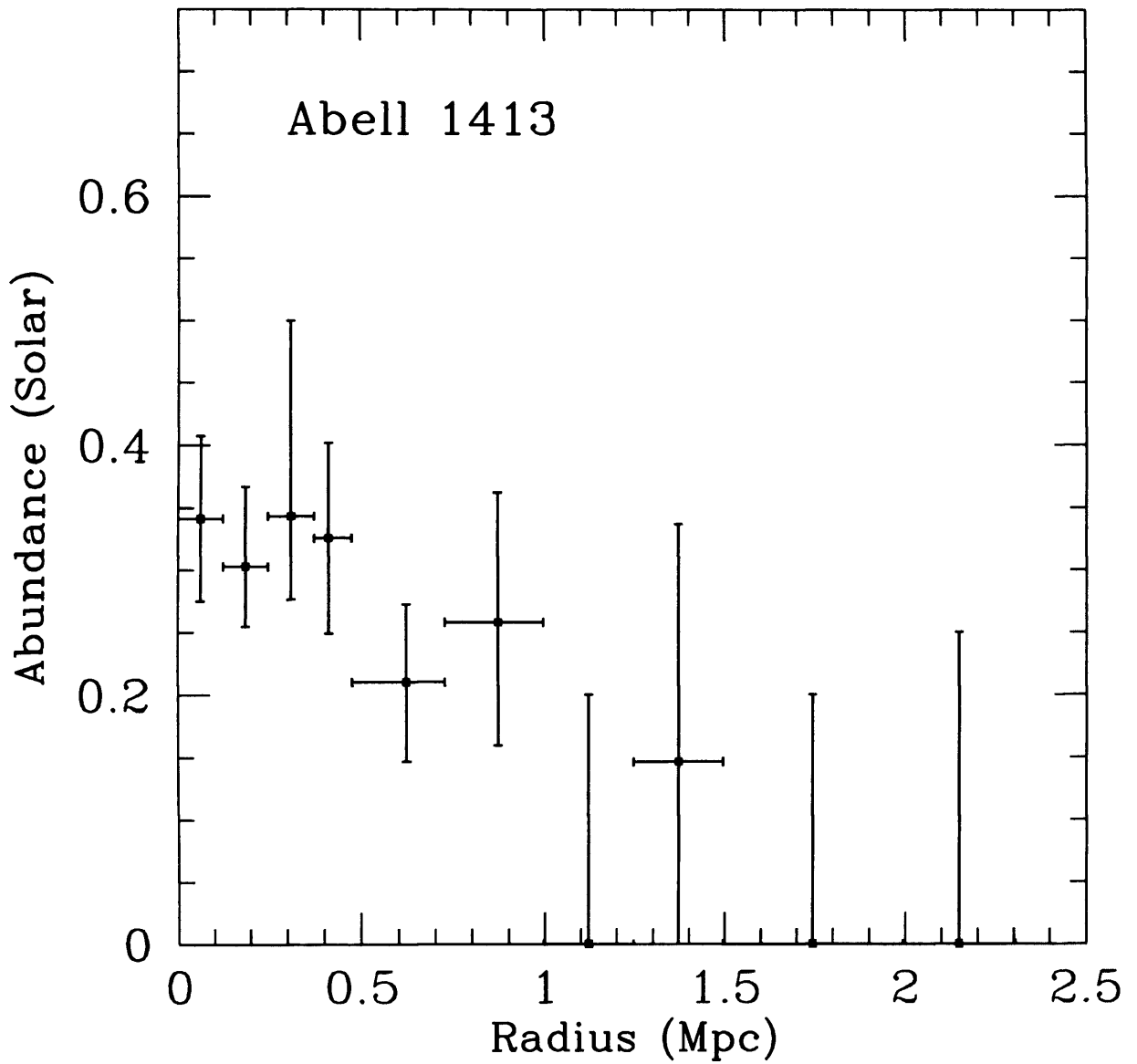


FIGURE 5.10. Abundance profile of the simultaneous fit of A1413 data with error bars at 90% confidence. The values are compared to the solar value.

concentration of metals towards the cluster centre seen in the current data suggests that there has been little mixing of the gas on a global scale in recent times. The abundances found are typical for a cluster even at the centre suggesting Abell 1413 is not particularly metal rich.

### 5.6.5 Determination of Gas Mass and Gravitational Mass

From the fit it is possible to calculate the central gas density  $\rho_0$  and thus estimate the gas mass,  $M_{gas}$ , as this is the integral of gas density  $\rho(r)$  over volume. Values of  $\rho$  at any particular radius were gained using the King approximation of the gas density, shown in equation 1.11. For a radius of 2 Mpc the gas mass can be calculated as  $1.41 \pm 0.34 \times 10^{14} M_{\odot}$ . Using Einstein data, White et. al. (1993) calculated the gas mass to be  $1.56 \pm 0.17 \times 10^{14} M_{\odot}$  for an analysis out to 1.65 Mpc. The gas mass for the XMM data estimated to the same radius is  $1.10 \pm 0.26 \times 10^{14} M_{\odot}$ . A plot of how the calculated gas mass varies with radius from the centre of the cluster is shown in figure 5.11.

The gas mass was also calculated using the NFW profile. This gave gas masses calculated at 1.65 and 2 Mpc of  $1.26 \pm 0.21 \times 10^{14} M_{\odot}$  and  $1.65 \pm 0.27 \times 10^{14} M_{\odot}$  respectively. This is larger than the  $\beta$  estimates but is still slightly lower than the White value, which is a factor of 1.2 times the corresponding NFW value. The values should be similar between the two fits as the density profiles are similar. However since the fits to the surface brightness profiles are slightly different, the masses will not be identical. Within uncertainties, however the two fits are consistent.

The gravitational mass enclosed within a certain radius,  $r$  was also calculated using equation 1.26. The full version of this equation was used with a constant temperature being used for the central regions of the cluster and then a gradient determined from the temperature profiles via least square fitting was implemented at larger values where the temperature began to decrease. The gravitational mass profile is shown in figure 5.12. This profile shows that the gravitational mass levels off as the cluster temperature goes

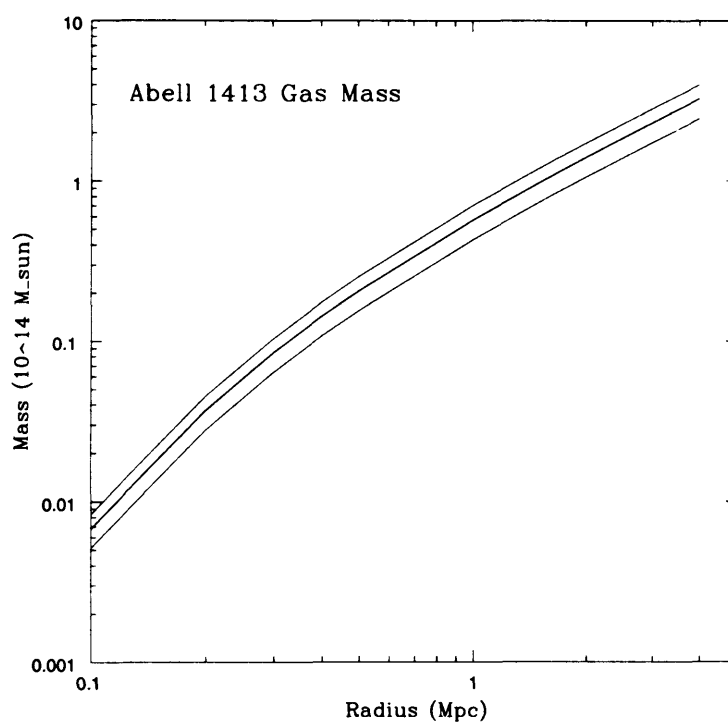


FIGURE 5.11. Plot of the variation in gas mass with radius in the cluster (black line) with associated errors (blue line). The plot is extrapolated out to approximately  $r_{200}$  which corresponds to  $4.2 \pm 0.15$  Mpc

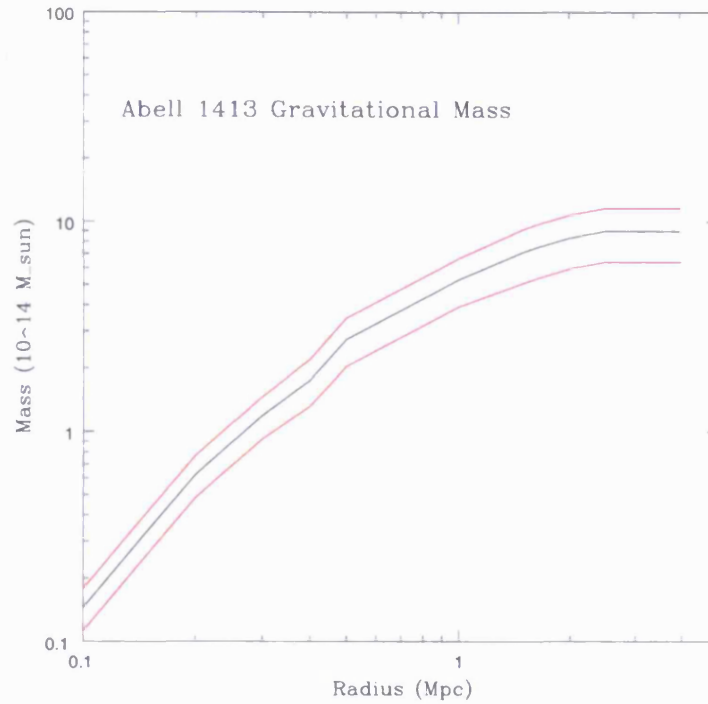


FIGURE 5.12. Plot of the variation in gravitational mass with radius in the cluster (black line) with associated errors (red line). The profile is extrapolated out to approximately  $r_{200}$

to zero at high radius. For a radius out to 2 Mpc the gravitational mass enclosed was calculated to be  $8.37 \pm 2.40 \times 10^{14} M_{\odot}$  and  $7.57 \pm 2.17 \times 10^{14} M_{\odot}$  for a radius of 1.65 Mpc. The value obtained using Einstein, (White et al. 1993) for the gravitational mass was  $1.56 \times 10^{15} M_{\odot}$ . Therefore the current estimates are approximately a factor of 2 down on those from White. One reason for this is that in this analysis the gradient from temperature profile is used as described above, whilst White uses the deprojection temperature which in this case is  $8.9 \pm_{4.7}^{2.0}$  keV. He also uses a higher core radius of 0.5 Mpc. Both will result in larger values of  $M_{grav}$ .

The gas mass and the gravitational mass were also calculated out to the radius  $r_{500}$ . This radius is defined as the radius where the over-density of the cluster is 500 times the critical density of the universe, where the critical density of the Universe is  $\sim 10^{-30} \text{ gm cm}^{-3}$ . The value of  $r_{500}$  calculated for our data is  $3.1 \pm 0.1$  Mpc. The gravitational mass and

gas mass determined using this value are approximately  $9.01 \pm 2.585 \times 10^{14} M_{\odot}$  and  $2.308 \pm 0.552 \times 10^{14} M_{\odot}$ . A value for  $r_{200}$  was also calculated and was found to be  $4.2 \pm 0.15$  Mpc. This is higher than the value found by (Pratt & Arnaud 2002), using a NFW model which was 2.17 Mpc. The NFW density profile does however fall off faster at larger radii than the  $\beta$  profile used here, which could account for some of this difference.

The cluster gas mass fraction is  $\frac{M_{\text{gas}}}{M_{\text{grav}}}$  for which White finds a value of  $10 \pm 1.1\%$  for the Einstein data. The mass fraction determined from the XMM data was  $\sim 17 \pm 6\%$  for 2 Mpc,  $\sim 15 \pm 5\%$  for 1.65 Mpc. The uncertainty is greater on the XMM-Newton estimates due to the use of the gradient of the temperature profile in the estimate the total gravitational mass. This results in a gravitational mass which more realistically derived from the data but results in a larger errors. Therefore within errors the gas mass fractions from the XMM-Newton data agree with those for the Einstein data. A profile of how the gas mass fraction varies with radius is shown in 5.13. The profile shows that the gas mass fraction increases with radius. This is mainly due to the gravitational mass leveling off earlier than the gas mass. The profile levels off slightly in the middle which is where the values we are considering lie, hence there is not much variation in the mass fraction obtained at 1.65 and 2 Mpc. This is similar to that reported by (Pratt & Arnaud 2002) who see a mass fraction increasing with radius up to  $\sim 0.2$ .

### 5.6.6 Determination of Cluster Iron Mass

The abundance profile discussed earlier enables us to calculate the amount of iron in the cluster. This is useful as it gives an indication of the amount of star formation that has occurred in the cluster. As can be seen from figure 5.10 the abundance is fairly constant for the inner radii and then falls off towards zero at higher radii. Once again we used linear regression in order to calculate the change in abundance over this region. A solar iron abundance of  $2.27 \pm 0.53 \times 10^{-5}$  was used. This was an average of the values used in XSPEC (Anders & Grevesse 1989, Feldman 1992, Anders & Ebihara 1982).

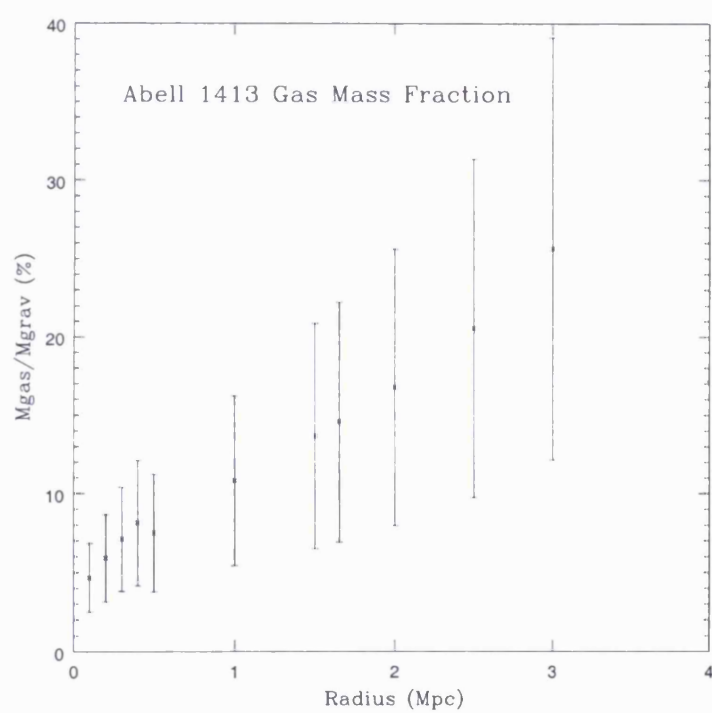


FIGURE 5.13. Plot of the variation in gas mass fraction with radius in the cluster. The profile increases with radius and is plotted out to approx  $r_{200}$  as with the two Mass plots

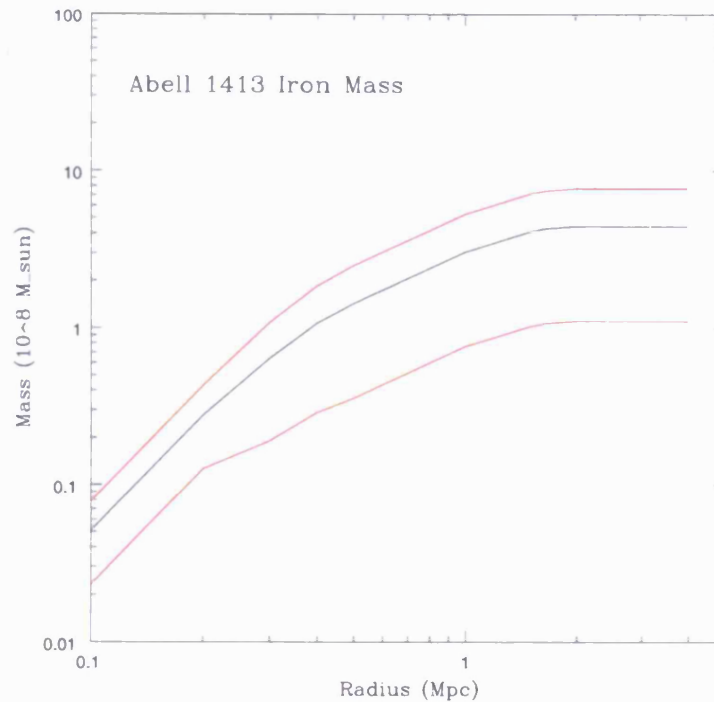


FIGURE 5.14. Iron mass profile of Abell 1413 with errors (red).

The integrated iron mass with radii found at 1.65 and 2 Mpc were  $4.30 \pm 3.22 \times 10^8 M_{\odot}$  and  $4.45 \pm 3.34 \times 10^8 M_{\odot}$  respectively. This is a factor of approx  $3 - 4 \times 10^6$  smaller than the gas mass and a factor of approx  $5 - 6 \times 10^7$  smaller than the gravitational mass, which is as expected. The profile of the variation of iron mass with radius is shown in figure 5.14. From the profile we can see that the iron mass increases from the centre and then levels off as the abundance decreases to zero. This suggests that the iron is concentrated towards the cluster centre which is as expected as there is more gas in this region and therefore a greater likelihood of star formation.

## 5.7 Summary

- The Surface Brightness profile can be fit with a King model using values for  $\beta = 0.62 \pm 0.02$  and  $r_c = 0.16 \pm 0.012$  Mpc.  $\beta$  was spectrally determined to be higher

at  $1.1 \pm 0.1$ . The surface brightness profile was also fitted with a NFW model with  $\eta = 8.05 \pm 0.05$  and  $r_s = 0.57 \pm 0.01$ . The  $\beta$  model provides a better fit to the data in the central regions and the NFW model worked better at large radii.

- The gas mass of the cluster has been estimated at  $1.41 \pm 0.34 \times 10^{14} M_\odot$  at  $r = 2$  Mpc and the gravitational mass as  $8.37 \pm 2.40 \times 10^{14} M_\odot$  at the same radius. This gives a mass fraction of  $17 \pm 6\%$ . The gas mass was also estimated with the NFW model and found to be  $1.65 \pm 0.27 \times 10^{14} M_\odot$ .
- The iron mass of the cluster was calculated to be  $4.45 \pm 3.34 \times 10^8 M_\odot$  out to 2 Mpc which is a factor of  $3 \times 10^6$  smaller than the gas mass and  $5 \times 10^7$  times smaller than the gravitational mass. The mass profile also suggests that most of the iron mass is centrally concentrated which is as expected since star forming regions also tend to be concentrated in the centre of the cluster potential.
- Spectral data was profiled suggesting a decreasing temperature and abundance between the cluster centre and the edge. This trend is seen in all the data when fitted separately and in the simultaneous fits. The cluster temperature decreases from  $7.49 \pm 0.3 - 1.57 \pm 0.18$  keV and the abundance decreases from  $0.34 \pm 0.07 - 0 \pm 0.23$  solar between the cluster centre and 2 Mpc.
- A marginal cooling flow was detected in the cluster with a mass inflow rate of  $56.5 \pm 17.5 M_\odot \text{yr}^{-1}$  and a low temperature cutoff of  $\sim 0.2$  keV. The central cooling time of the cluster was found to be  $5.49 \pm 0.11 \times 10^9$  yr.
- The Steady state conduction model was used to fit the temperature profile in the region where it was decreasing ( $x = 0.18-0.7$ ). This model provided a statistically acceptable fit to the data over these radii, although it was not possible to distinguish the better of the two fits lines at large radii due to the data not extending out to the virial radius ( $x = 1$ ).
- The affect on the value of the temperature parameter caused by varying the column density ( $n_H$ ) instead of keeping it constant, is negligible compared to other

uncertainties in the spectral fit to the data.

# Chapter 6

## A study of the galaxy cluster A665

### 6.1 Overview

Abell 665 is a hot, intermediate redshift cluster ( $z=0.18$ ) (Markevitch 1996). It is the richest cluster in the Abell catalogue and has therefore been subject to a great deal of study in many wave bands. The X-ray centre is slightly offset from the optical centre (Gomez, Hughes & Birkinshaw 2000) and the kinematics of the cluster galaxies suggest that the cluster may have undergone a recent merger. The centre of the X-ray emission is defined as RA 8:30:59.8, dec +65:50:31.3 (J2000) by the ROSAT HRI (Gomez et al. 2000). A665 has an X-ray luminosity of  $1.5 \times 10^{45} \text{ergs s}^{-1}$  as calculated from Ginga data (Hughes & Tanaka 1992). The velocity dispersion of the cluster galaxies is  $1390 \text{ kms}^{-1}$  (Gomez et al. 2000)

### 6.2 Introduction

Abell 665 has been found to have a global X-ray temperature of  $8.3 \pm 1.5 \text{ keV}$  by ASCA, and  $8.8 \pm 0.8 \text{ keV}$  using Chandra (Markevitch & Vikhlinin 2001). This makes Abell 665 one of the hotter clusters observed. It has been seen that Abell 665 exhibits a variation

in X-ray temperature over the extent of the cluster, which suggests that it has undergone a recent merger (Markevitch & Vikhlinin 2001). The X-ray emission associated with the cluster core is elongated in the same direction as the galaxy distribution. The X-ray core is travelling in a southerly direction with respect to the main cluster emission and the ROSAT and Chandra data suggests a shock in front of this core (Markevitch & Vikhlinin 2001). A temperature map of produced from the Chandra data suggests that there is excess hard emission associated with the shock region. Comparisons by Markevitch to the radio halos suggest that in addition to thermal bremsstrahlung emission the cluster may also emit synchrotron and Inverse Compton radiation, which produce emission in the radio and UV bands respectively.

The spectral results from ASCA and Chandra suggest that the temperature of the cluster decreases with increasing radius, although the Chandra data suggests that the cluster has a slightly cool core (Markevitch & Vikhlinin 2001). Deprojection results from earlier studies (Allen 2000) suggest that the cluster central cooling time is of order  $12 \times 10^9$  years. Therefore the cluster has had little time to cool within the age of the universe. Previous spectral studies have also shown no evidence of a cooling flow. This chapter presents a spectral and spatial analysis of the EPIC MOS data for Abell 665 from XMM-Newton.

### **6.3 Observation and Data Reduction**

Abell 665 was observed several times by XMM-Newton as part of the XMM Guaranteed time program. The observation detailed here was made on 23rd September 2001. The prime instrument was RGS1. As with the other observations a light-curve was produced in order to look for flares in the X-ray background. The exposure times before any filtering were 78487 seconds for MOS1 and 78484 seconds for MOS2. The unfiltered light-curve obtained for the data is shown in figure 6.1. The light-curve shows that there are several flares in the data, but also several long periods of time where the data has

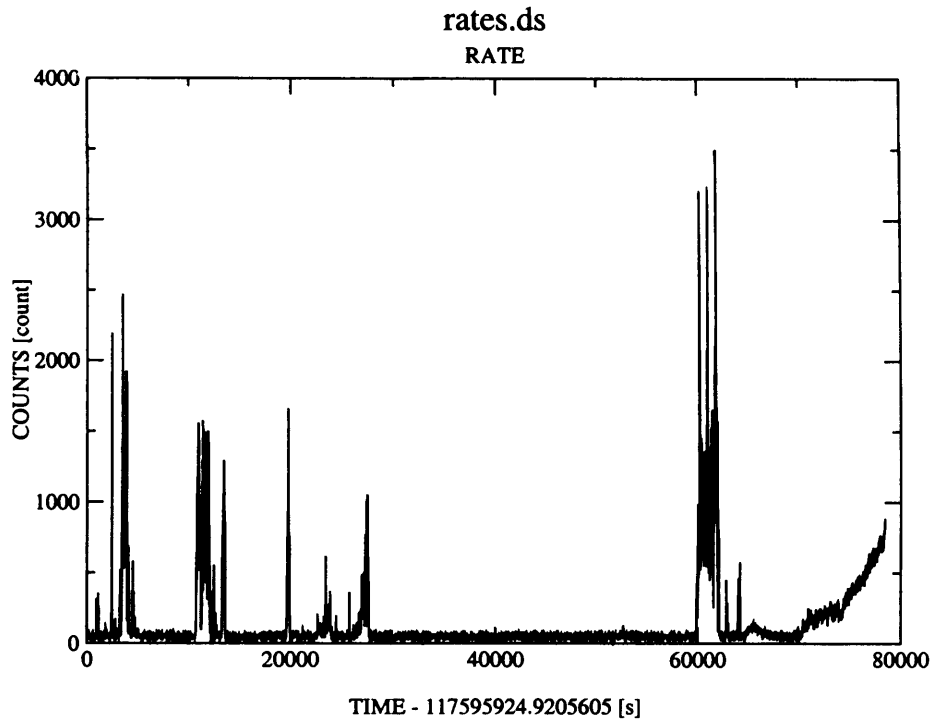


FIGURE 6.1. Un-cut light-curve of Abell 665

The light-curve of Abell 665 before filtering to remove flares. This shows that the light-curve increases by several thousand counts during flare events with the normal count rate level being of order a hundred counts

a quiet background. It is clear to see that the count rate during the flares increases to several thousand counts from a normal level of less than 100 counts. After the event lists had been filtered to remove the flaring events then the resulting exposure times were 42700 seconds for MOS1 and 43100 seconds for MOS2. No PN data was taken for this cluster.

As with Abell 1413 the cluster data reduction was undertaken with XMMSELECT and EVSELECT as described earlier. The filtering of the light-curve described above was carried out using the light-curve facility of these routines. This data reduction method also produces spectra, which were created in concentric annuli in the 0.3-10 keV band. Additionally for this cluster the software was used to produce hard and soft band images of the cluster and the routine EEXPMAP was used to create exposure maps of the data. These images were then used to create the temperature map as described later.

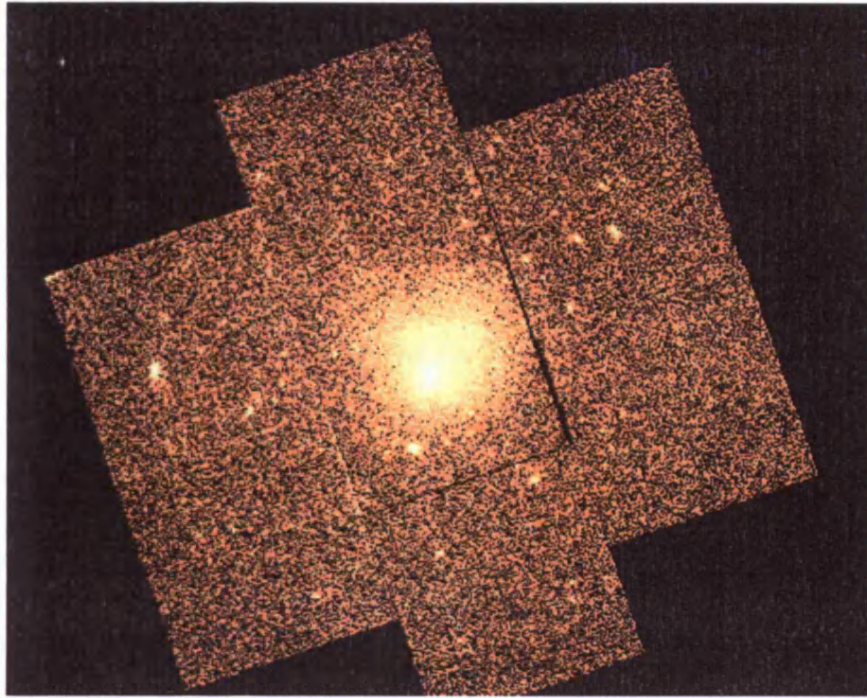


FIGURE 6.2. Image of Abell 665

An image of Abell 665 in the 0.3-10 keV band. The image was binned so that there are 600 pixels in both the x and y directions. This corresponds to 20 binned pixels per arcminute. The image is on the MOS1 detector and is shown in image co-ordinates and with a logarithmic scaling. The cluster is clearly visible as an extended source. There is a bright point source visible close to the cluster on the central chip. This is removed for all spectral fits

The emission from Abell 665 is extended, but not as elliptical as in Abell 1413. An image of Abell 665 is shown in figure 6.2. It appears to be slightly asymmetric with its brightest point occurring in a south-westerly direction. The X-ray centre as determined from the image is RA 08:30:58.290, dec +65:50:32.07(J2000). This value is consistent with the ROSAT value of RA 8:30:59.8, dec +65:50:31.3 (J2000) (Gomez et al. 2000).

## 6.4 Spatial Analysis

The surface brightness profiles were created using ASTERIX and then put into QDP in order to fit a King profile to the data as discussed previously. The values for the

central surface brightness,  $S_0$ , the core radius,  $r_c$ , the index of the slope and, hence,  $\beta$  were obtained. The profile obtained for MOS1 is shown in figure 6.3. The profile shows a steady fall off with radius after the core radius ( $r_c = 0.44 \pm 0.05$  arcmin which corresponds to  $0.165 \pm 0.019$  Mpc). The core radius as measured from ROSAT data is  $0.773 \pm_{0.209}^{0.240}$  Mpc (Pownall 1997) and 1.0 Mpc as measured from Einstein data (White et al. 1993). Both of these values are significantly larger than the values obtained from XMM. It is clear from the profile that the model does not fit the data particularly well, with significant deviations occurring once the profile begins to fall off. This suggests that there is possibly a central excess in the cluster and that the fit may be improved by fitting a second  $\beta$  profile to the data but this time with the central ( $R \leq 0.5$  arcmin) region excluded. A central excess was not anticipated for this cluster since they are usually only seen in cooling flow clusters. The profile is curtailed at 10 arcmin (1.91Mpc) as it has levelled off by this point. A profile was also made which extended out to 15 arcmin but this gave no improvement to the fit.

The value of the slope ( corresponding to  $(0.5 - (3\beta))$ ) is 1.10 which gives a  $\beta$  of  $0.53 \pm 0.02$  This compares to a value of  $\beta = 0.75 \pm_{0.10}^{0.14}$  for ROSAT data (Pownall 1997), which is much larger than we see. The spectral value of  $\beta$  for this cluster was calculated as  $1.3 \pm 0.1$  which once again is significantly larger than the spatially determined value.

#### 6.4.1 Comparison between the $\beta$ profile and the NFW profile

The  $\beta$  profile fit was compared to the NFW profile in order to see which best described the spatial properties of the cluster. The NFW model was fitted directly to the surface brightness profile of the data. The values from the fit are  $\eta = 6.55 \pm 0.05$   $r_s = 0.682 \pm 0.01$  Mpc. The  $\beta$  and NFW fits to the surface brightness profile are shown in figure 6.4

The figure shows that the NFW profile seems to be fitting better than the  $\beta$  profile especially at large radii, with the  $\beta$  profile showing fairly large deviations. This suggests that if there is a central excess seen in the data then the NFW profile is less affected by it.

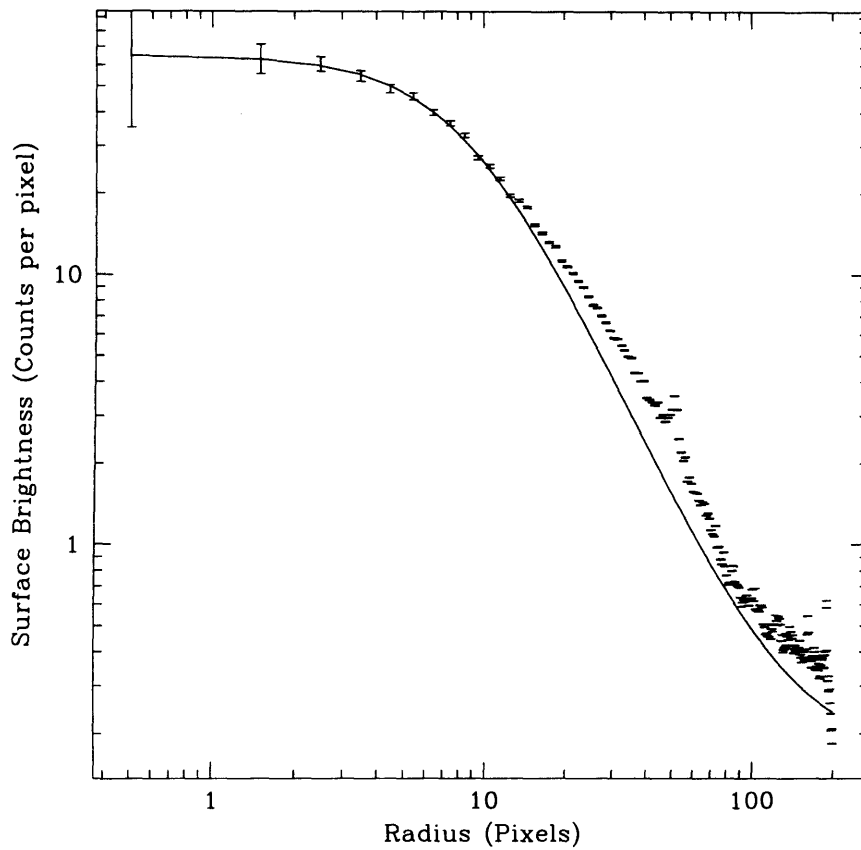


FIGURE 6.3. Surface Brightness profile of Abell 665

This profile goes out to 1.9 Mpc. The fit is poor for this cluster which suggests that a simple model like the King model is not adequate to explain the complex morphology of this cluster.

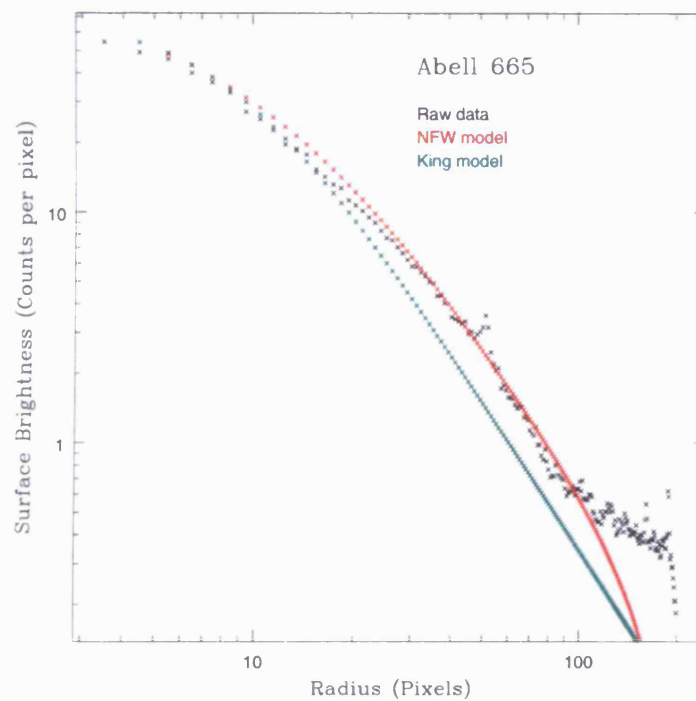


FIGURE 6.4. Comparison of the  $\beta$  and NFW models to the raw surface brightness profile. The plots are normalised to the raw data. The plots use the following values  $\beta = 0.53$ ,  $r_c = 0.165$  Mpc,  $\eta = 6.55$ ,  $r_s = 0.682$  Mpc

The fact that there is a significant difference between the NFW and  $\beta$  profiles determined for this cluster suggests that the spatial morphology of this cluster may be more complex than is seen for other clusters such as Abell 1413.

## 6.5 Spectral Analysis

The spectra of Abell 665 were investigated using ten concentric annuli centred on the brightest point of cluster emission. This position is slightly offset from the centre of the cluster and is possibly the position of the shock rather than the cluster core. The annuli and the background subtracted count rates for the two MOS detectors are summarised in table 6.1. The count rates are consistent between detectors and it is evident that the cluster flux is still just about significant out to 10 arcminutes.

### 6.5.1 Background subtraction

The background subtraction was undertaken using the standard background files generated by D. Lumb as before. Since the analysis of Abell 1413 had been undertaken a new set of background files had been released. These files were also used to make background files to fit to the data and the two sets of fits were found to be consistent within the accepted uncertainties (90% confidence levels).

A check was made on the normalisation of the background as described in chapter 5. This showed that the best background subtraction for Abell 665 was with no scaling applied to the background files. This applied for both MOS1 and MOS2 detectors.

### 6.5.2 Spectral Fitting

Abell 665 was fitted with a single temperature plasma emission model (MEKAL) with photometric absorption (PHABS). In this case the galactic column density was set to

Table 6.1. The background subtracted count rates for the ten annuli over which spectra were taken. The count rates are for the energy range 0.3-10 keV for the MOS1 and MOS2 detectors.

Region	Inner Radius arcmin	Outer Radius arcmin	Mean Radius Mpc	MOS1 Count Rate $cts^{-1}$	MOS2 Count Rate $cts^{-1}$
i	0	0.5	0.0786	$0.1501 \pm 0.0019$	$0.1444 \pm 0.0019$
ii	0.5	1	0.2357	$0.2895 \pm 0.0027$	$0.2798 \pm 0.0026$
iii	1	1.5	0.3929	$0.2310 \pm 0.0024$	$0.2461 \pm 0.0025$
iv	1.5	2	0.5500	$0.1884 \pm 0.0023$	$0.1935 \pm 0.0023$
v	2	3	0.7857	$0.2979 \pm 0.0029$	$0.3048 \pm 0.0029$
vi	3	4	1.1000	$0.2032 \pm 0.0026$	$0.2144 \pm 0.0027$
vii	4	5	1.4143	$0.1245 \pm 0.0023$	$0.1284 \pm 0.0024$
viii	5	6	1.7285	$0.0626 \pm 0.0021$	$0.0633 \pm 0.0021$
ix	6	8	2.2001	$0.0561 \pm 0.0029$	$0.0692 \pm 0.0029$
x	8	10	2.8287	$0.0003 \pm 0.0030$	$0.0067 \pm 0.0030$

$4.24 \times 10^{20} \text{cm}^{-2}$ , which was the value found from previous fits to the data. The initial temperature was taken from an ASCA fit (Markevitch 1996) with  $T=8.3$  keV and the initial abundance was set at 0.3 solar.

An initial individual fit of the two datasets was undertaken and the results of these fits are shown in table 6.2. The errors are once again at 90% confidence. It can be seen from these results that there is a decrease in temperature in both cases. There is also slight evidence of an abundance decrease with radius.

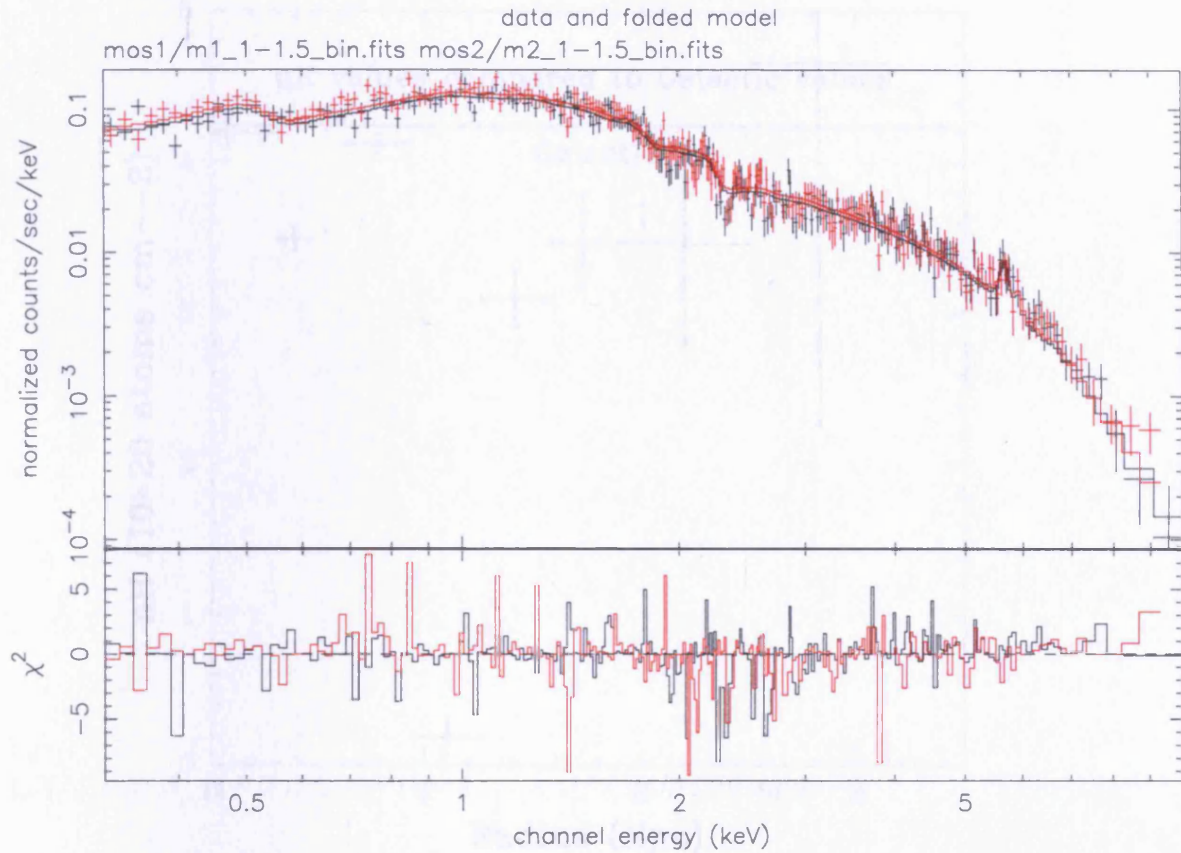
As the individual detector fits were mostly consistent, the data was fitted simultaneously with the temperature and abundance tied between the two detectors. An example of one of the simultaneous fits is shown in figure 6.5. It can be seen from the figure that both the MOS spectra are well fitted by the model. The results for the simultaneous fit for all of the annuli are summarised in table 6.3. This fit shows the same trends as the individual fits with the temperature decreasing slowly out to 6 arcminutes and then falling off more rapidly. The abundance is basically constant out to 3 arcminutes within errors and then drops toward zero. The temperature and abundance profiles are discussed in greater detail later in this chapter.

The single temperature thermal model provides a good fit to the data with the reduced  $\chi^2$  being close to one, particularly for the inner rings. Abell 665 has not been previously classified as a cooling flow cluster, since it has a long central cooling time (Allen 2000) and a spectrum which does not require a second cooling component to the model. Due to the possible excess seen in the spatial data however the data was checked in order to see if a cooling component was required for this fit. The central cooling time for the cluster as calculated from the XMM data is indeed shorter than the Allen value and the age of the universe ( $t_{cool} = 6.69 \pm 0.13 \times 10^9$  yr). However adding a cooling component to the spectral fits of the central regions gave no significant improvement to the fit, in agreement with earlier studies.

Another check on the data was also carried out by freeing the galactic column density  $n_H$  on the simultaneous fit data. For the fixed fits the column density had been set to

Table 6.2. Single temperature fits over different regions for the 2 EPIC MOS detectors fitted separately. Temperature, Abundance and  $\chi^2$  per degree of freedom parameters are shown.

Region	MOS1			MOS2		
	Temperature keV	Abundance Solar	$\chi^2 D.O.F$	Temperature keV	Abundance Solar	$\chi^2 D.O.F$
i	$7.89 \pm_{-0.72}^{+0.81}$	$0.37 \pm_{-0.15}^{+0.14}$	186/196	$7.28 \pm_{-0.66}^{+0.77}$	$0.18 \pm_{-0.12}^{+0.13}$	227/182
ii	$7.14 \pm_{-0.44}^{+0.49}$	$0.14 \pm_{-0.08}^{+0.08}$	277/248	$6.51 \pm_{-0.38}^{+0.42}$	$0.34 \pm_{-0.09}^{+0.09}$	206/241
iii	$7.61 \pm_{-0.56}^{+0.63}$	$0.30 \pm_{-0.11}^{+0.11}$	244/236	$6.79 \pm_{-0.47}^{+0.53}$	$0.17 \pm_{-0.09}^{+0.09}$	249/236
iv	$6.82 \pm_{-0.54}^{+0.62}$	$0.17 \pm_{-0.11}^{+0.11}$	236/222	$7.87 \pm_{-0.66}^{+0.76}$	$0.31 \pm_{-0.13}^{+0.14}$	205/222
v	$6.42 \pm_{-0.53}^{+0.56}$	$0.37 \pm_{-0.30}^{+0.28}$	223/217	$6.90 \pm_{-0.47}^{+0.53}$	$0.26 \pm_{-0.09}^{+0.10}$	283/279
vi	$6.66 \pm_{-0.66}^{+0.79}$	$0.02 \pm_{-0.02}^{+0.11}$	246/225	$5.96 \pm_{-0.49}^{+0.56}$	$0.13 \pm_{-0.10}^{+0.10}$	263/251
vii	$5.54 \pm_{-0.64}^{+0.81}$	$0.14 \pm_{-0.14}^{+0.18}$	262/228	$5.19 \pm_{-0.60}^{+0.73}$	$0.08 \pm_{-0.08}^{+0.15}$	257/232
viii	$3.94 \pm_{-0.65}^{+0.87}$	$0.001 \pm_{-0.001}^{+0.23}$	230/200	$4.38 \pm_{-0.79}^{+1.01}$	$0.44 \pm_{-0.30}^{+0.39}$	215/206
ix	$1.63 \pm_{-0.29}^{+0.49}$	$0.0 \pm_0^{+0.16}$	305/289	$2.12 \pm_{-0.42}^{+0.76}$	$0.02 \pm_{-0.02}^{+0.37}$	289/290
x	$0.67 \pm_{-0.27}^{+0.32}$	$0.0 \pm_0^{+0.22}$	433/305	$0.31 \pm_{-0.09}^{+0.13}$	$0.005 \pm_{-0.005}^{+0.46}$	366/300



ies 7-May-21

FIGURE 6.5. Spectrum of Abell 665 fitted simultaneously for MOS1 and MOS2. The spectrum is from the 1.5-2 arcmin region

Table 6.3. Simultaneous single temperature fits for EPIC MOS detectors. Temperature, abundance and  $\chi^2$  per degree of freedom are shown.

Region	Temperature	Abundance	$\chi^2 D.O.F$
i	$7.60 \pm_{0.50}^{0.55}$	$0.27 \pm_{0.09}^{0.10}$	418/380
ii	$6.84 \pm_{0.30}^{0.31}$	$0.23 \pm_{0.06}^{0.06}$	492/491
iii	$7.19 \pm_{0.37}^{0.40}$	$0.22 \pm_{0.06}^{0.07}$	500/474
iv	$7.32 \pm_{0.43}^{0.48}$	$0.23 \pm_{0.08}^{0.09}$	447/446
v	$6.95 \pm_{0.35}^{0.38}$	$0.25 \pm_{0.06}^{0.07}$	565/561
vi	$6.20 \pm_{0.37}^{0.44}$	$0.08 \pm_{0.07}^{0.08}$	537/505
vii	$5.43 \pm_{0.46}^{0.54}$	$0.12 \pm_{0.11}^{0.11}$	520/462
viii	$4.11 \pm_{0.53}^{0.64}$	$0.18 \pm_{0.17}^{0.19}$	448/405
ix	$1.88 \pm_{0.27}^{0.37}$	$0.0 \pm_{0.0}^{0.17}$	596/581
x	$0.41 \pm_{0.11}^{0.13}$	$0.0 \pm_{0.0}^{0.23}$	804/607

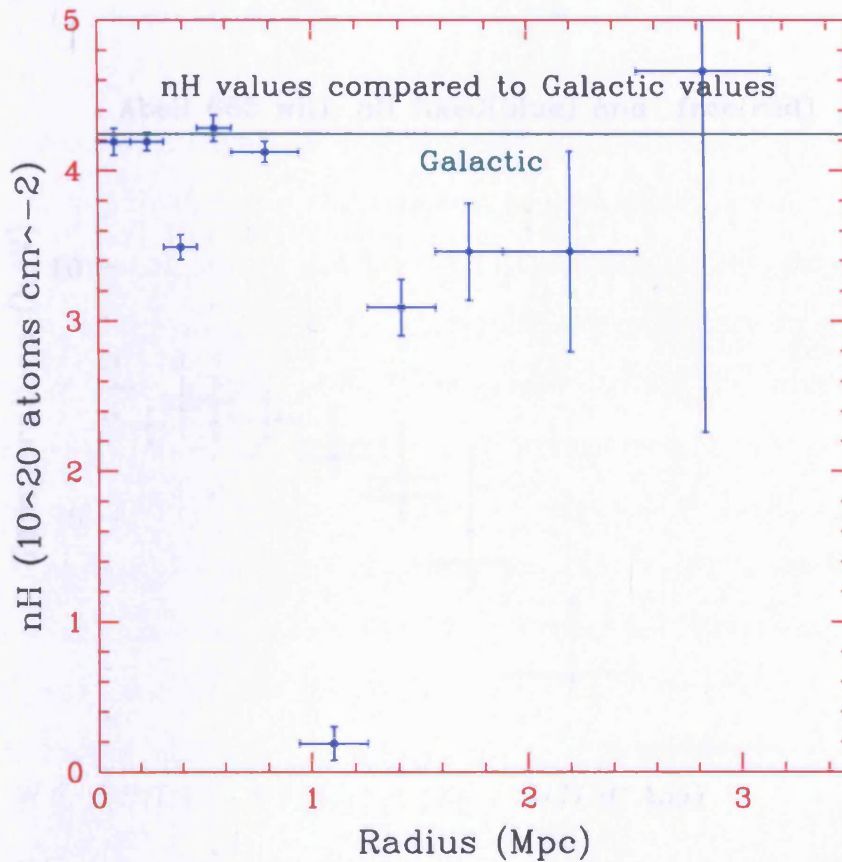


FIGURE 6.6. Freed galactic column density values for simultaneous fit with line of fixed values marked on.

$4.24 \times 10^{20}$ . The values of  $n_H$  obtained are plotted in figure 6.6, with the fixed value of the Galactic column density marked in green. This plot shows that the column density oscillates around the fixed value with the point corresponding to the 2-3 arcminute ring deviating the most from this value. This could be due to an unsubtracted soft source which may be affecting the measured column density. The values are the same as the fixed value, within uncertainties, for 3 out of 5 of the innermost annuli and for the outermost annuli. It is also evident that the degree of uncertainty in  $n_H$  increases with increasing radius. There is no trend of column density with radius which would suggest an incorrect background subtraction as described in (Pratt & Arnaud 2001).

Another implication of incorrect background subtraction would be a change in the

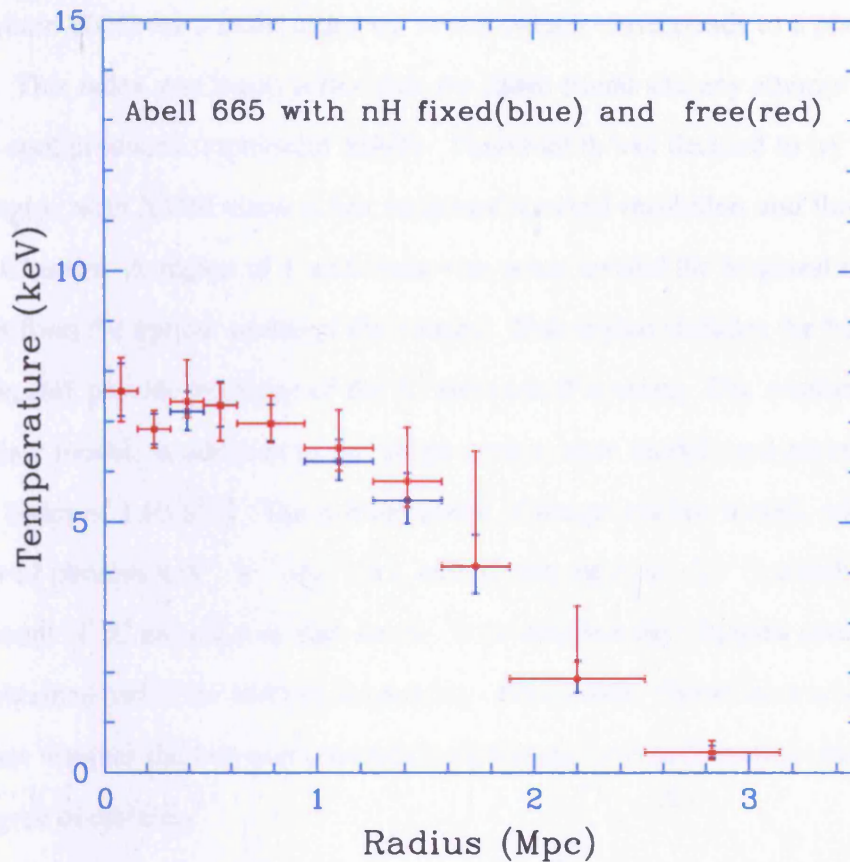


FIGURE 6.7. Temperature profile with  $n_H$  fixed and free.

temperature profile. Therefore, the temperature profile was plotted for both the fixed and free cases and compared. This comparison is shown in figure 6.7. The plot shows that temperatures in both fits agree within given uncertainties. This suggests that the background subtraction is indeed working correctly and not leaving a high level of low energy background in the data.

### 6.5.3 Power Law Fits

It has been suggested by (Markevitch & Vikhlinin 2001) that the relativistic electrons which produce the radio emission in Abell 665 should also be producing inverse Compton (IC) emission. The spectral index of the X-ray inverse Compton emission should cor-

respond with the radio synchrotron index. This was tested with Chandra by (Markevitch & Vikhlinin 2001) for a radio index  $\alpha_r \sim 0.8$  (which corresponds to a photon index of  $\sim 1.8$ ). This index was much softer than the index found and any attempt to reproduce the hot-spot produced unphysical results. Therefore it was decided to try to model the same region with XMM since it has increased spectral resolution and throughput over that of Chandra. A region of 1 arcminute was taken around the brightest region (which is offset from the optical centre of the cluster). This region includes the hot-spot and so may possibly provide evidence of the IC emission if it exists. The resulting fit, using a power law model, in addition to the single temperature model used previously, gave a photon index of  $1.93 \pm_{1.03}^{7.01}$ . The normalisation of the power law model, which gives the number of photons  $\text{keV}^{-1}\text{s}^{-1}\text{cm}^{-2}$  at 1 keV is very small ( $\sim 10^{-5}$ ) which suggests that the amount of IC emission is also small. This supports the Chandra result both in the value obtained and in the level of uncertainty of the result. Therefore it is not possible to constrain whether the hot-spot contains a significant inverse Compton component with any degree of certainty

## 6.6 Temperature Maps

The Chandra data (Markevitch & Vikhlinin 2001) was used to produce a temperature map in order that any hot-spots in the data would become clear. This was repeated with the XMM data of the cluster. The map was made by creating images in two different energy bands, soft (0.3-2 keV) and hard (2-8 keV). These images were background subtracted and then exposure corrected. The hard band image was then divided by the soft band image to produce a hardness ratio map. This hardness ratio map was then rescaled by producing a MEKAL spectrum in the two temperature bands with XSPEC and gaining model predicted count rates at different fixed temperatures. The resulting map is shown in figure 6.8.

The temperature map shows that the maximum temperature is approximately 7 keV

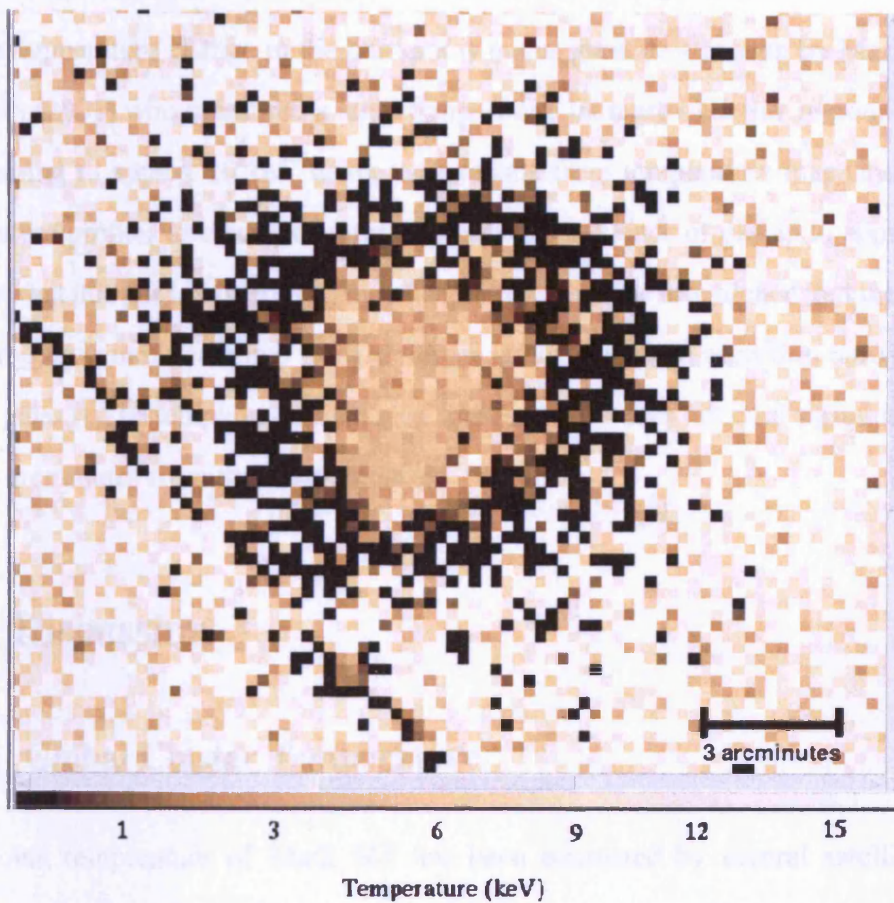


FIGURE 6.8. Temperature map of A665 showing the variation in temperature across the cluster.

and is slightly offset from the centre. There also seems to be evidence of cooler gas out past 2 arcminutes as is demonstrated by the darker ring in the data, although this could just be a result of over subtraction of the background. Beyond this region the values increase again but it is possible that this is caused by the count-rate decreasing significantly in this region which may result in the ratio increasing due to small number statistics as the same increase is not seen in the spectral data.

The temperature change in the hot-spot is not as great as was seen by Markevitch & Vikhlinin (2001) who measured a large temperature increase over this region. They saw  $T$  increasing to approx 10 keV using their results from temperature maps and also the temperature profiles as discussed later. We only see evidence of gas up to approx 7 keV. The fact that this gas is offset from the cluster optical centre is evidence that the emission in this region is likely to come from a merger rather than from accretion onto the centre cluster galaxy. The temperature map also shows the gas does not cool significantly until several arcminutes from the cluster centre.

## 6.7 Discussion

### 6.7.1 Global Cluster Temperature

The global temperature of Abell 665 has been estimated by several satellites. The temperatures found from Chandra and ASCA observations within the first 6 arcminutes and was found to be  $8.8 \pm 0.8$  keV (Markevitch & Vikhlinin 2001) and  $8.3 \pm 1.5$  keV (Markevitch 1996) respectively. The global temperature using the Ginga LAC was  $8.2 \pm_{0.81}^{0.95}$  keV (Hughes & Tanaka 1992). The XMM-Newton data for the inner 6 arcminutes was fitted simultaneously for the MOS1 and MOS2 detector using a MEKAL plus PHABS model as before in order to find the global temperature of the Cluster. The global temperature was found to be  $5.46 \pm_{0.13}^{0.14}$  keV which is significantly lower than the temperature in the same region for the other satellites. It is also lower than the central temperature by

approximately 2 keV which is a more extreme difference than was anticipated. The cause of this low global temperature estimate is as yet unknown, but is not thought to be due to background or calibration effects as different background estimations and calibration settings made little difference to the fit.

## 6.7.2 Temperature profiles

An important part of the spectral analysis was to create temperature profiles of the cluster. The profiles were created using the data from the simultaneous fit of the two MOS detectors. These fits were used as they gave the best constraints on the profile shape. The profile produced is plotted in figure 6.9, with the profiles produced for ASCA and Chandra plotted on the same graph (Markevitch & Vikhlinin 2001). The profile shows that the temperature is highest in the central region, at 7.6 keV and then decreases significantly in the next region to 6.8 keV, it increases slightly again before starting to fall off steadily by 3 arcminutes radius. The falloff also gets steeper after 6 arcminutes decreasing to 0.4 keV by the outermost ring.

It is evident that the Chandra data gives temperatures consistently higher than those obtained with XMM (albeit with larger error-bars). There are several possible causes for this inconsistency including incorrect modelling of the instrument response or background subtraction. The XMM response and background were reasonably well understood by the time the observations were taken, and results obtained in the same manner for other clusters tend to be consistent with earlier results. Also XMM has a higher spectral resolution than Chandra and so it would be expected that the spectra produced would be of better quality than those produced by Chandra. The ASCA results lie in the middle of the two other sets of results with the outer result lying close to the outer XMM result. The inner result is consistent with our results and the Chandra results but since it covers a much larger annular region it is difficult to draw any firm conclusions from this.

The temperature has been constrained to within approximately  $\pm 0.5$  keV for most of

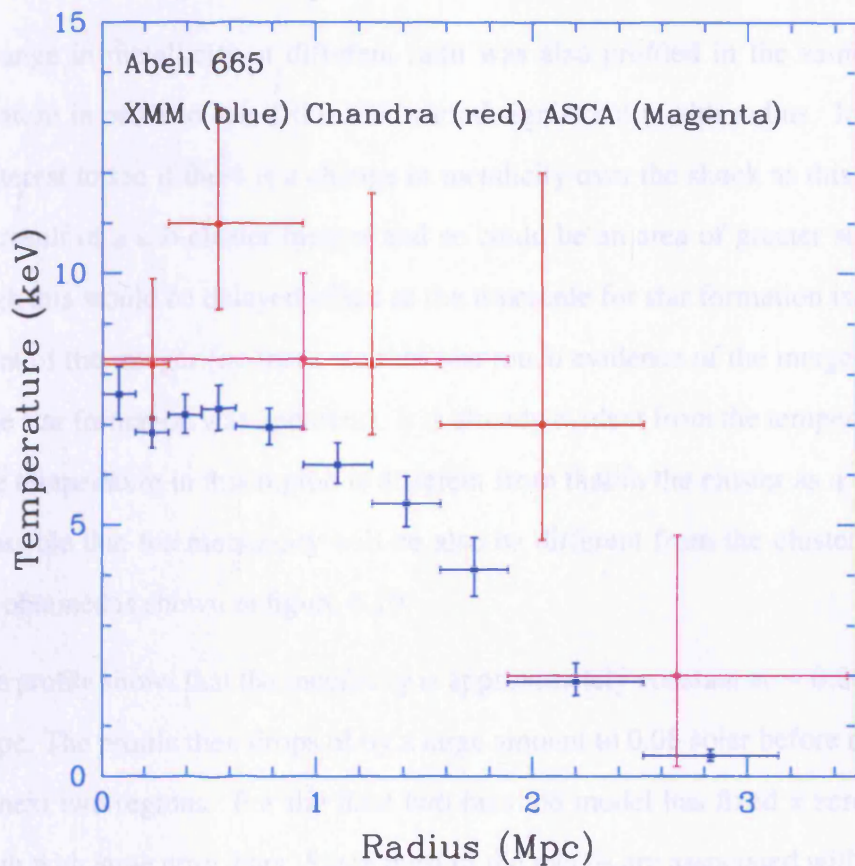


FIGURE 6.9. Temperature profile produced from simultaneous MOS1 and MOS2 fits. The results from Chandra and ASCA (Markevitch & Vikhlinin 2001) are also plotted for comparison

the annuli, although the error on the outer two regions may be underestimated by the error routine in XSPEC and actually be larger than shown. This is a significant improvement on the previous results and gives one of the best constrained temperature profiles out to a very large radius.

### 6.7.3 Abundance profiles

The change in metallicity at different radii was also profiled in the same way as the temperature in order to see if this also varied significantly with radius. In particular it is of interest to see if there is a change in metallicity over the shock as this region could be the result of a sub-cluster merger and so could be an area of greater star formation, although this would be a delayed effect as the timescale for star formation is much longer than that of the merger (i.e. there wouldn't be much evidence of the merger even by the time the star formation was apparent). It is already evident from the temperature profiles that the temperature in this region is different from that in the cluster as a whole and so it is possible that the metallicity will also be different from the cluster whole. The profile obtained is shown in figure 6.10.

The profile shows that the metallicity is approximately constant at  $\sim 0.26$  solar, out to  $\sim 1$  Mpc. The profile then drops off by a large amount to 0.08 solar before rising slightly in the next two regions. For the final two bins the model has fixed a zero abundance, although with large error-bars. Since most of the metals are associated with stripped gas from galaxies, which are expected to be more concentrated in the cluster centre due to the cluster potential, then the lack of a central concentration of metals suggests that some mixing has occurred. It is also evident that the metallicity drop at 1 Mpc is significant even within the given errors and so it suggests that the mixing is incomplete as the gas at large radii is still less enriched than the gas at the centre of the cluster.

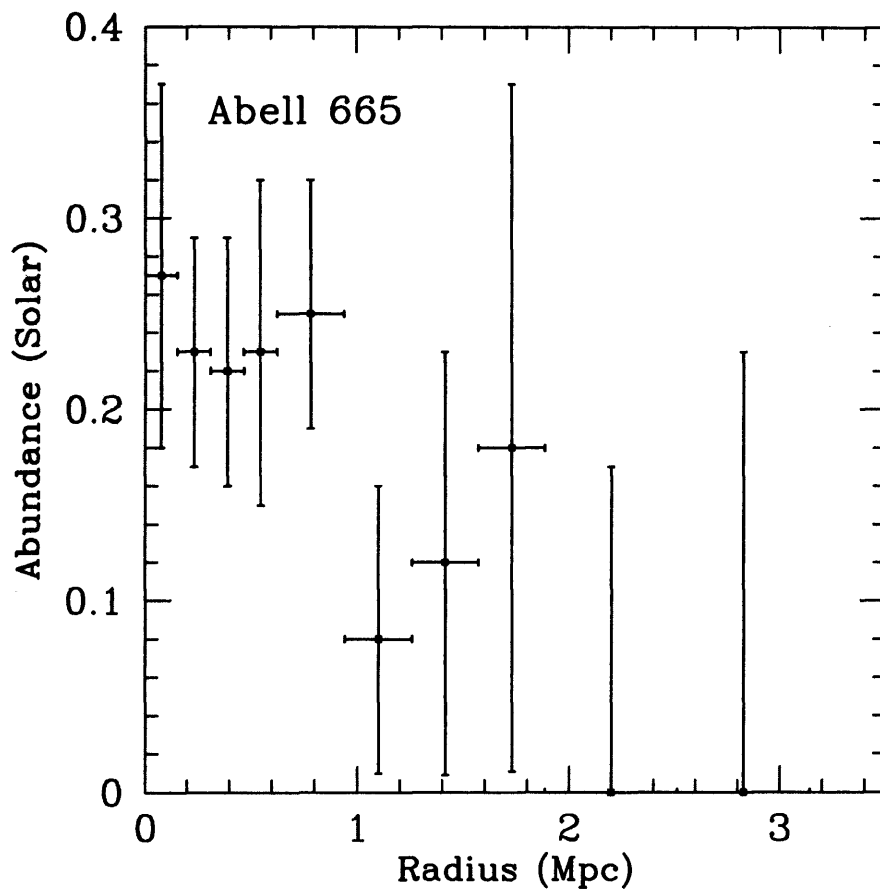


FIGURE 6.10. Abundance profile of Abell 665. This profile was produced from a simultaneous MOS1 and MOS2 fit to the data.

### 6.7.4 Gas and Gravitational Mass Estimates

As with Abell 1413 a gas mass estimate was made by calculating the central density  $\rho_0$  and using the relation between density  $\rho(r)$  and gas mass  $M_{gas}$ . The gas mass in the cluster was found to be  $M_{gas} = 1.80 \pm 0.43 \times 10^{14} M_{\odot}$  out to 2Mpc. The value determined for Einstein data via a deprojection analysis by White et al. (1993) was  $M_{gas} = 4.07 \pm 0.57 \times 10^{14} M_{\odot}$  where the analysis was taken out to 2.65 Mpc. Calculating the value for the XMM data out to the same radius gives  $M_{gas} = 2.74 \pm 0.649 \times 10^{14} M_{\odot}$ . This is much lower than the Einstein value, but the core radius used in this analysis is also much lower and so may account for some of the difference. It is also possible that if there is a central excess in the data as seems to be suggested from the surface brightness profile that the values for  $\beta$  and  $r_c$  obtained may be too low and henceforth the gas mass. The gas mass profile for this cluster is shown in figure 6.11. This profile shows that the gas mass is increasing with radius with only a slight indication of the mass leveling off with radius. The profile is steeper than that of Abell 1413.

The gas mass at 2 and 2.65 Mpc was also calculated using the NFW model. This gave a gas mass of  $2.32 \pm 0.63 \times 10^{14} M_{\odot}$  at 2 Mpc and a value of  $3.70 \pm 1.00 \times 10^{14} M_{\odot}$  at 2.65 Mpc. The  $\beta$  values are smaller than our NFW values, but the White values are still slightly larger being approx a factor of 1.1 larger than the NFW values. The values are much closer to the White values however, than the  $\beta$  determined values. The difference in the estimated values obtained from the  $\beta$  and NFW could be due to the differences seen in the fits to the surface brightness profiles. The two fits are still consistent within uncertainties, so therefore the change of values in the NFW profile has not made a large difference to the statistics.

The gravitational mass of the cluster is calculated using equation 1.26. The gravitational mass of the cluster from our estimates is  $8.27 \pm 3.37 \times 10^{14} M_{\odot}$  at 2 Mpc and  $9.71 \pm 3.96 \times 10^{14} M_{\odot}$  at 2.65Mpc. The value obtained for Einstein by White et al. (1993) at 2.65 Mpc was  $2.37 \times 10^{15} M_{\odot}$ , which once again is much larger. In the Einstein case a higher temperature of 8.2 keV was used to estimate the cluster gravitational mass which

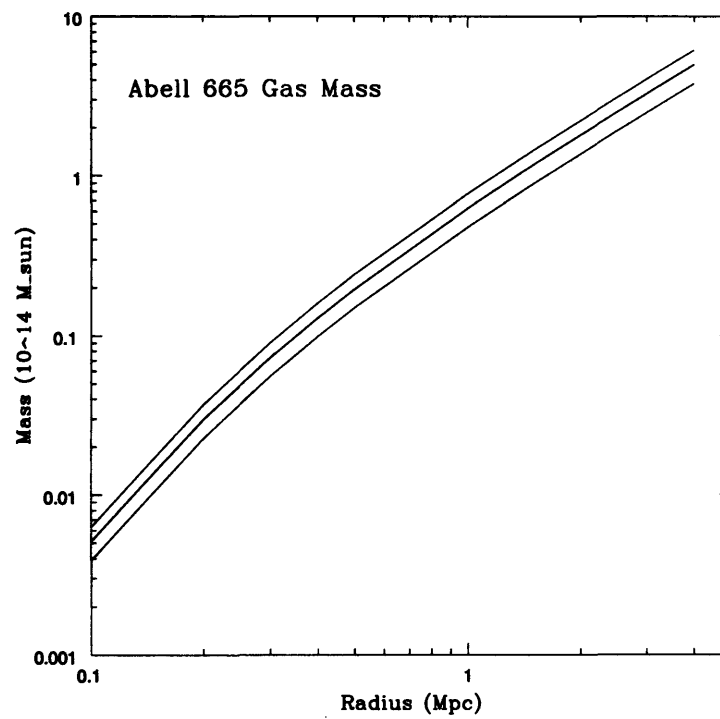


FIGURE 6.11. Plot of the variation in gas mass with radius in A665 (black line) with associated errors (blue line). The values are extrapolated out to approximately  $r_{200}$  which corresponds to  $4.3 \pm 0.15$  Mpc for this cluster

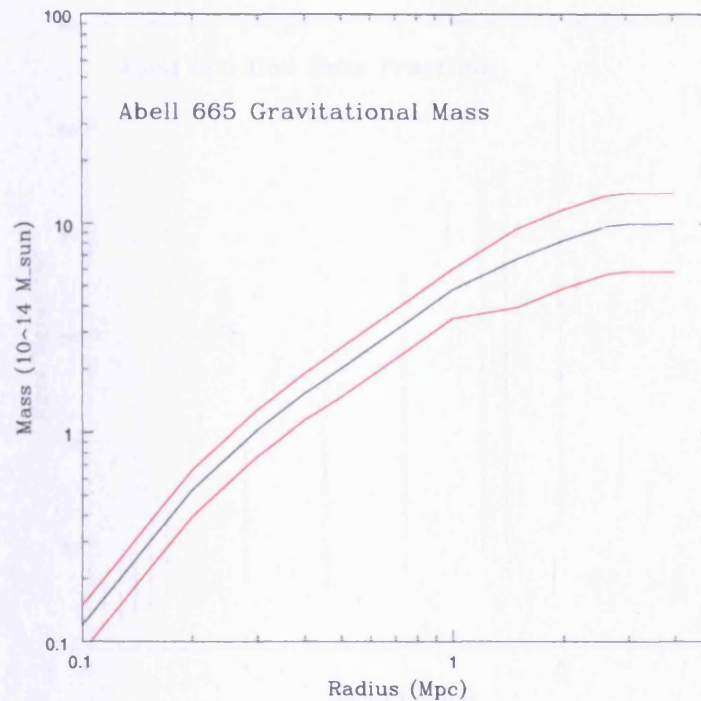


FIGURE 6.12. Plot of the variation in gravitational mass with radius in the cluster (black line) with associated errors (red line). Values are extrapolated out to approx  $r_{200}$

may account for some of the difference.

The value of  $r_{500}$  was found to be  $r_{500} = 3.2 \pm 0.1$  Mpc. This value suggests that the cluster potential is very deep and that the mass is very centrally concentrated since the density profile has dropped off within a short radius for this cluster. The gas mass and gravitational mass calculated with  $r_{500}$  are approximately  $3.28 \pm 0.778 \times 10^{14} M_{\odot}$  and  $9.95 \pm 4.06 \times 10^{14} M_{\odot}$  respectively. The variation of gravitational mass with radius is shown in 6.12. This shows that the gravitational mass begins to level off at high radii but at a fairly slow rate. This is because the temperature profile stays constant for a fair while before dropping off quite sharply at higher radii. The value of  $r_{200}$  was also calculated and found to be  $4.3 \pm 0.15$  Mpc.

The gas mass fraction,  $\frac{M_{\text{gas}}}{M_{\text{grav}}}$ , was also calculated for the two cluster radii. For a 2 Mpc radius the fraction was  $22 \pm 10\%$  increasing to  $28 \pm 13\%$  for a 2.65 Mpc radius.

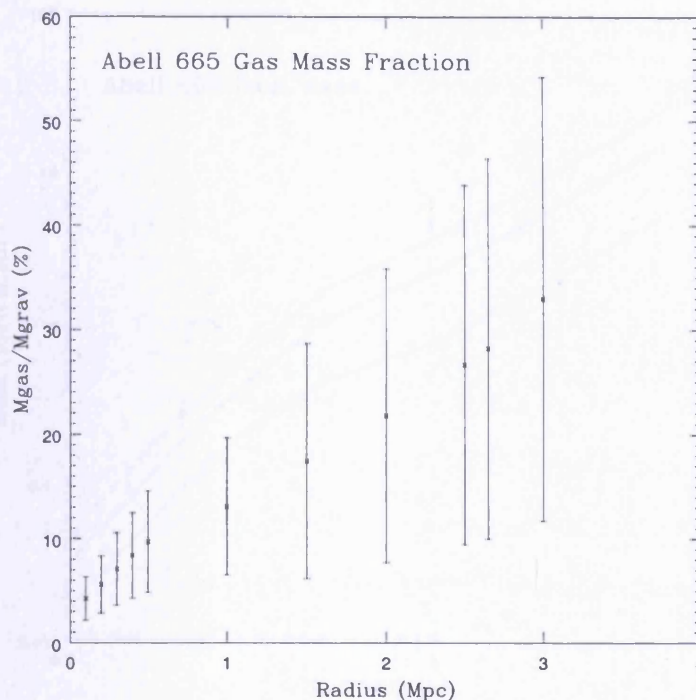


FIGURE 6.13. Plot of the variation in gas mass fraction with radius in the cluster. The profile increases sharply with radius indicating the fact that the gas mass profile does not level off greatly at high radii.

### 6.7.3 Iron Mass Estimation

White et al found the fraction to be  $17 \pm 2.4\%$  which is significantly lower than our value at the same radius. The variation of the gas mass fraction with radius for our data is shown in figure 6.13. This plot shows that the gas mass fraction increases quite sharply with radius, which is expected from the gas mass profile which shows little evidence of levelling off to any great extent at high radius. The gravitational mass has leveled off though hence the gas mass fraction rise gets steep at very large radius suggesting that the relation is breaking down at this point. At the radii considered there are still large uncertainties on the gas mass fraction and so the two values are consistent with each other and the White value.

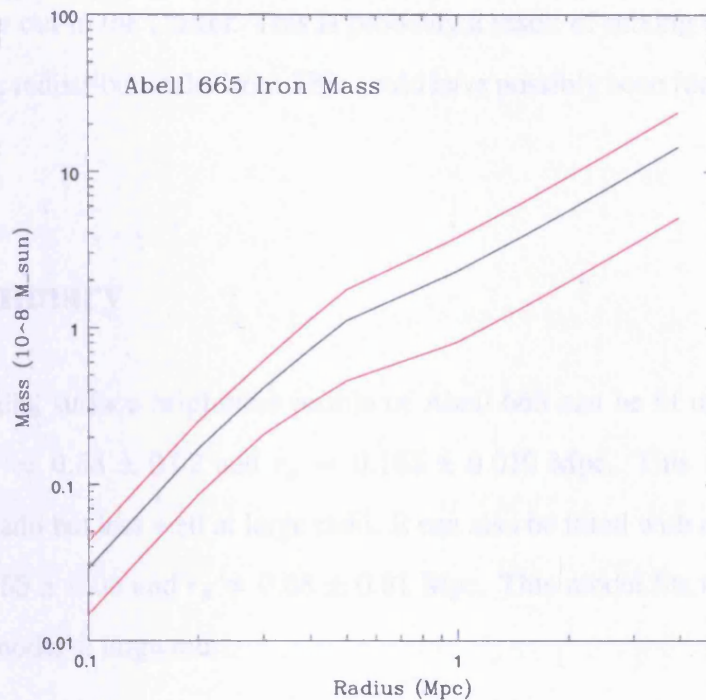


FIGURE 6.14. Iron mass profile (black) errors (red). The profile shows a gradual increase in mass with radius.

### 6.7.5 Iron Mass Estimate

An estimate of the iron mass in the cluster was undertaken using the methods described in the previous chapter. The major difference in this case was that the abundance profile did not exhibit a clear gradient decreasing to zero and so the estimates of the abundance at different radii were undertaken using two constant values,  $0.33 \pm 0.10$  solar for  $r < 0.5$  Mpc and  $0.1 \pm 0.05$  solar for  $r > 0.5$ . Using these constant abundances does mean that the mass profile does not level as is seen in figure 6.14, but instead has a gradual increase with radius. The change in slope represents where the value of the abundance is altered.

The values of most interest are the values at 2 and 2.65 Mpc as before. The values of the iron mass at 2 and 2.65 Mpc are  $5.60 \pm 3.52 \times 10^8 M_{\odot}$  and  $8.18 \pm 5.29 \times 10^8 M_{\odot}$  respectively. These values are approx  $3 - 3.5 \times 10^5$  smaller than the gas mass and approx  $1 - 1.5 \times 10^6$  smaller than the gravitational mass. The profile also suggests that the iron

mass is still quite centrally concentrated but a significant fraction of the mass has also moved further out in the cluster. This is probably a result of mixing of the intra-cluster gas which has redistributed the iron. This could have possibly been fuelled by the merger in the cluster.

## 6.8 Summary

- The radial surface brightness profile of Abell 665 can be fit using a King model with  $\beta = 0.53 \pm 0.02$  and  $r_c = 0.165 \pm 0.019$  Mpc. This model fits well for small radii but less well at large radii. It can also be fitted with a NFW profile with  $\eta = 6.55 \pm 0.05$  and  $r_s = 0.68 \pm 0.01$  Mpc. This model fits the data better than the  $\beta$  model at large radii.
- The gas mass of the cluster has been estimated at  $1.80 \pm 0.43 \times 10^{14} M_\odot$  at  $r = 2$  Mpc and the gravitational mass as  $8.27 \pm 3.37 \times 10^{14} M_\odot$  at the same radius. This gives a mass fraction of  $22 \pm 10\%$ . The gas mass was also estimated with the NFW model and found to be  $2.32 \pm 0.63 \times 10^{14} M_\odot$ .
- There is no clear evidence of inverse Compton emission being produced by the material also producing the radio emission, since the errors on the photon index (and therefore IC emission) from the shock region are very large.
- The global temperature of the cluster is determined to be  $5.46 \pm 0.14$  keV which is lower than the global temperature estimates made by other telescopes.
- The spectral fits to the data support previous studies in that they give no evidence that the cluster contains a cooling flow. The fits show a decrease in temperature with increasing radius and a slightly higher central temperature possibly caused by a merger shock region.
- There is evidence of a slight abundance decrease with increasing radius, but due to the large error-bars on the profile, it is difficult to determine the decrease in any

detailed manner. The abundance does not show a sharp decrease to zero at large radii, which could be evidence of mixing due to the merger.

- The iron mass of the cluster at 2 Mpc  $5.60 \pm 3.52 \times 10^8 M_{\odot}$ . The iron mass profile is fairly centrally concentrated but does not level off completely at high radius as the abundance never falls to zero.
- The temperature map of the cluster shows a hot-spot offset from the centre of the cluster in a south westerly direction. It also shows the cluster is quite hot (6-7 keV) out to 2-3 arcminutes and then begins to cool, which supports the spectral data. Beyond this, the temperature seems higher again but this is not supported by the spectral data and may be due to small number statistics.
- The temperature profile of the cluster also shows that the cluster contains a hot-spot and otherwise behaves as a relaxed cluster cooling with increasing radius. The temperatures obtained are cooler than the Chandra results but roughly consistent with the ASCA ones.

# Chapter 7

## A study of the galaxy cluster A2163

### 7.1 Overview

Abell 2163 is a rich cluster containing at least 119 optically identified galaxies (Struble & Rood 1987). Its distance ( $z=0.201$  (Elbaz, Arnaud & Bohringer 1995)), means that it is one of the few clusters for which it is possible to measure physical properties, such as temperature, out to a good fraction of the virial fraction (i.e.  $r \geq 0.5r_v$  Pratt & Arnaud (2001)). It is a luminous cluster, with an X-ray luminosity in the 2-10 keV range of  $6 \times 10^{45}$  ergs  $s^{-1}$ . Being a hot, massive cluster, Abell 2163 is of interest in the context of formation on structure in the universe. The velocity dispersion of the cluster galaxies is  $1680 \text{ kms}^{-1}$  (Markevitch, Mushotzky, Inoue, Yamashita, Furuzawa & Tawara 1996a)

### 7.2 Introduction

Abell 2163 is one of the hottest clusters known with an average X-ray temperature measured to be  $14.9 \pm_{0.8}^{0.9}$  keV through a combination of Ginga and ROSAT PSPC data (Elbaz et al. 1995). More recently this estimate has come down slightly to  $11.5 \pm 1.5$  keV from ASCA data and to  $12.3 \pm_{1.1}^{1.3}$  with Chandra (Markevitch & Vikhlinin 2001). The tem-

perature from the XMM-Newton analysis performed by Pratt & Arnaud (2001) is 14.0 keV. Pratt et al also produced a temperature profile from the XMM-Newton data which suggests that the temperature increases slightly with radius. This is in contrast with earlier results from Chandra and ASCA (Markevitch & Vikhlinin 2001) which suggest the temperature falls off with radius. Abell 2163 is considered to be a non cooling flow cluster.

Abell 2163 is very massive with a gas mass, as determined from Ginga and ROSAT data, of  $M_{gas}(r \leq 4.6\text{Mpc}) = 1.43 \pm 0.05 \times 10^{15}M_{\odot}$  (Elbaz et al. 1995). The total cluster mass from XMM-Newton (Pratt & Arnaud 2001) is  $M(r \leq 2.2\text{Mpc}) = 2.8 - 3.0 \times 10^{15}M_{\odot}$ . The mass distribution of the cluster (Markevitch, Mushotzky, Inoue, Yamashita, Furuzawa & Tawara 1996b) suggests that Abell 2163 does not have a significant amount of sub-clustering, but the high value of  $\beta_T$  found for the cluster suggests that the cluster is not fully relaxed. More recently (Markevitch & Vikhlinin 2001) has suggested that the cluster may have undergone a merger, which would help to explain its complex morphology.

This chapter presents spectral and spatial results from an analysis of XMM-Newton EPIC data for Abell 2163. The aim of the spectral analysis is to try to determine which temperature profile is correct and also to investigate the variation in abundance across the cluster. The spatial analysis was undertaken to investigate the extent of the cluster emission as well as to investigate the cluster mass distribution. Due to the distance of the cluster it is expected that profiles will be achievable out to larger radii than is possible for nearer clusters.

### 7.3 Observation and data reduction

Abell 2163 was observed several times by XMM-Newton as part of the Guaranteed Time program of observations. The observation detailed here was of the central region of the cluster and was taken on 28th August 2000. The prime focus for this observation was the

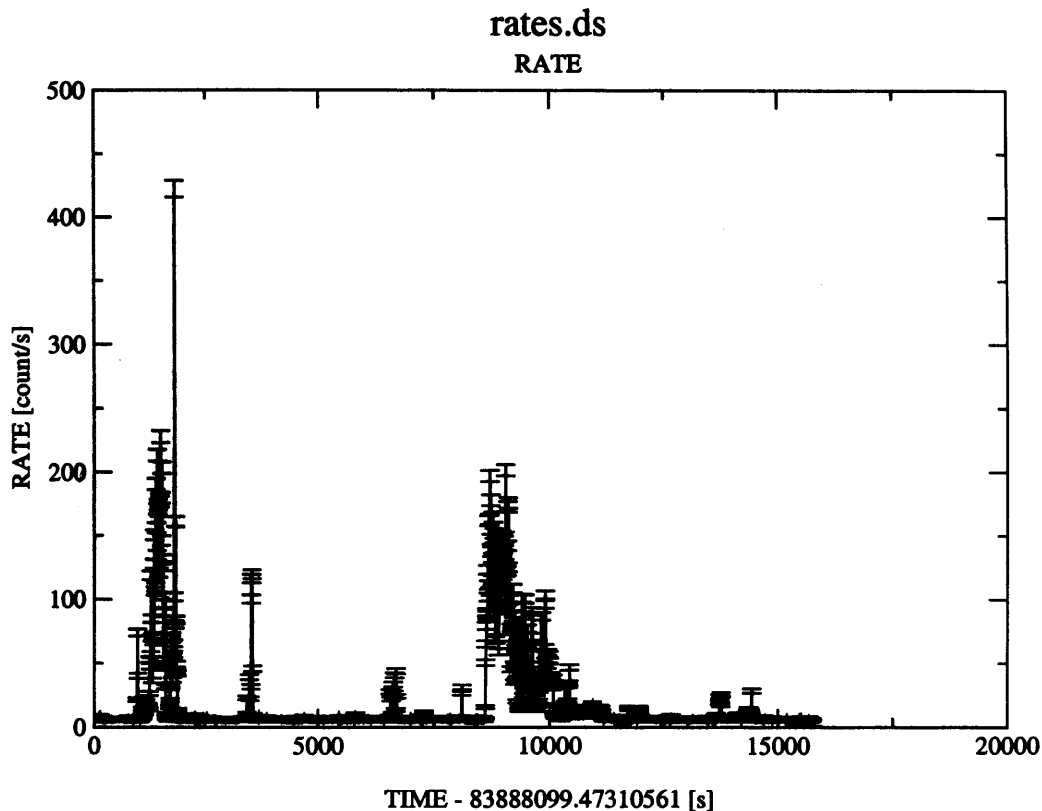


FIGURE 7.1. Un-cut light-curve of Abell 2163

The MOS1 light-curve of Abell 2163 before filtering to remove flares. This shows that the light-curve increases by several hundred counts during flare events with the normal count rate level being of order tens of counts

PN instrument. The lightcurve of the observation was produced in order to look for flares in the soft proton background. The resulting raw lightcurve is shown in figure 7.1. This figure shows that there are several flares in this observation and so the lightcurve was cut as appropriate in order to remove them. After the cuts the exposure times were 15591 seconds for MOS1, 15363 seconds for MOS2 and 10764 seconds for the PN. The cuts make a significant difference in the quality of images and spectra than can be produced so all future work has been undertaken using the filtered lightcurves.

The data reduction was undertaken using the standard XMM-Newton software de-

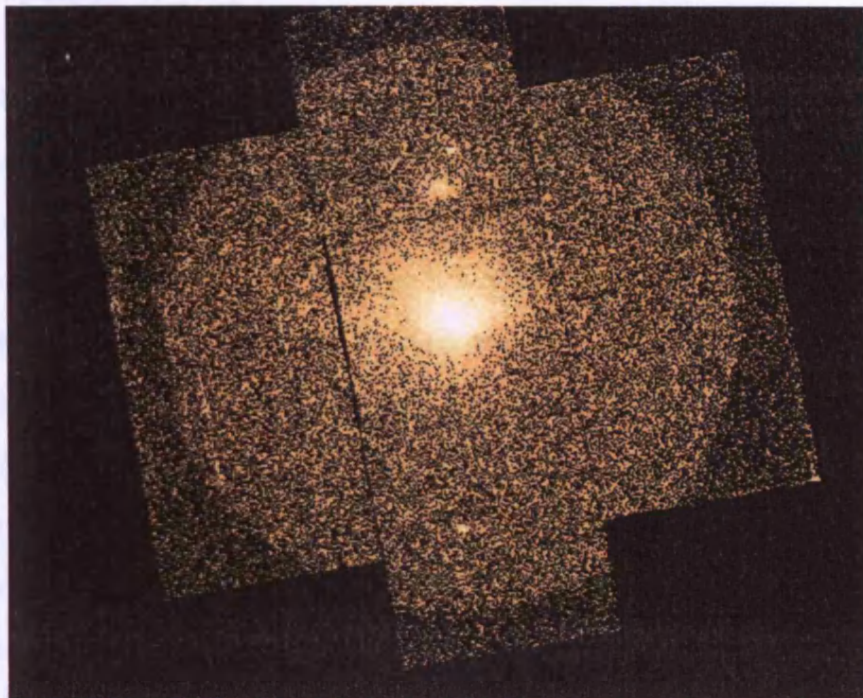


FIGURE 7.2. Image of Abell 2163

An image of Abell 2163 in the 0.3-10 keV band. The image was binned so that there are 600 pixels in both the x and y directions. This corresponds to 20 binned pixels per arcminute. The image is on the MOS1 detector and is shown in image co-ordinates and with a logarithmic scaling. The cluster is centred on the central chip and is clearly visible as an extended source. There are two bright point sources in the image which are removed when spectral fits are undertaken

tailed in earlier chapters in order to produce images and spectra, as well as the lightcurves discussed above. The data was taken in the range 0.3-10 keV as in the other chapters.

An image of the cluster on the MOS1 detector is shown in figure 7.2. This image shows that the cluster emission is extended and roughly circular, with a slight asymmetry along the horizontal. The brightest point of the cluster emission is in the centre of the cluster with the X-ray centre corresponding to RA 16:15:42.781, dec -06:07:24.02(J2000). This differs from the ROSAT determined X-ray centre of RA 16:15:46, dec -06:08:55(J2000).

## 7.4 Spatial Analysis

The cluster surface brightness profile was extracted from the image and then fitted in qdp as before in order to fit a King profile to the data. From this fit the values of the central surface brightness,  $S_0$ , the slope index  $\beta$  and the core radius  $r_c$  can be determined. One of the profiles obtained is shown in figure 7.3. This profile shows that the emission falls off steadily once the core radius has been exceeded ( $r_c = 0.75 \pm 0.05$  arcmin which is equivalent to  $0.263 \pm 0.018$  Mpc). The core radius from the ROSAT data (Pownall 1997) was  $0.457 \pm 0.05$  Mpc which is about double the current measurement. For Einstein data White et al. (1993) find the core radius was 0.7 Mpc. The plot is curtailed at 10 arcmin, which corresponds to 3.51 Mpc. This radius is far enough out that most of the cluster emission should have fallen off towards levels that are not significantly detectable. There is also quite a large uncertainty in the fit at large radii and the statistics are much poorer than in the cluster centre.

The value for the slope ( $0.5 - (3\beta)$ ) for this cluster is 1.144 which corresponds to a  $\beta$  of  $0.55 \pm 0.02$ . This compares to a value of  $\beta$  from ASCA of 0.66 (Markevitch 1996) and  $0.69 \pm 0.04$  for ROSAT data (Pownall 1997). Both of these values are larger than our estimate, which also has a smaller core radius than previous work. The spectrally determined value of  $\beta$  for this cluster is  $0.85 \pm 0.08$ , which is within errors of the ROSAT spectral value, but is still significantly larger than the value determined here.

### 7.4.1 Comparison between the $\beta$ profile and the NFW profile

As an alternative to the King model the NFW profile was fitted to the surface brightness profile of the data. The NFW profile was fitted to the surface brightness profile by integrating the density profile. The values of  $\eta$  and  $r_s$  were then iterated until the best fit values for the real data were found. The best fitting values for the NFW profile were  $\eta = 8.05 \pm 0.05$  and  $r_s = 1.403 \pm 0.01$  Mpc. A plot of the surface brightness profile fits obtained using the NFW profile, the  $\beta$  profile compared to the real data are shown

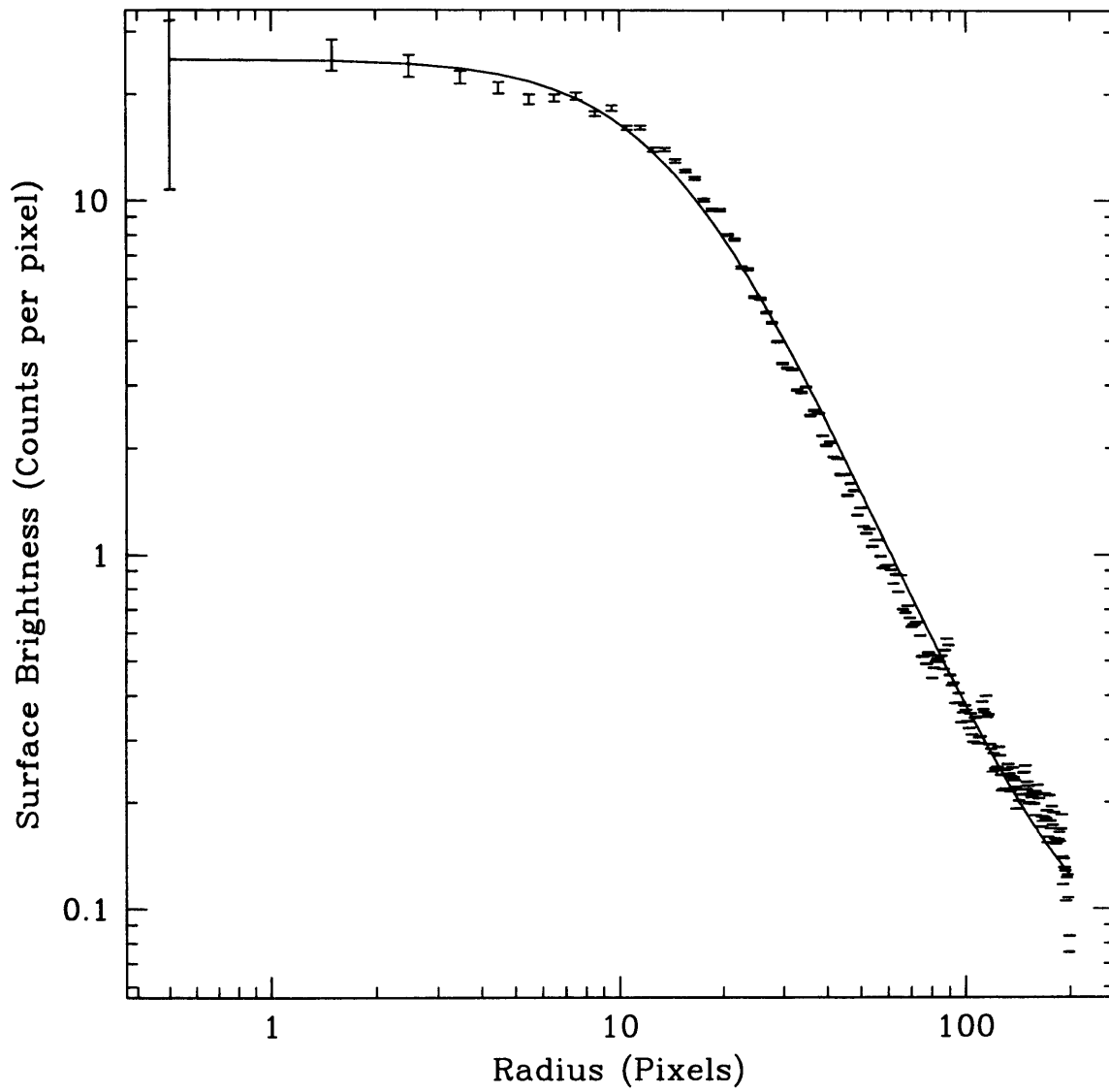


FIGURE 7.3. Surface Brightness profile of Abell 2163  
This profile goes out to a radius of 3.51Mpc

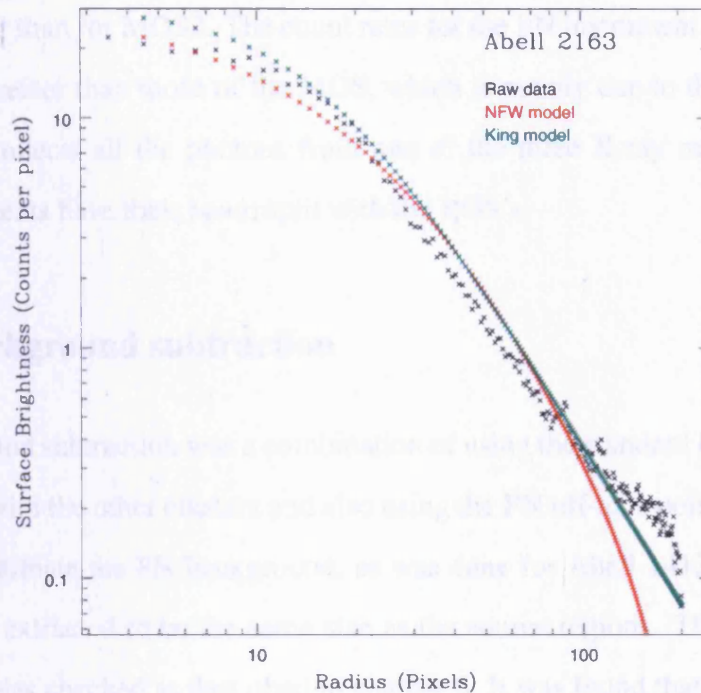


FIGURE 7.4. Comparison of the  $\beta$  and NFW models to the raw surface brightness profile. The plots are normalised to the raw data. The plots use the following values  $\beta = 0.53$ ,  $r_c = 0.165$  Mpc,  $\eta = 8.05$ ,  $r_s = 1.403$  Mpc

in 7.4.

This figure shows that the NFW profile fits the real profile shape better than the  $\beta$  profile especially at small radii. In the most central regions both profiles fit equally well but the  $\beta$  profile fits the data better at larger radii as it drops off more slowly.

## 7.5 Spectral Analysis

The spectra of Abell 2163 were analysed in 8 concentric annuli centred on the brightest point of emission from the cluster. The annuli used, and the background subtracted count rates for the three EPIC detectors are summarised in table 7.1. This table shows that the count rate starts to fall off with increasing radius and so the size of the outermost annuli is increased to ensure that the number of counts in this annuli are statistically significant.

The count rates are fairly similar for the two MOS's, with the rates for MOS1 being slightly higher than for MOS2. The count rates for the PN instrument are approximately 1.5-2 times greater than those of the MOS, which is mainly due to the fact that the PN instruments collect all the photons from one of the three X-ray mirrors whereas the MOS instruments have their beam split with the RGS's.

### 7.5.1 Background subtraction

The background subtraction was a combination of using the standard background files of D.Lumb, as with the other clusters and also using the PN off-axis pointing of this cluster in order to estimate the PN background, as was done for Abell 1413. The background regions were extracted to be the same size as the source regions. The normalisation of background was checked as described in chapter 5. It was found that for MOS1 a 110% background scaling was needed, with 90% needed for MOS2 and 110% for the PN.

### 7.5.2 Spectral Fitting

The cluster was fit with the standard single temperature plasma emission model, with photometric absorption. The column density in this cluster was allowed to vary for the fits since keeping it fixed may have an effect on the temperature as described in (Pratt & Arnaud 2001) and discussed in detail in chapter 5. The variation in  $n_H$  values obtained is shown in figure 7.5. From this figure it is clear that fixing the value of  $n_H$  to the previously determined ROSAT column density value gives a very different result to that found when  $n_H$  is allowed to vary. Therefore in order to avoid under-estimating the temperature of the cluster the parameter must be freed. All fits discussed in later sections are undertaken with  $n_H$  free.

The three datasets were fitted individually in the first instance in order to check for any inconsistencies in the data as well as to normalise the background. The results of this initial fit are shown in table 7.2. The results for all three datasets suggest that the

Table 7.1. The eight annuli over which spectra were taken. The count rates are for the energy range 0.3-10 keV. The detectors MOS1, MOS2 and PN have different count rates, with the PN count rate being much larger than the other two

Region	Inner Radius arcmin	Outer Radius arcmin	Mean Radius Mpc	MOS1 Count Rate $cts^{-1}$	MOS2 Count Rate $cts^{-1}$	PN Count Rate $cts^{-1}$
i	0	0.5	0.0886	$0.21 \pm 0.0037$	$0.18 \pm 0.0035$	$0.34 \pm 0.0057$
ii	0.5	1	0.2658	$0.51 \pm 0.0055$	$0.43 \pm 0.0053$	$0.73 \pm 0.0084$
iii	1	1.5	0.4656	$0.47 \pm 0.0056$	$0.42 \pm 0.0053$	$0.84 \pm 0.0090$
iv	1.5	2	0.6203	$0.36 \pm 0.0049$	$0.32 \pm 0.0047$	$0.62 \pm 0.0079$
v	2	3	0.8861	$0.49 \pm 0.0059$	$0.45 \pm 0.0057$	$0.80 \pm 0.0093$
vi	3	4	1.2405	$0.32 \pm 0.0050$	$0.29 \pm 0.0048$	$0.55 \pm 0.0082$
vii	4	5	1.5950	$0.20 \pm 0.0045$	$0.20 \pm 0.0043$	$0.39 \pm 0.0076$
viii	5	8	2.3038	$0.36 \pm 0.0068$	$0.31 \pm 0.0062$	$0.63 \pm 0.012$

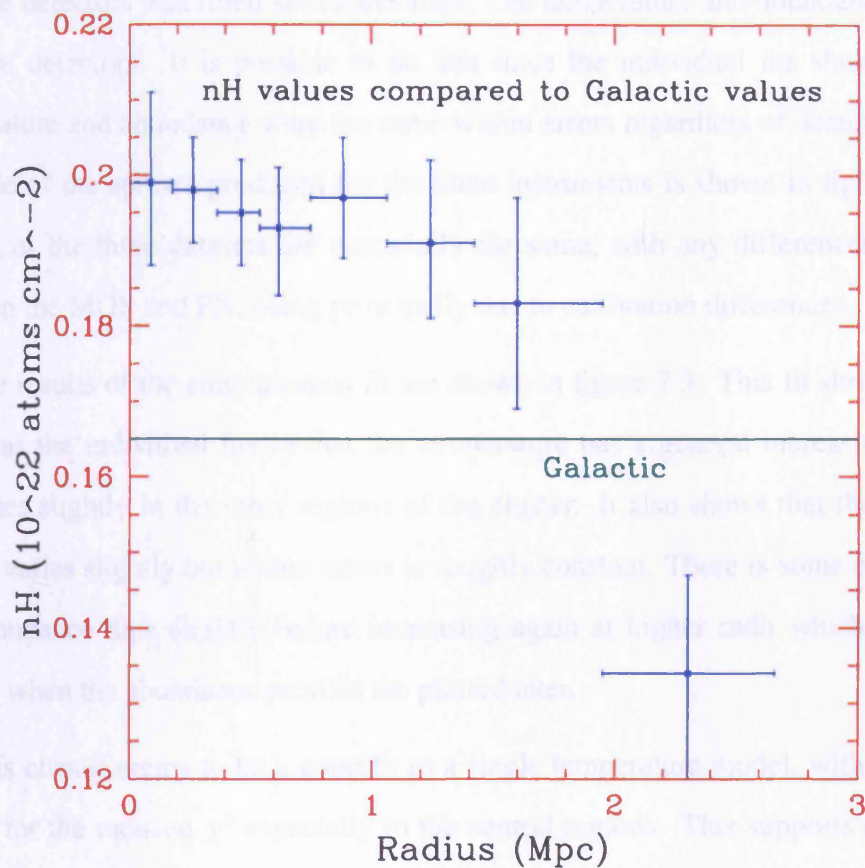


FIGURE 7.5. Freed galactic column density values for simultaneous fit with line of fixed values marked on.

temperature is increasing with radius, although it should be noted that at large radii there is a large error on the values. At large radii the lower count rates increase the uncertainty in the fits and the large outer region means that the temperature is determined over a large area and so is less accurate. The abundance seems fairly constant for the entire cluster but there are large error bars on the fits.

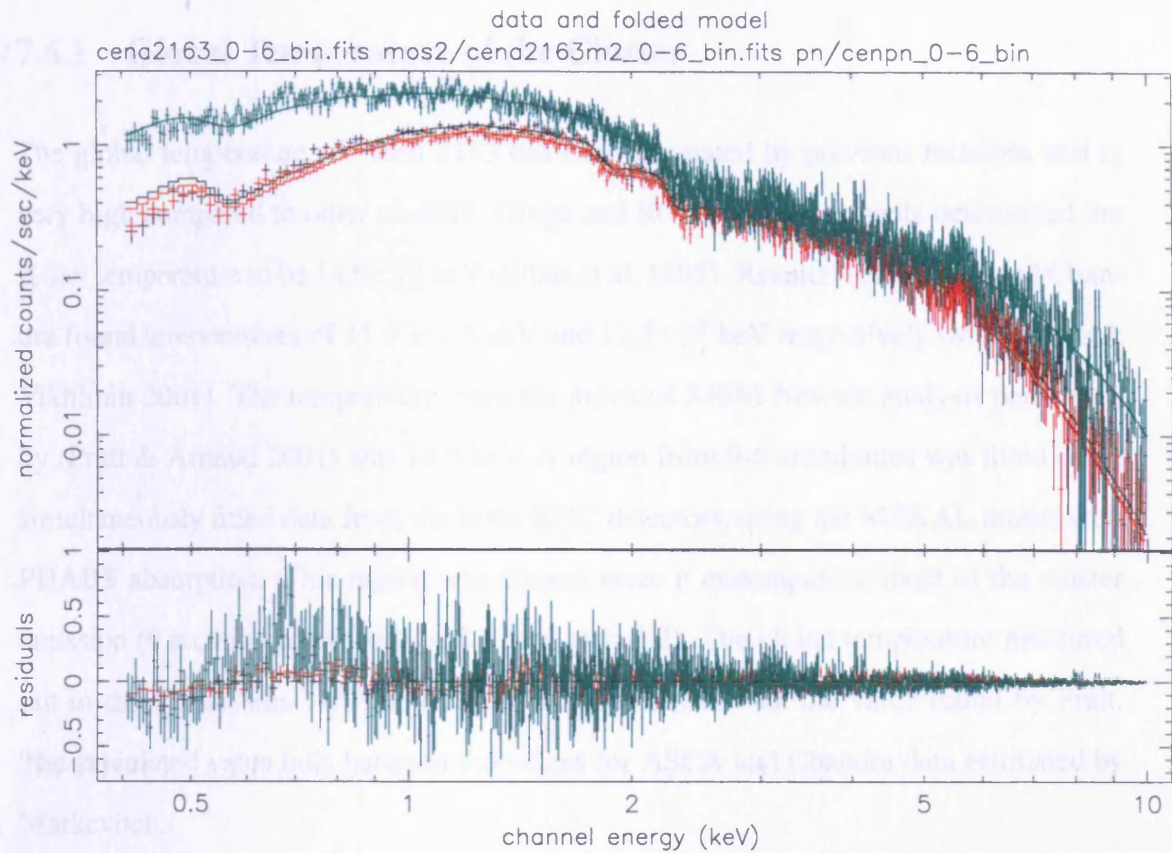
In order to reduce the uncertainties and improve the statistics of the fit the data from all three detectors was fitted simultaneously. The temperature and abundance were tied between detectors. It is possible to do this since the individual fits showed that the temperature and abundance were the same within errors regardless of detector used. An example of the spectra produced for the three instruments is shown in figure 7.6. The spectra of the three datasets are essentially the same, with any differences, especially between the MOS and PN, being principally due to calibration differences.

The results of the simultaneous fit are shown in figure 7.3. This fit shows the same trends as the individual fits in that the temperature has a general increasing trend but oscillates slightly in the inner regions of the cluster. It also shows that the abundance profile varies slightly but within errors is roughly constant. There is some evidence that the abundance dips slightly before increasing again at higher radii which is explored further when the abundance profiles are plotted later.

This cluster seems to be a good fit to a single temperature model, with fairly small values for the reduced  $\chi^2$  especially in the central regions. This supports the previous analyses which classified the cluster as a non-cooling flow cluster. Cooling flow model fits to this cluster result in a much larger value of reduced  $\chi^2$  than has already been found for the data using single temperature fits.

Table 7.2. Single temperature fits over different regions for the 3 different EPIC detectors fitted separately. Temperature, Abundance and  $\chi^2$  per degree of freedom parameters are shown.

Region	MOS1			MOS2			PN		
	Temperature keV	Abundance Solar	$\chi^2 D.O.F$	Temperature keV	Abundance Solar	$\chi^2 D.O.F$	Temperature keV	Abundance Solar	$\chi^2 D.O.F$
i	$11.66 \pm_{2.38}^{3.60}$	$0.24 \pm_{0.24}^{0.24}$	132/123	$8.91 \pm_{1.63}^{2.61}$	$0.23 \pm_{0.20}^{0.20}$	98/110	$11.23 \pm_{1.97}^{2.85}$	$0.16 \pm_{0.16}^{0.20}$	331/311
ii	$9.62 \pm_{0.99}^{1.11}$	$0.36 \pm_{0.14}^{0.14}$	219/217	$10.85 \pm_{1.54}^{1.93}$	$0.13 \pm_{0.13}^{0.14}$	207/204	$10.28 \pm_{1.17}^{1.34}$	$0.18 \pm_{0.13}^{0.13}$	331/311
iii	$9.97 \pm_{1.19}^{1.51}$	$0.15 \pm_{0.12}^{0.12}$	208/214	$9.93 \pm_{1.23}^{1.60}$	$0.30 \pm_{0.15}^{0.15}$	259/204	$10.11 \pm_{1.07}^{1.25}$	$0.22 \pm_{0.12}^{0.12}$	329/353
iv	$12.08 \pm_{1.79}^{2.76}$	$0.26 \pm_{0.19}^{0.20}$	177/189	$11.52 \pm_{1.92}^{2.6}$	$0.16 \pm_{0.16}^{0.18}$	208/174	$12.87 \pm_{1.95}^{2.08}$	$0 \pm_0^{0.16}$	262/269
v	$11.81 \pm_{1.63}^{2.28}$	$0.08 \pm_{0.08}^{0.15}$	232/235	$12.77 \pm_{2.04}^{2.66}$	$0.28 \pm_{0.18}^{0.18}$	197/225	$10.17 \pm_{1.27}^{1.49}$	$0.16 \pm_{0.10}^{0.10}$	493/470
vi	$12.71 \pm_{2.53}^{3.75}$	$0.31 \pm_{0.24}^{0.26}$	226/200	$14.0 \pm_{3.25}^{5.56}$	$0.38 \pm_{0.31}^{0.30}$	214/185	$10.37 \pm_{1.50}^{1.98}$	$0.29 \pm_{0.18}^{0.20}$	275/280
vii	$18.05 \pm_{6.08}^{12.2}$	$0.14 \pm_{0.14}^{0.41}$	191/173	$15.45 \pm_{4.28}^{8.54}$	$0.50 \pm_{0.41}^{0.52}$	160/165	$10.52 \pm_{2.49}^{3.75}$	$0.15 \pm_{0.15}^{0.25}$	220/240
viii	$36.1 \pm_{15.9}^{39.7}$	$0.34 \pm_{0.34}^{0.77}$	357/296	$45.02 \pm_{22.8}^{55.0}$	$0.45 \pm_{0.45}^{1.16}$	319/261	$11.23 \pm_{2.63}^{3.92}$	$0.03 \pm_{0.03}^{0.26}$	512/485



ies 23-May-20

FIGURE 7.6. Spectrum of Abell 2163 fitted simultaneously for MOS1, MOS2 and PN instruments. The spectrum is from the 0-6 arcmin region

Table 7.3. Simultaneous single temperature fits for 3 EPIC detectors. Temperature, abundance and  $\chi^2$  per degree of freedom are shown.

Region	Temperature	Abundance	$\chi^2 D.O.F$
i	$10.7 \pm_{1.26}^{1.62}$	$0.20 \pm_{0.13}^{0.12}$	396/400
ii	$10.2 \pm_{0.72}^{0.85}$	$0.21 \pm_{0.08}^{0.08}$	769/738
iii	$9.94 \pm_{0.62}^{0.79}$	$0.22 \pm_{0.07}^{0.07}$	900/778
iv	$11.9 \pm_{1.11}^{1.35}$	$0.11 \pm_{0.10}^{0.10}$	730/639
v	$11.1 \pm_{0.91}^{1.05}$	$0.12 \pm_{0.08}^{0.08}$	984/826
vi	$11.7 \pm_{1.30}^{1.65}$	$0.32 \pm_{0.13}^{0.13}$	779/672
vii	$13.0 \pm_{2.15}^{3.18}$	$0.18 \pm_{0.18}^{0.19}$	595/575
viii	$22.3 \pm_{5.22}^{7.75}$	$0.09 \pm_{0.09}^{0.27}$	1208/1037

## 7.6 Discussion

### 7.6.1 Global Temperature of the Cluster

The global temperature of Abell 2163 has been estimated by previous missions and is very high compared to other clusters. Ginga and ROSAT measurements determined the X-ray temperature to be  $14.9 \pm_{0.8}^{0.9}$  keV (Elbaz et al. 1995). Results from ASCA and Chandra found temperatures of  $11.5 \pm 1.5$  keV and  $12.3 \pm_{1.1}^{1.3}$  keV respectively (Markevitch & Vikhlinin 2001). The temperature from the previous XMM-Newton analysis performed by (Pratt & Arnaud 2001) was 14.0 keV. A region from 0-6 arcminutes was fitted using simultaneously fitted data from the three EPIC detectors, using the MEKAL model with PHABS absorption. This region was chosen since it encompassed most of the cluster emission (6 arcmin corresponds to 2.1 Mpc at  $z=0.2$ ). The global temperature measured out to this radius was  $11.98 \pm 1.2$  keV which is lower than the value found by Pratt. The calculated value falls between the values for ASCA and Chandra data estimated by Markevitch.

### 7.6.2 Temperature profiles

A temperature profile was derived from the simultaneous spectral fits described in the previous section as this gave the smallest amount of uncertainty to the fit. The derived temperature profile for Abell 2163 is shown in figure 7.7. The profile shows that the temperature starts off at 10.7 keV and stays fairly constant for the first three annuli before increasing in the outer annuli.

This is consistent with the ASCA and Chandra profiles (Markevitch & Vikhlinin 2001) as shown in figure 7.8 which is taken from the paper. This figure shows the temperature out to 6 arcminutes is consistent with our data. They see a temperature drop by 8 arcminutes, but like the current results there is a large uncertainty in the values by this radius. The ASCA results from (White 2000) and the SAX results, originally from

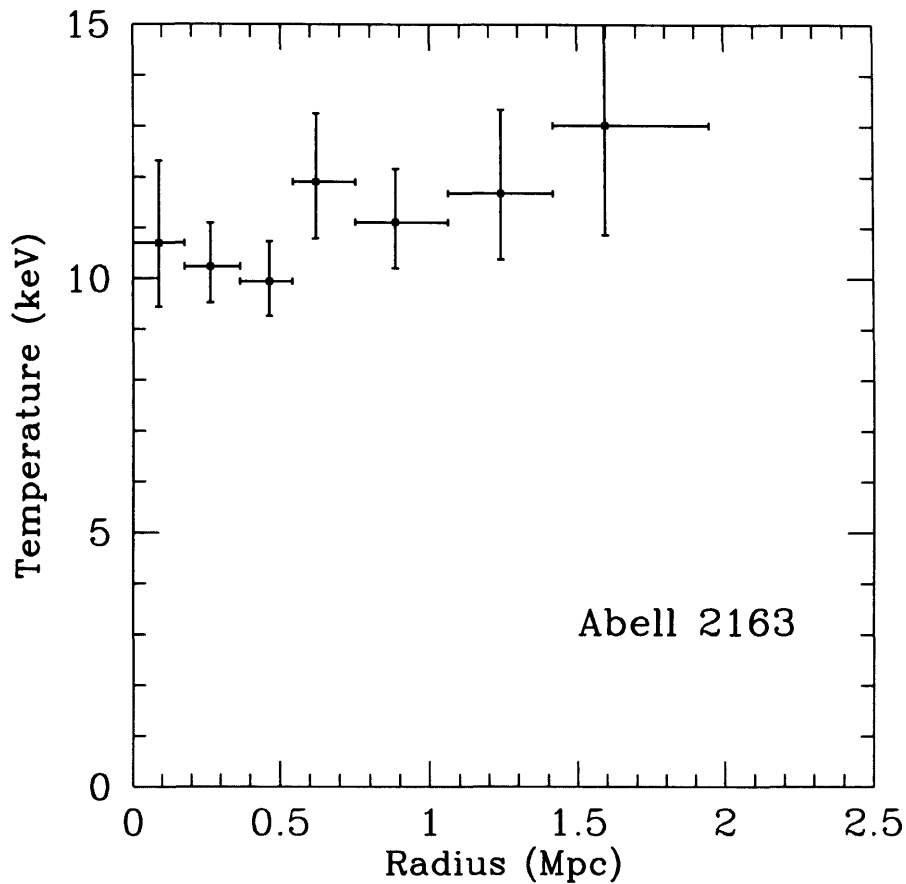


FIGURE 7.7. Temperature profile produced from simultaneous fits for the 3 EPIC detectors

(Irwin & Bregman 2000) also show a rise in temperature at this radius, but again have large errorbars on the fit. The XMM-Newton data analysed by (Pratt & Arnaud 2001) show a temperature drop by 8 arcminutes similar to that of seen in the Markevitch ASCA and Chandra data. At the present time it seems evident from all analyses that the cluster has a large, roughly constant temperature in the central regions, with slight increase with radius seen in all of the results. It is inconclusive as to whether this temperature increase is sustained out to larger radii or whether in fact there is a temperature fall off, as the uncertainties are too large in all cases to rule either possibility out completely.

The temperature increases after the central annulus which could correspond to a shock (Markevitch 1996, Markevitch & Vikhlinin 2001). Here the shock heated gas

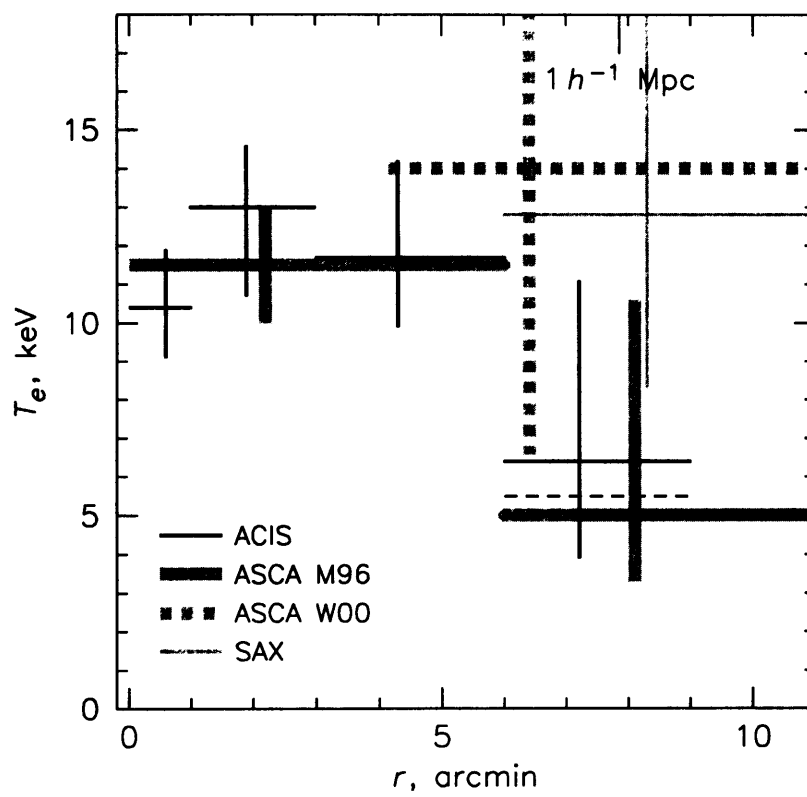


FIGURE 7.8. Temperature profile from (Markevitch & Vikhlinin 2001) for Chandra, ASCA and SAX data

is at a higher temperature than the cooler, denser sub-cluster which is seen in the centre. The temperature profile also shows signs of fluctuation and the large error bars also support Markevitch's claim that the cluster morphology is complex.

### 7.6.3 Abundance Profiles

The metallicity variation across the cluster is another important probe as it gives an indication into the regions where there has been star formation and also in a cluster which is thought to have undergone a merger, such as Abell 2163 it can provide an indication on whether the cluster gas has been disturbed or mixed by the merger. Also since there is thought to be a shock region in the cluster it is interesting to see if this has produced a region of star formation which would then result in an increase in the local metallicity. As discussed in the previous chapter, however the star formation timescale is much longer than the merger timescale meaning that this won't be directly evident from the data. The profile was produced from the simultaneous fit data and is shown in figure 7.9

The profile shows that there is no overall trend of a decrease in metallicity with radius as has been seen in other clusters (such as Abell 1413). The central abundance is 0.2 solar, and the abundance stays approximately constant for the next two annuli before it seems to drop slightly for 2 annular bins after which it increases slightly again before beginning to fall off again at large radii. The small scale variation is not significant given the large uncertainties on the data points.

The overall trend over the cluster is that the abundance remains approximately constant and we do not see evidence of an strong abundance gradient in the data. However the errorbars on the data are large and so it is difficult to draw any strong conclusions from the data. From the shape of the profile it seems that the metals in the cluster are reasonably well mixed on a global scale and there is not strong evidence of a metallicity concentration in the centre where most of the star formation is likely to have occurred. This suggests that there may have been a significant amount of mixing in the cluster in

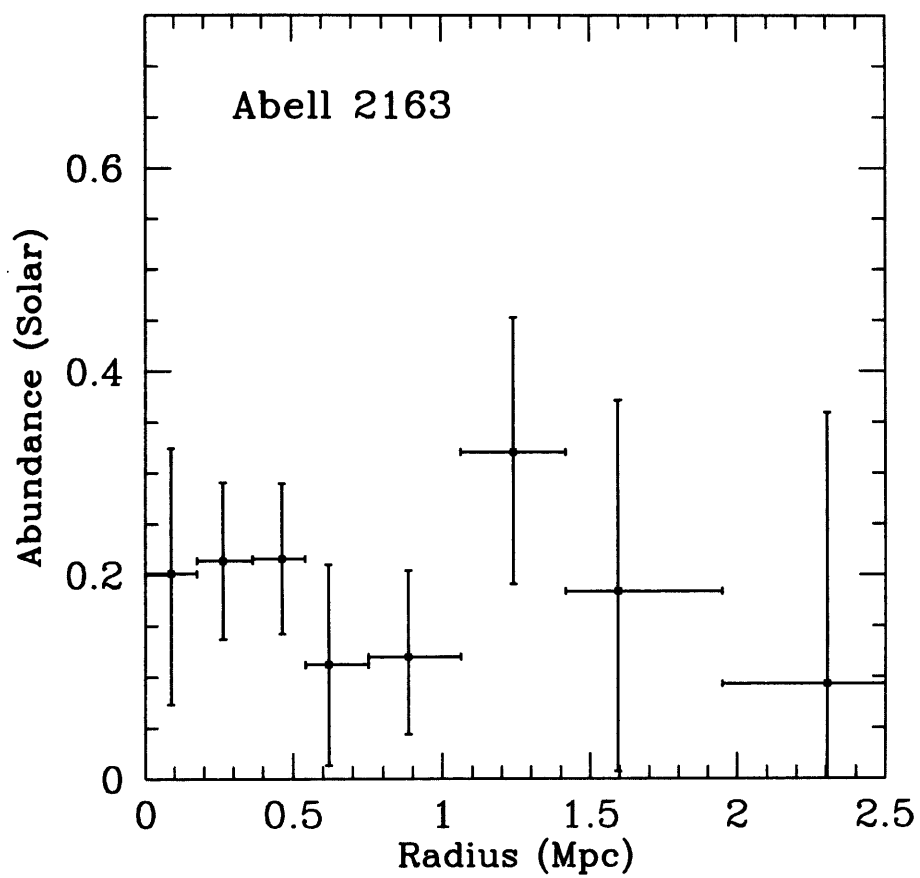


FIGURE 7.9. Abundance profile of Abell 2163. This profile was produced from a simultaneous fit to the data from the 3 EPIC detectors.

order to distribute the metals out to large radii. Since the cluster is not particularly relaxed it is also possible that mergers have produced regions of star formation other than in the centre of the cluster, which would also result in the amounts of metals seen further out in the cluster.

#### 7.6.4 Gas and Gravitational Mass Estimates

An estimate of gas mass was made using the integral of the density profile of the  $\beta$  model, as described previously. The gas mass in the cluster was found to be  $M_{\text{gas}} = 3.44 \pm 0.95 \times 10^{14} M_{\odot}$  out to 2 Mpc. For Einstein data (White et al. 1993), the gas mass calculated was  $8.43 \pm 0.89 \times 10^{14} M_{\odot}$  out to 3.24 Mpc. At this radius the calculated gas mass is  $M_{\text{gas}} = 6.98 \pm 1.91 \times 10^{14} M_{\odot}$ , which is a bit lower than the White estimate but is consistent within errors. The variation of gas mass over the radius of the cluster is shown in figure 7.10. This shows that the gas mass increases steadily with radius. The profile is very steep and does not show evidence of leveling off at high radius. The cluster has a fairly low spatially determined  $\beta$  from this analysis, which accounts for the steepness of the profile.

The gas mass can also be estimated using the NFW density profile in place of the  $\beta$  profile. This was estimated at the same radii as in the previous sections for comparison. The gas mass at 2 Mpc was  $3.36 \pm 0.68 \times 10^{14} M_{\odot}$  and  $6.89 \pm 1.39 \times 10^{14} M_{\odot}$  at 3.24 Mpc. This is still less than the Einstein value (White 2000) and close to the  $\beta$  model values. The differences in the fits mainly come from the slightly different shapes of the two profiles and the uncertainties in the fit.

The gravitational mass was also calculated, with the temperature variation calculated using a least square fit to the gradient of the temperature profile. The density values were found by using the King density profile with the appropriate values for  $\beta$  and  $r_c$ . The gravitational mass of Abell 2163 was calculated as  $1.25 \pm 0.65 \times 10^{15} M_{\odot}$  at 2 Mpc and  $2.663 \pm 2.27 \times 10^{15} M_{\odot}$  at 3.24 Mpc. The value at 3.24 Mpc for the White, Einstein data

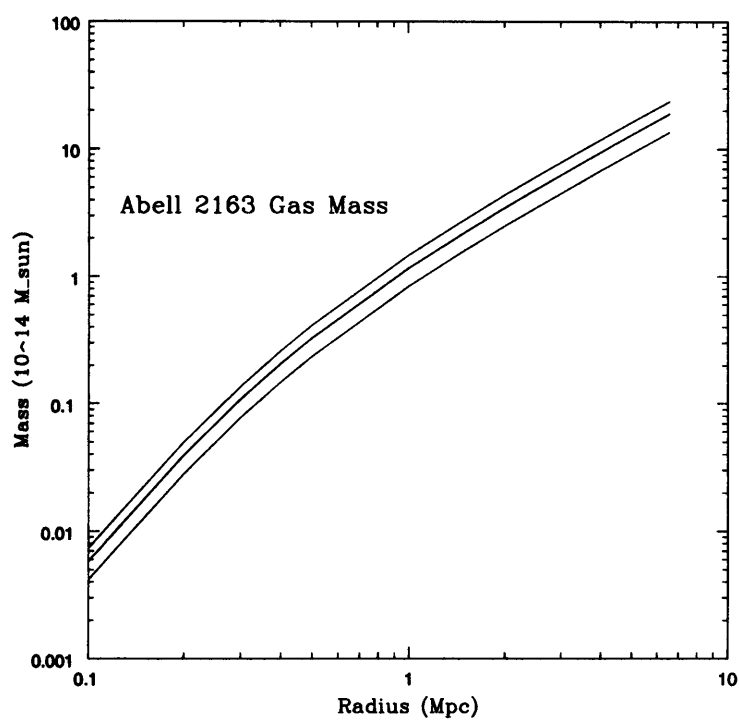


FIGURE 7.10. Plot of the variation in gas mass with radius in A2163 (black line) with associated errors (blue line) The plot is extrapolated out to  $r_{500}$  which for this cluster is  $6.6 \pm 0.2$  Mpc

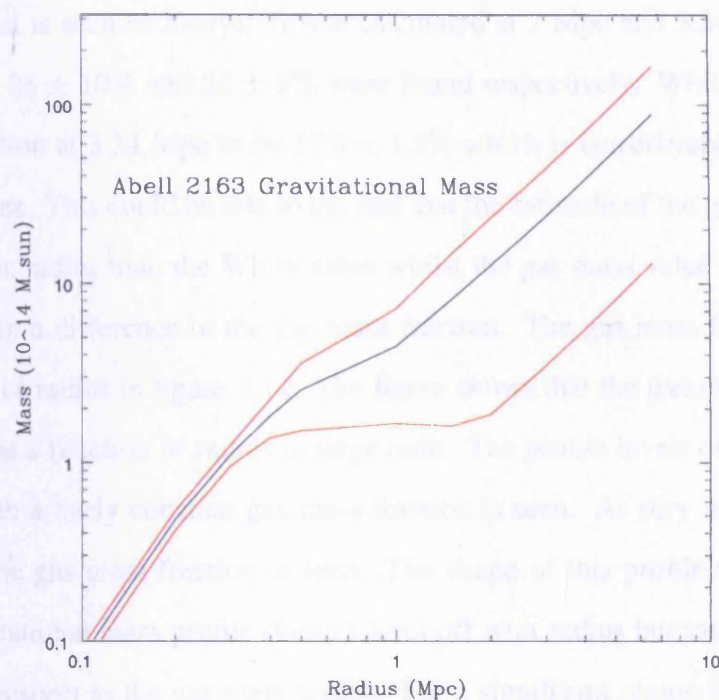


FIGURE 7.11. Plot of the variation in gravitational mass with radius in the cluster (black line) with associated errors (red line). This is extrapolated out to  $r_{500}$

is  $4.72 \times 10^{15} M_{\odot}$  which is about a factor of two larger than the value calculated here. The errorbars on the data are quite large because of the large uncertainty on the temperature and temperature gradient at large radius. As can be seen from the temperature profile the gradient is quite shallow and due to the large uncertainty in temperature at this radius there is a correspondingly large uncertainty on the gradient and thus the mass.

The value of  $r_{500}$  for the cluster was also calculated using the gravitational masses and the critical density of the universe. For this cluster the calculated value of  $r_{500} = 6.6 \pm 0.1$  Mpc. If these estimates are used to calculate the gas mass and gravitational mass at  $r_{500}$  values of  $M_{\text{gas}} = 18.94 \pm 5.11 \times 10^{14} M_{\odot}$ , and  $M_{\text{grav}} = 8.79 \pm 7.50 \times 10^{15} M_{\odot}$  are obtained for each respectively. The large errors on these values are mainly from the error on the temperature gradient. The value of  $r_{200}$  was estimated to be very large at  $14.2 \pm 0.5$  Mpc.

The gas mass fraction of the cluster,  $\frac{M_{\text{gas}}}{M_{\text{grav}}}$ , gives an estimate of how much of the cluster material is seen in X-rays. It was calculated at 2 Mpc and 3.24 Mpc as before, and values of  $28 \pm 10\%$  and  $26 \pm 9\%$  were found respectively. White et al found the gas mass fraction at 3.24 Mpc to be  $17.8 \pm 1.9\%$  which is considerably lower than the current estimate. This could be due to the fact that the estimate of the gravitational mass is lower at this radius than the White value whilst the gas mass value is similar as this would result in a difference in the gas mass fraction. The gas mass fraction is plotted as a function of radius in figure 7.12. The figure shows that the gas mass fraction does not increase as a function of radius at large radii. The profile levels off at about 1 Mpc and henceforth a fairly constant gas mass fraction is seen. At very large radii a slight decrease in the gas mass fraction is seen. The shape of this profile is due to the fact that the gravitational mass profile doesn't level off with radius but instead gets slightly steeper with respect to the gas mass profile. For a significant region the increase is the same for both masses resulting in the constant value of the mass fraction.

### 7.6.5 Iron Mass Estimate

The iron mass of the cluster is estimated as described previously. This is of interest for this cluster in particular because of the fact that it has undergone a recent merger. Since the abundance profile shows little global variation with radius the iron abundance was set at a constant value of 0.21 solar was taken to be the abundance. This is different from the other cases where the abundance varied and resulted in a change in the rate the mass profile increased.

The iron mass at 2 Mpc and 3.24 Mpc (the radii used for the gas and gravitational masses in the previous section) are  $16.90 \pm 13.35 \times 10^8 M_{\odot}$  and  $34.16 \pm 26.99 \times 10^8 M_{\odot}$  respectively. These are approximately a factor of  $2 - 2.5 \times 10^5$  times smaller than the gas masses and a factor of approximately  $5 - 8 \times 10^5$  times smaller than the gravitational mass. The iron mass profile is shown in figure 7.13. As can be seen the profile increases in the same way as the gas mass profile, as is expected since the abundance is constant

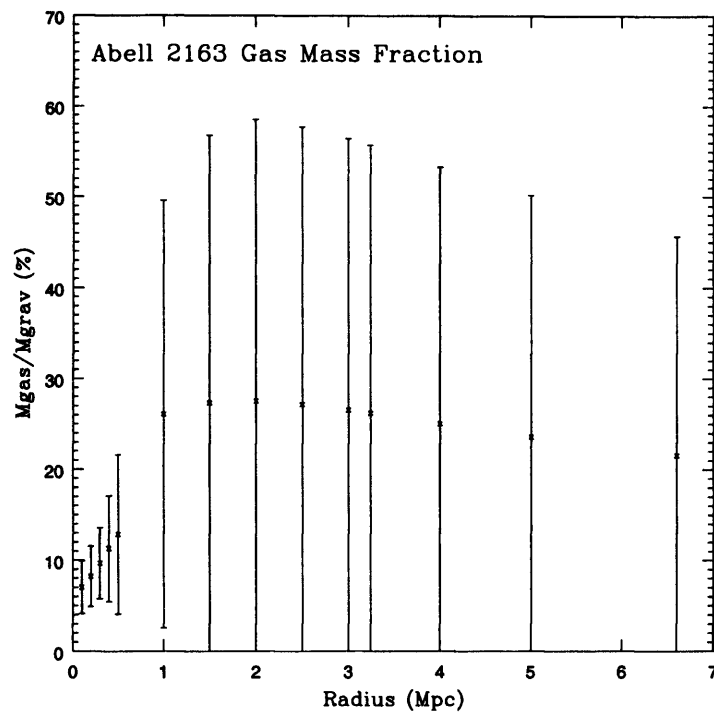


FIGURE 7.12. Plot of the variation in gas mass fraction with radius in the cluster. The profile initially increases with radius before leveling off.

with radius and  $\beta$  increases towards zero at large radii, which would tend to level off the profile at large radius. Therefore it is difficult to tell whether the metals are centrally concentrated or fairly evenly distributed through the cluster. The large uncertainties on the abundance profile exacerbate this problem. As with the iron mass profile and the iron mass profile suggests that either the cluster gas has undergone mixing since the merger such that the iron rich gas has mixed with primordial gas, or that star formation may have occurred further out in the cluster possibly as a result of a star-forming compression of the gas. Either scenario could explain why the abundance profile and thus the iron mass does

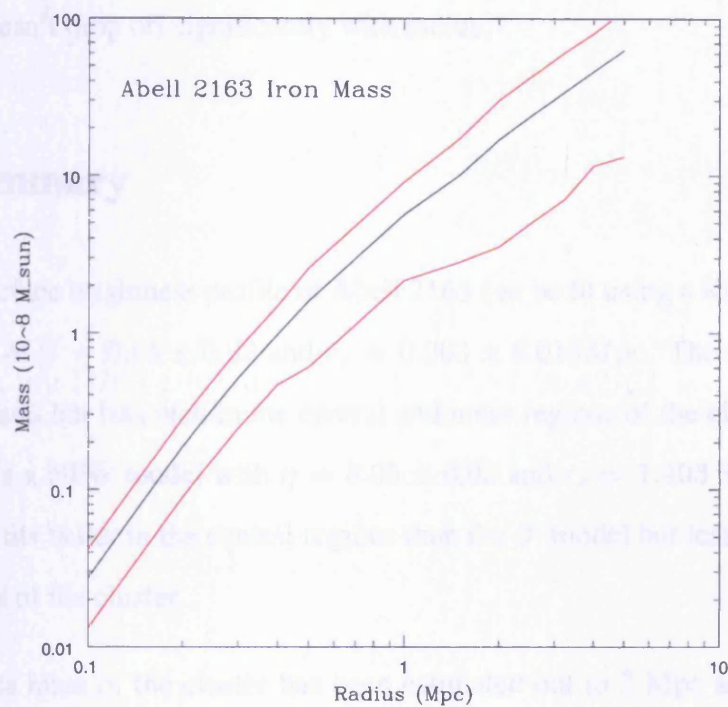


FIGURE 7.13. Iron mass profile (black) with associated errors (red). The profile shows an increase in mass with radius.

with radius and doesn't decrease towards zero at large radii which would tend to level off the profile at large radius. Therefore it is difficult to tell whether the metals are centrally concentrated or fairly evenly distributed through the cluster. The large uncertainties on the abundance profiles exacerbate this problem. As with the abundance profile itself the iron mass profile suggests that either the cluster gas has undergone mixing after the merger such that the iron rich gas has mixed with primordial gas, or that star formation may have occurred further out in the cluster possibly as a result of a shock front compressing the gas. Either scenario could explain why the abundance profile and thus the iron mass doesn't drop off significantly with radius.

## 7.7 Summary

- The surface brightness profile of Abell 2163 can be fit using a King  $\beta$  model with values of  $\beta = 0.55 \pm 0.02$  and  $r_c = 0.263 \pm 0.018 \text{ Mpc}$ . The model fits well at large radii but less well in the central and inner regions of the cluster. The profile also fits a NFW model with  $\eta = 8.05 \pm 0.05$  and  $r_s = 1.403 \pm 0.01 \text{ Mpc}$ . This model fits better in the central regions than the  $\beta$  model but less well in the outer regions of the cluster.
- The gas mass of the cluster has been estimated out to 2 Mpc as  $M_{\text{gas}} = 3.44 \pm 0.946 \times 10^{14} M_{\odot}$  and the gravitational mass out to the same radius as being  $8.27 \pm 6.54 \times 10^{14} M_{\odot}$ . This results in a gas mass fraction of  $26 \pm 9\%$ . The gas mass estimated using the NFW model gives a lower value of  $3.36 \pm 0.68 \times 10^{14} M_{\odot}$  at 2 Mpc.
- The global cluster temperature has been estimated as  $11.98 \pm 1.2 \text{ keV}$  which is between several other estimates made using earlier satellites.
- The spectral fits to the data support previous studies in that they give no evidence that the cluster contains a cooling flow. The fits show a gradual temperature in-

crease with radius and a slightly lower central temperature which is possible a sub-cluster remnant sitting at the centre of a shock.

- There is evidence that the cluster metallicity varies on a local scale within the cluster, but there is no evidence of a global abundance decrease with radius. The uncertainties on the metallicity estimates do however remain large.
- The iron mass of the cluster at 2 Mpc  $16.90 \pm 13.35 \times 10^8 M_{\odot}$ . The iron mass does not level off at large radii and so does not appear to be centrally concentrated, but there is a large amount of uncertainty in the data at these radii and so it is difficult to determine the iron mass accurately at large radii.
- The cluster temperature profile shows that the cluster temperature varies locally with radius. This could be a result of a previous merger, which would have resulted in shock heated gas. The temperature is also seen to increase with radius on a global scale. This agrees with some earlier results which see a temperature rise at large radii, but other results contradict this. Due to the uncertainties on all the fits it is not possible to resolve this issue conclusively at this time.

## **Chapter 8**

# **How Self Similar are Clusters of Galaxies?**

### **8.1 Overview**

One of the assumptions that is often made about clusters of galaxies is that they are self similar and can therefore all be modeled in the same manner. For example they are often approximated as isothermal, self gravitating spheres, which does not take into account the temperature gradients seen in many clusters. Also assumptions are made about the self-similarity of the mass and surface brightness distributions. Approximations are also made based on the dynamical state of the cluster, whereby clusters are assumed to be relaxed, virialised and in hydrostatic equilibrium. In this chapter the 3 clusters observed with XMM-Newton are compared in order to investigate whether these assumptions are valid.

## 8.2 Comparisons of Physical Properties between the three clusters

### 8.2.1 Temperature Profiles

The temperature profiles of clusters are used to investigate the morphology of clusters and enable estimates of cluster mass to be made. Therefore in order to explain the differences between the three clusters, the differences in the three observed temperature profiles must be considered. Figure 8.1 shows the temperature profiles of the three clusters both in Mpc and as a fraction of  $r_{500}$ . Abell 665 and Abell 1413 have been profiled out to a significant fraction of  $r_{500}$  whereas Abell 2163 is only observed out to approximately  $0.4r_{500}$ .

From the figure it is clear that Abell 665 and Abell 1413 have similar temperature profiles despite having apparently very different morphologies. Abell 1413 is defined as a cooling flow cluster with the spectral results provide a marginal detection of one. Abell 665, however has been classified as a non cooling flow cluster which has undergone a merger between two very differently sized sub-cluster fragments which have now passed through each other (Markevitch & Vikhlinin 2001). The similarity of the two temperature profiles suggests that the clusters may have evolved in a similar manner and have a similar mass.

The temperature profile of Abell 2163 is very different as it has a high temperature which increases with radius. This cluster has also undergone a merger but appears less relaxed and has a more complex morphology than Abell 665. This suggests the merger components of Abell 2163 were more equal in size which resulted in more disruption to the cluster. The cluster seems to be almost isothermal in the central regions but then a temperature increase is seen in outer radii, which is possibly due to shock heating of the intra-cluster gas. Abell 665 is also thought to contain a shock, but seeming more centrally concentrated than in Abell 2163. The high temperature of the gas seen throughout the

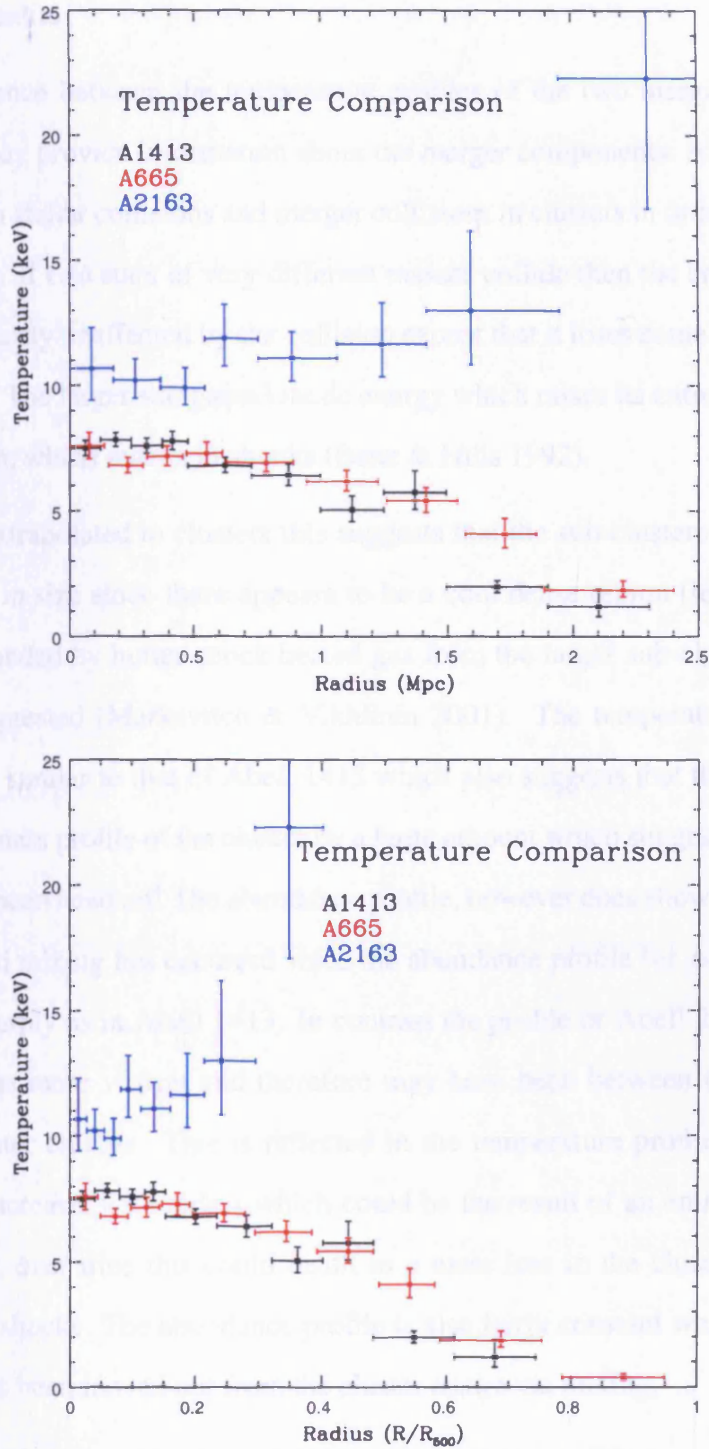


FIGURE 8.1. Temperature profile comparison between the three clusters studied. This shows how the profiles for A665 and A1413 are very similar but A2163 is vastly different. The top plot gives the radial increment in Mpc with the lower plot giving the increment as a fraction of  $r_{500}$

Abell 2163 profile also implies the cluster is massive since the gas cannot escape from the cluster potential.

The difference between the temperature profiles of the two merging clusters is of interest as it may provide information about the merger components. An analogy can be drawn between stellar collisions and merger collisions in clusters in order to help explain this difference. If two stars of very different masses collide then the smaller, and hence denser star is fairly unaffected by the collision except that it loses some kinetic energy to the larger star. The larger star gains kinetic energy which raises its entropy causing some tidal disruption, which results in shocks (Benz & Hills 1992).

If this is extrapolated to clusters this suggests that the sub-clusters in Abell 665 are very different in size since there appears to be a cool dense region (ie the smaller sub-cluster) surrounded by hotter shock heated gas from the larger sub-cluster, as has been previously suggested (Markevitch & Vikhlinin 2001). The temperature profile of the cluster is very similar to that of Abell 1413 which also suggests that the merger has not disrupted the mass profile of the cluster by a large amount which suggests that the merger may not have been head on. The abundance profile, however does show that some energy dissipation and mixing has occurred since the abundance profile for Abell 665 does not drop off as sharply as in Abell 1413. In contrast the profile of Abell 2163 suggests that the merger was more violent and therefore may have been between two more equally sized sub-cluster clumps. This is reflected in the temperature profile, which shows a temperature increase, with radius which could be the result of an entropy increase due to the merger, over time this could result in a mass loss in the cluster as this energy dissipates via shocks. The abundance profile is also fairly constant which suggests a lot of material has been moved out from the cluster centre via mixing.

Using the global temperatures for the clusters it is possible to work out the virial radii for the three clusters; ( $R_{vir} \sim 2.49 \pm 0.05$  Mpc for A1413,  $R_{vir} \sim 2.07 \pm 0.06$  for A665 and  $R_{vir} \sim 2.99 \pm 0.3$  for A2163). This indicates that the clusters are dynamically evolved at least to this radius. The radius is approximately  $0.8r_{500}$  for Abell 1413,  $0.6r_{500}$

Abell 665 and about  $0.45r_{500}$  for Abell 2163. The virial radius is the radius out to which the cluster obeys the virial theorem. This supports the belief that Abell 1413 and Abell 665 are fairly relaxed evolved clusters, since their virial radius is a large fraction of  $r_{500}$ . It suggests that the cluster merger did not have significant effect on the overall morphology of Abell 665. Abell 2163, however does not seem to be dynamically relaxed and may have been more disturbed by its merger since it is not virialised to such a large extent of the cluster radius.

### 8.2.2 Abundance Profiles

The abundance profiles of the cluster are of interest as they give an indication of the location of metals in the cluster and also give an indication of whether there is mixing of the ICM. The three profiles are compared to each other in figure 8.2. It is clear that the three profiles all suffer from large uncertainties especially at large radii, and so all conclusions drawn from the data must be considered in light of these uncertainties.

The 3 abundance profiles for the clusters give evidence of the differences between the cluster morphologies. The profile for Abell 1413, which is thought to be the most relaxed cluster falls off most steeply with radius, with the metallicity tending to zero at large radii. This suggests that when the metals are stripped from the cluster galaxies they remain towards the centre of the cluster potential (this is also where most of the galaxies and therefore star forming regions are). This is a reasonable assumption because for relaxed clusters the thermal energy of the gas is of order the velocity of the galaxies. Therefore if there is nothing to mix the gas then it is likely to remain concentrated towards the centre of the cluster potential as seen here.

It is evident in both of the other clusters that some form of mixing has occurred as the abundance profiles in both cases do not drop off towards zero at large radii. For Abell 665 the process seems incomplete since the abundance is only maintained out to approximately 1 Mpc after which the abundance falls off slightly to a lower, but still

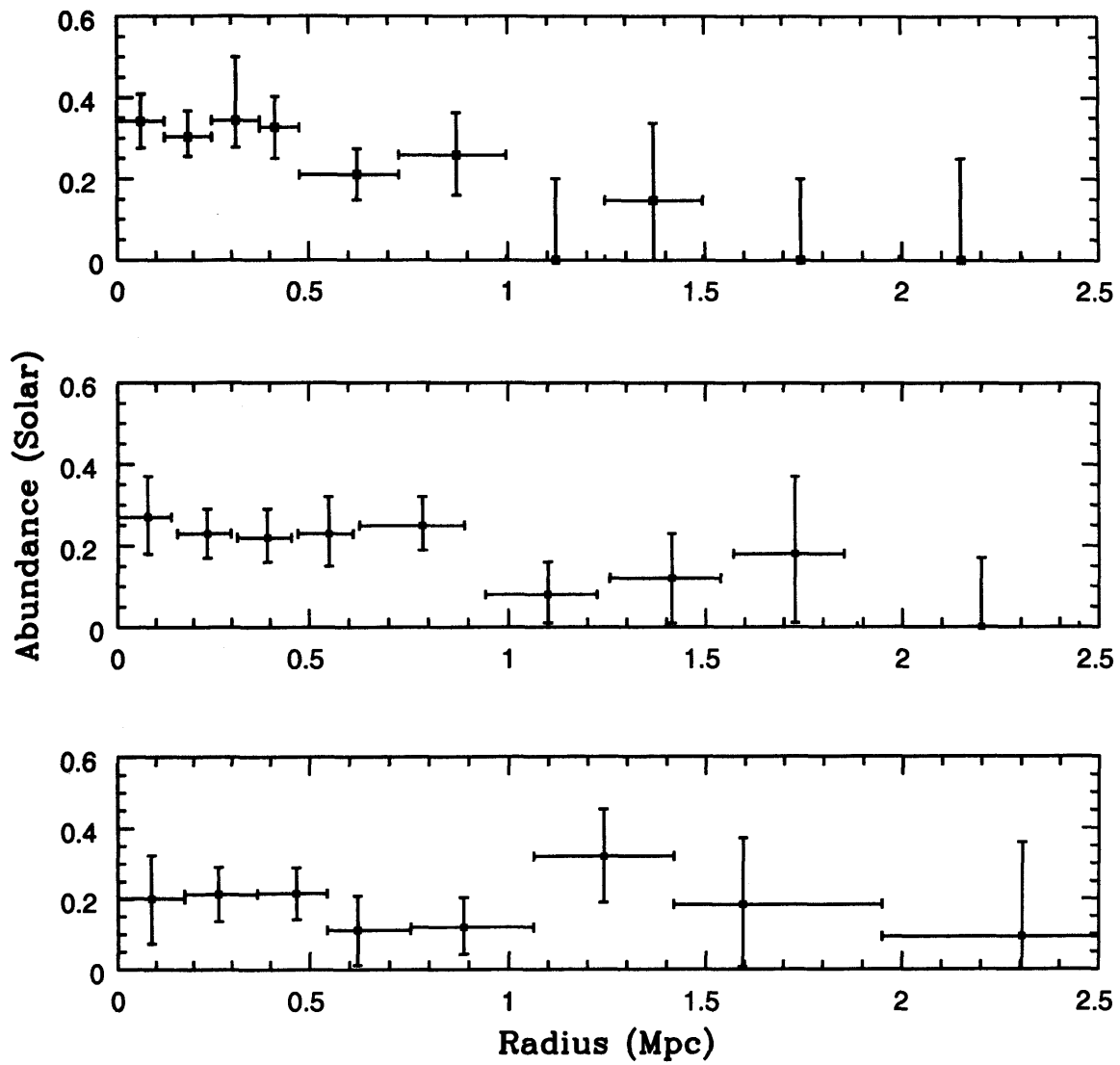


FIGURE 8.2. Comparison of abundance profiles for three clusters. The top profile is Abell 1413, the middle is Abell 665 and the bottom one is Abell 2163. This shows that the A1413 profile falls off steeply with radius whereas the others do not fall off much with radius.

roughly constant level. At very large radii there is some evidence that the abundance tends to zero, but the upper limit on the uncertainty at this radius is very large to the extent that the lower, roughly constant value is not ruled out. This suggests that some of the metal rich gas has been moved into the outer regions of the cluster, possibly via shocks that resulted from the cluster merger. The variation in the abundance on a local scale especially in the inner regions could be a result of the shocks causing renewed star formation in the cluster.

Abell 2163 shows even more variation on a local scale than Abell 665, but the global abundance value is approximately constant over the cluster. This suggests that the merger which happened in Abell 2163 was more violent than in Abell 665 and resulted in more mixing of the intra-cluster gas. On a local scale the shocks in the cluster could have resulted in renewed star formation, as is suggested for Abell 665, or could also result in gas being pushed out from the central regions of the cluster via the shock fronts. Either could result in localised regions of increased and decreased metallicity.

It is clear to see that the abundance profiles and the temperature profiles reveal different things about the cluster especially in the case of Abell 665. From the temperature profile it is not immediately evident that this cluster has undergone a merger since its profile is very similar to that of Abell 1413. However when the abundance profile is studied it is seen to be very different from that of Abell 1413 and suggests that the gas has been mixed by the merger, even though the temperature profile doesn't show much variation due to this. Abell 2163 appears to be very different from the other two clusters from its temperature profile, since it is a good deal hotter and doesn't show signs of a strong temperature decrease with radius. The abundance profile however, is fairly similar to that of Abell 665, showing that they do share some similarities in morphological structure.

Table 8.1. Gas mass and gravitational mass estimates at a radius of 2 Mpc and at  $r_{500}$  for the three clusters

Cluster	$M_{gas}$ ( $r=2$ Mpc) $10^{14}M_{\odot}$	$M_{grav}(r=2$ Mpc) $10^{14}M_{\odot}$	$r_{500}$ Mpc	$M_{gas}$ ( $r=r_{500}$ ) $10^{14}M_{\odot}$	$M_{grav}$ ( $r=r_{500}$ ) $10^{14}M_{\odot}$
A1413	$1.41 \pm 0.34$	$8.37 \pm 2.40$	$3.1 \pm 0.1$	$2.31 \pm 0.55$	$9.01 \pm 2.58$
A665	$1.80 \pm 0.43$	$8.27 \pm 3.37$	$3.2 \pm 0.1$	$3.28 \pm 0.78$	$9.95 \pm 4.06$
A2163	$3.44 \pm 0.95$	$12.54 \pm 6.54$	$6.6 \pm 0.1$	$18.94 \pm 5.11$	$87.9 \pm 75.0$

### 8.2.3 Gas and Gravitational Masses

The three clusters also have different gravitational and gas masses. The values of the gas mass and gravitational mass were calculated out to the corresponding radius of  $r_{500}$  for each cluster. The values of the two masses for the three clusters were as show in table 8.1. The values of the masses at 2 Mpc are also shown since  $r_{500}$  is at a different radius for each cluster and so is not directly comparable.

The gravitational masses for Abell 1413 and Abell 665 are similar at 2 Mpc, which is as expected since the temperature profiles, which enable estimates of the mass to be made, are very similar. At  $r_{500}$  Abell 665 is slightly more massive than Abell 1413, which seems to be a result of the temperature profile falling off a little more slowly for Abell 665, combined with the fact that the density profile falls off less steeply due to the lower value of  $\beta$  for this cluster. The gas mass is also larger for Abell 665, due to the low  $\beta$  and higher temperature. Abell 2163 is much more massive than either of the other two, which explains why it is the hottest cluster. The temperature profile is also increasing with radius for this cluster which means that the gravitational mass profile gets steeper with radius which is in contrast to the other two. The gas mass for this cluster is also much higher, but this cluster has a much higher core radius than the other two clusters, meaning that the gas mass and thus the surface brightness does not fall off as quickly as for other clusters with radius. More importantly the high cluster temperature combined with the recent merger suggests that not all of the cluster is in hydrostatic equilibrium and so the calculation of the gravitational mass in particular will be overestimated, particularly at

large radii where the cluster is less likely to be in hydrostatic equilibrium, and where the results have been extrapolated.

When the mass profiles are studied it is evident that the gravitational mass of Abell 2163 does not level off at high radius as is seen for Abell 1413 and Abell 665. This suggests that the dark matter potential of this cluster is larger than for the other two clusters. This is in fact required since the cluster is so hot and must therefore have a deeper potential well than the other clusters in order to retain the gas. The gas masses of the three clusters also follow the same trends as the gravitational mass although they don't level off with radius and their initial increase is not so steep. This suggests the visible part of the cluster extends out further than the dark matter potential.

A simplistic estimate of the galaxy mass of the cluster can be made if the number of galaxies in the cluster is known. From previous work the number of galaxies in Abell 1413 is 150 and in Abell 2163 is 119. Abell 665 has a richness of class of 5 and so contains at least 300 galaxies with some estimates quoting 1689 galaxies in the cluster (Wilson, Smail, Ellis & Couch 1997). In this case the lower limit of 300 galaxies is used for Abell 665 as it is likely that many of the other galaxies are dwarfs and so contribute less to the galaxy mass. If each galaxy is of order  $10^{11} M_{\odot}$  then the galaxy mass of Abell 1413 is  $1.5 \times 10^{13} M_{\odot}$ ; Abell 2163 is  $1.19 \times 10^{13}$  and Abell 665 is  $3 \times 10^{13}$  (which rises to  $1.6 \times 10^{14}$  if the upper galaxy number estimate is used). The galaxy mass is approximately a factor of 10 lower than the  $r_{500}$  gas mass for Abell 1413 and Abell 665 and a factor of 100 times lower for Abell 2163. This suggests that most of the visible matter in the clusters is in the form of intra-cluster gas, with only a small amount in the galaxies. This has implications for cluster formation and enrichment as it suggests that the galaxies were stripped of most of their gas fairly early on in the clusters history, enriching the ICM in the process. It also suggests that Abell 2163 has had more of its gas stripped from the galaxies than the other two clusters, which may have been a result of the merger, or a consequence of the high cluster temperature which will aid gas stripping, however this is very speculative given the optical data on the cluster (it lies close to the

galactic plane). A better estimate of the total galaxy mass could be made using a Press Schechter model, although even this model still contains some simplistic assumptions.

It is important to consider the masses of the cluster in context of other physical parameter as this gives us an indication of the values for important cosmological parameters such as  $\Omega_m$ . They also are used to gain M-L and L-T functions as are described in the following sections.

## 8.3 Global Implications

### 8.3.1 Supernovae and chemical enrichment

The hot X-ray emitting gas that surrounds cluster of galaxies is heavily enriched with iron. The iron mass luminosity ratio (Ishimaru and Arimoto, 1997 and references therein) suggests that most of the iron is created in cluster elliptical galaxies and then ejected into the ICM via supernovae (SN) driven galactic winds. Observations have shown that the iron abundance of the intra-cluster gas contained in rich clusters is approximately 25–50% (Finoguenov, David & Ponman 2000). Studies have also shown that the amount of iron contained in the cluster gas is several times larger than the amount locked up in stars. It has also been found that type II SN material is widely distributed throughout the intergalactic medium (IGM) which suggests that most of the ejecta was released early in the life of the cluster and released into the cluster via galactic winds. It has also been seen that rich clusters, such as the three investigated, retain their iron mass out to a large fraction of the virial radius. This is seen for all three clusters; in Abell 1413 the iron mass profile levels off at 2 Mpc (approximately  $0.8R_{vir}$ ); in Abell 665 and Abell 2163 the iron mass profile is still increasing out past the virial radius.

The comparison between the ICM iron mass and the total gas mass has also been extensively investigated. This has provided evidence that the some of the cluster gas must be primordial in origin as even if all the gas from SN was returned from the galaxies

into the ICM it would not be enough to explain the observed gas and iron masses (Chiosi 2000) and references therein. The gas mass was compared to the iron mass observed and it is clear that the two masses are strongly correlated and the correlation is related to the iron abundance. The three clusters lie on a line of approximately constant abundance, as has been seen for earlier studies (Chiosi 2000). This suggests that the three clusters have a similar amount of enrichment regardless of the cluster gas mass or the cluster richness (Abell 2163 is considerably less rich than Abell 665). It is difficult to reproduce this mass correlation via theoretical models as they tend to either underestimate the total gas mass or over estimate the iron abundance of the ICM. Multi-zone galactic models improve things by ensuring that in external regions of the galaxies a larger amount of gas is returned to the ICM. Also the amount of iron produced depends on the initial mass fraction (IMF) used in the models (eg Pettini et al 1997 as discussed in (Chiosi 2000). Whatever IMF is used however, some dilution of the metals by primordial gas is required. One thing that is clear from the results is that despite the differences in the abundance profiles and gas masses, the ratio  $M_{fe}/M_{gas} \sim \text{constant}$  which implies that star formation is not highly dependent on cluster environment.

It is also possible to estimate the number of SN than have occurred in the cluster from the iron mass. In order to do this the assumption is made that most of the gas expelled into the ICM was produced early (Finoguenov et al. 2000) and sent into the ICM via galactic winds. The abundance of the  $\alpha$  burning elements compared to iron in clusters suggests that the ICM is primarily enriched by SN type II (Mushotzky, Loewenstein, Arnaud, Tamura, Fukazawa, Matsushita, Kikuchi & Hatsukade 1996). Since SN Ia's are thought to produce mostly iron, the amount silicon present in the ICM constrains the amount of gas enriched by SN II's. The iron yield of SN II's is also known, and so using the silicon abundances an estimate of the iron produced by SN II's can be made. An estimate can then be made of how many SN Ia's are needed to produce the rest of the observed iron abundances. Since only information about the iron mass is found from this study and following the earlier assumption that the majority of gas was

produced early on in the cluster lifetime, it is also assumed that most of the enrichment is from SN II, which evolve quickly. The iron yield of SN II is  $0.07 M_{\odot}$  (Finoguenov et al. 2000). Based on these assumptions the numbers of SN II necessary to reproduce the observed  $r_{500}$  iron masses in the three clusters studied are:  $6.35 \pm 4.76 \times 10^9$  for Abell 1413;  $1.38 \pm 0.89 \times 10^{10}$  for Abell 665 and  $1.29 \pm 1.02 \times 10^{11}$  for Abell 2163. This is equivalent to a supernova rate of approximately a few per century in each galaxy which is consistent to what is seen in our own galaxy. These values are lower than those estimated by (Mushotzky et al. 1996) who predicts  $\sim 10^{12}$  SN II must have occurred to produce the required iron masses. Their estimate was based on assuming that a SN II with a  $25M_{\odot}$  progenitor (the mass weighted average of SN II) could enrich  $225M_{\odot}$  of primordial gas. More importantly they also assume that the iron distribution is constant across the cluster, which as has been seen is not generally the case, which could explain why they require a larger number of supernovae. Neither estimate takes into account the range in masses of the SN II progenitor, which is dependent on the IMF and causes a factor of 2-3 difference in the iron yield.

The three clusters are also of different richness, with Abell 665 being the richest cluster (class 5) with over 300 galaxies, (with some estimates as high as 1690 (Wilson et al. 1997)). Abell 1413 is less rich (class 3) with approximately 150 galaxies. Abell 2163 is the poorest (class 2) with only about 119 galaxies. From the number of galaxies it is expected that Abell 665 would have had the largest number of supernovae with at least a factor of two more than Abell 1413, which is as estimated. The number of supernovae calculated for Abell 2163 is factor of 10 larger than that of Abell 665 and a factor 20 larger than that of Abell 1413. It is however the poorest cluster and so therefore suggests that there is some process increasing the number of supernovae in this cluster. It is possible that the merger shocks in the cluster has increased the star formation, which in turn will increase the number of supernovae. However, it would take a significant amount of extra star formation to account for the difference in the number of supernovae in the cluster. It is also possible that the cluster has a strange IMF, which is skewed to

produce more high mass stars, however this is also fairly unlikely.

### 8.3.2 Mass-Luminosity Relation

The mass to luminosity ratio of clusters of galaxies is important as it is used as a method of estimating the mass density of the universe. When applied to rich clusters on average  $M/L_b \sim 300h$  which gives  $\Omega_m \sim 0.2$  where  $\Omega_m$  is in units of the of the critical density. This model assumes the mass to luminosity ratio of clusters is a fair representation of the universal value, if it is larger or smaller  $\Omega_m$  will be overestimated or underestimated accordingly (Bahcall & Comerford 2002).

The mass to luminosity ratio for a number of clusters observed with ROSAT is shown in figure 8.3. The results for Abell 1413 and Abell 665 have been added to this plot, using ROSAT luminosities taken from (Ebeling et al. 1996). These luminosities were used, as to compare with previous data luminosities in the ROSAT band were needed. Abell 2163 was not added to the plot as the estimated mass at  $r_{200}$  is very large and beyond the range of the plot, it would however lie below the general trend, being over massive for it's luminosity. The values seem consistent with the other results, with both clusters lying close to the line. The line of best fit for this dataset has an index of  $1.54 \pm 0.1$ . It is predicted that  $L_{bol} \propto M^{4/3}$  (Navarro, Frenk & White 1995) for a self similar relation and increases to  $L_{bol} \propto M^{11/6}$  for a pre-heating scenario. The results do not support a steep profile in either case as both results are very close to the line of best fit, with Abell 1413 lying slightly above it. This does not support the pre-heating scenario. It is possible to estimate the mass function of clusters from the  $L_x - M$  relation and from this estimate  $\Omega_m$ . For clusters obeying the relation plotted this gives a value of  $\Omega_m \sim 0.12 \pm_{0.04}^{0.06}$  (Reiprich & Bohringer 2002). Abell 1413 was previously analysed for the original graph, but had a higher mass estimate and slightly higher luminosity which put the value further up the plot, but still on the line of best fit.

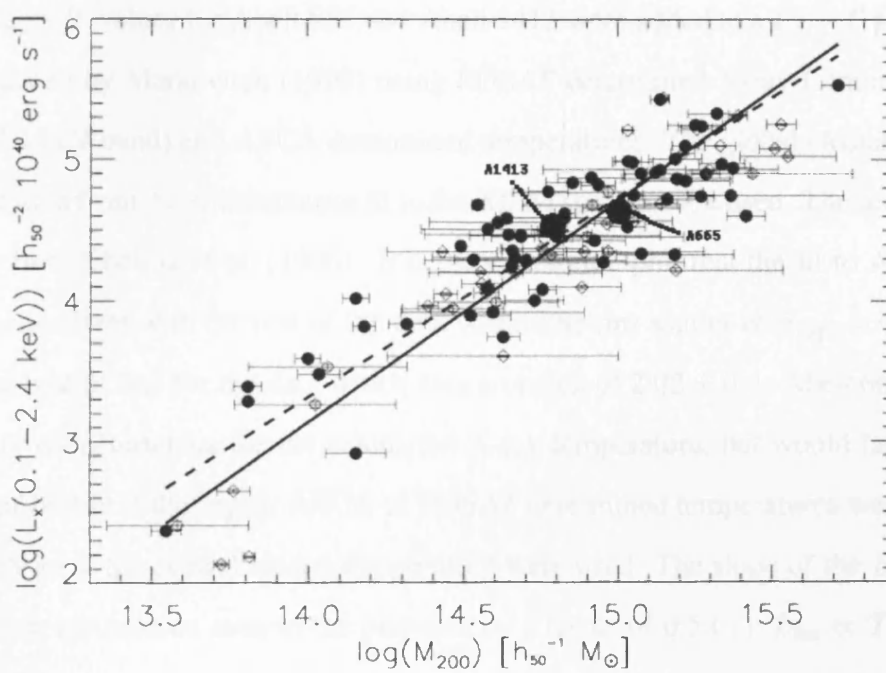


FIGURE 8.3. Luminosity Mass relation from (Reiprich & Bohringer 2002) with the two new data points added to the data (large filled circles).

### 8.3.3 Luminosity-Temperature relation

Observations have shown that clusters show a correlation between their Luminosity and Temperature of  $L_{bol} \propto T^3$ , which is different from the theoretical relation of  $L_{bol} \propto T^2$  Markevitch (1998) and references therein. This suggests that the gas distribution evolves in a different way to the dark matter. A possible reason for this could be pre-heating of the gas at the time when it was enriched with heavy metals. Pre-heating models are able to approximately reproduce the observed  $L_x - T$  relation.

The  $L_x - T$  values for Abell 665 and Abell 1413 were added to a  $L_x - T$  plot (figure 8.4) produced by Markevitch (1998) using ROSAT determined X-ray Luminosities (in the 0.1-2.4 keV band) and ASCA determined temperatures. The global cluster temperatures as found from the simultaneous fit to the XMM spectra were used. The luminosities used are from Ebeling et al. (1996). It is clear from the plot that the fit to Abell 1413 is about consistent with the rest of the data within the rms scatter of  $\sigma_{\log L} = 0.18$  but is above the best fit line for the data which uses an index of  $2.02 \pm 0.4$ . Abell 665 appears to be very over-luminous for the calculated X-ray temperature, but would fall close to the line of best fit if the higher ASCA or ROSAT determined temperatures were used ( $T \sim 8.3$  keV) or if the central cluster temperature were used. The slope of the  $L_{bol} - T$  is steeper than the relation seen in the plot data by a factor of 0.5 (i.e.  $L_{bol} \propto T^{2.52}$ ). The scatter in the graph is thought to be due to the difference between cooling flow clusters and regular clusters, (Fabian, Crawford, Edge & Mushotzky 1994) this scatter is reduced when the cooling flow region is removed from the fit. Since Abell 1413 is close to the line and only seems to contain a marginal cooling flow, this has not been corrected for in this fit.

It has been suggested that cluster merging has an effect on the luminosity temperature relation of clusters by steepening the slope. This is because shock heating increases the specific entropy of the cluster gas resulting in an energy injection equivalent to 0.5-0.8 keV per particle (Markevitch 1998). This would explain why Abell 665 sits above the observed luminosity temperature relation whilst Abell 1413 sits on the line. It has been

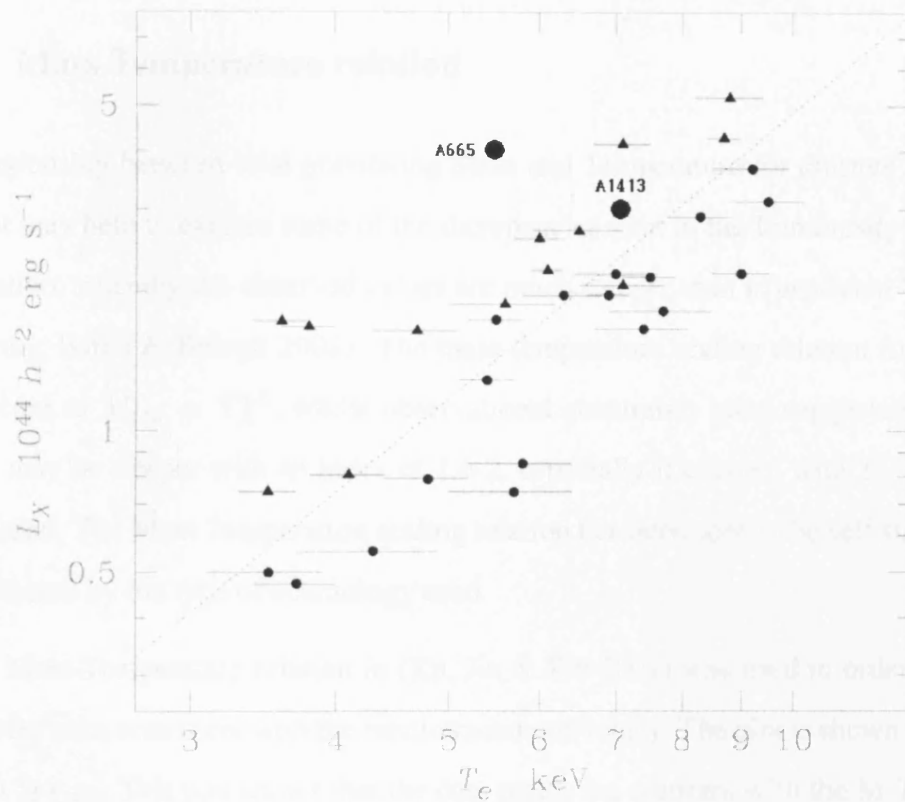


FIGURE 8.4. Luminosity Temperature relation from (Markevitch 1998) with the two new data points added to the data (large black circles) The errors on the temperature for these points are  $\pm 0.13$  keV and are of order the size of the points themselves.

seen that Abell 2163 is very hot and also very luminous, so much so that it was off the scale of figure 8.4 ( $L_x(0.1 - 2.4) \text{ keV} = 9.38 \times 10^{44} h^{-2} \text{ erg s}^{-1}$  for Abell 2163). This cluster is also a merging cluster and so it is expected that this cluster would also sit above the observed  $L_x - T$  relation as Abell 665 has been seen to do. However, the results show that Abell 2163, although it sits just above the line is consistent with the rest of the data at least as well as Abell 1413 is.

### 8.3.4 Mass Temperature relation

The relationship between total gravitating Mass and Temperature for clusters is important as it may help to explain some of the discrepancies seen in the Luminosity temperature relation, whereby the observed values are much steeper than is predicted by theory (McCarthy, Babul & Balogh 2002). The mass-temperature scaling relation for clusters is predicted as  $M_{gas} \propto T_X^{1.5}$ , whilst observational constraints have suggested that this relation may be steeper with an index of 1.6-2, especially if clusters with  $T_X \leq 4 \text{ keV}$  are included. The Mass Temperature scaling relation has been seen to be self similar and is not affected by the type of cosmology used.

The Mass-Temperature relation in (Xu, Jin & Wu 2001) was used in order to see if the clusters were consistent with the relation seen previously. The plot is shown in 8.5 for radii out to  $r_{200}$ . This plot shows that the data points are constant with the M-T relation seen in the paper, particularly for Abell 665 which sits on the line exactly. Abell 1413 is slightly below the line suggesting a shallower profile than is predicted. Abell 2163 was not included on the graph, since its value gravitational mass at  $r_{200}$  is extremely large. If it was included on the plot it would lie just on the trend. The index of the fit found by (Xu et al. 2001) was  $1.54 \pm 0.05$  for a  $\beta$  profile fit used to estimate the masses.

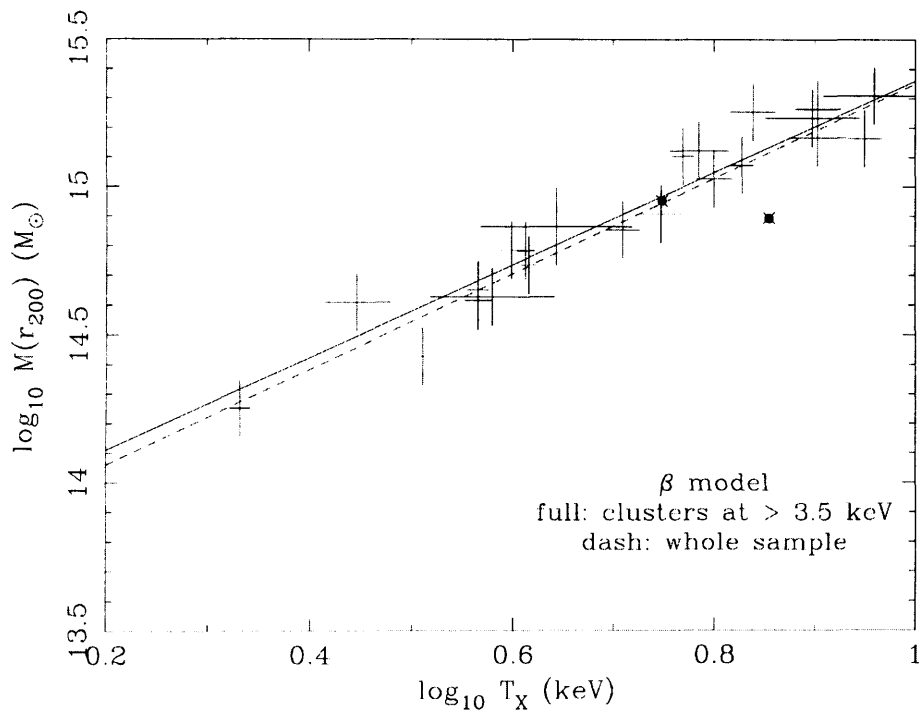


FIGURE 8.5. Mass Temperature relation from (Xu et al. 2001) with the two new data points added to the data (black circles)

### 8.3.5 Gas Mass fractions

The gas mass fractions of clusters of galaxies are useful, as using the assumption that most of the baryons in the cluster are located in the gas, it can be used to make an estimate of the baryon fraction. The baryon fraction in turn can be used to give an upper limit to the cosmological density parameter  $\Omega_0$  where  $\Omega_0 = \gamma(r_{500})\Omega_b/f_b(r_{500})$ , where  $\gamma \sim 0.91$  is the baryon depletion as estimated from simulations. The baryonic density of the Universe has been estimated from primordial nucleo-synthesis to be  $\Omega_b \sim 0.03 - 0.08h_{50}^{-2}$  (Sadat & Blanchard 2001). The gas mass fractions of clusters obtained from X-ray measurements are generally about 15-20 %. Theoretical arguments, such as inflation predict a flat universe with  $\Omega_0 = 1$ , whereas observational values predict  $\Omega_0 \sim 0.2 - 0.4$ . Therefore the baryon fraction seen in clusters are larger than those predicted for an  $\Omega_0 = 1$  universe. The uncertainties on the baryon density arise from the uncertainties in the measurements of the abundances of the light elements and a value of 0.08 is used, which assumes all the baryons in the cluster are seen (Sadat & Blanchard 2001).

For the three clusters out to a radius of  $r_{500}$  the gas mass fractions are  $0.25 \pm 0.05$ ,  $0.33 \pm 0.13$  and  $0.22 \pm 0.1$  for Abell 1413, Abell 665 and Abell 2163 respectively. This leads to values of  $\Omega_0$  of  $0.29 \pm 0.06$  for Abell 1413,  $0.22 \pm 0.08$  for Abell 665 and  $0.33 \pm 0.1$  for Abell 2163. These are consistent with the observational values seen by Sadat et al. These values suggest that we live in a low density universe, which is contrast to the theory which favors a value of  $\Omega_0$  closer to one. One explanation for this may be the difference in the  $f_{gas}$  profiles obtained from observations to those from numerical simulations. Observations have shown that the gas mass fraction profiles increase with increasing radius, as found for the Abell 1413 and Abell 665 data. Conversely the numerical simulations suggest that the gas mass profiles should flatten off in the outer regions approaching the universal value at the virial radius. The numerical simulations result is closer to what is seen with Abell 2163 where the gas mass fraction does not level off at large radii. It is clear that the results tend towards a low density Universe, but it is

important to take into account that the results are extrapolated in order to get them out to  $r_{500}$ . As has been seen the gas mass fraction estimates do not tail off at large radii, as has been predicted by simulations and so the gas mass fractions may be over-predicted by extrapolating to these radii and therefore under estimating  $\Omega_0$ .

## 8.4 Self Similarity

As has become evident from the three clusters of galaxies compared in this chapter, there are many deviations from self similarity in galaxy clusters, both in the measured and calculated parameters. It is evident that the temperature and abundance profiles of the cluster differ greatly between the three clusters and seem dependent on the individual morphologies of the clusters. The same is also seen with the spatial surface brightness profiles and therefore the mass estimates, as these are estimated using the spatially determined density profiles and the spectrally determined temperatures.

The deviations from self similarity seen in the three clusters studied imply that some of the approximations based on self similarity may not always be appropriate. It is clear in clusters such as Abell 2163, some of the approximations made do not seem valid, for example the estimate of the gas mass assumes that the cluster is in hydrostatic equilibrium. It is quite possible that this is not the case for Abell 2163 since the cluster is not fully relaxed and virialised. This would result in overestimates of the gravitational mass of the cluster, which from the results could have occurred. Also the assumption that all clusters can be modeled as isothermal spheres (used in the King model) has been shown to be inaccurate, as seen by the significant temperature gradients across the measured regions of the clusters.

When it comes to measuring cosmological parameters, clusters have been seen to follow certain trends of self similarity in that the M-T, L-M, and L-T relations follow the same general trends for all clusters. In most cases the results agree with these trends in the given scatter, agreeing particularly well for the L-M relation. However some of the

data points, particularly the temperature of Abell 665, seems to deviate by a significant amount. All of the scaling relations show a significant amount of scatter, suggesting deviations from self similarity are still evident.

If clusters of galaxies are not self similar as seems to be the case from the limited study then to improve on the estimates of parameters like cluster masses it may be necessary to remove some of the assumptions made in order to improve the accuracy of the calculated values. Otherwise a more careful application of the approximations is necessary in order to account for the differences between individual clusters.

## 8.5 Future Work

The XMM-Newton data for these three clusters has provided useful insights into the temperature and mass profiles of the three clusters. The data is also of limited use in determining cosmological parameters and metallicity variations in the clusters. It would be useful to extend on this work by looking at more clusters and therefore getting a better understanding of different cluster morphologies as well as providing tighter constraints on the cosmological parameters discussed. With 20 or 30 clusters it would be possible to produce results for the M-L, L-T and M-T scaling relations solely from XMM-Newton data. This would hopefully constrain their shapes more accurately than is possible by adding one or two clusters to plots obtained for different telescopes as it will account for any systematic differences between the telescopes such as calibration effects.

It would also be useful to have more long exposures of clusters in order to tie down more accurately temperature and abundance profiles out to large radii. This would be useful as it may then be possible to measure quantitatively the gas mass fraction out to radii closer to the virial radius, removing the need to extrapolate out to these radii and making it simpler to accurately reconcile the data with the theory, since it is difficult to tell if it is the extrapolation or the theory that is incorrect at the current time. It would also be advantageous to reduce the uncertainty on the abundance profiles as these put

large errors on estimates of the iron mass and therefore the enrichment of the cluster at different radii. Spatially, higher count rates will lead to better signal to noise which should reduce the errors in the radial surface brightness profiles which will hopefully lead to more accurate fits of the data using the spatial models.

Future missions such as XEUS, Astro-E2 and Constellation-X, will all be more sensitive than XMM-Newton and with them it may be possible to improve on the temperature and abundance estimates made with XMM-Newton. The micro-calorimeter on Astro-E2 which is due to be launched in 2005, will provide greatly improved energy resolution and so will hopefully provide more accurate estimates of these parameters. The improved resolution of XEUS and Constellation-X will enable better spatial resolution and the large effective area, particularly that of Constellation-X will enable estimates to be made out to larger fractions of the virial radius even for closer clusters, which are currently too large to observe out to large radii in a single observation.

To make improvements in the future it will also be important to improve on the models used to fit the data, in particular the spectral models for the cooling flow fits need to be improved to take into account why the gas stops cooling at 1 or 2 keV. In order to do this a better understanding of the physical processes, such as conduction, which are probably halting the cooling, is needed in order that the models can be correctly applied to the data. Spatial refinements to the NFW profile are currently being made by several groups in order to provide a better fit to the spatial data. This is necessary as although the King model fits the data well in most cases, it does not include all the physics considered necessary to correctly model the data.

# Bibliography

- AbdelSalem, H. M., Saha, P. & Williams, L. L. R. (1998), 'Non-parametric reconstruction of abell 2218 from combined weak and strong lensing', *The Astronomical Journal* **116**, 1541–1552.
- Abell, G. O. (1958), 'The distribution of rich clusters of galaxies', *Astrophysical Journal Supplement* .
- Allen, S. & Fabian, A. (1995), 'Cooling flows, central galaxy-cluster alignments, X-ray absorption and dust', *MNRAS* **275**, 741–754.
- Allen, S. W. (2000), 'The properties of cooling flows in X-ray clusters of galaxies', *MNRAS* **315**, 269–296.
- Anders, E. & Ebihara, M. (1982), 'Solar-system abundances of the elements', *Geochimica et Cosmochimica Acta* **46**, 2363–2380.
- Anders, E. & Grevesse, N. (1989), 'Abundances of elements -meteoritic and solar', *Geochimica et Cosmochimica Acta* **53**, 197–214.
- Austin, T. & Peach, J. (1974), 'Studies of rich clusters of galaxies -II the structure and luminosity function of A1413', *MNRAS* **168**, 591–602.
- Bahcall, J. N. & Sarazin, C. L. (1977), 'Parameters and predictions for the X-ray emitting gas of coma, perseus and virgo', *Astrophysical Journal* **213**.

- Bahcall, N. A. & Comerford, J. M. (2002), 'Anti-bias in clusters: The dependence of the mass to light ratio on cluster temperature', *The Astrophysical Journal* **565**, L5–L8.
- Bahcall, N. A., Fan, X. & Cen, R. (1997), 'Constraining  $\omega$  with cluster evolution', *The Astrophysical Journal* **485**, L53–L56.
- Benz, W. & Hills, J. G. (1992), 'Three dimensional hydrodynamical simulations of colliding stars. iii collisions and tidal capture of unequal-mass main-sequence stars', *The Astrophysical Journal* **389**, 546–557.
- Birkinshaw, M. (1999), 'The sunyaev-zeldovich effect', *Phys.Rept* **310**, 97–195.
- Burkert, A. (1995), 'The structure of dark matter halos in dwarf galaxies', *ApJ* **447**, L25–L28.
- Carroll, B. W. & Ostlie, D. A. (1996), *Modern Astrophysics*, Addison Wesley, chapter 26, pp. 1206–1214.
- Cavaliere, A. & Fusco-Femiano, R. (1976), 'X-rays from hot plasmas in clusters of galaxies', *A and A* **49**(1), 137–144.
- Chiosi, C. (2000), 'Gas and iron content of galaxy clusters', *Astronomy and Astrophysics* **364**, 423–442.
- Daultrey, S. (1976), *Principal Components Analysis*, Institute of British Geographers.
- David, L., Forman, W. & Jones, C. (1991), 'Enrichment and heating of the intracluster medium through galactic winds', *The Astrophysical Journal* **380**, 39–48.
- David, L. P., Slyz, A., Jones, C., Forman, W., Vrtilrk, S. & Arnaud, K. A. (1993), 'A catalog of inter-cluster gas temperatures', *ApJ* **412**, 479–488.
- Desert, F. (2002 (in press)), Sunyaev-zel'dovich effect review, in 'XXI Moriond Conference: Galaxy Clusters and the High Redshift Universe Observed in X-rays'.

- Diaferio, A., Kauffmann, G., Balogh, M. L., White, S. D. M., Schade, D. & Ellingson, E. (2001), 'The spatial and kinematic distributions of cluster galaxies in a lambda;cdm universe: comparison with observations', *MNRAS* **323**, 999–1015.
- DosSantos, S. (2001), 'Steady-state conduction-driven temperature profile in clusters of galaxies', *MNRAS* **323**, 930–938.
- Dressler, A. (1980), 'Galaxy morphology in rich clusters-implications for the formation and evolution of galaxies', *Astrophysical Journal* **236**, 351–365.
- Ebeling, H., Voges, W., Bohringer, H., Edge, A. C., Huchra, J. P. & Briel, U. G. (1996), 'Properties of the X-ray brightest abell-type clusters of galaxies (XBACs) from ROSAT all-sky survey data-I. the sample', *MNRAS* **281**, 799–829.
- Edge, A. C. (2001), 'The detection of molecular gas in the central galaxies of cluster cooling flows', *MNRAS* **328**, 762–782.
- Edge, A. C. & Stewart, G. (1991), 'EXOSAT observations of clusters of galaxies-part two-X-ray to optical correlations', *MNRAS* **252**, 428–441.
- Elbaz, D., Arnaud, M. & Bohringer, H. (1995), 'The gas distribution and binding mass in the a 2163 cluster', *Astronomy and Astrophysics* **293**, 337–346.
- Ettori, S. (1998), Studies of the distribution of gas in clusters and superclusters of galaxies, PhD thesis, University of Cambridge.
- Ettori, S. & Fabian, A. C. (2001), Cluster cores as observed with chandra, in 'Astroph/0110254'.
- Evrard, A. E., Metzler, C. A. & Navarro, J. F. (1996a), 'Mass estimates of X-ray clusters', *ApJ* **469**, 494–507.
- Evrard, A. E., Metzler, C. A. & Navarro, J. F. (1996b), 'Mass estimates of X-ray clusters', *ApJ* **469**, 494–507.

- Gomez, P. I., Hughes, J. P. & Birkinshaw, M. (2000), 'A merger scenario for the dynamics of abell 665', *The Astrophysical Journal* **540**, 726–740.
- Grainge, K. & Jones, M. (1996), 'A resolved image of the Sunyaev-Zel'dovich effect in Abell 1413', *MNRAS* **278**, L17–L22.
- HEASARC (2001), 'A subroutine interface to FITS format files for fortran programmers', online at [http://heasarc.gsfc.nasa.gov/docs/software/fitsio/c/f\\_user/fitsio.html](http://heasarc.gsfc.nasa.gov/docs/software/fitsio/c/f_user/fitsio.html).
- Helsdon, S. F. & Ponman, T. J. (2000a), 'Are X-ray properties of loose groups different from those of compact groups?', *MNRAS* **319**, 933–938.
- Helsdon, S. F. & Ponman, T. J. (2000b), 'The intragroup medium in loose groups of galaxies', *MNRAS* **315**, 356–370.
- Hughes, J. & Tanaka, Y. (1992), 'The X-ray spectrum of abell 665', *The Astrophysical Journal* **398**, 62–68.
- Irwin, J. A. & Bregman, J. N. (2000), 'Radial temperature profiles of 11 clusters observed with BEPOSAX', *The Astrophysical Journal* **538**, 543–554.
- Ishimaru, Y. & Arimoto, N. (1997), 'Roles of SN Ia and SN II in ICM enrichment', *PASJ* **49**, 1–8.
- Jones, C. & Forman, W. (1984), 'The structure of clusters of galaxies observed with einstein', *ApJ* **276**, 38–55.
- Katayama, H., Takahashi, I., Ikebe, Y., Matsushita, K., Tanaka, Y. & Freyberg, M. (2002), Properties of the background of EPIC onboard XMM-Newton, in F.Jansen, ed., 'New Visions of the X-ray Universe in the XMM-Newton and Chandra era'.
- King, I. (1966), 'The structure of star clusters. III. some simple dynamical models', *The Astronomical Journal* **71**, 64–75.

- Lloyd-Davies, E. J., Ponman, T. J. & Cannon, D. B. (2000), ‘The entropy and energy of intergalactic gas in galaxy clusters’, *MNRAS*.
- Lumb, D. (2002a), Epic in orbit background, *in* F.Jansen, ed., ‘New Visions of the X-ray Universe in the XMM-Newton and Chandra era’.
- Lumb, D. (2002b), In-orbit calibration of vignetting in EPIC, *in* F.Jansen, ed., ‘New Visions of the X-ray Universe in the XMM-Newton and Chandra era’.
- Lumb, D. (2002c), XMM-Newton calibration-an overview, *in* F.Jansen, ed., ‘New Visions of the X-ray Universe in the XMM-Newton and Chandra era’.
- Machacek, M. E., Bautz, M. W., C.Canizares & Garmire, G. P. (2002), ‘Chandra observations of galaxy cluster a2218’, *The Astrophysical Journal* **567**, 188–201.
- Markevitch, M. (1996), ‘Temperature structure of four hot clusters obtained with ASCA data’, *The Astrophysical Journal* **465**, L1–L4.
- Markevitch, M. (1998), ‘The  $L_x - T$  relation and temperature function for nearby clusters of galaxies’, *The Astrophysical Journal* **504**, 27–34.
- Markevitch, M., Forman, W., Sarazin, C. L. & Vikhlinin, L. (1998), ‘Temperature structure of clusters’, *The Astrophysical Journal* **503**, 76–96.
- Markevitch, M., Mushotzky, R., Inoue, H., Yamashita, K., Furuzawa, A. & Tawara, Y. (1996a), ‘Abell 2163: temperature, mass and hydrostatic equilibrium’, *The Astrophysical Journal* pp. 437–444.
- Markevitch, M., Mushotzky, R., Inoue, H., Yamashita, K., Furuzawa, A. & Tawara, Y. (1996b), ‘Abell 2163: temperature, mass and hydrostatic equilibrium’, *The Astrophysical Journal* **456**, 437–444.
- Markevitch, M. & Vikhlinin, A. (2001), ‘Merger shocks in galaxy clusters A665 and A2163 and their relation to radio halos’, *The Astrophysical Journal* **563**, 95–102.

- Markevitch, M., Vikhlinin, A., Forman, W. R. & Sarazin, C. L. (1999), 'Mass profiles of the typical relaxed galaxy clusters a2199 and a496', *The Astrophysical Journal* **527**, 545–553.
- Matthews, T. A., Morgan, W. W. & Schmidt, M. (1964), 'A discussion of galaxies identified with radio sources', *ApJ* **140**, 35–49.
- Maurogordato, S., Proust, D., Cappi, A., Slezak, E. & J.Martin (1997), 'A sample of galaxy clusters to study the fundamental plane: Redshift measurements', *Astronomy and Astrophysics* **123**, 411–422.
- McCarthy, I. G., Babul, A. & Balogh, M. L. (2002), 'The cluster  $M_{gas} - T_x$  relation: Evidence for a high level of pre-heating', *The Astrophysical Journal* **573**, 515–523.
- Mewe, R. (1994), *X-Ray Spectroscopy A physical Background of the Software Package SPEX*, SRON.
- Mewe, R. & Gronenschild., E. (1985), 'Calculated X-radiation from optically thin plasmas. V', *Astronomy and Astrophysics Supplement Series* **62**, 197–254.
- Mewe, R., Lemen, J., & van den Oord, G. (1986), 'Calculated X-radiation from optically thin plasmas VI.', *Astronomy and Astrophysics Supplement Series* **65**, 511–536.
- Mohr, J. J., Mathieson, B. & Evrard, A. E. (1999), 'Properties of the intracluster medium in an ensemble of nearby galaxies', *ApJ* **517**, 627–649.
- Molnar, S. M., Birkinshaw, M. & Mushotzky, R. F. (2002), 'Constraints in cosmological parameter space from the sunyaev-zel'dovich effect and thermal bremsstrahlung', *The Astrophysical Journal* **570**, 1–16.
- Morris, R. G. & Fabian, A. C. (2001), 'Inhomogeneous metallicities and cluster cooling flows', *Astro-ph/0108091* .
- Mushotzky, R., Loewenstein, M., Arnaud, K. A., Tamura, T., Fukazawa, Y., Matsushita, K., Kikuchi, K. & Hatsukade, I. (1996), 'Measurement of the elemental abundances

- in four rich clusters of galaxies. I. observations', *Astrophysical Journal* **466**, 686–694.
- Mushotzky, R. & Szymkowiak, A. E. (1988), Einstein observatory solid state detector observations of cooling flows in clusters of galaxies, in A. Fabian, ed., 'Cooling Flows in Clusters and Galaxies', pp. 53–62.
- Navarro, J. F., Frenk, C. & White, S. (1997), 'A universal density profile from hierarchical clustering', *The Astrophysical Journal* **490**, 493–508.
- Navarro, J., Frenk, C. & White, S. (1995), 'Simulations of X-ray clusters', *MNRAS* **275**, 720–740.
- Navarro, J., Frenk, C. & White, S. (1996), 'The structure of cloud dark matter halos', *The Astrophysical Journal* **462**, 563–575.
- Neumann, D. M. & Arnaud, M. (1999), 'Regularity in the X-ray surface brightness profiles of galaxy clusters and the M-T relation', *Astronomy and Astrophysics* **348**, 711–727.
- Noonan, T. (1972), 'The cluster of galaxies Abell 1413', *The Astronomical Journal* **77**(1), 9–12.
- Numerical, Algorithms & group (2002), 'Nag fortran library manual, mark 20', online at <http://www.nag.co.uk/muneric/fl/manual/html/mark20.html>.
- Oegerle, W. R. & Hill, J. M. (2001), 'Dynamics of cD galaxies IV conclusion of a survey of 25 abell clusters', *ApJ* **122**, 2858–2873.
- Pownall, H. R. (1997), *The Morphology of X-ray emission from Clusters of Galaxies*, PhD thesis, University of Leicester.
- Pratt, G. & Arnaud, M. (2001), 'XMM-Newton observations of galaxy clusters: The radial temperature profile of A2163', *astro-ph/0105431* .

- Pratt, G. W. & Arnaud, M. (2002), 'The mass profile of a1413 observed with XMM-newton: implications for the M-T relation', *Astronomy and Astrophysics (in press)*
- Press, W. H., Teukolsky, S. A., Vetterling, W. T. & Flannery, B. P. (1999), *Numerical recipes in Fortran 77*, Vol. 1, 2nd edn, Cambridge.
- Raymond, J. & Smith, B. (1977), 'Soft X-ray spectrum of a hot plasma', *Astronomical Journal Supplement series* **35**, 419–439.
- Reiprich, T. H. & Bohringer, H. (2002), 'The mass function of an X-ray flux limited sample of galaxy clusters', *The Astrophysical Journal* .
- Rood, H. J. & Sastry, G. N. (1971), 'Tuning fork classification of rich clusters of galaxies', *PASP* **83**, 313–319.
- ROSAT Users Handbook* (1996).
- Sadat, R. & Blanchard, A. (2001), 'New light on the baryon fraction on galaxy clusters', *Astronomy and Astrophysics* **371**, 19–24.
- Sarazin, C. (1986), 'X-Ray emission from clusters of galaxies', *Reviews of Modern Physics* **58**(1).
- Sarazin, C. (1988), *X-ray emission from clusters of galaxies*, Cambridge.
- Shapiro, P. R., Iliev, I. I. & Raga, A. C. (1999), 'A model for the post collapse equilibrium of cosmological structure: truncated isothermal spheres from top-hat density perturbations', *MNRAS* .
- Shu, F. (1982), *The Physical Universe*, University Science Books.
- Snowden, S. L. & Kuntz, K. D. (1994, Revised 1998), *Cookbook for Analysis Procedures for ROSAT XRT observations of Extended Objects and the Diffuse Background, Part I: Individual Observations*.

- Spurgeon, L. E., DosSantos, S. & Stewart, G. C. (2002, in press), PCA of cluster surface brightness profiles, in 'Tracing Cosmic Evolution with Galaxy Clusters'.
- Struble, M. F. & Rood, H. J. (1982), 'Morphological classification (revised rs) of abell clusters in d<sub>4</sub> and an analysis of observed correlations', *Astronomical Journal* **87**, 7–46.
- Struble, M. F. & Rood, H. J. (1983), 'Binary galaxy rich clusters of galaxies', *Astr.soc.pacific.mercury* **12**(4), 105.
- Struble, M. F. & Rood, H. J. (1987), 'A catalog of morphological properties of the 2712 abell clusters', *Astrophysical Journal Supplement Series* **63**, 555–613.
- Tamura, T., Peterson, J. S. K. J. R., Paerels, F. B. S., Mittaz, J. P. D., Trudolyubov, S. P., Stewart, G., Fabian, A. C., Mushotzky, R. F., Lumb, D. H. & Ikebe, Y. (2001), 'X-ray spectroscopy of the cluster of galaxies abell 1795 with xmm-newton', *Astronomy and Astrophysics* **365**, L87–L92.
- The XMM users handbook* (1999), 1:1 edn.
- Tremaine, S. (1987), Summary-structure and dynamics of elliptical galaxies, in 'Structure and Dynamics of Elliptical Galaxies IAU Synp', pp. 367–373.
- Vikhlinin, A., Forman, W. & Jones, C. (1999), 'Outer regions of the cluster gaseous atmospheres', *ApJ* **525**, 47–57.
- Voigt, L. M., Schmidt, R. W., Fabian, A. C., Allen, S. W. & Johnstone, R. M. (2002), 'Conduction and cooling flows', *submitted to MNRAS astro-ph/0203312*.
- White, D. (2000), 'Deconvolution of ASCA X-ray data - II. radial temperature and metallicity profiles for 106 galaxy clusters', *MNRAS* **312**, 663–688.
- White, D., Jones, C. & Forman, W. (1993), 'An investigation of cooling flows and general cluster properties from an X-ray image deprojection analysis of 207 clusters of galaxies', *MNRAS* **292**, 419–467.

Wilson, G., Smail, I., Ellis, R. S. & Couch, W. J. (1997), 'The faint end of the galaxy luminosity function in moderate-redshift clusters', *MNRAS* **284**, 915–930.

*XMM European Photon Imaging Camera (EPIC)* (1999).

*XMM X-ray mirrors* (1999).

Xu, H., Jin, G. & Wu, X. (2001), 'The mass temperature relation of 22 nearby clusters', *The Astrophysical Journal* **553**, 78–83.

Xue, Y.-J. & Wu, X.-P. (2000), 'Properties of the double beta model for intracluster gas', *MNRAS* **318**, 715–723.

Zwicky, F., Herzog, E. & Wild, P. (1961), *Catalogue of Galaxies and Clusters of Galaxies*, Pasadena: CIT.